Ph.D. thesis

Programa de doctorat dels Estudis Oficials de Postgrau: Doctorat de Física

UNIVERSITAT DE BARCELONA

Magnetized Dense Cores

Observational characterization
and
comparison with models

Pau Frau Méndez

Advisors: Dr. J. M. Girart, Dr. M. T. Beltrán

Tutor: Dr. R. Estalella

Thesis committee: Dr. J. Alves, Dr. D. Galli, Dr. S. Viti

Barcelona, Catalunya

June 2012

An es qui m'han donat sa vida

Sa natura és es millor mestre de sa veritat

El Món és un llibre, i aquells que no viatjen en llegeixen només una pàgina

Sant Agustí

Agraïments

Aquesta secció és sa última que escric de sa tesi, no per deixadesa, sinó per ser sa més difícil. Al llarg de quatre anys i busques han passat moltes coses, he fet moltes coses i he anat a molts llocs. Tot aquest conjunt d'experiències ha influït en es resultat final que no és altre que aquesta tesi. Així i tot, són ses persones que he conegut al llarg d'aquest període ses que l'han fet especial, i és an aquestes persones a ses qui no puc manco que agrair sa contribució, suport i ànims que m'han regalat. Me permet es luxe d'escriure en mallorquí aquest apartat tan personal, encara que intentaré personalitzar els agraiments a cadascú en sa llengua en sa que mos hem comunicat.

En primer lloc, es meu agraïment an es meus directors de tesi, Josep Miquel i Maite. Sobre es paper, dos investigadors de renom mundial amb molta experiència en recerca, com a *referees*, com a membres de *TACs* . . . Sobre es paper, garantia d'esperit crític i gust per sa feina ben feta. A sa realitat, això i molt més. Vos agraesc s'haver-me introduït an es món de sa formació estel·lar i de sa investigació. Haver-me ensenyat sa major part de lo que he après en aquest camp, aconsellat amb paciència i donat suport sempre que el necessitava. M'heu posat en contacte amb grups de recerca i investigadors punters, enviat a escoles i conferències, tot a nivell mundial i sense donar un no per resposta quan he estat jo qui ho proposava. M'heu preparat de forma excel·lent. Gràcies.

Vull agrair an es membres des grup de formació estel·lar sa seva ajuda i consells durant aquests anys: Robert, Chema, Rosario, Óscar, Àngels, Inma i Aina. També agraesc an els estudiants des grup sa relació que hem establert al llarg d'aquests anys, an es que a més d'hores de feina hem compartit grans moments d'oci (parcs naturals de Taiwan, una boda a Brasil, platges de Mallorca . . .). Gemma, Josep Maria, Felipe i Álvaro, heu fet que fer feina an es grup sigui quelcom més que feina.

Vorrei ringraziare gli Arcetrini che hanno fatto delle mie permanenze dei grandi periodi. A Daniele, con cui ho imparato tantissimo e che è stato quasi come un co-direttore quando sono stato lì. Ringrazio anche Riccardo, Claudio, Luca, Fabrizio e tanti altri. Ai Chelazziani per i due autunni speciali: Enrico, Andrea, Alessandro, Marco, Mari, Melo . . . Alle compagne di ufficio dell'osservatorio: Rosa, Elisabetta e Ana, che hanno reso le mie permanenze molto gradevoli. Infine a Marco, con cui abbiamo preso tanti caffè e fatto chiacchiere antistress sul piazzale di Arcetri ed a Barcellona.

I would like to thank the CfA people for a great three-month period in Boston. Qizhou and Izaskun, I learned a lot from you and your careers are truly inspiring. Roberto, me enseñaste Boston y también como trabaja un estudiante muy motivado. Sin esperarlo me encontré un amigo, mi estancia no habría sido lo mismo sin ti.

Katharina, ich danke dir für die schönsten Momente in Boston und überall wo wir zusammen waren. Ich habe eine wunderbare Freundin gefunden, die meinen Aufenthalt in den Staaten sehr angenehm gemacht und mich während der manchmal schwierigen Momente meiner Doktorarbeit immer unterstützt hat. Vielen Dank für alles!

La mayoría de los datos de esta tesis (cinco de los seis artículos) se obtuvieron con la antena IRAM 30-m a lo largo de múltiples visitas. En ellas conocí a un grupo de personas capaz de hacer reír y olvidar el trabajo incluso tras una semana bajo tres metros de nieve. Quiero agradecer al personal del 30-m su hospitalidad y buen hacer durante mis estancias, además de la fabulosa comida: Juan, Salvador, Manolo, Quique, Frederic, Ignacio, Joaquín, Víctor, Paco, Pepe, Esther, Isabel, Rosa, Carmen, M. Carmen … Perdonadme si me dejo a alguien.

Vull agrair an es personal de secretaria de s'ICE i des DAM sa seva feina lluitant contra sa burocràcia per jo: Isabel, Delfi, Josefa, J.R., Rosa i Montse. També an els informàtics, Josep, Jordi i Gabi, per enfrontar-se contra internet i linux (que no mac) per jo. Sense voltros sa tesi hauria estat molt més difícil.

He d'agrair an els estudiants des DAM moltíssimes hores d'estar junts, dinars, sopars, cafès, berenars, aniversaris, i demés activitats que hem anat fent durant aquests anys. Jordi, Sinué, Javi M., Víctor, Albert, Benito, Rosa, Neus, Carme, Laura, Javi C., Nàdia, Héctor, Andreu F., Andreu P., Maria, Marisia, Adolfo, Kike, Santi … Me sap greu si m'he deixat a qualcú … Heu fet que ses estones de desconnexió de sa feina siguin molt agradables.

He d'agrair an els amics fets durant sa carrera a sa UIB es suport que m'han donat durant aquests anys cada vegada que he tornat a Mallorca, i es bons moments que hi hem passat junts: Min, Pi, Toni i Felipe, gràcies. També an els que, coneguts a sa UIB, m'estan acompanyant encara: Pere i Victori, a més de fer que no me "catalanitzi" hem passam grans moments a Barcelona, gràcies.

Gran part de sa "culpa" de que hagi fet es doctorat la tenen els amics de tota sa vida, es que m'acompanyen des de s'època de s'institut, inclús de s'escola, i esper que encara durant molts anys més. Erem sa "promoció bona", volíem ser es millors, i a més d'aconseguir-ho mos n'hem enduit un gran grup d'amics que hem anat ampliant. Aquesta és una tesi més de ses cinc que començaren com a discussions de cafè i gelat, billar i *futbolín*, fa més de deu anys a Porto Pi. Víctor, Toni, Javi, Llucia, Lorena i Júlia, moltes gràcies! Miquel, a tu en especial t'he d'agrair tot lo anterior i moltes discussions "transcendentals" que han estat bàsiques, encara que no ho sabis, en alguns moments d'aquests anys, gràcies per estar sempre allà.

Agraesc an es meus germans que m'han aguantat tots aquests anys. Carme, Gabriel i Lida, sempre m'heu rebut amb es braços oberts quan he tornat a sa roqueta i m'heu fet recordar lo bé que s'està a casa. Xerrar, riure, jugar, molestar-mos, enfadar-mos ... Feis que Mallorca sigui més que una illa.

Finalment, agraesc profundament an es meus pares s'estar sempre allà, i els hi dedic aquest treball. En sou es vertaders responsables. Mentre vaig estar amb voltros vareu fer que no m'hagués de preocupar mai de res que no fos créixer, en tots es sentits. M'heu donat ses bases per ser qui som, coneixement per decidir i força per aconseguir. Sempre hi sou, sempre sabeu escoltar i sempre sabeu aconsellar. Heu estat pilars fonamentals de tot aquest procés. Vos estim!

The work presented here was done under the affiliation of the *Institut de Ciències de l'Espai* (ICE) funded by the *Centro Superior de Investigaciones Científicas* (CSIC) from the *Gobierno de España* and the *Institut d'Estudis Espacials de Catalunya* (IEEC). This thesis was done within the Doctorate Program of the *Departament d'Astronomia i Meteorologia* of the *Universitat de Barcelona* with the financial support of a FI predoctoral fellowship (2008FI_A00344) funded by the *Agència de Gestió d'Ajuts Universitaris i de Recerca* (AGAUR) from the *Generalitat de Catalunya, Departament d'Innovació Universitat i Empresa*, during the initial seven months, and a FPU predoctoral fellowship (AP2007-01001) funded by the *Ministerio de Ciencia e Innovación* (MICINN) from the *Gobierno de España* during the final three years and a five months. Partially supporting sources of this work were the MICINN research projects AYA2008-06189-C03 and AYA2011-30228-C03, and the AGAUR research project 2009SGR1172.

Contents

Resum en català **xv**

I Introduction & aims 1

1 The raw materials and the factories of stars **3**

1.1 Components of the interstellar medium 3

1.1.1 Interstellar dust 3

1.1.2 Interstellar gas 4

1.2 Molecular clouds: the sites of star formation 5

1.3 Observational tools at radio wavelengths 7

1.3.1 Spectral line emission 7

1.3.2 Continuum emission from interstellar dust 8

2 Low-mass star Formation **11**

2.1 Protostellar evolution: from molecular clouds to protostars 11

2.2 Classification of low-luminosity Young Stellar Objects 14

3 Dense cores **17**

3.1 Physical structure in equilibrium 17

3.1.1 Isothermal sphere in hydrostatic equilibrium 17
3.1.2 The Jeans criterion 23
3.1.3 Magnetic field support 24
3.1.4 Support from MHD waves 28
3.1.5 Empirical fits 32
3.2 Dynamical evolution 33
3.2.1 Inside-out collapse 33
3.2.2 Magnetized configurations 35
3.2.3 Rotating configurations 40
3.2.4 First core and protostar overview 41
3.3 Chemical properties 42
3.3.1 Observations 42
3.3.2 Models 43
3.3.3 Freeze-out secondary effects 44

4 Aims, selected sources and work plan 47

4.1 Context 47
4.2 Aims 48
4.3 Selected sources 49
4.3.1 Pipe nebula starless cores 49
4.3.2 NGC 1333 IRAS 4A 52
4.4 Work plan 53
4.4.1 Strategy 53
4.4.2 Selected telescopes 55

II Publications & conclusions 59

5 Starless cores in the magnetically dominated Pipe nebula I. Narrow band high spectral resolution observations 61

Continuum and molecular line emission I [ApJ, 723, 1665 (2010)] 63

Continuum and molecular line emission II [Submitted to ApJ] 77

6 Starless cores in the magnetically dominated Pipe nebula II. Wide band low spectral resolution observations 95

Chemical differentiation of the Pipe nebula starless cores [A&A, 537, L9 (2012)] 97

7 Starless cores in the magnetically dominated Pipe nebula III. Physical structure 103

Physical structure of the Pipe nebula starless cores [To be submitted to A&A] 105

8 Barnard 59 111

Barnard 59: no evidence for further fragmentation [ApJ, 747, 149 (2012)] 113

9 The collapsing magnetized cloud in NGC 1333 IRAS 4A 119

Comparing models with interferometric observations [A&A, 535, A44 (2011)] 121

10 Summary and conclusions 135

10.1 Summary of results and conclusions 136

10.2 General conclusions 139

10.3 Future prospects 140

References 143

List of Figures

2.1 Stages of low-mass formation 13

2.2 Classification of young stellar objects 14

3.1 Numerical solution of the Bonnor-Ebert density profile 19

3.2 Radial column density profile of Barnard 68 20

3.3 Stability analysis of a Bonnor-Ebert sphere 21

3.4 Radial column density profiles of four Bok globules 22

3.5 Equilibrium configurations of magnetized clouds 26

3.6 Magnetized collapse critical mass 27

3.7 Empirical fit to the dense core density profile 32

3.8 Radial distribution of velocity in a collapsing Bonnor-Ebert sphere 33

3.9 Collapse expansion wave of an isothermal sphere 34

3.10 Mass-to-flux distribution of a dense core 37

3.11 Time evolution of an infalling spherical dense core 38

3.12 Inner region of an infalling magnetized toroid 39

3.13 Evolution of a star-forming core 41

3.14 Selective molecular freeze-out onto grains 43

3.15 Gas-phase chemistry in a contracting Bonnor-Ebert sphere 45

4.1 Extinction map and large-scale magnetic field of the Pipe nebula 49
4.2 Extinction map of Barnard 59 51
4.3 Multiscale maps of NGC 1333 IRAS 4A 52

List of Tables

1.1 Phases of the gas content in the interstellar medium 4

1.2 Physical parameters of molecular clouds 6

1.3 Some useful interstellar molecules and physical parameters of some transitions . . . 8

4.1 Telescopes used in this thesis 56

List of Acronyms

2MASS	Two Micron All Sky Survey
ALMA	Atacama Large Millimeter Array
A_V	visual extinction
B59	Barnard 59
B68	Barnard 68
BE	Bonnor–Ebert
BIMA	Berkeley Illinois Maryland Association
CMF	Core Mass Function
FTS	Fast Fourier Transform Spectrometer
GMC	Giant Molecular Cloud
HPBW	Half Power Beam Width
ISM	InterStellar Medium
IR	InfraRed
IRAM	*Institut de RadioAstronomie Millimétrique*
IRAS	InfraRed Astronomical Satellite
IMF	Initial Mass Function
LOS	Line-Of-Sight
LTE	Local Thermodynamic Equilibrium
MHD	Magneto-HydroDynamic
PI	Principal Investigator
POS	Plane Of the Sky
SED	Spectral Energy Distribution
SIS	Singular Isothermal Sphere
SMA	SubMillimeter Array
rms	root mean square
YSO	Young Stellar Object

Resum en català

1 Introducció

1.1 De la Via Làctia als nuclis densos

La **Via Làctia**, la nostra Galàxia, està formada per tres components visibles: un disc aplanat d'un radi aproximat de 25 kpc i una alçada de uns 250 pc, una bulb central dens d'uns 3 kpc de radi, i un halo molt estès constituït per grups globulars i estrelles velles. El nostre Sol i el sistema solar estan situats a una distància de 8.5 kpc del centre galàctic, dins de l'estructura de braços espirals del disc galàctic. La major part de la massa de la Galàxia es troba concentrada a les prop de $\sim 10^{11}$ estrelles que la conformen, però, amb una densitat mitjana de una estrella per pc^3, representa una petita part del seu volum total. El medi interestel·lar és la matèria que omple l'espai entre les estrelles i constitueix només l'1% de la massa de la Galàxia. Aquesta matèria difusa està formada principalment per dos components: una fase sòlida o pols interestel·lar, i una fase gasosa o gas interestel·lar.

Els grans de **pols interestel·lar** són extremadament petits, amb mides des de 0.01 a 1 μm, i de forma irregular. Estan formats per nuclis de silici, carboni i/o ferro amb un mantell de gel format bàsicament per aigua i monòxid de carboni. La pols interestel·lar és capaç d'interactuar amb la llum incident produint tres efectes diferenciats: extinció, envermelliment i polarització. L'extinció es dóna quan els grans de pols absorbeixen la llum de longituds d'ona similars a la seva mida que després reemeten al rang de l'infraroig i ràdio. Aquest efecte depèn de la densitat i mida del material a travessar, pel que les regions més denses de la Galàxia generen taques fosques que contrasten amb el fons brillant d'estrelles. L'envermelliment es produeix perquè les longituds d'ona més blaves són dispersades amb més facilitat, pel que la llum que rebem en conté menys. Finalment, la polarització es genera quan els grans de pols asfèrics en rotació s'alineen amb el camp magnètic. Quan l'eix del gra de pols amb major moment angular és perpendicular al camp magnètic i a l'eix de rotació, el moment de forces es fa zero i el sistema s'estabilitza. Això implica que els grans de pols s'alineen perpendicularment al camp. A longituds d'ona òptiques els vectors de polarització són paral·lels al camp magnètic ja que en la direcció perpendicular la llum és absorbida pels grans. Al rang (sub)mil·limètric, la radiació prové de la reemissió dels grans de pols i està, per tant, polaritzada en la direcció perpendicular al camp.

El **gas interestel·lar** té ∼160 vegades més massa que la pols i $\sim 10^{12}$ vegades més partícules, pel que n'és el component principal. Està format principalment per hidrogen, que es pot trobar en diferents fases: atòmic (H_{I}, aproximadament la meitat de la massa), molecular (H_2, aproximadament l'altra meitat) i ionitzat (H_{II}). A banda de l'hidrogen, més d'un centenar de molècules s'han detectat al medi interestel·lar. Les més comunes són monòxid de carboni (CO), amoníac (NH_3), aigua (H_2O) i hidroxil (OH). L'hidrogen atòmic està localitzat al disc galàctic en grumolls freds i densos anomenats núvols H_{I}, o bé en forma calenta i difusa, no confinada, ocupant un 50% del volum total de la Galàxia. L'hidrogen molecular és el més abundant però es troba a molt baixes temperatures (∼20 K), el que fa que no sigui observable directament. Per tant, la seva presència s'infereix a partir d'observacions de CO usant abundàncies relatives calibrades. Multitud de sondejos amb CO localitzen el gas molecular molt proper al disc galàctic, majoritàriament en forma de núvols confinats. Aquests unitats, anomenades núvols moleculars, tenen un gran protagonisme donat que són el lloc on es dóna el procés de formació d'estrelles.

Els **núvols moleculars** són regions fredes (10–30 K) i denses (10^3–10^5 cm^{-3}) de mida variable (0.1–100 pc). Malgrat contenir el 50% de la massa de la Galàxia en representen un volum negligible. Es poden classificar en diversos tipus en funció de l'extinció visual (és a dir, de la densitat) que presenten: difusos, núvols moleculars gegants, núvols foscos i nuclis densos. Els núvols difusos presenten extincions molt baixes i són una petita fracció del gas molecular on no es dóna formació estel·lar. En canvi, als núvols gegants moleculars és on aquest procés es dóna majoritàriament. Aquests últims contenen prop del 80% del gas molecular, es troben als braços espirals, poden mesurar fins a 100 pc i contenir masses de fins a $10^7\ M_{\odot}$ (Elmegreen, 1985, 1993). Una estructura tan massiva és capaç de mantenir-se lligada per acció de la seva pròpia força gravitatòria però, per altra banda, necessita ésser contrarestada per forces de sustentació per evitar que el núvol col·lapsi sobre si mateix. La pressió tèrmica del gas és insuficient pel que altres mecanismes, tals com forces magnètiques o la turbulència del núvol, estan actius evitant el col·lapse. Una vegada començat el procés de formació estel·lar s'estima que el núvol sobreviu $\sim 3\times 10^7$ anys abans d'ésser destruït per l'efecte dels vents de les estrelles O i B formades al seu interior. Observats amb detall, els núvols moleculars gegants presenten estructura interna en forma de filaments i grumolls (Williams et al., 2000). L'organització és jeràrquica amb estructures menors a l'interior d'estructures de major escala. Els grumolls poden ser massius, d'uns parsecs i milers de masses solars, que poden originar una granja d'estrelles; o petits nuclis densos, amb una mida típica de ∼0.1 pc i massa de $\sim 1\ M_{\odot}$, amb capacitat per formar estrelles aïllades o un petit sistema múltiple (Myers, 1985; André, Ward-Thompson, & Barsony, 2000). Aquests últims cossos, els nuclis densos, són l'objecte d'estudi d'aquesta tesi.

1.2 Formació estel·lar de baixa massa

La formació estel·lar es divideix tradicionalment en dues branques diferenciades. Per una banda hi ha les estrelles anomenades de **baixa massa** ($M < 8M_{\odot}$) que presenten lluminositats dominades per l'acreció de material, i es poden formar ja sigui de forma aïllada com en granges. L'altre grup el constitueixen les estrelles d'alta massa ($M > 8M_{\odot}$) que es formen mitjançant mecanismes diferents, és a dir, a nuclis massius que contenen a la vegada sub-nuclis que produiran un grup d'estrelles. La tesi s'enfoca en l'estudi de la formació estel·lar de baixa massa.

A petites escales (fraccions de parsec) sembla que la única pressió que actua de forma eficient contra l'acció de la gravetat és la pressió tèrmica. Per tant, les condicions ideals per a la formació estel·lar són una combinació de baixa temperatura i alta densitat. Ambdues condicions s'acompleixen als nuclis densos i dos models bàsics s'han proposat per explicar-ne la possible evolució. Ambdós models prediuen que una petita part de la massa amb densitat suficient pot iniciar el procés, i que aquest és isoterm durant un temps considerable. Inicialment es va proposar un model de col·lapse ràpid (Hayashi, 1966; Larson, 1969) basat en un nucli marginalment inestable on les capes externes col·lapsen i el procés avança cap a les capes internes. Es caracteritza per un creixement desmesurat de la densitat central i prediu perfils de velocitat, densitat i temperatura en forma de lleis de potències. Posteriorment, es va proposar el model quasi-estàtic explicat amb més detall a la següent secció. Assumeix que el nucli està inicialment estabilitzat pel camp magnètic i es contreu gradualment mitjançant el procés de difusió ambipolar (Shu, 1977; Shu et al., 1987). El perfil de densitat esdevé el d'una esfera singular isoterma ($\rho \propto r^{-2}$) que, una vegada assolit, detona el procés de col·lapse que avança des de les capes internes cap a les externes. El radi al qual les capes comencen a col·lapsar es propaga cap a l'exterior en forma d'ona sonora, amb el material d'aquesta regió accelerat fins arribar a la velocitat de caiguda lliure produint un perfil de densitat de la forma $\rho \propto r^{-3/2}$.

El model més acceptat és el del **col·lapse quasi-estàtic** de Shu (1977). Segons aquest model, l'evolució típica passa per quatre fases diferenciades representades a la Figura 2.1. En primer lloc, (a) el núvol molecular es fragmenta i forma nuclis densos en lleugera rotació. Al següent pas, (b) un nucli dens en procés de condensació quasi-estàtica comença el procés de col·lapse de dins cap a fora i forma una protoestrella al centre amb un embolcall de gas i pols. Posteriorment, (c) els vents estel·lars frenen el material en caiguda en la direcció de l'eix de rotació, que és ejectat en forma de flux molecular col·limat pels pols. Finalment, (d) el flux molecular obre l'angle a mida que evoluciona. En aquesta fase, la massa de gas i pols ha estat absorbida per la protoestrella o dispersada cap al medi interestel·lar, pel que l'objecte és ja visible clarament a l'ultraviolat, òptic i infraroig.

Existeix una **classificació dels objectes estel·lars joves** de baixa massa en funció de les característiques observacionals que presenten. La forma de la distribució espectral d'energia és molt distintiva de cada fase i es divideixen en quatre categories (Figura 2.2). Les fonts Classe–0 són les més joves, on la protoestrella presenta encara l'embolcall de gas i pols. Són molt dèbils a l'infraroig i intenses al submil·limètric. Es pensa que les estrelles adquireixen quasi tota la seva massa en aquesta fase en la que solen estar associades a fluxos moleculars. Les fonts Classe–I tenen una edat de 10^5 anys, són més lluminoses que les anterior però encara no són visibles a l'òptic. Presenten un embolcall en caiguda lliure ($\sim 10^4$ AU), una cavitat al voltant d'elles ($\sim$ 200 AU) i un disc aplanat ($<$ 200 AU). Els objectes Classe–II ja són visibles a l'òptic i infraroig. Tenen una edat de 10^6 anys i encara presenten un disc circumestel·lar òpticament gruixut d'una massa de $\sim$0.01 $M_\odot$. Les estrelles T Tauri són un exemple d'aquesta categoria. Finalment, les fonts Classe–III són els objectes estel·lars més evolucionats amb una edat de 10^7 anys. Emeten pràcticament com un cos negre amb un factor d'atenuació a causa del disc de pols vestigial. Són conegudes com a T Tauri nues.

1.3 Nuclis densos

Els anomenats nuclis densos, categoria que recull els núvols moleculars més petits i densos, es troben a l'interior dels núvols moleculars gegants i dels núvols moleculars foscos. Un exemple prototípic d'aquests objectes té una densitat de 10^4 cm^{-3}, temperatura de $\sim$10 K, mida de $\sim$0.1 pc i turbulència subsònica. Molts d'ells estan associats a fonts infraroges, fluxos moleculars i estrelles T Tauri. Aquests fets consisteixen la prova més directa de que aquestes estructures formen estrelles. Existeixen, a més, altres regions compactes i denses que no es troben dins de núvols moleculars, els anomenats glòbuls de Bok. A banda de trobar-se aïllats, comparteixen la majoria de les propietats dels nuclis densos i també es troben associats amb fonts infraroges i fluxos moleculars. Les fonts infraroges associades a ambdós tipus d'objectes són de baixa lluminositat, el que suggereix que són llocs de formació estel·lar de baixa massa.

Diversos estudis dirigits a mapar nuclis densos n'han revelat una **estructura** senzilla. El seu perfil de densitat consisteix en una regió interna de densitat aproximadament constant, i una regió externa que es pot parametritzar com $\rho \propto r^{-2}$ (Figures 3.1 i 3.4). Aquesta morfologia es pot entendre de forma senzilla en termes del balanç de la força gravitatòria, que tendeix a fer contreure el nucli sobre si mateix, i la pressió tèrmica, que tendeix a dispersar-lo. Dins de la regió més interna la poca massa continguda genera una força gravitatòria dèbil. Com a conseqüència, hi domina la pressió tèrmica que tendeix a homogeneïtzar el medi generant una densitat uniforme. A radis majors, la massa continguda és major, i la força gravitatòria esdevé important. Quan aquesta es troba en equilibri hidrostàtic amb la pressió tèrmica genera un perfil del tipus $\rho \propto r^{-2}$ com l'observat.

Estabilitat

Aquestes regions es poden **modelitzar en estat d'equilibri hidrostàtic**. L'aproximació més senzilla és la de **Bonnor–Ebert**. Per definició, és una esfera isoterma suportada únicament per la pressió tèrmica contra al col·lapse gravitatori. Assumint que el gas a l'interior es comporta en forma de gas ideal, la pressió d'aquest és proporcional a la densitat (Eq. 3.5) a través de la velocitat del so (C_s). Incloent l'expressió pel potencial gravitatori (Eq. 3.2), es poden derivar totes les propietats d'aquest objecte. Una particularitat important és que es comporta de forma auto-similar, és a dir, totes les esferes de Bonnor–Ebert tenen la mateixa estructura i l'únic que en canvia és un factor d'escala. Això simplifica l'anàlisi, donat que ens permet reescriure les expressions en forma adimensional en termes dels paràmetres, també adimensionals, ξ (radi, Eq. 3.7) i u (potencial gravitatori, Eq. 3.6). L'únic que manca és fixar les condicions de contorn, pel que imposem una densitat coneguda el centre, ρ_c, i un medi exterior difús que exerceix una pressió que confina l'esfera, $P_{\rm Out}$. Donada la proporcionalitat entre pressió i densitat, i que la densitat depèn del radi, aquesta última condició també ens fixa el radi màxim de l'esfera, $R_{\rm Out}$ (Eq. 3.9). En termes adimensionals, $R_{\rm Out}$ esdevé el paràmetre $\xi_{\rm max}$ (Eq. 3.10), de gran importància ja que ens caracteritza de forma única la solució de les esferes de Bonnor–Ebert. Un estudi en profunditat de les seves propietats en funció del paràmetre $\xi_{\rm max}$ revela que hi ha un valor crític, $\xi_{\rm crit} = 6.5$, per sobre del qual l'esfera és inestable al col·lapse gravitatori. Aquest resultat ens limita la densitat màxima que es pot assolir únicament amb el suport de la pressió tèrmica a un valor de $\sim$14.1 vegades la densitat del medi exterior difús. Com a conseqüència, la massa màxima queda també limitada al valor conegut com a massa de Bonnor–Ebert (Eq. 3.18). Per tant, un objecte amb valors superiors als crítics és inestable i experimentarà col·lapse gravitatori. Una aproximació diferent, que no assumeix cap simetria, és el **criteri de Jeans**. En aquest cas s'estudia un fluid uniforme sobre el que s'aplica una pertorbació que, essent de mida suficientment petita, es comporta com una ona sonora. En canvi, si la pertorbació és de grans dimensions, s'indueix el col·lapse gravitatori. Això permet definir el cas límit com la distància de Jeans (Eq. 3.23). Comparat amb l'estudi de Bonnor–Ebert, aquesta distància equival a $\xi = \pi$.

Una altra forma de suport pot venir per part del **camp magnètic**. Aquest ha estat mesurat en diversitat d'objectes on mostra una contribució dinàmica important. Al cas dels nuclis densos, es pot considerar que es troben en estat de *flux congelat*, és a dir, que camp magnètic i gas estan lligats i en podem negligir els efectes òhmics. Aquesta aproximació s'anomena de magnetohidrodinàmica idealitzada. Com al cas de Bonnor–Ebert, podem definir una pressió magnètica (Eq. 3.34) i, a partir d'ella, la fracció de pressió magnètica respecte a pressió tèrmica, α (Eq. 3.35). Malgrat aquesta semblança, el camp magnètic es comporta de forma molt diferent a la pressió tèrmica a causa de dos factors: només actua sobre elements amb càrrega elèctrica no nul·la (que anomenarem ions en contraposició als neutrals) i la seva acció no és isotròpica. La pressió magnètica s'exerceix pels ions, congelats al camp magnètic, al xocar contra els neutrals, que es mouen tèrmicament (de forma aleatòria). El camp magnètic té la direcció marcada per les línies de camp, pel que la pressió magnètica només s'exerceixi al desplaçar-se a través d'aquestes, on els ions hi estan fixats, mentre que no té cap efecte si els neutrals s'hi desplacen paral·lelament. Com a conseqüència, la pressió és major en la direcció perpendicular a les línies de camp, el que hi genera major suport contra la gravetat i produeix objectes aplanats al pla equatorial (Fig. 3.5). La pressió magnètica augmenta la capacitat de concentrar massa sense iniciar el procés de col·lapse (Eq. 3.37). Aquesta massa, M_Φ, en condicions de flux congelat és proporcional únicament al flux magnètic inicial de l'objecte, $\Phi_{\rm cl}$ (Eq. 3.38). Aquesta proporcionalitat fa que sigui convenient definir el paràmetre λ (Eq. 3.39) que mesura la relació massa-a-flux ($M/\Phi_{\rm cl}$) en funció del valor crític. Això implica que els núvols amb $\lambda > 1$ són núvols super-crítics que no poden ser suportats únicament per l'acció del camp magnètic, mentre que els núvols amb $\lambda < 1$ són sub-crítics i no els hi és necessària la pressió tèrmica per a l'estabilitat. Això també fa que qualsevol objecte amb massa inferior a M_Φ no pugui col·lapsar gravitatòriament a menys que perdi flux magnètic en condicions no-idealitzades. La importància del camp magnètic en l'estabilitat de l'objecte augmenta a mida que α i $\Phi_{\rm cl}$ augmenten. Una última forma de suport mitjançant el camp magnètic són les **ones magnetohidrodinàmiques**. De forma semblant a una ona sonora, que és la propagació d'una pertorbació mecànica a través d'un medi continu, el camp magnètic també és capaç de propagar pertorbacions. Això succeeix quan es deformen les línies de camp, que s'oposen a aquesta modificació a causa de la tensió magnètica. Aquesta pertorbació viatja a través de la línia de camp, de forma semblant a una corda vibrant, a la velocitat d'Alfvén, V_A (Eq. 3.45), i interacciona amb el medi proper generant una pressió addicional. Mesures experimentals demostren que els núvols grans estan virialitzats[1] i, a més, sembla existir equipartició entre l'energia gravitacional i magnètica. Això implica que la velocitat virialitzada és semblant a la velocitat d'Alfvén pel que les ones magnetohidrodinàmiques poden tenir una contribució dinàmica important.

---

[1] Equipartició entre energia cinètica i gravitacional.

Col·lapse

Com s'ha dit prèviament, els nuclis densos es troben associats a indicadors de formació estel·lar, pel que en algun moment de la seva evolució poden reunir les condicions necessàries per iniciar el col·lapse gravitatori. Comencem l'anàlisi amb una esfera de Bonnor–Ebert en estat crític, per la que incrementem la massa un petit percentatge. Aquest excés de massa no pot ser suportat per la pressió tèrmica pel que comença el col·lapse. Una quantitat molt important és la taxa d'acreció de massa, $\dot{M}$, que mesura la variació temporal de material en col·lapse gravitatori caient a l'objecte central en formació. A mida que el procés avança, aquest indicador tendeix a un valor asimptòtic (Eq. 3.54) que és proporcional a la taxa de variació del radi a partir del qual el material comença a col·lapsar, $\dot{R}$ (Eq. 3.56). Aquesta important relació implica que, com que $\dot{M} > 0$, $\dot{R} > 0$ amb el que aquest radi sempre augmenta i el col·lapse s'expandeix viatjant cap a fora en forma d'ona a la velocitat del so (Fig. 3.9). Aquest procés es coneix com **col·lapse de dins cap a fora**. Dins del radi de col·lapse la densitat es modifica i segueix un perfil més pla del tipus $\rho \propto r^{-3/2}$ (Eq. 3.57) mentre que fora d'aquest radi, on el medi segueix en equilibri hidrostàtic, manté el perfil $\rho \propto r^{-2}$.

La inclusió del camp magnètic canvia lleugerament aquest procés. El primer factor a tenir en compte és la **difusió ambipolar**. Aquest procés és fruit del desdoblament en el comportament dels ions i neutrals en presència de camp magnètic en condicions de flux congelat. A efectes pràctics, tenim dos fluids mesclats amb comportaments diferents. Els ions, fixats al camp magnètic, es poden moure paral·lelament a les línies de camp però no perpendicularment. Per altra banda, els neutrals veuen com la pressió magnètica els dificulta travessar línies de camp però, depenent de la fracció de ionització del medi, no els ho impedeix. Això fa que els neutrals tinguin una velocitat relativa respecte als ions (Eq. 3.58), i que puguin desplaçar-se lentament cap al centre del núvol per efecte de la força gravitatòria. L'escala temporal típica d'aquest procés és de l'ordre del milió d'anys, el que el fa significatiu donat que és comparable a la dels nuclis densos. Aquest mecanisme, a més, permet que el centre del núvol vagi incrementant paulatinament la seva densitat i massa de forma quasi-estàtica, és a dir, a través de successius estats d'equilibri, produint també un augment gradual del quocient $M/\Phi_{\rm cl}$ (Fig 3.10). Aquest mecanisme és molt probablement el més important durant la fase d'evolució quasi-estàtica i, a més, pot ser capaç de generar un nucli suficientment massiu com per vèncer la pressió tèrmica i magnètica, i acabar iniciant el col·lapse gravitatori. Una vegada que el col·lapse s'inicia, aquest també evoluciona de dins cap a fora, però amb característiques pròpies a causa de la ruptura de simetria que suposa la inclusió del camp magnètic. L'ona de col·lapse viatja a velocitat C_s en la direcció del camp magnètic, però com una ona magnetohidrodinàmica a velocitat $C_s + V_A$ en la direcció perpendicular (Fig. 3.11). Malgrat això, el col·lapse de material és més ràpid en la direcció paral·lela al camp magnètic ja que la pressió magnètica és menor, el que provoca una desviació del material cap al pla equatorial formant una estructura gravitacionalment inestable anomenada "pseudo-disc" (Fig. 3.12). A mida que la massa central augmenta, la importància relativa del camp magnètic disminueix i els ions són arrossegats pels neutrals. Això provoca que les línies de camp, lligades als ions pel congelament del flux, siguin arrossegades cap al centre i adoptin la morfologia coneguda com a de "rellotge d'arena". La sobre-densitat acumulada respecte al cas no-magnetitzat fa que la taxa d'acreció sigui més alta (Eq. 3.62) i, per tant, l'evolució més ràpida.

Química

Multitud de treballs han estudiat el més d'un centenar d'espècies químiques detectades al medi interestel·lar. Una de les principals conclusions és que la química de la fase gasosa està dominada per les reaccions ió-molècula. Estudis de l'absorció efectuada pels grans de pols sobre l'emissió brillant infraroja de les estrelles de rerefons, han permès estudiar la composició dels mantells de gel i determinar que contenen majoritàriament aigua (H_2O) i monòxid i diòxid de carboni (CO i CO_2). Això fa que el monòxid de carboni no sigui un bon traçador de la densitat donat que es congela als mantells i desapareix de la fase gasosa. Paral·lelament, mitjançant l'emissió de transicions moleculars rotacionals (les úniques activades a la temperatura dels nuclis densos), s'han observat diferències en la mida i forma de la distribució de les diferents molècules (Fig. 3.14), a més de en l'amplada i velocitat central dels espectres.

Les diferències anteriors poden ser interpretades gràcies a la descripció acurada de l'estructura física i del perfil de temperatura de nombrosos nuclis densos. Aquesta descripció millorada es deu, per una banda, a la millora dels mapes (sub)mil·limètric que permeten traçar directament la columna de H_2, i a l'ús de codis de transport radiatiu que permeten usar perfils de densitat, temperatura i abundància molecular per predir l'espectre emès. Un dels primers resultats d'aquests anàlisis va permetre interpretar que el monòxid de carboni es congela a la superfície dels grans de pols a mida que la densitat augmenta de $\sim 10^4$ cm^{-3}. Posteriorment s'ha mostrat que aquest comportament el comparteixen més molècules. Les espècies químiques portadores de carboni (*p.ex.* CO i CS) desapareixen de la fase gasosa quan la densitat incrementa. Poden arribar a diferències d'abundància de 1–2 ordres de magnitud respecte a les zones difuses pel que tracen el medi menys dens i extern dels nuclis. Contràriament, les molècules portadores de nitrogen (*p.ex.* N_2H^+ i NH_3) romanen al gas a densitats més altes, mantenint l'abundància constant o reduint-la succintament, traçant per tant el medi més dens i interior. Aquestes troballes expliquen la diferent morfologia dels mapes de les molècules. També expliquen les diferent propietats dels espectres, donat que el medi interior té menys variacions de velocitat i, per tant, les línies són més estretes. Diversos treballs teòrics segueixen l'evolució dinàmica i química de nuclis densos i, mitjançant micro-física bàsica, són capaços d'explicar i, en alguns casos, predir aquests comportaments. Un resultat físic important d'aquests estudis és establir que el col·lapse no pot evolucionar excessivament ràpid o les amplades de línia serien majors que les observades. També que el col·lapse no pot durar més de 0.5–1 milió d'anys perquè, en cas contrari, la desaparició de monòxid de carboni seria superior a l'observada. Aquests resultats impliquen que condicions inicials supercrítiques semblen més adients.

La desaparició del monòxid de carboni té altres efectes molt importants per a la química del nucli dens. Aquesta espècie és la principal destructora dels ions del medi, que són a la vegada els precursors d'altres molècules com N_2H^+ i HCO^+, pel que l'abundància d'aquestes últimes s'incrementa a mida que el CO desapareix. Un altre efecte important és sobre la deuteració del medi ja que el CO destrueix els ions H_3^+ i H_2D^+. Aquests ions són els responsables de la cadena de deuteració de ions que pot arribar a formar fins a D_3^+, encarregats de transferir el deuteri a molècules més complexes a través de les seves respectives cadenes de reaccions.

2 Objectius i pla de treball

És una evidència observacional que els nuclis densos són llocs de naixement d'estrelles de baixa massa. Si bé en podem trobar dels anomenats sense-estrella i pre-estel·lars, ambdós sense objectes estel·lars joves, n'hi ha del tipus Classe–0/I associats amb fonts infraroges, fluxos moleculars i d'altres indicadors del procés de formació estel·lar. Malgrat la seva importància, se'n coneixen pocs detalls dels primers estadis evolutius d'aquests objectes. Aquestes regions aparentment inactives són capaces de sobreviure diverses vegades l'escala temporal de caiguda lliure i, potencialment, col·lapsar per formar estrelles. Com ho fan? El desafiament observacional que representa estudiar objectes tan difusos i estesos dificulta revelar-ne la resposta. Resulta molt més senzill, des d'un punt de vista observacional, estudiar fonts més brillants com les més evolucionades Classe–0. És possible revertir-ne la història en base a models teòrics i trobar-ne les condicions inicials que són, idealment, les dels nuclis densos on s'han format. La qualitat de les dades actuals permet fer aquest tipus d'estudis de forma fiable. Des d'un punt de vista teòric, molts estudis han considerat l'efecte del camp magnètic en els seus models durant dècades. No obstant això, la mancança d'instrumentació i tècniques observacionals impedien contrastar-ne les prediccions. Per fortuna, diversos telescopis han desenvolupat durant els darrers anys sistemes polarimètrics que permeten estudiar per primera vegada i de forma fiable el camp magnètic.

Per tot això, la complexa interacció als nuclis densos entre gravitació, pressió tèrmica, turbulència, rotació i camp magnètic no està ben caracteritzada observacionalment i, com a conseqüència, tampoc ben entesa teòricament. L'**objectiu** és, aleshores, aprofundir en la comprensió de com es formen, sobreviuen i evolucionen els nuclis densos de baixa massa. Aquest objectiu l'enfrontem seguint dues vessants. *En primer lloc, volem caracteritzar observacionalment les propietats físiques, químiques i magnètiques dels nuclis densos magnetitzats als seus estadis més primigenis, a fi d'entendre les vertaderes condicions inicials del procés de formació estel·lar. En segon lloc, comparem les observacions interferomètriques d'una font Classe–0 amb models teòrics de col·lapse de núvols magnetitzats, per a derivar-ne les condicions inicials més adients per formar-la i els processos físics que n'han dominat l'evolució.*

El **pla de treball** es diferencia segons les dues vessants empreses:

- **Propietats dels nuclis densos primigenis.** Per estudiar les propietats d'aquests objectes extremadament joves la millor regió és la nebulosa de la Pipa. És un núvol molecular amb una eficiència de formació d'estrelles molt baixa que conté més d'un centenar de nuclis densos en un estadi molt poc evolucionat. Són nuclis densos de baixa massa inactius, no lligats gravitatòriament i aparentment confinats per la pressió externa (Muench et al., 2007; Lada et al., 2008; Rathborne et al., 2008). A més, les propietats magnètiques varien significativament d'un extrem a l'altre del núvol (Alves et al., 2008; Franco et al., 2010), amb el que es pot estudiar quin efecte té sobre els objectes d'estudi. De tots els nuclis de la nebulosa de la Pipa, en seleccionem diversos candidats i n'estudiem la química i l'emissió de la pols. Per la part de l'*estudi químic* hem seguit dues estratègies: hem fet un estudi a alta resolució d'una sèrie de molècules, categoritzades segons els models com a joves i tardanes, a fi de poder datar químicament els nuclis. Tembé hem fet un sondeig amb un gran ample de banda per a detectar totes les espècies químiques presents als nuclis densos. Les publicacions resultants es presenten als capítols 5 i 6. Referent a l'*estudi de l'emissió de la pols*, hem fet mapes d'alta resolució de l'emissió de la pols a 1.2 mm i n'hem derivat les propietats físiques. Els resultats és presenten també al capítol 5. Addicionalment, hem ajustat un model d'esfera de Bonnor–Ebert als mapes i hem derivat els paràmetres que millor els ajusten. L'article resultant (pendent d'enviament) es presenta al capítol 7. Finalment, hem inclòs l'estudi de l'emissió de la pols del nucli dens massiu situat a Barnard 59, a l'extrem nord-est de la nebulosa de la Pipa. Aquest nucli ha format una petita granja d'estrelles però encara manté una gran reserva de massa inactiva al seu interior amb propietats molt semblants a la resta de nuclis menys massius. Analitzem els mecanismes que el poden mantenir fora d'un estat de col·lapse i en presentem els resultats al capítol 8. Les observacions s'han dut a terme usant el radiotelescopi IRAM-30m, que presenta una gran superfície col·lectora i els receptor més sensibles muntats en una antena d'aquest tipus.

- **Comparació d'observacions d'un objecte Classe–0 amb models de col·lapse de núvols magnetitzats.** Per començar aquest tipus d'estudis, la millor elecció és un exemple prototípic de camp magnètic amb morfologia de rellotge d'arena com la predita pels models. NGC 1333 IRAS 4A és una font Classe–0 de baixa massa amb un embolcall en col·lapse de $\sim$1 $M_\odot$ i clara morfologia de rellotge d'arena. L'estratègia va ser generar mapes sintètics de l'emissió generada pels diferents models variant els valors dels seus paràmetres i de l'orientació de la font. Aquests mapes són comparats amb les dades experimentals després d'haver-los-hi aplicat el filtratge de l'interferòmetre, és a dir, simular els efectes instrumentals. D'aquesta comparació en derivem els paràmetres dels models que millor ajusten les dades. La publicació resultant es presenta al capítol 9. Les observacions s'han fet usant l'interferòmetre SMA, que aporta la resolució necessària per aquestes fonts de mida angular molt menor i presenta les millors capacitats polarimètriques d'entre els de la seva classe.

3 Publicacions

3.1 Propietats dels nuclis densos primigenis: els nuclis pre-estel·lars a la nebulosa de la Pipa

Per a l'estudi dels nuclis densos primigenis s'ha seleccionat la nebulosa de la Pipa. Aquest sistema és un núvol molecular massiu ($\sim 10^4$ $M_\odot$), proper (145 pc) i amb aparença filamentosa (Fig. 4.1) que presenta una eficiència de formació estel·lar molt baixa ($\sim$0.06%). El núvol és penetrat per un camp magnètic uniforme, perpendicular al seu eix principal, que només mostra alteracions significatives a la única regió amb formació estel·lar activa, Barnard 59. Els resultats de polarització òptica revelen que les propietats magnètiques del núvol canvien d'un extrem a l'altre: el camp és ordenat i aparentment intens a l'extrem sud-est, i desordenat i aparentment dèbil a l'extrem nord-oest. La nebulosa alberga més d'un centenar de nuclis densos majoritàriament inactius. Estudis anteriors han mostrat que són químicament molt joves, amb emissió brillant en CO però minsa en NH_3. La majoria d'ells no estan lligats gravitatòriament i, aparentment, es troben confinats per la pressió externa. Totes aquestes propietats fan que els nuclis densos de la nebulosa de la Pipa siguin els candidats ideals per a estudiar els estadis inicials de formació i evolució d'aquest tipus objectes i, a més, la interacció del camp magnètic en el procés.

Propietats físiques

Dels nou nuclis mapats n'hem derivat els paràmetres mitjans que concorden amb els valors estàndard d'aquests objectes: diàmetre de 0.08 pc, densitat de $\sim 10^5$ cm^{-3} i massa de ~ 1.7 $M_\odot$. Hem trobat que els mapes d'emissió de la pols a 1.2 mm presenten bona concordança amb els treballs anterior basats en la tècnica de l'extinció a l'infraroig, encara que aquests últims tracen millor les regions difuses. Hem derivat un factor d'escala entre l'extinció visual (A_V) i la densitat de columna de H_2 de $(1.27 \pm 0.12) \times 10^{-21}$ mag cm^2, molt proper al valor estàndard. No obstant això, hem trobat que els mapes d'emissió subestimen de forma sistemàtica la densitat de columna en un factor mitjà de $\sim$6.7 mag respecte als mapes d'extinció. Aquesta manca de material detectat pot provenir de la part difusa del núvol que és cancel·lada per la nostra tècnica de mapat. Les morfologies són variades, des de nuclis circulars a nuclis filamentosos, abraçant un ventall de densitats d'un ordre de magnitud. La major part d'ells no presenta simetria esfèrica, el que apunta a que no només la pressió tèrmica té un paper important dinàmicament. Hem trobat diverses tendències relacionades amb la densitat creixent dels nuclis: la mida sembla reduir-se, la massa sembla incrementar i la riquesa química sembla augmentar. Tots aquests fets apunten a objectes o bé en equilibri hidrostàtic o bé en un estat que li és molt proper. El que és més, no hem trobat indicis de correlació entre la direcció del camp magnètic i l'eix principal dels nuclis densos, encara que els efectes de projecció poden ser importants. Tots aquests resultats han motivat un intent de modelització dels nuclis com a esferes de Bonnor–Ebert usant simultàniament els mapes d'emissió i extinció. Tots els nuclis presenten un perfil de densitat compatible amb el model. Vuit d'ells no estan lligats gravitacionalment, i presenten contrastos de densitat baixos amb densitats centrals de unes quantes vegades 10^4 cm^{-3}. El nucli 109 és l'excepció, essent l'únic gravitatòriament lligat i inestable al col·lapse. La combinació dels dos mapes permet determinar temperatures de la pols dins del rang de 9–12.6 K excepte pel nucli 48 (18 K). Per a tots els nuclis n'hem derivat una component difusa que els envolta amb valors d'extinció visual significatius dins del rang 4–9 mag, essent majors a la regió sud-est ($\simeq 9$) que a la resta de la nebulosa, compatible amb els resultats experimentals anteriors.

Propietats químiques

Els nostres resultats confirmen que els nuclis densos estudiats a la nebulosa de la Pipa estan en un estadi d'evolució química molt primerenc. Hem descobert una química molt rica, inesperada en base als treballs anterior, gràcies al sondeig químic no-esbiaixat de $\sim$15 GHz a longitud d'ona de 3 mm sobre catorze nuclis densos. Hem proposat una classificació observacional en termes de la composició química i de les propietats dels espectres. Existeix una clara diferenciació química entre els nuclis densos en base a emissió a la banda de 3 mm normalitzada pel valor màxim d'extinció visual. Hem definit tres grups de nuclis moleculars. Els nuclis “difusos” ($A_V \lesssim 15$ mag) presenten una química pobre formada bàsicament per molècules ubiqües (*p.ex.* CO, CS i C_2H) similar a la química de la nebulosa que els alberga. Els nuclis "deuterats", més densos ($A_V \gtrsim 22$ mag), mostren una emissió normalitzada més feble en les molècules ubiqües però presenten emissió en espècies portadores de nitrògen (N_2H^+) i deuteri (C_3H_2), a més de en algunes cadenes carbonades (HC_3N), mostra d'una química prèvia a l'inici del procés de formació estel·lar. Finalment, els nuclis "oxo-sulfurats" tenen densitats intermèdies ($A_V \simeq 15$–20 mag) i aparentment estan en un estat de transició entre la química del núvol i la dels nuclis densos evolucionats. S'hi detecta una química amb característiques pròpies, marcada per ser abundant en espècies com CH_3OH i molècules oxo-sulfurades (*p.ex.* SO i SO_2) que desapareixen a densitats més altes. En base a aquestes categories, un dels nuclis difusos (nucli 47) presenta una química pròpia dels nuclis oxo-sulfurats, el que indueix a especular que sigui un nucli fallit que va assolir densitats altes però ara s'està difonent dins del núvol matern. L'anàlisi de les amplades de línia reporta dos comportament característics: (*a*) un valor constant de prop de 2.5 vegades l'eixamplament tèrmic (*p.ex.* CO i CH_3OH) que probablement traça les capes externes dels nuclis, i (*b*) un valor constant d'aproximadament 2 vegades l'eixamplament tèrmic (*p.ex.* C_2H i N_2H^+) per a nuclis amb $A_V > 20$ mag i valor molt més grans per als més difusos (*p.ex.* el fallit nucli 47). Les amplades de línia no-tèrmica són subsòniques, el que confirma que la major part de la pressió interna té origen tèrmic. L'estat evolutiu químic no està correlacionat amb la localització dels nuclis a la nebulosa i, per tant, tampoc ho està amb el camp magnètic a gran escala. Per altra banda, els nuclis més rics químicament són els més densos, pel que sembla existir una correlació amb les propietats físiques dels nuclis (densitat i mida).

Barnard 59

El complex Barnard 59 és la única regió de la nebulosa de la Pipa amb activitat de formació estel·lar. En un període de 2–3 milions d'anys ha format una petita granja de estrelles de baixa massa. Malgrat això, l'anàlisi dels mapes previs d'extinció, i dels nostres mapes d'emissió, mostren que la regió central és un grumoll molecular massiu i inactiu de $\sim 18.9\ M_\odot$. No mostra indicis de fragmentació a escales d'un miler de AUs, sinó que té un perfil suau compatible amb una única estructura isoterma amb major densitat cap al centre. Aquest perfil de densitat és semblant al de la resta de nuclis de la nebulosa encara que a molt major escala. Un ajust de Bonnor–Ebert indica que és inestable al col·lapse, a més d'estar sub-virialitzat (l'energia gravitatòria és major que la cinètica). Moviments interns subsònics, i el fet de que hagi sobreviscut uns milions d'anys, semblen apuntar a que fonts de suport addicionals estan actuant. La retroalimentació per part de les estrelles sembla poc probable donat el seu baix nombre, pel que el camp magnètic n'és l'agent més plausible. Una estimació del camp necessari per a sostenir el nucli dóna valors raonables de 0.1–0.2 mG. Recapitulant, l'explicació més plausible per aquesta regió sembla ser un nucli massiu suportat per fonts no-tèrmiques, possiblement el camp magnètic, mentre ha format una petita granja d'estrelles. Simulacions numèriques mostren que aquest nucli està prop del límit de supervivència d'aquestes estructures pel que sembla que acabarà col·lapsant. La manca de fragmentació apunta a que formarà una estrella o, com a molt, una binària.

3.2 Comparació d'observacions d'un objecte Classe–0 amb models de col·lapse de núvols magnetitzats: NGC 1333 IRAS 4A

Hem comparat observacions a alta resolució angular de l'emissió submil·limètrica polaritzada de la pols (que traça la direcció del camp magnètic al pla del cel) d'una protoestrella de baixa massa, amb les prediccions teòriques de tres models de col·lapse de núvols magnetitzats isoterms per tal de constrènyer-ne els valors dels paràmetres. NGC 1333 IRAS 4A és la font ideal per a testejar aquests models. És una Classe–0 jove amb un embolcall de gas i pols en fase de col·lapse, on es detecta un camp magnètic amb clara morfologia de rellotge d'arena. Hem calculat l'emissió de la pols que sorgiria dels models, i hem generat mapes sintètics per els paràmetres de Stokes I, Q i U variant els paràmetres dels models i l'orientació al cel. Després, hem convolucionat aquests mapes amb la resposta instrumental de l'interferòmetre de les observacions de IRAS 4A, els hem comparat amb les dades experimentals, i hem assegurat la qualitat de l'ajust per medi d'un anàlisi de χ^2. El millor acord amb les dades s'obté per models de núvols amb un index de massa-a-flux > 2, un camp inicial d'aproximadament 0.5 mG, i una edat de 10^4 anys des de l'inici del col·lapse. Els models que assumeixen congelació del flux proporcionen millors resultats i la dissipació magnètica, si es dóna, està per sota de la resolució de les observacions ($\sim$350 AU). Aquest resultat suggereix que la hipòtesi de congelament del flux és manté vàlida durant la major part del procés de col·lapse. La inclusió d'un perfil de temperatura observacional condueix a millors resultats pel que, encara que la variació de temperatura altera lleument l'evolució dinàmica del núvol, s'ha de tenir en compte al simular l'emissió de la pols que n'és molt sensible. Un estudi exploratori dels angles d'orientació mostra que els mapes dels diferents paràmetres de Stokes en són molt sensibles, i que podrien ser usats per determinar l'orientació de les fonts, sempre assumint una determinada topologia per al cap magnètic. Hem mostrat que l'interferòmetre ALMA tindrá la capacitat per distingir entre els diferents models estudiat en aquest treball i, per tant, posseeix un gran potencial per a ser usat com a eina per destriar-los. Els resultats generals mostren que l'escenari teòric estàndard és compatible, al menys, amb IRAS 4A. Segons aquest, núvols inicialment penetrats per camps magnètics de gran escala esdevenen inestables i col·lapsen. El camp magnètic es arrossegat pel material en caiguda i és atrapat dins de l'estrella naixent i del disc circumestel·lar. Al núvol en col·lapse, la dinàmica està dominada per la gravitació i, inclús per núvols inicialment supercrítics, per les forces magnètiques.

4 Conclusions generals

Els estudis previs duts a terme pel nostre grup sobre el camp magnètic a la nebulosa de la Pipa (Alves et al., 2008; Franco et al., 2010) havien mostrar un camp molt uniforme perpendicular al seu eix principal, i que la turbulència al núvol era sub-Alfvénica. Això suggereix que el núvol s'ha format per la caiguda de material en la direcció de les línies de camp de forma quasi-estàtica. Malgrat això, algunes regions de la nebulosa de la Pipa mostren turbulència. Aquest és el cas de la regió central on aquesta turbulència podria haver provocat la fallida del core 47 (Frau et al., 2012a). Es creu que l'extrem nord-est, la regió de Barnard 59, és la regió més vella amb una edat estimada de 2–3 milions d'anys. Ja s'hi està formant una granja d'estrelles, el que provoca que el camp magnètic es distorsioni i la turbulència sigui super-Alfvénica. En canvi, a la regió sud-oest, el camp magnètic es manté ordenat i la química del nucli més evolucionat és compatible amb una edat propera al milió d'anys (Frau et al., 2010, 2012b). Aquestes estimes d'edat són un ordre de magnitud inferiors a l'edat d'altres núvols amb formació estel·lar, com els situats a Taure i Orió. De fet, diversos estudis mostren que la formació estel·lar s'hi va iniciar fa uns 10 milions d'anys, i que posteriorment es va accelerar produint la major part d'estrelles en els darrers milions d'anys. Aleshores, és possible que la nebulosa de la Pipa estigui en un estadi evolutiu massa primerenc com per començar a formar estrelles de forma eficient. És possible que les condicions immaculades d'aquest núvol fossin les condicions inicials a Taure i Orió, molt distorsionades ara a causa de l'activitat de formació estel·lar.

En aquesta tesi hem afrontat l'estudi de les etapes més primerenques de la formació estel·lar. Hem mapat nuclis densos amb densitat per sota de 10^5 cm^{-3} (Frau et al., 2010, 2012b), molt per sota dels valors reportats a la literatura. Aquests nuclis presenten una estructura compatible amb esferes de Bonnor–Ebert (Frau et al., 2012c), el que suggereix que es poden trobar en situació d'equilibri hidrostàtic amb el seu entorn. A més, hem descobert una química molt rica i variada (Frau et al., 2012a), inesperada tenint en compte els treballs previs en fonts d'aquest tipus. Inclús en objectes tan joves i difusos, és possible distingir característiques químiques pròpies que permeten definir grups i establir una possible seqüència química evolutiva. Alguns dels objectes mostren propietats químiques típiques d'edats de 1 milió d'anys, però la manca d'indicis de col·lapse gravitatori suggereix que hi ha actives fonts de suport no tèrmiques. La falta de simetria esfèrica també implica que alguna força anisotròpica està actuant. La turbulència sub-Alfvénica apunta a que el camp magnètic pot ser aquest agent, el que causaria la forma aplanada de molts nuclis. La manca de correlació entre la direcció del camp magnètic i l'eix principal dels nuclis densos pot ser un efecte de projecció que necessita ser investigat.

Finalment, l'estudi de NGC 1333 IRAS 4A ha confirmat que les seves propietats poden ser explicades satisfactòriament amb el model estàndard de formació estel·lar (Frau et al., 2011). Els models de magnetohidrodinàmica idealitzada condueixen a millors resultats, i l'ús de un perfil de temperatura millora l'acord amb les dades. Les condicions inicials dels models, amb mides de $\sim$0.1 pc i densitats creixents cap al centre, concorden amb els resultats als nuclis densos de la nebulosa de la Pipa. La intensitat del camp magnètic inicial usat pels models, $\sim$0.5 mG a densitats de $\sim 10^5$ cm^{-3}, poden ser escalats als valors obtinguts per al gas difús de la nebulosa de la Pipa, fins a $\sim$65 mG a densitats del núvol de $\simeq 3\times10^3$ cm^{-3}, amb una llei del tipus $B \propto \rho^{1/2}$ típica de núvols magnetitzats. Des d'un punt de vista més tècnic, el mètode que hem emprat pot establir un punt de referència en la manera en que les futures dades d'ALMA seran analitzades. La alta qualitat de les dades farà possible aquest tipus d'anàlisis i fa preveure una gran millora en l'enteniment del procés de formació estel·lar.

Part I

Introduction
&
Aims

I

The raw materials and the factories of stars

The Milky Way, our Galaxy, has 3 visible components: a flattened disk of about 25 kpc of radius and 250 pc of scale height, a central dense bulge with a radius of 3 kpc, and an extended stellar halo consisting of globular clusters and old stars. Our Sun and the Solar System are located at a distance of 8.5 kpc from the galactic center, within the well-delineated spiral arm structure of the galactic disk. Most of the total mass of the Galaxy sits on the $\sim 10^{11}$ stars, but, with an average density of 1 star per pc^3, they represent a very small percentage of the total volume. The InterStellar Medium (ISM) is the matter that fills the space between the stars and constitutes only 1% of the mass of the Galaxy. It is formed fundamentally by a solid phase, the interstellar dust, and a gas component, the interstellar gas.

1.1 Components of the interstellar medium

1.1.1 Interstellar dust

Dust grains are extremely small, with sizes from 0.01 to 1 μm, of irregular shapes, and formed by silicate, carbon and/or iron nuclei with ice mantles. Interstellar dust interacts with passing light causing extinction, reddening, and polarization. Dust grains absorb radiation with wavelengths shorter than their sizes and produce extinction. This radiation is then re-emitted at longer wavelengths, mainly infrared and radio wavelengths. The amount of attenuation depends on the thickness and density of the dust cloud. If it is thick enough, the light can be totally blocked or scattered off by the dust particles, preventing the light from reaching us and producing dark regions. A typical value of the extinction in the Galaxy is about 1 magnitude per kpc of distance. However, there are places where the extinction is higher. Ultraviolet and blue wavelengths are more easily scattered off due to the sizes of dust grains. Therefore, the light that we see through the ISM has less of the blue light, and this produces the interstellar reddening. Finally, the polarization of light is produced when aspherical dust grains align with magnetic fields. It is generally accepted that dust grains rotate with their long axis perpendicular to magnetic field lines. When the axis of larger angular momentum lies parallel to the magnetic field and to the grain angular speed, the torque vanishes and the system achieves a stable state (Davis & Greenstein, 1951). The observed polarization vectors depend on the wavelength. In the optical range the randomly polarized passing light is less absorbed by dust grains in the direction perpendicular to the elongation thus polarization vectors are parallel to the magnetic field. At sub-mm/mm wavelengths dust grains reemit the absorbed photons, and the emission is partially linearly polarized in the elongation direction, and therefore, polarization vectors are perpendicular to the magnetic field.

The molecular component of the interstellar gas is associated with the dust grains, and both are located inside the molecular clouds (Section 1.2). Indeed, visual extinction (A_V) studies have found a correlation between the amount of H_2 gas and dust:

$$\left[\frac{N\left(\mathrm{H_2}\right)}{\mathrm{cm^{-2}}}\right] \approx 10^{21}\left[\frac{A_V}{\mathrm{mag}}\right]. \tag{1.1}$$

It is important to note that the chemical models show that the most abundant interstellar molecule (H_2) can only be formed in presence of dust grains, which operate as catalysts, absorbing the excess energy of the molecule formed by the union of two hydrogen atoms.

1.1.2 Interstellar gas

The gas is the main component of the ISM. As compared to dust, the relative abundances are ∼160 in mass, and $\sim 10^{12}$ in number of particles. The most common element is hydrogen, and can be found in three main different phases: molecular hydrogen (H_2, roughly half of the mass), atomic hydrogen (H_I, roughly the other half of the mass), and ionized hydrogen (H_{II}). Table 1.1 summarizes the main physical parameters of the different phases of interstellar gas (from Estalella & Anglada, 1996).

Cold molecular regions (H_2): Molecular hydrogen is the most abundant component. In addition there are more than one hundred different molecules detected but with much lower abundances (typically several order of magnitudes lower). Among the detected ones, the most abundant or observationally common are carbon monoxide (CO), ammonia (NH_3), water (H_2O), or hydroxil (OH). At the typical temperatures of these regions, about 20 K,

Table 1.1: Phases of the gas content in the interstellar medium

Phase	Fractional Volume	Temperature (K)	Density (cm^{-3})	Components
Molecular clouds	$< 1\%$	10–30	10^3–10^5	molecules (H_2, CO, NH_3, ...)
Cold atomic gas	2–3%	50–150	10–100	atomic hydrogen (neutral)
Warm neutral gas	10–50%	8×10^3	0.01–10	atomic hydrogen (partially ionized)
H_{II} regions	∼10%	10^3–10^4	10^2–10^4	ionized hydrogen
Coronal gas	30–70%	5×10^5	10^{-4}–10^{-3}	highly ionized hydrogen and metals

only rotational transitions can be excited. Homopolar molecules like H_2 do not have dipolar rotational transitions since the dipole moment for this kind of molecules is zero. Thus, other molecules, like for example CO must be used as tracers of the molecular gas in the Galaxy. Numerous surveys studying the CO line emission have established that the molecular gas is spread throughout the Galaxy, and mostly contained in discrete clouds closely confined near the galactic plane with a height scale of 60 pc. The molecular density profile shows a falloff for galactocentric radii greater than 10 kpc, and a maximum peak at a radius of 6 kpc (the molecular ring) presumably related to the galactic spiral structure. A sharp rise in molecular density is also observed within 1 kpc of the galactic center, where large numbers of massive stars are being born. These discrete units, the molecular clouds (Section 1.2), play a major role in the star formation process, being the birthplaces of stars.

Cold atomic regions (H_I): Radio studies at 21 cm of the hyperfine line of hydrogen, complemented by numerous observations of optical and ultraviolet absorption lines seen against background stars, provide a detailed picture of the distribution of the H_I gas in the Galaxy. H_I is located within the galactic disk, with a scale height of about 100 pc (nearly twice the scale height of the molecular gas). Throughout the Galaxy, most of the atomic gas is in discrete clumps known as H_I clouds. Although cloud properties vary broadly, representative temperatures are 50–150 K, with sizes of 1–100 pc, masses of 50–500 $M_\odot$, and densities ranging from 10 to 100 cm^{-3}. Atomic clouds correspond to 2–3% of the total volume and 50% of the total mass.

Warm atomic regions (intercloud gas): It is a second component of atomic gas not confined to individual clouds, with a height scale twice that of the cold component, and occupying 50% of the total volume. The number density is about 0.5 cm^{-3} and its temperature, although difficult to calculate because of the medium transparency, is estimated to be $\sim 8 \times 10^3$ K. A significant fraction (10–20%) of this atomic intercloud gas is ionized by stellar photons.

Ionized regions (H_{II}): The ionization of the hydrogen atom can be produced by photoionization or by collisions with other particles. Photoionized H_{II} regions are observed associated with young massive stars, with typical sizes of ~ 1 pc, densities of 10^2–10^4 cm^{-3}, and temperatures ranging from 5×10^3 to 1×10^4 K. The coronal gas is formed by hydrogen collisionally ionized by the passage of a supernova shock wave. This gas has densities of $\sim 3 \times 10^{-3}$ cm^{-3} and temperatures of 5×10^5 K. It is also possible to find ionized hydrogen surrounding planetary nebulae and in ionized stellar winds. Although its density and mass are negligible, the coronal gas represents about 50% of the total volume. Regarding its distribution in the Galaxy, the coronal gas is located also in the galactic plane with peaks of maximum density at radii near 5 kpc (similar to the molecular component), while the photoionized hydrogen is found near young massive stars, and thus near the spiral arms of the Galaxy.

1.2 Molecular clouds: the sites of star formation

Molecular clouds are cold (10–30 K) and dense (10^3–10^5 cm^{-3}) regions, with sizes and masses that change from cloud to cloud. They represent 50% of the total ISM mass, but have a negligible volume in the Galaxy. The main physical properties of different types of galactic molecular clouds are summarized ordered by A_V, from less to more opaque clouds, in Table 1.2 (from Stahler & Palla, 2005).

Diffuse molecular clouds, with typically low visual extinctions, are relatively isolated entities, with similar amounts of atomic and molecular gas, and representing a minor fraction of the molecular gas. Thermal pressure and gravity control the evolution of these clouds, allowing them to persist for long periods of time. Diffuse molecular clouds are never found to form stars.

Giant Molecular Cloud (GMC)s, with sizes up to 100 pc, are located within larger structures or spiral arms segments that have sizes up to a kpc, masses up to $10^7\ M_\odot$ (Elmegreen, 1985, 1993). The GMCs contain more than 80% of the molecular hydrogen of the Galaxy. The GMC are the preferred site for stars to form. Most of the GMCs have masses between 10^5 to $10^6\ M_\odot$ (but they may have up to $5 \times 10^7\ M_\odot$ near the galactic center; Duley & Williams, 1984). With these masses the main cohesive force is the cloud own gravity, with the internal thermal pressure playing only a minor role in the overall balance. Indeed, if thermal pressure was the only force opposing gravity, all molecular clouds should collapse rapidly and efficiently into stars. However, most molecular clouds show a low star-formation efficiency. Thus, additional mechanisms, such as magnetic fields or turbulence support, must be present and act against the gravity, preventing a rapid collapse. Once the star formation has begun, a typical giant cloud survives for $\sim 3 \times 10^7$ years before being destroyed by the intense winds and UV photons from newly formed O and B stars. By considering that the cloud converts about 3% of its mass into stars during this time, the galactic star-formation rate is $\sim 2\ M_\odot\ \mathrm{yr}^{-1}$ for a total galactic mass of H_2 of about $2 \times 10^9\ M_\odot$.

Looking inside GMCs, filamentary or clumpy substructures appear over a wide range of scales (Blitz, 1993; Williams et al., 2000). These substructures range from massive clumps with sizes of several pc and masses of thousands of solar masses, which may form entire clusters of stars, to small dense cloud cores with sizes of ~ 0.1 pc and masses $\sim 1\ M_\odot$, which may form individual stars or small multiple systems (Myers, 1985; André, Ward-Thompson, & Barsony, 2000).

Although the structure of molecular clouds is mainly hierarchical, consisting of small subunits within larger ones, clumps similar to those belonging to giant molecular clouds

Table 1.2: Physical parameters of molecular clouds

Cloud Type	A_V (mag)	n_{tot} (cm^{-3})	L (pc)	T (K)	M ($M_\odot$)	Examples
Diffuse	1	500	3	50	50	ζ Ophiuchi
Giant Molecular Clouds	2	100	50	15	10^5	Orion
Dark Clouds						
Complexes	5	500	10	10	10^4	Taurus-Auriga
Individual	10	10^3	2	10	30	B1
Dense Cores / Bok Globules	10	10^4	0.1	10	10	TMC-1 / B335

can be found in isolation, not directly associated with giant complexes. They correspond to the individual dark clouds in Table 1.2. The largest clumps, with masses of 10^3–10^4 $M_\odot$, are the dark cloud complexes. They are the site of a significant fraction of galactic star formation, although they do not form massive O and B stars. Massive stars are only formed in giant molecular clouds. The smallest and densest cloud entities, called dense cores, are described in detail in Chapter 3.

1.3 Observational tools at radio wavelengths

In order to know what happens during the first stages of star formation, it is necessary to study the dense cores, which are the basic units in the formation of stars (see Chapter 2). To explore the conditions within molecular clouds, the observation of molecular spectral lines are a powerful tool. Luckily, the conditions of dense cores, and molecular clouds in general, allow the formation and existence of a high variety of molecules. The dust associated with molecular clouds that allows to form H_2, also acts as a shield against ultraviolet radiation that could reach the newly-formed molecules and photodissociate them. Furthermore, high densities are necessary to cool the gas through collisionally excited atomic and molecular emission processes, and keep the molecular gas at the low temperatures needed for the survival of molecules.

1.3.1 Spectral line emission

By studying molecular spectral lines, it is possible to determine properties of the cloud as kinematics, temperature, and density (see Stahler & Palla, 2005 for details). The two-level model is a good approximation to understand the excitation conditions of the molecular lines (for a comprehensive description see Stahler & Palla, 2005). This model considers transitions between two energy levels with density populations n_u and n_l for the upper and lower states, respectively. These density populations are usually described by the excitation temperature, T_{ex}, through the Boltzmann's equation

$$\frac{n_u}{n_l} = \frac{g_u}{g_l} \exp\left(- \frac{\Delta E_{ul}}{k_B \, T_{ex}} \right) , \tag{1.2}$$

where g_u and g_l are the degeneracies of the two energy levels, and ΔE_{ul} is the energy difference between both states. Transitions between both levels can be excited radiatively or collisionally. If the density of the medium is high enough, collisions control the transitions between states, and the excitation temperature will be equal to the kinematic temperature characteristic of the collisions, $T_{ex} = T_k$. However, if density is low, radiation controls the population of the states, and the excitation temperature is equal to the background temperature, $T_{ex} = T_{bg}$. In this situation no line emission is detected, and only a black-body continuum spectrum, with temperature T_{bg}, is observed. Thus, to detect molecular spectral lines, collisions have to control the transitions between energy states. In this case, the transition is collisionally thermalized, and the system is in Local Thermodynamic Equilibrium (LTE). The critical density, $n_{\rm crit}$, estimates the minimum ambient density at

Table 1.3: Some useful interstellar molecules and physical parameters of some transitions

Molecule	Abundance[a]	Transition	λ	T_o [b] (K)	$n_{\rm crit}$ [c] ($\rm cm^{-3}$)	Comments
H_2	1	1→0	2.1 μm	6600	7.8×10^7	shock tracer
CO	8×10^{-5}	J=1→0	2.6 mm	5.5	3.0×10^3	low density probe
		J=2→1	1.3 mm	11.0	2.0×10^4	low density probe
OH	3×10^{-7}	$^2\Pi_{3/2};J=3/2$	18 cm	0.08	1.4×10^0	magnetic field probe
NH_3	2×10^{-8}	(J,K)=(1,1)	1.3 cm	1.1	1.9×10^4	temperature probe
H_2CO	2×10^{-8}	$2_{12}\rightarrow1_{11}$	2.1 mm	6.9	1.3×10^6	high density probe
CS	1×10^{-8}	J=2→1	3.1 mm	4.6	4.2×10^5	high density probe
HCO^+	8×10^{-9}	J=1→0	3.4 mm	4.3	1.5×10^5	tracer of ionization
H_2O		$6_{16}\rightarrow5_{23}$	1.3 cm	1.1	1.4×10^3	maser

[a] number density of main isotope relative to hydrogen
[b] equivalent temperature of the transition energy; $T_o\equiv\Delta E_{ul}/k_B$
[c] evaluated at T=10 K, except for H_2 (T=2000 K)

which collisions dominate the molecular transitions over radiation. If $n \gg n_{\rm crit}$, the transition is thermalized and we observe the spectral line; if $n \ll n_{\rm crit}$, the transition is not observed. The $n_{\rm crit}$ is defined as

$$n_{\rm crit}=\frac{A_{ul}}{\gamma_{ul}}\,, \tag{1.3}$$

where A_{ul} is the Einstein coefficient for spontaneous emission, and γ_{ul} the collisional de-excitation coefficient. Every transition of every molecule has a different critical density (see Table 1.3), and therefore, it can be used to trace different regions within a molecular cloud. Transitions with higher critical densities are the best tracers of densest regions.

For high column densities of the molecular species the transitions can be optically thick. In this case, the optically thick lines trace only the emission coming from the surface layers of molecular clouds. In a situation of optically thick emission, rarer isotopologues (*e.g.* ^{13}CO or C^{18}O for the CO) should be used to trace the inner regions of the molecular clouds, because they are usually optically thinner.

1.3.2 Continuum emission from interstellar dust

Young stellar objects, formed inside molecular clouds, are surrounded by large amounts of gas and dust. The dust grains absorb the radiation emitted by the protostar, causing high extinction at optical wavelengths in star-forming regions. The absorbed radiation is then reemitted at longer wavelengths, mainly at InfraRed (IR) and millimeter (mm) wavelengths, due to the low temperature of dust. While the dust emission in the mm range can be observed with radio telescopes, the IR emission between ∼20 and 100 μm can only be observed from space satellites, because of the opacity of the terrestrial atmosphere at these wavelengths.

Dust emission can be approximated by a modified blackbody law characterized by the temperature of dust, T_d. Such a spectrum corresponds to a blackbody law, $B_\nu(T_d)$, with an optical depth τ_ν that depends on frequency. The observed flux density at a frequency ν for an isothermal source of solid angle Ω_S is

$$S_\nu = B_\nu(T_\mathrm{d})\,(1 - e^{-\tau_\nu})\,\Omega_\mathrm{S}\,. \tag{1.4}$$

The optical depth is proportional to the column mass density along the line of sight, $\tau_\nu = \int_\mathrm{los} \rho\,\kappa_\nu\,\mathrm{dl}$, with κ_ν being the absorption coefficient per unit of total mass (gas and dust) density. In the millimeter and submillimeter regime, κ_ν is generally well described by

$$\left[\frac{\kappa_\nu}{\mathrm{cm^2~g^{-1}}}\right] = \kappa_0 \left[\frac{\nu}{1000~\mathrm{GHz}}\right]^\beta , \tag{1.5}$$

with β, the dust emissivity index, which has values close to 2 in the ISM, and between 1 and 2 in most of star-forming regions, depending on the composition, and geometry of dust grains, and on variations of the homogeneity and size of the region (Walker et al, 1990; Mezger et al., 1991). In general, the value of κ_0 is not well constrained (Beckwith et al., 1990). Specifically, for dense pre/proto-stellar cores and for different gas densities, Ossenkopf & Henning (1994) computed and tabulated the dust opacities at wavelengths between 1 μm and 1.3 mm.

Sometimes, in order to fit all the spectrum together, from IR to mm wavelengths, it is useful to consider different components contributing to the total emission: the young stellar object, a circumstellar disk with a compact and hot component, and a more extended and cold dust envelope. By fitting the spectral energy distribution one can estimate a range of masses, dust temperatures, and dust emissivity indices for each component (Section 2.2). The mass of gas and dust can be estimated from the observed flux density. From Eq. 1.4, and assuming optically thin emission one can obtain

$$S_\nu \simeq B_\nu(T_\mathrm{d})\,\Omega_\mathrm{S}\,\tau_\nu = B_\nu(T_\mathrm{d})\,\frac{A}{d^2}\,\kappa_\nu \int_\mathrm{los} \rho\,\mathrm{d}l\; = B_\nu(T_\mathrm{d})\,\kappa_\nu\,\frac{M}{d^2}\,, \tag{1.6}$$

where M is the mass of gas and dust estimated from the observed flux density S_ν at frequency ν, A is the area of the source, and d is the distance to the source. Thus, from Eq. 1.6 it is possible to obtain

$$M = \frac{S_\nu\,d^2}{B_\nu(T_\mathrm{d})\,\kappa_\nu}\,. \tag{1.7}$$

For a more detailed description see Appendix A in Frau et al. (2010).

II

Low-mass star Formation

Star formation in our Galaxy takes place out inside molecular clouds, which are massive and cold enough to undergo gravitationally collapse. The star formation process is traditionally divided into two different modes: one related to the formation of low-mass stars, and the other one of high-mass stars. Low-mass stars, with masses $<8\ M_{\odot}$, have luminosities dominated by accretion and can form in isolation or in clusters of stars. On the other hand, massive stars, with masses $>8\ M_{\odot}$, seem to form only in massive cores, containing closely-packed “subcores”, that produce a group of stars. In this Chapter we will expose the more relevant details about low-mass star formation (more details can be found in the reviews of Larson 2003, and McKee & Ostriker 2007, and references therein).

2.1 Protostellar evolution: from molecular clouds to protostars

Molecular clouds are the sites of star birth, but to form a star, clouds must begin to collapse. At galactic scales, this collapse is counteracted by tidal galactic forces. At intermediate scales, magnetic fields and turbulence seem to be sufficiently strong to stop collapse. But at smaller scales, the scale of prestellar cores, only thermal and magnetic pressure appears to act efficiently and permanently against self-gravity. Thus, the ideal conditions in clouds to form stars are low thermal pressures (*i.e.*, low kinetic temperatures T_k), and high densities, that is, the conditions found in molecular dense cores.

Two models illustrate the different possibilities on how the collapse of a spherical cloud core might be initiated: a fast collapse model, in which gravity exceeds thermal pressure (Hayashi, 1966; Larson, 1969); and a slow magnetically supported collapse (Shu, 1977; Shu et al., 1987). In both models, the temperature is predicted to remain in the range between 6 K and 12 K as long as the collapsing core remains optically thin to thermal emission from dust (for H_2 densities up to 10^{10} cm^{-3}; Larson, 1985; Masunaga & Inutsuka, 2000).

Fast collapse models consider that the collapse begins with an unstable or marginally stable clump of gas in which gravity overcomes thermal pressure, and causes runaway collapse to occur (Hayashi, 1966). The free fall collapse begins in the external layers and propagates to the inner regions. A universal result of calculations of isothermal collapse is that the collapse is always highly non-uniform and characterized by the runaway growth of a central density peak (Larson, 1969). This occurs because the collapse of the outer layers is always slowed by an outward pressure gradient that develops when the inner pressure rises but the boundary pressure does not. It produces a collapse in a shell-structure mode, from inner to outer shells, with a contraction timescale for each shell similar to the free-fall time for the inner sphere average density

$$t_{\rm ff} = \sqrt{\frac{3\pi}{32 G \rho_c}}\,. \tag{2.1}$$

As a result, the denser inner regions collapse faster than the less dense outer regions. The velocity, density, and temperature distributions in an infalling cloud follow power-laws (Larson, 1972b)

$$\begin{aligned} v &\propto r^{-1/2}\,, \\ \rho &\propto r^{-3/2}\,, \\ T &\propto r^{-1/2}\,. \end{aligned} \tag{2.2}$$

Quasi-static collapse is described in more detail in Chapter 3. Essentially, the model assumes that prestellar cores are initially magnetically supported and condense gradually by ambipolar diffusion, whereby the gas contracts slowly across the field lines (Shu, 1977; Shu et al., 1987). Shu (1977) predicted that such a quasi-static contraction process causes the core to become a Singular Isothermal Sphere (SIS) with no magnetic support and with a density distribution

$$\rho = \frac{C_s^2}{2\,\pi\,G\,r^2}\,, \tag{2.3}$$

with C_s being the isothermal sound speed in the medium,

$$C_s = \sqrt{\frac{\partial P}{\partial r}} = \sqrt{\frac{kT}{\mu m_H}}. \tag{2.4}$$

Once this configuration is achieved, the collapse is initiated at the center, and the radius at which the gas begins to fall propagates outward at the sound speed, producing an expansion wave with radius $R_{\rm ew} = C_s\,t$. This solution is termed an "inside–out" collapse. For radii greater than the expansion wave radius, $r \geq R_{\rm ew}$, the density is that of a SIS (Eq. 2.3), for radii smaller than the expansion wave, $r \leq R_{\rm ew}$, the gas accelerates until it reaches the free-fall speed, with $\rho \propto r^{-3/2}$.

Both models predict that only a very small fraction of the mass of the collapsing core initially attains high enough densities to form a star, while most of the mass remains in an extended infalling envelope which is accreted onto the new formed protostar until it gets its final total mass. Some additional effects can be taken into account in these models. Small departures from spherical symmetry in the collapse have been studied by Larson

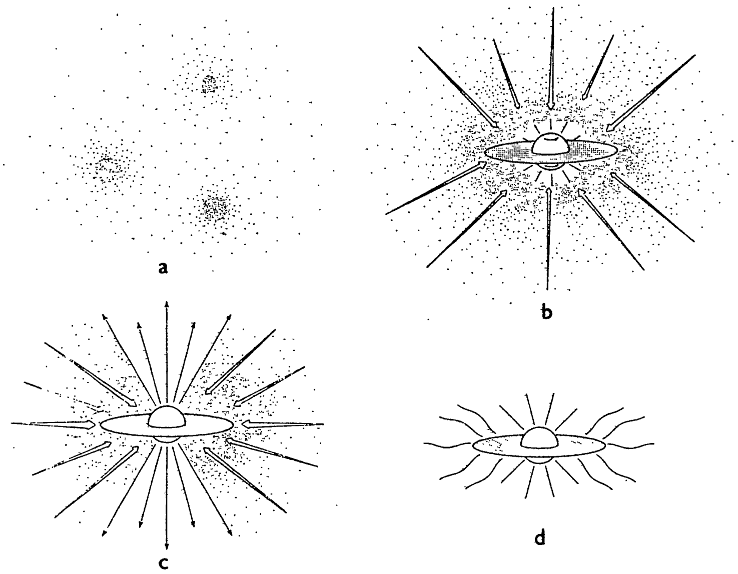

Figure 2.1: The four stages of low-mass star formation extracted from Shu et al. (1987) *(a)* Cores form within molecular clouds as magnetic and turbulent support is lost through ambipolar diffusion. *(b)* A protostar with a surrounding nebular disk forms at the center of a cloud core collapsing inside-out. *(c)* A stellar wind breaks out along the rotational axis of the system, creating a bipolar flow. *(d)* The infall terminates, revealing a newly formed star with a circumstellar disk

(1972a), Hanawa & Matsumoto (2000); and Lai (2000), with the conclusion that these departures do not modify significantly the qualitative results of a spherical collapse. The angular momentum of a collapsing cloud core in rotation (some orders of magnitude higher than the typical angular momentum of stars; Goodman et al. 1993) has to be redistributed or lost when forming a single star. Viscous transport processes in a protostellar accretion disk (Larson, 2002), or fragmentation in binary or multiple systems (Larson, 1972a) can account for much of the initial angular momentum. Numerical models of non-spherical clouds, with rotational motions predict the formation of circumstellar disks, precursors of planetary systems.

In the star formation process, from a prestellar cloud core to a protostar, four stages can be distinguished as proposed by Shu et al. (1987) (see Fig. 2.1). The first stage of star formation, phase (a), is the contraction and fragmentation of the molecular cloud forming slowly rotating cloud cores. In stage (b) a condensing cloud core begins to collapse “inside–out” and a protostar deeply embedded within an envelope of dust and gas forms at the center of the core. The distribution of mass, initially spherical, becomes flattened due to the centrifugal force. In stage (c), a strong stellar wind along the rotational axis stops the infalling of material through the poles, and breaks out as a collimated outflow of gas and dust. New observational evidences seem to indicate that outflow motions begin earlier, at the same time as the collapse. The opening angle of the outflow begins to widen until the infall is stopped, in stage (d). During this last phase, the total mass of gas and dust has been accreted or pushed away. All the system becomes observable at ultraviolet, optical and near-infrared wavelengths.

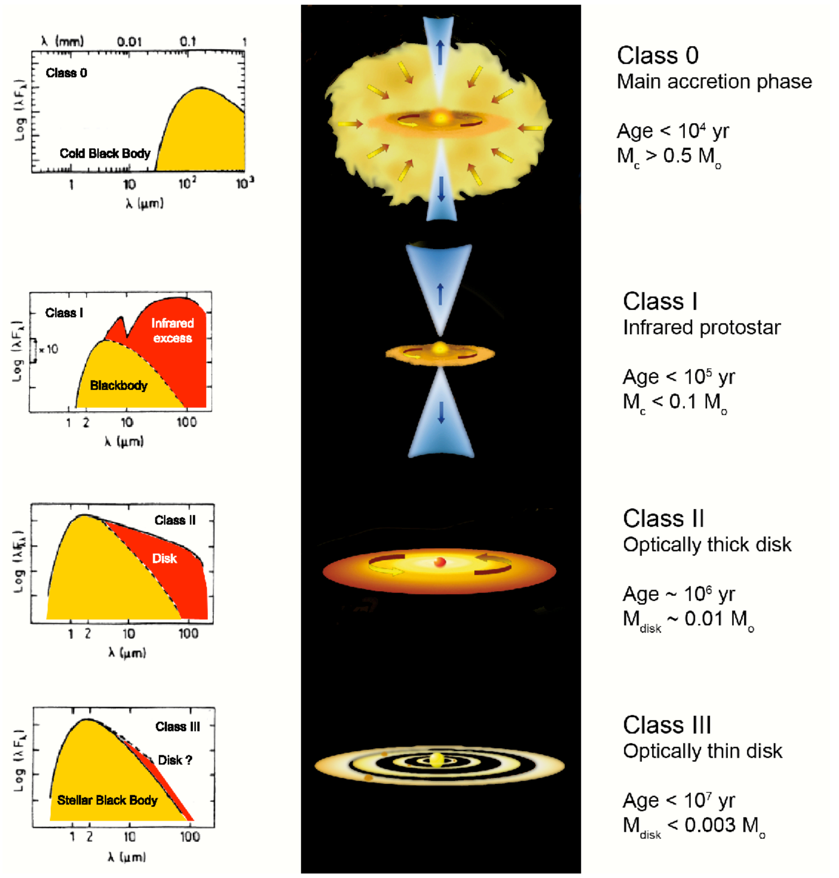
λ (mm)
0.01
0.1
1
Class 0
Log (λF_λ)
Cold Black Body
1
10
10²
10³
λ (μm)
Class I
Infrared excess
×10
Blackbody
1 2
10
100
λ (μm)
Class II
Disk
Class III
Disk ?
Stellar Black Body
Class 0
Main accretion phase
Age < 10⁴ yr
M_c > 0.5 M_o
Class I
Infrared protostar
Age < 10⁵ yr
M_c < 0.1 M_o
Class II
Optically thick disk
Age ~ 10⁶ yr
M_disk ~ 0.01 M_o
Class III
Optically thin disk
Age < 10⁷ yr
M_disk < 0.003 M_o

Figure 2.2: Classification of low-luminosity Young Stellar Objects. Spectral energy distribution, and schematic representation of the evolutionary stage of the Class 0, I, II, and III objects. Courtesy of Luca Carbonaro.

2.2 Classification of low-luminosity Young Stellar Objects

During the first stages of the star formation processes, a Young Stellar Object (YSO) is deeply embedded in the molecular cloud and emits most of its luminosity in the infrared wavelengths. The Spectral Energy Distribution (SED) at these wavelengths (between 1 and 100 μm) depends on the nature and distribution of the material surrounding the YSO. The YSO's SEDs are conventionally divided into four classes, which are believed to represent an evolutionary progression. Myers et al. (1987) divided sources into two categories; Lada (1987) introduced the definition of the Classes I–III YSO; Adams, Lada, & Shu (1987) discussed a similar classification; and André, Ward-Thompson, & Barsony (1993) added the, very embedded protostellar, Class 0 stage. Figure 2.2 shows a scheme of the different evolutionary stages of a YSO, and its spectral distribution at infrared wavelengths. The spectral index, between 2.2 and 20 μm, used to classify the YSO is defined as

$$\alpha_{\mathrm{IR}} = -\frac{d\log \nu F_\nu}{d\log \nu} = \frac{d\log \lambda F_\lambda}{d\log \lambda} \,. \tag{2.5}$$

Class 0 objects: The youngest stellar objects are in this evolutionary stage, which was proposed by André, Ward-Thompson, & Barsony (1993) and is similar to the Extreme

Class I objects of Lada (1991). These young protostars are extremely faint in the near-IR (indeed, usually undetectable at wavelengths shorter than 10 μm), and have a large submillimeter luminosity, $L_{submm}/L_{bol} > 5 \times 10^{-3}$ [1]. The spectral energy distribution is typical of a black body at a low temperature, < 30 K, coming from a cold dust envelope, $M_{\rm envelope} \gtrsim m_*$. Protostars are believed to achieve a significant fraction, if not most, of their mass in this embedded phase. Most of the known Class 0 objects are associated with intense and collimated molecular outflows and Herbig–Haro objects, and a major fraction shows centimeter emission coming from a thermal radio jet.

Class I objects: They have a positive spectral index of $0 \leq \alpha_{\rm IR} \leq 3$, which suggests the presence of large amounts of dust. These objects, with typical ages of $\sim 10^5$ years and deeply embedded in the molecular cloud, are not observable at visible wavelengths. Three main structures can be found in a Class I source: a large-scale dust envelope ($\sim 10^4$ AU) in free fall, a cavity surrounding the YSO with a size of $\sim$200 AU, and a flattened disk at scales < 200 AU. Class I objects are more luminous than Class II and III sources, with the main contribution to their luminosity coming from the accretion of material.

Class II objects: A spectral index of $-2 \leq \alpha_{\rm IR} \leq 0$ indicates that the YSO is still surrounded by dust. These objects can be observed at optical and infrared wavelengths. The optical contribution corresponds to that of a black body consistent with a pre-main sequence cold star, with an age of $\sim 10^6$ years, while the excess at infrared wavelengths is due to an optically thick circumstellar disk of dust with a mass of ~ 0.01 $M_\odot$. Classical T Tauri stars or stars with FU Orionis episodes are typical of this evolutionary class.

Class III objects: They are the most evolved YSOs, characterized by a spectral index $-3 \leq \alpha_{\rm IR} \leq -2$. The spectral energy distribution corresponds to a black body law with a temperature of a typical reddened photosphere of a young star, attenuated by a factor $\exp(-\tau_\nu)$ due to the dust opacity. Class III objects are observable at visible wavelengths, with low luminosities at mid- and far-infrared wavelengths. These objects are known as naked T Tauri stars, and have typical ages of $\lesssim 10^7$ years.

It is important to note that the previous classification is only valid for low-mass young stellar objects. For more massive stars, the fast evolution to the main sequence makes more difficult to establish a similar classification.

---

[1] L_{submm} is the luminosity at wavelengths > 350 μm, and L_{bol} is the total luminosity.

III

Dense cores

The smallest and densest cloud entities, dense cores, are found in the inner and denser regions of giant and dark molecular clouds (Chapter 1). The low–mass dense cores (few solar masses) have densities that exceed 10^4 cm^{-3}, temperatures of $\sim$10 K, sizes of $\sim$0.1 pc and subsonic turbulence. Low-luminosity infrared sources ($L < 10\ L_\odot$), molecular outflows, and T Tauri stars are associated with many dense cores, being the most direct evidence that these structures form stars. There are also compact and dense regions not embedded within larger complexes, so called Bok globules, with embedded infrared sources and energetic molecular outflows associated with them. Apart from their isolation, they are similar to the dense cores found in the dark molecular cloud complexes. It is important to note that infrared sources detected toward Bok globules are of relatively low luminosity, and the same happens for those detected toward the major part of nearby dense cores, suggesting that this kind of compact clouds are sites of low-mass star formation. High-luminosity infrared sources, associated with massive young stars, are also observed within massive dense molecular cores. The main difference is that most of the massive dense cores are located at larger distances ($\gtrsim$1 kpc), which makes it more difficult to study them with high resolution. Observations of the Orion dense cores (Orion is the nearest massive star-forming complex, located at only 500 pc) show that they are warmer, two or three times more turbulent, three times more massive, and twice the diameter of their counterparts in, for example, the Taurus-Auriga molecular cloud (one of the nearest low-mass star forming regions, a dark molecular complex located at 140 pc).

3.1 Physical structure in equilibrium

3.1.1 Isothermal sphere in hydrostatic equilibrium

Definition

The most idealized case to start studying the initial stages of the star formation process is that of an isothermal sphere supported against gravitational collapse by its own thermal pressure. The equation for hydrostatic equilibrium, gravitational potential, and gravitational force read

$$\frac{dP}{dr} = -\frac{GM_r}{r^2}\rho, \tag{3.1}$$

$$\nabla^2\phi = \frac{1}{r^2}\frac{d}{dr}\left(r^2\frac{d\phi}{dr}\right) = 4\pi G\rho, \tag{3.2}$$

and

$$\frac{d\phi}{dr} = -\frac{GM_r}{r^2}, \tag{3.3}$$

respectively , where r is the radius, P the pressure, M_r the mass interior to radius r, ρ the mass volume density, ϕ the gravitational potential, and G the gravitational constant. The mass of the sphere will follow

$$\frac{dM_r}{dr} = 4\pi r^2\rho. \tag{3.4}$$

We need to make use of the equation of state for an ideal gas,

$$P = nkT = \frac{kT}{\mu m_H}\rho = C_s^2\rho, \tag{3.5}$$

where n is the volume number density of molecules, k the Boltzmann constant, T the temperature, m_H the mass of the Hydrogen atom, μ the weight of the median molecule ($\mu m_H = \rho/n$), and C_s is the isothermal sound speed (Eq. 2.4). To help in further analysis, one can define the non-dimensional variables

$$u = \phi/C_s^2 \tag{3.6}$$

and

$$\xi = \frac{\sqrt{4\pi G\rho_c}}{C_s}r, \tag{3.7}$$

where ρ_c is the central mass volume density, ξ the non-dimensional radius, and u the non-dimensional gravitational potential.

By combining equations 3.1, 3.4, and 3.5, and applying a variable substitution using equations 3.6 and 3.7, one obtains the Lane-Emden equation

$$\frac{1}{\xi}\frac{d}{d\xi}\left(\xi\frac{du}{d\xi}\right) = e^{-u}. \tag{3.8}$$

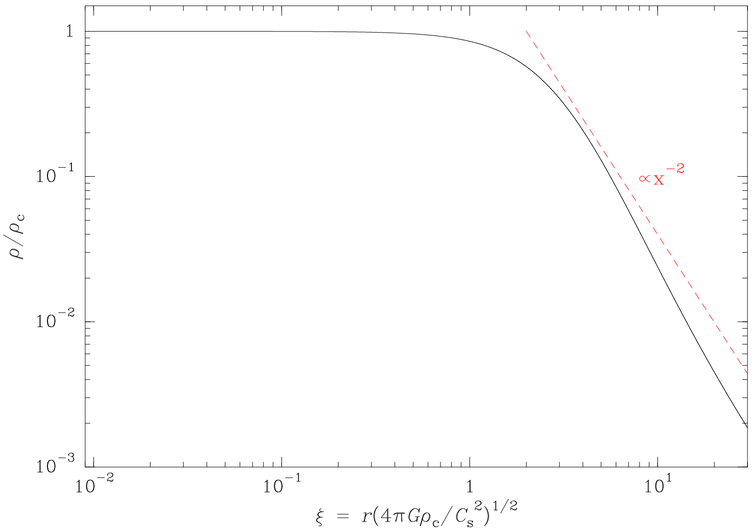

Figure 3.1: Numerical solution of the BE sphere density profile (Eq. 3.8) in logarithmic scale. ξ is the non-dimensional radius (Eq. 3.7) and ρ/ρ_c is the non-dimensional density.

The Bonnor-Ebert sphere

The Bonnor–Ebert (BE) sphere (Bonnor, 1956; Ebert, 1955) describes a self-gravitating, pressure-confined, isothermal gas sphere in hydrostatic equilibrium. The density profile can be derived by solving Eq. 3.8 imposing an outer confining pressure,

$$P_{\text{Out}} = C_s^2 \rho \left(R_{\text{Out}}\right), \tag{3.9}$$

exerted at the outer radius of the sphere, R_{Out}, which fixes the maximum non-dimensional radius,

$$\xi_{\max} = \frac{\sqrt{4\pi G \rho_c}}{C_s} R_{\text{Out}} \tag{3.10}$$

that characterizes uniquely the BE sphere solution. One can impose the boundary conditions at the core center, forcing the density to be ρ_c and its derivative to be 0,

$$\rho\left(0\right) = \rho_c, \qquad \frac{d\rho}{dr}\lfloor_{r=0} = 0. \tag{3.11}$$

These conditions, together with the combination of Eqs. 3.1 and 3.4, lead to a density profile of the form

$$\rho = \rho_c \, e^{-\phi/C_s^2}. \tag{3.12}$$

Figure 3.1 shows the numerical solution for the BE density profile (Eq. 3.12) as a function of the non-dimensional radius in units of the central density. The density is roughly flat in the inner region and falls as $\sim r^{-2}$, typical of spherical hydrostatic equilibrium, at the outer region. This profile can be better understood by finding the physically meaningful

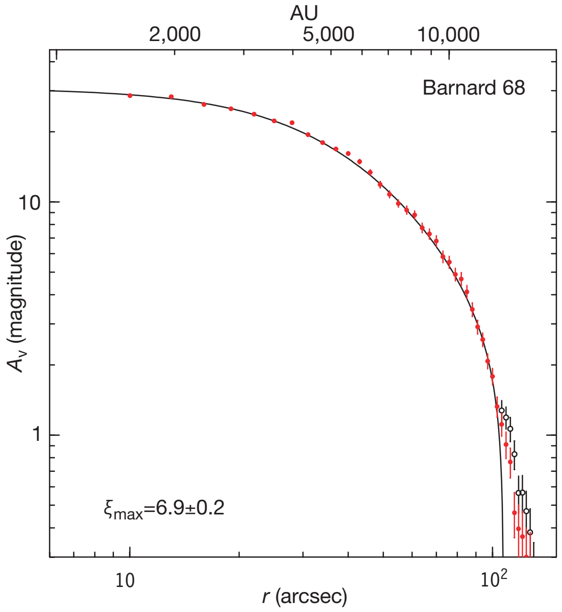

Figure 3.2: Radial column density profile of B68 extracted from Alves et al. (2001) in terms of magnitudes of A_V. Circles and bars show the data points and rms dispersion for the averaged profile of the extinction measurements. The solid line represents the best fit of a theoretical BE sphere to the data. The close match of the data with theory indicates that the internal structure of the cloud is well characterized by the equations for a self-gravitating, pressure-confined, isothermal sphere with gravity balanced by thermal pressure.

radius at which the free-fall time (Eq. 2.1) and the sound crossing time, $t_{\rm sc} = r/C_s$, are equal. This turnover radius (see *e.g.* Keto & Caselli, 2010),

$$r_t = \frac{C_s}{\sqrt{32\rho_c G/3\pi}}, \tag{3.13}$$

is equivalent to a non-dimensional radius of $\xi = 1.92$. For smaller radii, the sound crossing time is shorter than the free-fall time and, therefore, any density enhancement created gravitationally will be dispersed by sound waves. On the contrary, for larger radii, the free-fall time is smaller than the sound crossing time and the density will follow the typical r^{-2} profile. Alves et al. (2001) presented Barnard 68 (B68) as the prototype object following a BE profile. Figure 3.2 shows the good agreement between the B68 A_V data and the BE model, indicating that this object is a dynamical unit close to hydrostatic equilibrium.

It is critical to study the stability of the BE spheres because the dominating heating and cooling mechanisms may change depending on whether the cloud is collapsing. A stable cloud is heated up by cosmic rays and infrared photons, and cooled down by dust and molecular line radiation. On the other hand, a gravitationally unstable cloud is also heated mechanically through the work of the gravitational compression, and the cooling mechanisms will change if the dust becomes optically thick. This will eventually lead to temperature differences within the core and the isothermal condition will be no longer met.

Stability against gravitational collapse

We can measure the mass, M, of the object from observational maps and derive the confining pressure, $P_{\rm Out}$, from the surrounding medium properties (density and temperature). However, for the inside-out numerical integration of a BE sphere, the key parameters are ρ_c and r_0. We need to reformulate the equations in terms of the available observables. One can rewrite Eq. 3.4 and calculate the mass as

$$M = 4\pi \int r^2 \rho \, dr = 4\pi\rho_c \left(\frac{C_s^2}{4\pi G\rho_c}\right)^{3/2} \int_0^{\xi_{\rm Max}} e^{-u}\xi^2 d\xi, \tag{3.14}$$

which depends on the non-dimensional integral on the right-hand side and scales with the constant physical factor in front it. In Fig. 3.3a, we show the value of the integral as a function of $\xi_{\rm Max}$. For $\xi_{\rm Max} < 6.5$ (see later in the text), the mass roughly follows $\propto r^3$. For $\xi_{\rm Max} > 6.5$, there is a trend change and the BE can only support extra mass following a $\propto r^1$ rate.

We can rewrite the expression of the confining pressure (Eq. 3.9) making use of Eq. 3.14 as

$$P_{\rm Out} = C_s^2 \rho_c e^{-\phi} = \frac{C_s^8}{G^3 M^2} \left(\frac{e^{-u}\left(\int_0^{\xi_{\rm Max}} e^{-u}\xi^2 d\xi\right)^2}{4\pi} \right), \tag{3.15}$$

which depends on the non-dimensional parenthesis and scales by the constant physical factor in front. Figure 3.3b shows the value of the non-constant part as a function of $\xi_{\rm Max}$. It is clearly peaked toward $\xi_{\rm Max} = 6.5$ with a maximum value of ∼1.40. $\xi_{\rm Max} = 6.5$ turns to be the critical non-dimensional radius ($\xi_{\rm crit}$) for a BE sphere of a given mass M at a given temperature T. This value corresponds to $\rho_c/\rho_{\rm Out} \sim 14.1$, which is the critical density contrast, $(\rho_c/\rho_{\rm Out})_{\rm crit}$, achievable by a stable BE sphere. In Fig. 3.4, we show the measured and best fitting BE column density profiles for four Bok globules. Three of the four sources have $\xi_{\rm max}$ values larger that $\xi_{\rm crit}$. This produces a decrease in the confining pressure, and therefore, an unstable hydrostatic equilibrium that will lead to gravitational collapse.

We can define the non-dimensional mass as

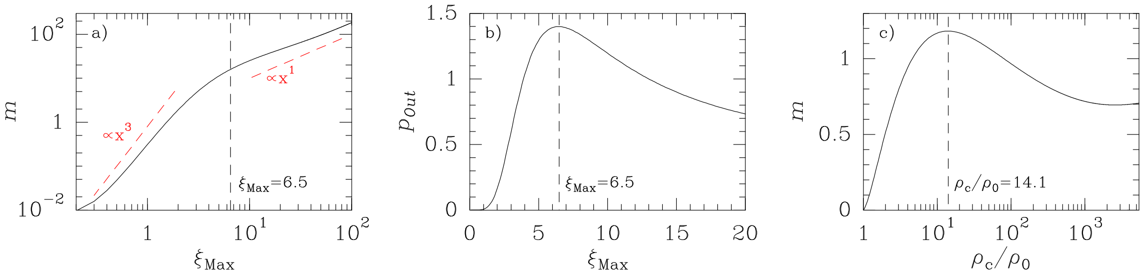

Figure 3.3: Numerical solution of the BE sphere. *Left panel*: non-dimensional mass m up to $\xi = \xi_{\rm max}$ as a function of $\xi_{\rm max}$. *Middle panel*: Outer confining pressure as a function of $\xi_{\rm max}$. *Right panel*: m up to $\xi = \xi_{\rm max}$ as a function of the density contrast.

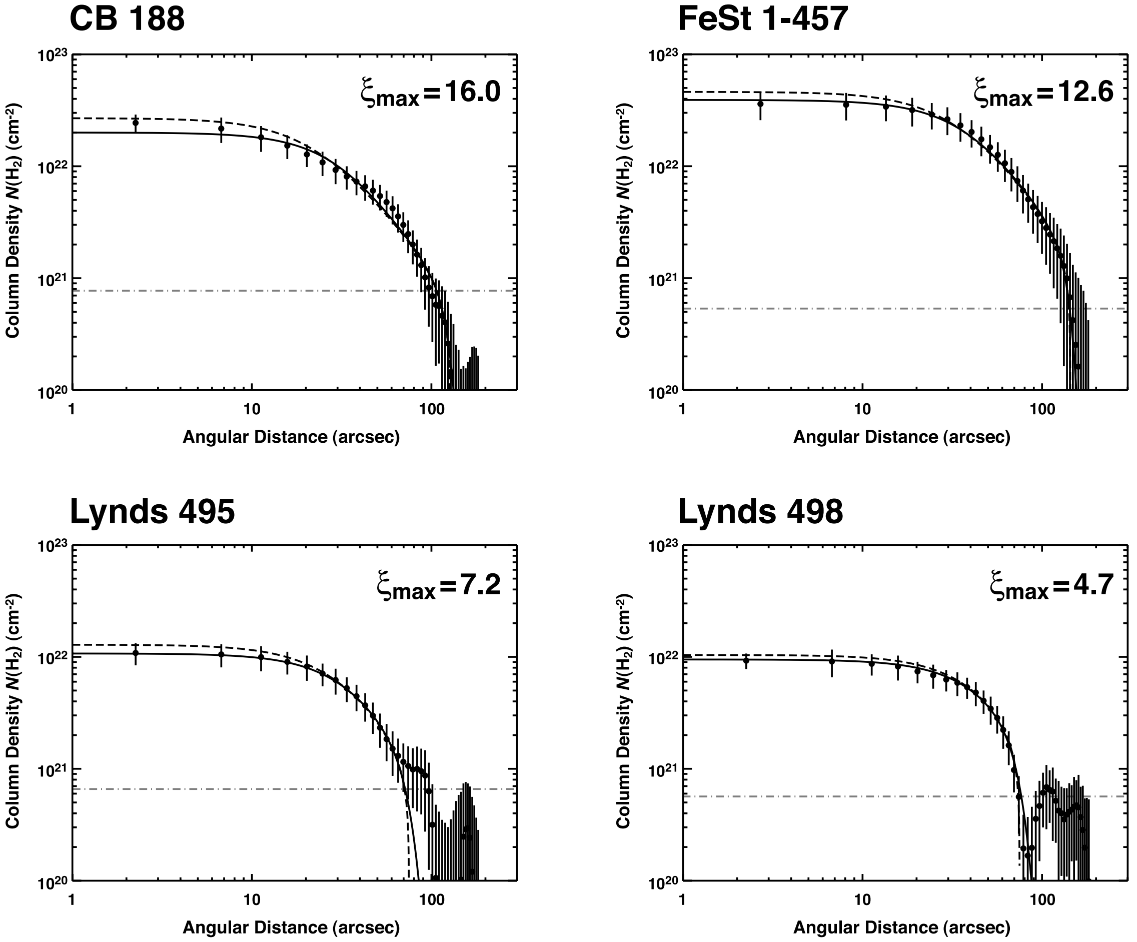

Figure 3.4: Radial column density profiles of four Bok globules extracted from Kandori et al. (2005). Circles and bars show the average and rms dispersion for each radial annulus. The solid line represents the best fit of a theoretical BE sphere to the data. The values of $\xi_{\max}$ indicate that three of the four are thermally unstable to gravitational collapse.

$$m \equiv \frac{P_{\text{Out}}^{1/2} G^{3/2} M}{C_s^4}, \tag{3.16}$$

and make use of Eqs. 3.9 and 3.14 to rewrite it as a function of the density contrast,

$$m = \left(4\pi \frac{\rho_c}{\rho_{\text{Out}}}\right)^{-1/2} \int_0^{\xi_{\text{Max}}} e^{-\phi} \xi^2 d\xi. \tag{3.17}$$

Figure 3.3c shows that the maximum mass is ~1.18 for the $(\rho_c/\rho_{\text{Out}})_{\text{crit}}$ value. Larger values of m will indicate that the object observed is thermally unstable to gravitational collapse. We can then define the BE mass using the critical value as

$$M_{\text{BE}} = 1.18 \frac{C_s^4}{P_{\text{Out}}^{1/2} G^{3/2}}. \tag{3.18}$$

3.1.2 The Jeans criterion

A more general approach to study the stability of dense cores, not limited to spherical symmetry, is the Jeans criterion. We study in this case the dynamics of a static fluid assuming uniform density (ρ) and temperature affected by a small perturbation ($\delta\rho$, $\delta\vec{v}$). It is possible to determine through this analysis whether a region of the isothermal gas is thermally supported against gravity regardless of the geometry. The continuity equation, which ensures the mass conservation, for the mean fluid and the first order term of a perturbative analysis for the small perturbation read

$$\frac{\partial\rho}{\partial t} + \vec{\nabla}\cdot(\rho\vec{v}) = 0 \tag{3.19a}$$

$$\frac{\partial\delta\rho}{\partial t} + \rho\vec{\nabla}\cdot\vec{v} = 0, \tag{3.19b}$$

respectively. The fluid dynamics follows the Euler equation. The general form and the perturbative linearized form for the perturbation read

$$\frac{\partial\vec{v}}{\partial t} + \left(\vec{v}\cdot\vec{\nabla}\right)\vec{v} + \frac{1}{\rho}\vec{\nabla}P + \vec{\nabla}\phi = 0 \tag{3.20a}$$

$$\frac{\partial\delta\vec{v}}{\partial t} + \frac{C_s^2}{\rho}\vec{\nabla}\delta\rho + \vec{\nabla}\delta\phi = 0, \tag{3.20b}$$

respectively. The solution in one dimension, for simplicity, is a plane wave of the form

$$\delta\rho = \delta\rho_0 \exp[i(kx - \omega t)], \tag{3.21}$$

where $k = 2\pi/\lambda$ is the wave number, λ the wavelength, ω the frequency, and $\delta\rho_0$ the perturbation amplitude. Substituting Eq. 3.21 into Eqs. 3.19b and 3.20b, and further using Eqs. 3.2 and 3.5 for the perturbations, we obtain

$$\omega^2 = k^2C_s^2 - 4\pi G\rho \tag{3.22}$$

for small λ, $\omega \approx kC_s$. In this regime, the perturbation acts as a sound wave. We can derive the critical wavelength forcing $\omega = 0$, known as the Jeans length

$$\lambda_{\mathrm{J}} \equiv \sqrt{\frac{C_s^2\pi}{G\rho}}. \tag{3.23}$$

Larger wavelengths have exponentially growing amplitudes that can collapse gravitationally. This wavelength is the size of the perturbed region. To compare it to the BE results, we can assume a spherical object and find the radius as $\lambda_{\mathrm{J}}/2$. This radius is equivalent to a non-dimensional radius $\xi = \pi$ (Eq. 3.7).

3.1.3 Magnetic field support

Dynamically important magnetic fields, noted as $\vec{B}$, have been measured through different techniques in different kind of clouds ranging from dense cores up to giant molecular clouds. We therefore turn our attention to the interstellar magnetic field. The cloud internal magnetic field may be important in counteracting gravity. This behavior is due to the flux freezing, *i.e.* qualitatively magnetic fields act as if they were tied to the gas. This phenomenon is also responsible for the increase of $\vec{B}$ with density.

Flux freezing

We start the analysis using the Ampère's law, which relates the magnetic field with the density current, $\vec{j}$, that originates it

$$\nabla \times \vec{B} = \frac{4\pi}{c}\vec{j}, \tag{3.24}$$

where c is the speed of light. The density current is carried by the free electrons, ions, and grains of the cloud. The Ohm's law relates this current to the electrical field, $\vec{E}$, in a medium at rest

$$\vec{j} = \sigma\vec{E}, \tag{3.25}$$

where σ is the conductivity. If we shift to a reference frame tied to the neutral matter, moving at velocity $\vec{u}$, the electrical field is

$$\vec{E'} = \vec{E} + \frac{\vec{u}}{c} \times \vec{B}, \tag{3.26}$$

where the prime refers to this new frame. The current density does not change from one frame to another, $\vec{j} = \vec{j}' = \sigma\vec{E}'$, therefore we can plug Eq. 3.26 into Eq. 3.25. The resulting expression for $\vec{j}$ can be combined with Eq. 3.24 leaving a dependence on $\vec{E}$,

$$\nabla \times \vec{B} = \frac{4\pi\sigma}{c}\left(\vec{E} + \frac{\vec{u}}{c} \times \vec{B}\right), \tag{3.27}$$

which we can eliminate by using Faraday's law

$$\nabla \times \vec{E} = -\frac{1}{c}\frac{\partial\vec{B}}{\partial t}. \tag{3.28}$$

Taking the curl in both sides of the resulting expression, we obtain the fundamental Magneto-HydroDynamic (MHD) equation for the magnetic field:

$$\frac{\partial\vec{B}}{\partial t} = \nabla \times \left(\vec{u} \times \vec{B}\right) - \nabla\left(\frac{c^2}{4\pi\sigma}\nabla \times \vec{B}\right). \tag{3.29}$$

The first right-hand term represents the *ideal* MHD situation while the second one represents the *non-ideal* effects, the Ohmic dissipation, that vanishes with large conductivities.

We may then justify the flux freezing state if the time variation of the Ohmic term is negligible as compared to the typical timescales. We can define the Ohmic dissipation timescale as

$$t_{\text{Ohm}} = L^2 \frac{4\pi\sigma}{c^2}, \tag{3.30}$$

where L is the lengthscale of interest. One can estimate the conductivity of the ISM as $\sigma \sim 10^7\ \mathrm{T}^{3/2}$ (Spitzer, 1962). In a typical core of $L \sim 0.1$ pc, $n \sim 10^4\ \mathrm{cm}^{-3}$, and $T \sim 10$ K, this timescale is of the order of 10^{15} yr, and therefore, Ohmic dissipation can be neglected.

If we drop the Ohmic dissipation term, we obtain the ideal MHD equation,

$$\frac{\partial \vec{B}}{\partial t} = \nabla \times \left(\vec{u} \times \vec{B} \right), \tag{3.31}$$

only accounting for flux freezing. This means that both fluid motion and magnetic field are tied. In the case of comparable kinetic and magnetic energies (roughly true for most clouds up to $n \sim 10^5\ \mathrm{cm}^{-3}$ according to current observational measures), both exert a strong mutual influence which could explain, among other facts, the filamentary structure of dark molecular clouds as an alignment to the large-scale magnetic fields (*e.g.* the Pipe nebula).

Sphere threaded by a uniform $\vec{B}$ field

We start with a spherical core threaded by a uniform magnetic field, $\vec{B_0}$, straight and parallel that permeates through all the cloud. The magnetic field is assumed to be inherited from the environment on which the cloud forms. We will use cylindrical coordinates and note the radial distance as ϖ, the azimuth as ϕ, and the vertical distance as z defined as the direction of $\vec{B}$. We may reformulate now the equation of hydrostatic equilibrium (Eq. 3.1) as a force balance equation making use of the gravitational potential (Eq. 3.2) and the isothermal equation of state (Eq. 3.5), and including the magnetic force

$$0 = -C_s^2 \nabla\rho - \rho \nabla\phi_g + \frac{\vec{j}}{c} \times \vec{B}. \tag{3.32}$$

If the cloud does not rotate, the magnetic field remains poloidal (*i.e.* in the $\varpi - z$ plane) and the current $\vec{j}$ is then toroidal (*i.e.* in the ϕ-direction, Eq. 3.24). As a consequence, the magnetic force is a poloidal vector with both ϖ- and z-components that will break the spherical symmetry of the purely thermal case.

Based essentially on Eqs. 3.2, 3.5, 3.24, and 3.32, one can model the magnetized spheres (see *e.g.* the works of Mouschovias, 1976a,b). The remaining key point is to select the mass-to-flux distribution, $dM/d\phi$, for which the current data is too scarce. For the simplified physical model considered, consisting of a uniform magnetic field parallel to the z-axis, one can write

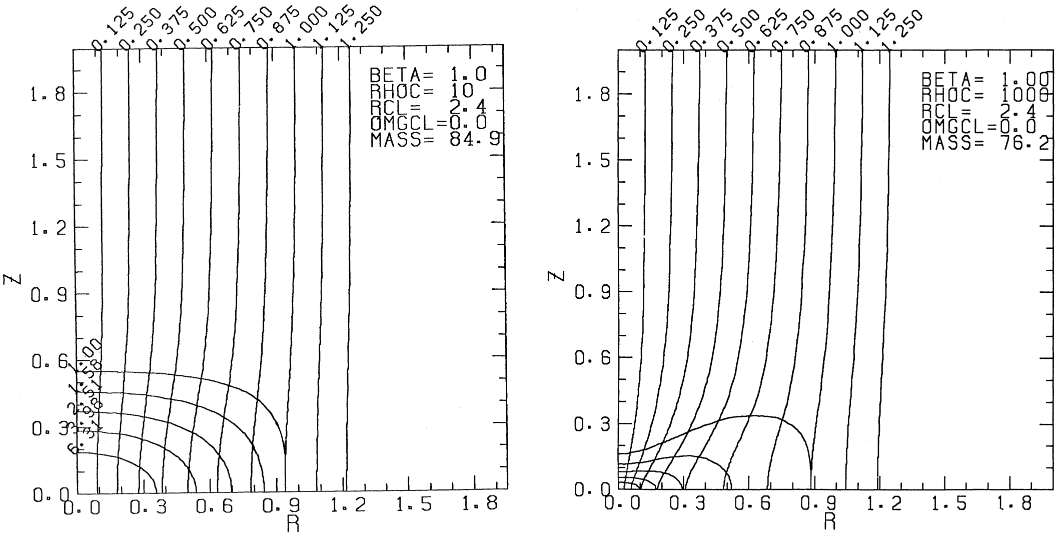

Figure 3.5: Equilibrium configurations of magnetized clouds with $\xi_0 = 2.4$ and $\alpha = 1.0$ extracted from Tomisaka et al. (1988b). The R and Z axis represent ϖ/R_0 and z/R_0, respectively. The left- and right-hand panels show the configuration for $\rho_c/\rho_0 = 10$ and $\rho_c/\rho_0 = 10^3$, respectively. The isodensity contours are the horizontal lines toward R=0. The magnetic field lines are the vertical lines toward large values of Z.

$$\begin{aligned} \frac{dM}{d\Phi_B} &= \frac{2\rho_i R_0}{B_0}\left(1 - \frac{\Phi_B}{\Phi_{\rm cl}}\right)^{1/2} & \Phi_B < \Phi_{\rm cl} \\ &= 0 & \Phi_B > \Phi_{\rm cl}, \end{aligned} \tag{3.33}$$

where Φ_B is the flux contained within the surface generated by rotating any field line about the axis, and $\Phi_{\rm cl} \equiv \pi B_0 R_0^2$ is the total flux threading the cloud. Numerical works make use of non-dimensional variables thus we introduce the magnetic pressure,

$$P_B \equiv \frac{B^2}{8\pi} \tag{3.34}$$

to define the magnetic to thermal pressure ratio,

$$\alpha \equiv \frac{B_0^2}{8\pi P_0}, \tag{3.35}$$

The non-dimensional radius of the initial sphere is

$$\xi_0 = \frac{\sqrt{4\pi G\rho_c}}{C_s} R_0. \tag{3.36}$$

Figure 3.5 shows the isodensity contours and magnetic field lines of the equilibrium configurations for two models sharing $\xi_0 = 2.4$ and $\alpha = 1.0$. The left- and right-hand side panels display the results for $\rho_c/\rho_0 = 10$ and $\rho_c/\rho_0 = 10^3$, respectively. In both cases, the cloud is flattened in the polar direction. Nearly straight and parallel magnetic fields lines exert a

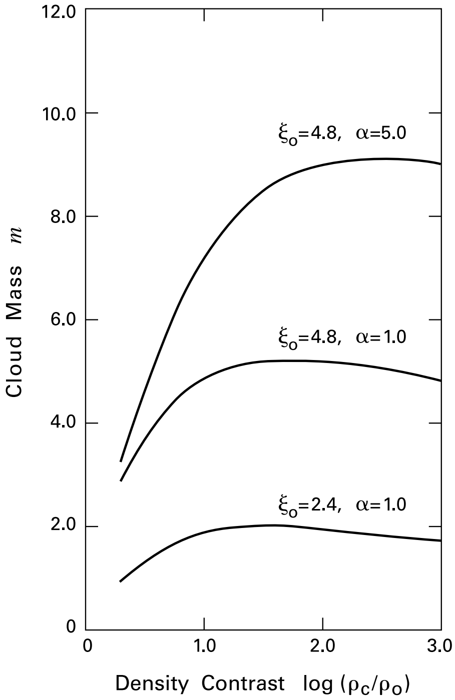

Figure 3.6: Non-dimensional critical mass, $m_{\rm crit}$, in equilibrium configurations of magnetized clouds (based on Tomisaka et al., 1988b, extracted from Stahler & Palla, 2005). $m_{\rm crit}$ is plotted as a function of the density contract for selected combinations of ξ_0 and α.

retarding pressure, to be added to thermal pressure, mostly in the horizontal axis. On the other hand, only thermal pressure is acting in the polar axis, and thus, needs larger densities to exert the equilibrium pressure required (Eq. 3.5). The flatter configuration of the $\rho_c/\rho_0 = 10^3$ case arises from the larger central density, and thus, the larger gravitational pull requires larger counteracting pressures. Raising α and ξ_0 also generate flatter clouds, the former one by increasing the magnetic pressure with respect to thermal pressure, and therefore, the difference of stopping pressures between the two axes, and the latter one by hosting more flux in the parental cloud leading to a larger equilibrium mass (Eq. 3.38). Figure 3.5b also shows the effect of flux freezing in the field lines that have been pulled inward with increasing densities.

Figure 3.6 shows three selected mass curves for equilibrium configurations with fixed ξ_0 and α as a function of the density contrast. In the three cases, m rises monotonically and then reaches a limit before declining. The trend change indicates the onset of gravitational collapse (see Fig. 3.3c for the purely thermal case), and therefore, the maximum corresponds to the critical mass $m_{\rm crit}$. A good fit to the numerical values is $m_{\rm crit} = 1.2 + 0.15\,\alpha^{1/2}\xi_0^2$, which in dimensional units is

$$M_{\rm crit} \approx M_{\rm BE} + M_\Phi, \tag{3.37}$$

where $M_{\rm BE}$ is as in Eq. 3.18 and M_Φ is defined as

$$\begin{aligned} M_\Phi &= 0.15\,\alpha^{1/2}\xi_0^2\,\frac{C_s^4}{P_{\rm Out}^{1/2}G^{3/2}} \\ &= 0.15\,\frac{2}{\sqrt{2\pi}}\frac{B_0\pi R_0^2}{G^{1/2}} \\ &= 0.12\,\frac{\Phi_{\rm cl}}{G^{1/2}}. \end{aligned} \tag{3.38}$$

M_Φ depends only on the flux threading the cloud. This means that, if the flux freezing assumption holds, it will remain constant regardless of the external pressure applied. A direct consequence is a richer casuistry in cloud stability against gravitational collapse. A cloud with $M < M_\Phi$ cannot be driven into collapse. Clouds with $M < 0.59\,M_{\rm BE} + M_\Phi$ have only one equilibrium configuration and is always stable. The 0.59 numerical factor is the first minimum shown in Fig. 3.3c for the purely thermal case. Those with $M > M_{\rm crit}$ have no equilibrium and are unstable to gravitational collapse. Finally, clouds with $0.59\,M_{\rm BE} + M_\Phi < M < M_{\rm crit}$ have two possible density contrasts for any ξ_0 and α (see Fig. 3.6), where the higher one is always unstable. As an example, we can use the bottom curve in Fig. 3.6 for which $m_{\rm crit}$ corresponds to a density contrast of ~ 50. Figure 3.5 represents two cases of that curve. The left-hand panel ($\rho_c/\rho = 10$) corresponds to a gravitationally stable configuration while the right-hand panel ($\rho_c/\rho = 10^3$) is unstable.

From Eq. 3.38, one can define the critical mass to flux ratio, $(M/\phi)_{\rm crit}$, as the maximum mass that a given magnetic flux can support against gravitational collapse. It is possible to define then the parameter

$$\lambda = \frac{(M/\phi)}{(M/\phi)_{\rm crit}} \tag{3.39}$$

as a measure of the relative strength of magnetic support. A $\lambda > 1$ cloud is magnetically super-critical and self-gravity cannot be supported by $\vec{B}$ alone. On the other hand, a sub-critical cloud ($\lambda < 1$) is supported against gravitational collapse regardless of the thermal support.

3.1.4 Support from MHD waves

We study now a more general approach independent of the geometry (as the Jeans criterion for the thermal case), the MHD waves. In addition, there is now a special interest on finding different approaches as the well-ordered field lines from the models of the previous section are able to reproduce the general trend but not the local deviations seen in optical and infrared polarization studies. Although MHD waves have not been seen directly, they could explain the super-thermal broadening of molecular tracers and provide significant support against gravitational collapse.

Simplified model

MHD waves originate when a perturbation in the fluid is transmitted to the field because of flux freezing. Magnetic tension acts to remove the local distortion on the field and causes the perturbation to propagate along the field line as a traveling wave. We consider then a small perturbation in a medium of uniform still gas permeated by a uniform magnetic field $\vec{B}_0$. As for the Jeans criterion, the solution is a plane wave (Eq. 3.21) that we generalize to point in any direction through the vector wave number $\vec{k}$ as

$$\delta\rho = \delta\rho_0 \exp[i(\vec{k}\vec{x} - \omega t)]. \tag{3.40}$$

To keep the gas isothermal and avoid self-gravity effects, we assume long periods and wavelengths smaller than λ_J. We may now recall the force balance equation (Eq. 3.32), drop the gravitational term, make use of Eq. 3.24, and allow to produce a net acceleration:

$$\rho\frac{D\vec{u}}{Dt} = -C_s^2\nabla\rho + \frac{1}{4\pi}\left(\nabla \times \vec{B}\right) \times \vec{B}. \tag{3.41}$$

A perturbation analysis of this equation, assuming flux freezing (Eq. 3.31), yields the expression

$$-i\,\omega\,\delta\vec{B} = i\,\vec{k} \times \left(\delta\vec{u} \times \vec{B}_0\right), \tag{3.42a}$$

which expanded is

$$-\omega\,\delta\vec{B} = \left(\vec{k}\cdot\vec{B}_0\right)\delta\vec{u} - \left(\vec{k}\cdot\delta\vec{u}\right)\vec{B}_0. \tag{3.42b}$$

A general property of the waves is $\vec{k}\cdot\delta\vec{B} = 0$, found by dotting $\vec{k}$ in Eq. 3.42a, which forces the magnetic field perturbation to be normal to the direction of propagation. The other properties of the MHD waves depend on the relative direction of $\vec{k}$ and $\vec{B}_0$.

Sound waves

Sound waves are generated as a special case on which $\delta\vec{u} \parallel \vec{k} \parallel \vec{B}_0$. The term $\delta\vec{u} \times \vec{B}_0$ vanishes in Eq. 3.42a so that $\delta\vec{B} = 0$. Magnetic tension is zero, so thermal pressure is the only restoring force. The waves generated are ordinary sound waves and it can be demonstrated that the dispersion relation is the usual

$$\frac{\omega^2}{k^2} = C_s^2. \tag{3.43}$$

Alfvén waves

Alfvén waves are also a special case on which $\delta\vec{u} \perp \vec{k} \parallel \vec{B}_0$. It can be demonstrated that these transverse waves ($\delta\vec{u} \perp \vec{k}$) force $\delta\rho = 0$, so density is unaltered. The dispersion relation in this case, projected in the x-axis, is

$$\frac{\omega^2}{k^2} = \frac{B_0^2}{4\pi\rho_0}. \tag{3.44}$$

The absence of the sound speed from the relation states that the restoring force is only magnetic tension due to the bending of the field lines. The phase velocity (ω/k) is defined as the Alfvén speed

$$V_A \equiv \frac{B_0}{\sqrt{4\pi\rho_0}} \tag{3.45}$$

that is the traveling speed of a field bending perturbation along the field line.

Magnetosonic waves

These waves are a combination of the previous two ones and arise if $\vec{k}$ and $\vec{B_0}$ are not parallel. We will focus first in the $\vec{B_0} \perp \vec{k}$ case. A transverse wave ($\delta\vec{u} \perp \vec{k}$) cannot exist because $\delta\rho = 0$ and in Eq. 3.42a the term $\delta\vec{u} \times \vec{B_0}$ vanishes so that $\delta\vec{B} = 0$. Therefore, neither thermal pressure nor magnetic tension act. Longitudinal waves ($\delta\vec{u} \parallel \vec{k}$) do exist. In this case, we see that in Eq. 3.42b the term $\vec{k} \cdot \vec{B_0} = 0$ while $\vec{k} \cdot \delta\vec{u} > 0$, so that $\delta\vec{B}$ is antiparallel to $\vec{B_0}$. Because $\delta\rho \neq 0$, the compression is now opposed by both thermal and magnetic forces. The dispersion relation in this case, projected in the x-axis, is

$$\frac{\omega^2}{k^2} = C_s^2 + \frac{B_0^2}{4\pi\rho_0}. \tag{3.46}$$

The effect of the so-called magnetosonic wave is alternating compression and rarefaction of the ambient field and gas with no bending of $\vec{B}$. The phase velocity is the maximum value achievable by an MHD wave and thus defined as

$$V_{\rm max} \equiv \sqrt{C_s^2 + V_A^2}. \tag{3.47}$$

The most general case is $\vec{k}$ tilted with respect to $\vec{B_0}$ at any angle θ_B except 0 or $\pi/2$. Three solutions are possible for this situation. The first one is a generalized Alfvén wave on which $\delta\vec{u}$ is perpendicular to the plane formed by $\vec{B_0}$ and $\vec{k}$ ($\delta\vec{u} \cdot \vec{k} = \delta\vec{u} \cdot \vec{B_0} = 0$), thus a transverse wave ($\delta\rho = 0$) with no acting thermal pressure. $\delta\vec{B}$ is again antiparallel to $\vec{B_0}$. The dispersion relation is now

$$\frac{\omega^2}{k^2} = V_A^2 \cos^2\theta_B. \tag{3.48}$$

The remaining two modes have $\delta\vec{u}$ on the $\vec{B_0} - \vec{k}$ plane, as well as $\delta\vec{B}$ that is normal to $\vec{k}$. In this case, $\delta\vec{u}$ can have any orientation with respect to $\vec{k}$, so the wave is a combination of part transverse part longitudinal waves. The dispersion relation then reads

$$\omega^4 - \omega^2\, k^2\, V_{\rm max}^2 + C_s^2\, V_A^2\, k^4\, \cos^2\theta_B = 0 \tag{3.49}$$

and the phase velocity responds to

$$\frac{\omega}{k} = \frac{1}{2}\left(V_{\max}^2 \pm \sqrt{V_{\max}^4 - 4C_s^2\, V_A^2 \cos^2\theta_B}\right)^{1/2}. \tag{3.50}$$

We are now generating two MHD waves designated as fast and slow magnetosonic waves, with the Alfvén velocity lying between the velocity of both. As $\vec{k}$ tends to be parallel to $\vec{B_0}$, the fast mode becomes an Alfvén wave and the slow mode a sound wave, while for the opposite orientation, $\vec{k}$ tends to be normal to $\vec{B_0}$, the fast mode becomes a magnetosonic wave and the slow mode disappears.

An important fact is that, in the extreme case of a magnetosonic wave, the fluid must travel faster than $V_{\max}$ to generate a shock, and thus, it is more difficult to form. The supersonic velocities derived from molecular linewidths are in some cases sub-Alfvénic and, in this case, the motion can survive longer than the Alfvénic crossing time ($\sim L/V_A$). However, we must take into account the wave steepening process. A pressure disturbance compresses the fluid and increases the temperature (ignored in our isothermal approximation), which results in an increase of the sound speed and the disturbance travels slightly faster. Piling up increases may generate a shock. In addition, heating the fluid leads to radiative energy loss and, as a consequence, supersonic motions and internal sound waves rapidly dissipate. If the observed supersonic motions in clouds are MHD waves, only the Alfvén mode can survive. This energy though can decay by mode conversion (transfer of energy to both fast and slow magnetosonic waves) or by the effect of ambipolar diffusion (Section 3.2.2).

MHD wave pressure

Although the perturbations introduced follow a sinusoidal pattern of fluctuations, one can calculate the average "steady" force over a cycle. For a generic MHD wave, the force depends on gradients in the orthogonal directions[1]. For an Alfvén mode instead, the force may be written as the gradient of a scalar, $\vec{F_{\rm wave}} = -\nabla P_{\rm wave}$, where the wave pressure can be calculated as

$$P_{\rm wave} = \frac{1}{16\pi}|\delta\vec{B}|^2. \tag{3.51}$$

This term may be added in Eq. 3.32 for a more complete description of the equilibrium. We do not have a sufficient knowledge of the wave amplitudes to construct detailed models. However, polarization measures indicate that $|\delta B| \approx B_0$ in large clouds, so the wave "speed", $(P_{\rm wave}/\rho_0)^{1/2}$, is close to V_A. The empirical result in large clouds of almost magnetic and gravitational energy equipartition implies that $V_A \approx V_{\rm vir}$, and therefore, that Alfvén waves could exert a pressure similar to self-gravity and be important in determining the cloud structure.

---

[1] $F_i^{\rm wave} = -\frac{\partial}{\partial x_j}\Pi_{ij}^{\rm wave}$, where $\Pi_{ij}^{\rm wave} = \frac{1}{2}\,\rho_0\,\delta u_i\,\delta u_j + \frac{1}{16\pi}\,\delta B_k\,\delta B_k\,\delta_{ij} - \frac{1}{8\pi}\,\delta B_i\,\delta B_j$. It behaves as an elastic membrane subject to mechanical stresses.

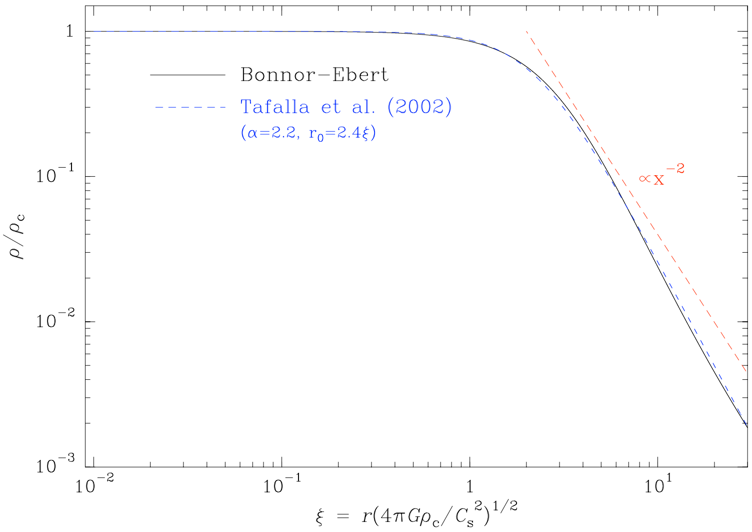

Figure 3.7: Same as Fig. 3.1. The blue dashed line depicts the density profile from Eq. 3.52 using $r_0 = 2.4\,\xi$ and $\alpha = 2.2$. The agreement to the BE profile is remarkable.

3.1.5 Empirical fits

The complex interplay among gravity, thermal pressure, magnetic fields, and turbulence makes it difficult to elaborate a theoretical model for dense cores. As a result, different ad-hoc profiles have been suggested to fit the experimental data. Single power-law density profiles do not fit the emission from dense cores and a central flattening is always needed to reproduce the data (see Fig. 3.2). Double power-laws with the inner region nearly flat improve the results, however, the discontinuous derivative implies a pressure jump and makes these profiles rather artificial. Real dense cores are likely to have smoother density profiles. A remarkable agreement to the data is achieved with the smooth, continuous family of functions proposed by Tafalla et al. (2002)

$$\rho = \frac{\rho_c}{1 + (r/r_0)^\alpha}, \tag{3.52}$$

where ρ_c is the central density, r_0 is the radius of the internal flat region, and α the asymptotic power index. This family of functions can reproduce both the internal flat region and the external decay of dense core density profiles with great accuracy. Figure 3.7 shows the good agreement up to $\xi = 30$ of the BE profile with Eq. 3.52 using $r_0 = 2.4\,\xi$ and $\alpha = 2.2$. Note that the turnover radius (Eq. 3.13) is equivalent to $\xi = 1.92$, very close to the best value found for r_0, giving a physical sense to this parameter. $\alpha = 2.2$ is very close to the value for an isothermal sphere. Therefore, Eq. 3.52 can be used as a generalization of the BE profile giving more flexibility to the analysis. The variation of the α and r_0 parameters with respect to the BE values can be understood as the effect of additional support pressures modifying the dense core profile.

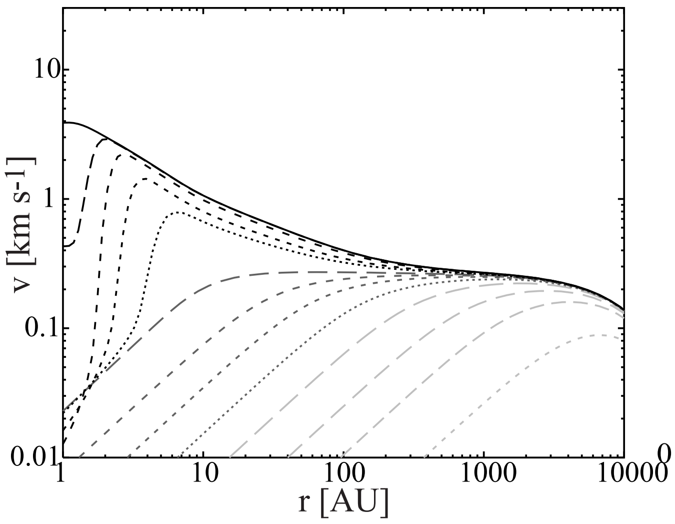

Figure 3.8: Radial distribution of velocity in a collapsing BE extracted from Aikawa et al. (2008). Their calculations allow for temperature variations but the process remain essentially isothermal for a few 10^5 yr up to densities of $n \sim 10^6$ cm^{-3} (dark gray dashed line). Times in yr. measured to the formation of the protostar for the "isothermal" profiles are, from right to left, -2.5×10^5, -1.1×10^5, -3.3×10^4, -1.5×10^4, -6.4×10^3, -3.4×10^3, -2.1×10^3, and -1.2×10^3.

3.2 Dynamical evolution

It is an observational evidence that many dense cores host infrared sources, and thus, that these structures can form stars. Many of these stable structures then must meet the conditions needed to evolve up to a state that leads to collapse.

3.2.1 Inside-out collapse

We start first of all ignoring the effect of magnetic fields (see Section 3.2.2) and rotation (see Section 3.2.3), and focus on a still spherical cloud supported by thermal pressure. We start with a cloud in marginally stable hydrostatic equilibrium, *i.e.* a BE sphere with $M_{\rm BE}$ mass (Eq. 3.18). By increasing its density a few percent, the cloud is too massive and the gas starts to accelerate inwards. The process starts at the outer edge and moves inward with time, as illustrated in Fig. 3.8 for different snapshots. This fast, inward, supersonic motion leads to strong compression of the central core and to the formation of shocks.

An important quantity is the mass accretion rate onto the central region, because it can provide an estimate of the timescale for protostar formation. In numerical calculations, it is common the use of "sink cells" as elements that accrete material with no further refinement in the spatial grid to simplify the calculations. As a consequence, the accretion rate is estimated as the mass falling onto the sink cell, noted as $\dot{M}$, although we ultimately want the inner limit

$$\dot{M} = \lim_{r \to 0} -4\pi\, r^2\, \rho\, u. \tag{3.53}$$

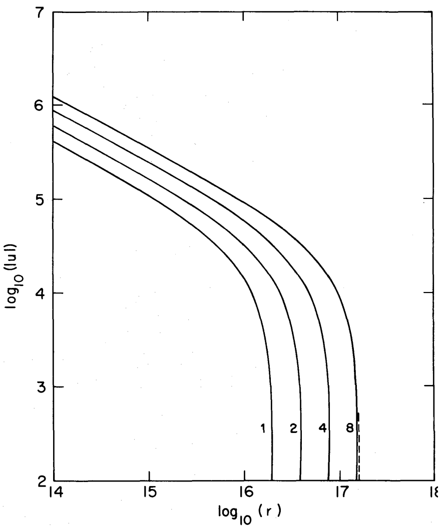

Figure 3.9: Collapse expansion wave solution of an isothermal sphere extracted from Shu (1977). Radius is in cm and velocity in cm s^{-1}. The velocity profile times label the curves in 10^{12} s units. The collapse wave front is expanding with time.

Once the protostar is born, it has a high $\dot{M}$ as the material previously set into motion soon accretes onto it. The rate then falls to eventually level off when reaching the asymptotic value,

$$\dot{M} = m_0 \frac{C_s^3}{G}, \tag{3.54}$$

where C_s^3/G has the proper dimensions and m_0 is a numerical parameter that varies depending on the simulations but is close to unity.

The asymptotic behavior means that once the protostar is born, the effect of pressure counteracting gravity is negligible, and therefore, the surrounding gas is nearly in a state of free fall with infalling velocities close to

$$V_{\rm ff} \equiv \sqrt{\frac{2\,G\,M_\star}{r}}, \tag{3.55}$$

where $M_\star$ is the central mass that grows as $M_\star = \dot{M}\,t$. Thermal pressure is unable to stop collapse once started because to increase, under the isothermal assumption, it is necessary an increase of density. This density growth also enhances the gravitational force. Therefore, isothermal structures can only support low density contrasts. The free-fall region extends up to the radius where the pressure effects are comparable to gravity ($C_s \approx V_{\rm ff}$) that, using Eq. 3.55 and assuming $R_{\rm ff}/t \approx \dot{R}_{\rm ff}$, can be written as

$$\dot{M} = \frac{C_s^2\,\dot{R}_{\rm ff}}{G}. \tag{3.56}$$

$\dot{M} > 0$ means that $\dot{R}_{\rm ff} > 0$ and, as a consequence, the free-fall radius grows with time as the $M_\star$ increases. The collapse then proceeds eroding shells in an inside-out fashion as they lose their pressure support and start infalling. Figure 3.9 shows that it is a wave-like process on which the boundary constitutes a rarefaction wave. As a mechanical traveling disturbance, it moves at the sound speed[2], which means that the cloud region beyond the wave front is unaware of the collapse process and still remains in hydrostatic equilibrium.

---

[2] Note that if $\dot{R}_{\rm ff} = C_s$ we recover Eq. 3.54 from Eq. 3.56.

Density profile

We focus now on the free falling region, largely dominated by the gravitational force, avoiding the central accreting core and the pressure supported external gas. A fluid element crosses supersonically this region in a time brief as compared to the evolutionary timescale $(M_\star/\dot{M})$. This allows to ignore the density variation with time in the continuity equation (Eq. 3.19a). Using Eq. 3.54 and setting $u = -V_{\rm ff}$, the density follows

$$\rho = \frac{\dot{M}\, r^{-3/2}}{4\pi\,\sqrt{2G\,M_\star}}. \tag{3.57}$$

Density, and therefore pressure, grows now as $\propto r^{-3/2}$. On the other hand, the part of the cloud in hydrostatic equilibrium follows $\propto r^{-2}$. Therefore, the density profile is flatter in the infalling region. This spherical profile is stable to fragmentation as the strain induced by the increase of $V_{\rm ff}$ with decreasing r pulls the fragments apart.

Validity of the isothermal assumption

Prior to collapse, the clouds are heated by cosmic rays. With the onset of collapse, two new energy inputs can heat the gas: mechanical compression due to gravitational collapse, and radiation from the protostar. The former one can be expressed as $(P\,u/\rho)(\partial\rho/\partial r)$ and is only appreciable at a scale of a few AU. The latter one depends on the infrared photons re-emitted by dust grains after absorbing the luminosity generated at the stellar surface arising from the infall kinetic energy. These photons are radiated away unless they can be efficiently trapped by the increasing density. Such trapping occurs at scales of ~ 10 AU. At these distances, the infalling gas is moving at high speed and collapse cannot be stopped. Therefore, the overall dynamics of inside-out collapse are not affected and the isothermality assumption still holds for the infalling region.

3.2.2 Magnetized configurations

Ambipolar diffusion

In the presence of magnetic field, the gas splits into two fluids: the neutrals and the charged particles. The former ones are affected by gravity while the latter ones are affected by magnetic fields as well. In the case of flux freezing, the charged species remain tied gyrating around the field lines and collide with the neutrals “exerting” an effective pressure that opposes the gravitational force. However, if the ionization level is low enough, this mechanism becomes inefficient and the difference of the two fluid velocities may become significant. At this point, the neutrals can gradually drift across magnetic field lines pulled by gravity.

It is reasonable to consider that all charged species, electrons and ions, move at the same velocity $\vec{u_i}$. We define the drift velocity as the velocity difference with respect to the neutrals, $\vec{v_{\text{drift}}} = \vec{u_i} - \vec{u}$. It can be estimated as

$$\vec{v_{\text{drift}}} \approx \frac{\left(\nabla \times \vec{B}\right) \times \vec{B}}{4\pi\, n\, n_e\, [m_n \langle \sigma_{\text{in}}\, u_i \rangle]}, \tag{3.58}$$

where n_e is the number density of electrons (equal to that of the ions), m_n is the mass of the average neutral, and σ_{in} is the ion-neutral collision cross section. Flux freezing still holds if the conductivity is large, but while electrons are tied to field lines the neutrals are allowed to move across them with velocity $-\vec{v_{\text{drift}}}$.

For a typical core, the timescale of ambipolar diffusion $L/\vec{v_{\text{drift}}}$ is $\sim 10^6$ yr, and therefore, significant. It is important then to determine the direction of $\vec{v_{\text{drift}}}$. Note that $\vec{v_{\text{drift}}}$ is proportional and points to the same direction that the magnetic drag force exerted by ions[3]. The magnetic force will oppose gravity and, therefore, $\vec{v_{\text{drift}}}$ will point outwards. This means that the neutrals will cross the field lines moving inwards and, as a consequence, the mass-to-flux distribution $(dM/d\Phi)$ is continuously modified. Figure 3.10 shows how the mass concentrates toward the center and the range of Φ_B containing mass decreases, which means, in turn, that the flux leaks out. Magnetic force essentially opposes gravity, so their strengths are roughly balanced, therefore, as gravity increases toward the center the magnetic force does it as well. In addition, n_e diminishes toward the denser regions where ions and electrons recombine in the grain surfaces. As a result, $\vec{v_{\text{drift}}}$ also increases toward the center "accelerating" ambipolar diffusion and helps creating an even denser central core.

Ambipolar diffusion is the more likely process to dominate the evolution of dense cores before collapse. At the light of these results, the structures of Section 3.1.3 reveal them as quasi-static structures. Although the gas moves, it can be considered as a sequence of quasi-static states. The quasi-static approximation fails when the dense core is dense enough for gravity to overcome the magnetic support ($u \approx C_s$). The cloud then undergoes MHD collapse (see below).

Alfvén waves

We remind from Section 3.1.4 that an Alfvén wave is the transverse displacement of a magnetic field line due to magnetic tension. Under flux freezing, the charged particles move with the field and drag the neutrals. Including ambipolar diffusion damps the Alfvén waves, because a field displacement too fast to allow enough collision with the neutrals will effectively reduce their amplitude.

The dispersion relation is in this case a generalization of that in Section 3.1.4 (Eq. 3.44)

$$\frac{\omega^2}{k^2} = \frac{B_0^2}{4\pi\rho_0}\left(1 - \frac{i\,\omega}{n_i \langle \sigma_{\text{in}} u_i \rangle}\right), \tag{3.59}$$

---

[3] The Lorentz force reads $\vec{f} = \vec{j} \times \vec{B}/c$, which combined with the Ampère's law (Eq. 3.24) results in $f = \left(\nabla \times \vec{B}\right) \times \vec{B}/4\pi$, similar to Eq. 3.58.

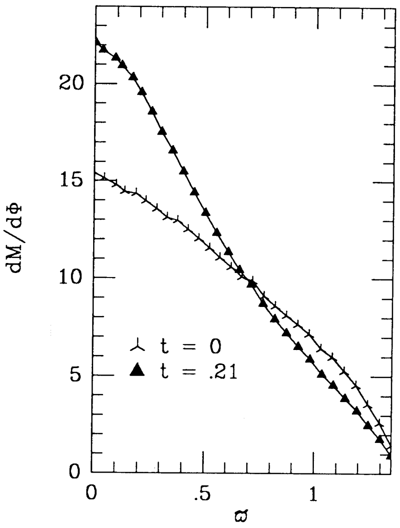

Figure 3.10: Mass-to-flux distribution of a dense core in quasi-static contraction as a function of the cylindrical radius extracted from Lizano & Shu (1989). With increasing time the mass-to-flux distribution narrows and flux leaks out.

where the former expression is the limit at low frequencies. Letting $\vec{k}$ be a real number, forces ω to be complex ($\omega = \omega_R + i\,\omega_I$) and the perturbation plane wave to have a time depending amplitude

$$\exp[i\left(\vec{k}\cdot\vec{r} - \omega\, t\right)] = \exp\left(\omega_I\, t\right)\exp[i\left(\vec{k}\cdot\vec{r} - \omega_R\, t\right)]. \tag{3.60}$$

Solving Eq. 3.59 leads to

$$\omega = -\frac{i\, V_A^2\, k^2}{2\, n_i \langle\sigma_{\rm in} u_i\rangle} \pm \frac{V_A\, k}{2}\sqrt{4 - \frac{V_A^2\, k^2}{n_i^2 \langle\sigma_{\rm in} u_i\rangle^2}}. \tag{3.61}$$

A propagating component demands the radicand to be positive. If we express this condition in terms of the wavelength $\lambda = 2\pi/k$, we need $\lambda > \lambda_{\rm min} = \pi\, V_A/n_i\langle\sigma_{\rm in} u_i\rangle$ that for a typical core has a value of ~ 0.06 pc. Even if $\lambda < \lambda_{\rm min}$, there is always a negative imaginary component. Therefore, all the waves decay in a time roughly the reciprocal of ω_I, which for a perturbation with wavelength $\lambda_{\rm min}$ in a typical core is $\sim 10^4$ yr. Given that $\lambda_{\rm min}$ is close to the size of dense cores, and that the decay time is much shorter than dense core lifetimes, this analysis lends support to the idea that cores form in a quiescent, wave-free environment.

MHD collapse

The addition of magnetic fields automatically implies that the analytical critical state, unique in the purely thermal case, depends now on the mass-to-flux function, $dM/d\Phi$. Furthermore, $dM/d\Phi$ changes with time so we need to trace back the core history. The initial stage of the formation of quiescent structures embedded in a more turbulent medium with different physical properties, the dense cores, is still unclear. An approach to this process are the computer simulations of turbulent clouds that often generate clumpy structures. However, none of them satisfactorily reproduce the initial core mass function and the internal velocities of the cores tend to be comparable to $V_{\rm ff}$ thus unlikely to collapse. The

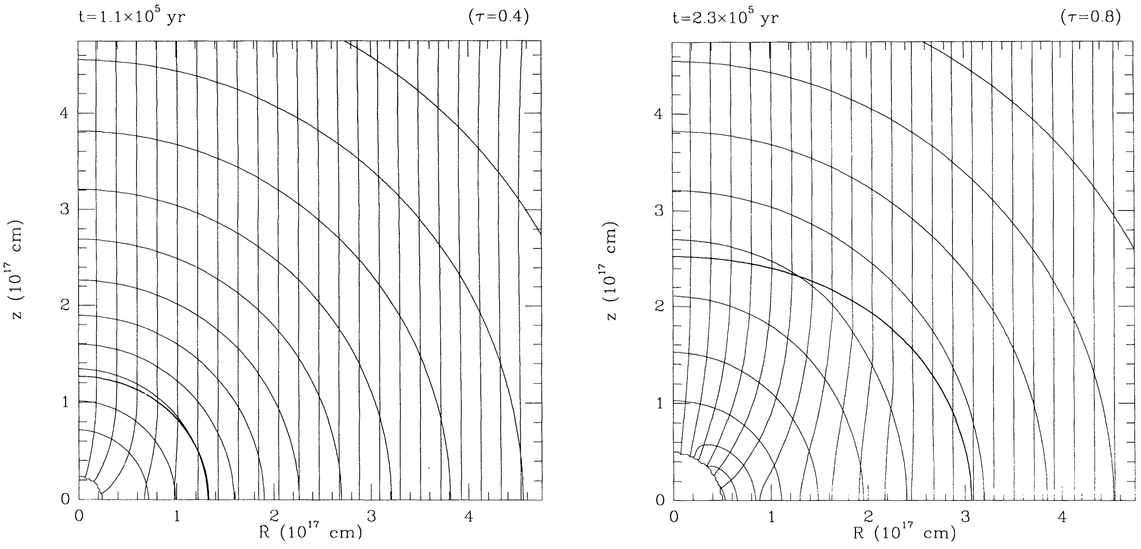

FIG. 5*a*

FIG. 5*b*

Figure 3.11: Semi-analytical solution for the time evolution of an infalling spherical dense core with ambipolar diffusion extracted from Galli & Shu (1993a). Density contours and magnetic field lines are shown. The infall wave front is depicted as a black thick contour. The semi-analytical solution fails toward the inner part and has been clipped.

formation of much denser structures seem to require inside-out collapse from a quiescent initial structure.

Assuming then that we start from a quiescent structure close to equilibrium, neutral matter would slip across the field lines in a typical timescale of $L/v_{\vec{\mathrm{drift}}} \sim 10^6$ yr. The result is that $dM/d\Phi$ becomes more centrally peaked and flux diffusively leaks out from the center. This modifies the force balance and the main supporting source varies depending on the distance. Toward the very center, thermal pressure dominates as magnetic field loses importance. Further away, the magnetic tension and pressure of the static field predominate. At the outer region, for $\lambda > \lambda_{\mathrm{min}}$, Alfvén-wave support is also significant. When the central density is large enough so that thermal pressure cannot counteract the gravitational pull, the collapse starts. This process proceeds in an inside-out way given that the growth of the central mass is related to the growth of R_{ff} (Eq. 3.56).

Figure 3.11 shows two snapshots of a semi-analytical calculation of the collapse of a spherical dense core threaded by an initially uniform magnetic field with ambipolar diffusion under the flux freezing assumption (Galli & Shu, 1993a). As the collapse starts, the wave front of the rarefaction wave (depicted by thick contours) travels outwards. In the equatorial direction, it travels as a fast magnetosonic wave, thus faster than in the axial direction, where it travels as a sound wave. As soon as the rarefaction wave hits a shell, it starts infall, dragging the field lines with it. As time evolves, field lines stretch, building up magnetic tension, and tend to a split-monopole configuration. This field line bending is known as "hour-glass" morphology due to the resemblance in the observational maps (see Section 4.3.2). Toward the center of the collapsing cloud, it tends to form a flattened structure which falls outside of the validity region of the Galli & Shu (1993a) model.

Figure 3.12 shows a close-up view of the inner region. This fully numerical simulation by

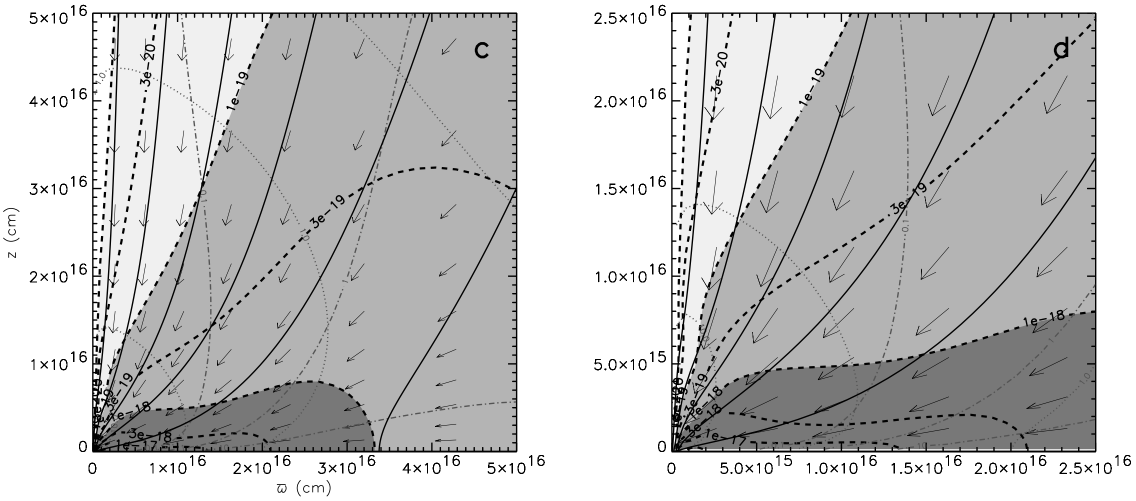

Figure 3.12: Snapshot of the inner region of a numerical simulation of an infalling magnetized toroid with ambipolar diffusion extracted from Allen et al. (2003a). Density contours (dashed lines), magnetic field lines (solid lines), and local velocities (arrows) are shown. The flow deflection due to magnetic fields forms a pseudo-disk around the protostar.

Allen et al. (2003a) has similar assumptions to those of Galli & Shu (1993a) but more realistic initial conditions in the form of a toroid, the equivalent magnetized equilibrium structure to the purely thermal BE sphere. The gas flows easier along the field lines as only thermal pressure opposes. Oppositely, across the field lines, the gas encounters the magnetic pressure exerted by the ions tied to the field. As a consequence, it is formed an out of equilibrium structure of enhanced density, the "pseudodisk", due to the flow deflection under the action of magnetic fields. This pseudodisk contracts under the effect of gravity and drags the field lines toward the center generating a severely pinched field morphology close to the split-monopole. The large field line stresses generated and the high density of field lines toward the center must play an important role in the dissipation of the magnetic energy through non ideal effects (*e.g.* Ohmic dissipation or magnetic reconnection, see below) not considered in this simulation. The mass accretion rate can be estimated as

$$\dot{M} = (1 + H_0)\,\frac{C_s^3}{G}, \tag{3.62}$$

where H_0 represents the fraction of overdensity supported by magnetic fields with respect to thermal pressure in the initial configuration. Note that we recover Eq. 3.54 if $H_0 = 0$. This expression means that collapse proceeds faster than in the unmagnetized case due to the larger density contrast accumulated thanks to magnetic fields during the slow quasi-static contraction dominated by ambipolar-diffusion.

Magnetic reconnection

This non-ideal effect, responsible *e.g.* of the solar flares, is likely to happen in collapsing dense cores at high densities where the flux freezing assumption breaks down. This phenomenon occurs when field lines are compressed and pinched while dragged in. This process eventually brings together field lines of opposite direction. As a result, the field lines break and rejoin in a lower energy state and partly dissipate the energy as heat in the local environment. Magnetic flux is destroyed, which partly solves the magnetic flux problem. Simultaneously, the local minimum of magnetic pressure along the former path of the reconnected field lines is compensated by the surrounding lines pressing inward and expelling the fluid sideways, which may help halting the collapse, transforming magnetic energy into kinetic energy. There are, however, no observational evidences in dense cores of this process that is theoretically not fully understood.

3.2.3 Rotating configurations

Hydrodynamical numerical simulations starting with a level of rotation consistent with observations, form centrifugally supported disks with diameters of the order of a few hundred AUs. These structures are a consequence of angular momentum conservation during the collapse. These massive disks are prone to gravitational instability and have often been found to fragment. Several mechanisms have been proposed to address this oversimplification of the models.

Magnetic braking

In a rotating configuration around the cylindrical z-axis, only the toroidal component of magnetic field B_ϕ generates torque. The effect of the magnetic torque is to bend the field line and modify the topology of the magnetic field. B_ϕ changes its direction as moves with the perturbed field line. The perturbation then travels along the field line as a torsional Alfvén wave[4] that transports angular momentum. The overall effect of magnetic braking is to favor co-rotation within the cloud (Galli et al., 2006). It propagates at V_A, close to C_s and $V_{\rm ff}$, so under the flux freezing assumption co-rotation should be a good approximation even during collapse. This effect can prevent the formation of disks even with low magnetization levels ($\lambda \simeq 5-10$, Eq. 3.39) leading again to unrealistic results.

Magnetic and rotational axis misalignment

Numerical studies, assuming ideal-MHD, investigate the interplay between the level of magnetization and the initial angle between the magnetic field and rotation axis angle, α (Price & Bate, 2007; Hennebelle & Ciardi, 2009). For relatively low values of $\alpha \simeq 10-20°$, disks can form for larger values of magnetization as compared to the non-rotating case ($\lambda \simeq 4-5$). This is the result of a less efficient magnetic braking due to the misalignment, linked to an increase of the thickness of the magnetized pseudo-disk. For $\alpha = 90°$, disks can be formed for $\lambda \simeq 2-3$. They find no fragmentation either. These results, arising from a more realistic initial configuration, explain better the observational results.

---

[4] A torsional Alfvén wave is a perturbation that, unlike Alvén waves, can have large $\delta\vec{B}$ and must have a component that twists around the propagation direction as in this case.

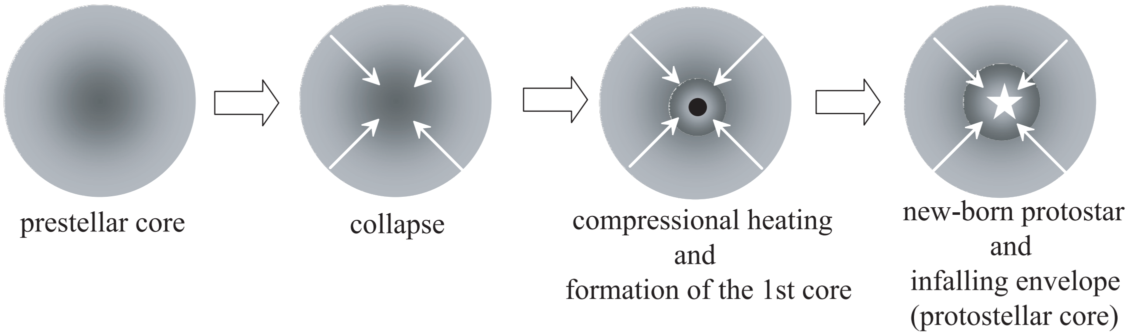

Figure 3.13: Evolution of a star-forming core extracted from Aikawa et al. (2008)

3.2.4 First core and protostar overview

We now examine the overall process of formation of the denser central region responsible of the gravitational pull that triggers the irrevocable start of the process to form a star. Figure 3.13 schematically shows the evolution of a star-forming dense core in the absence of magnetic fields and rotation. A quiescent starless dense core through a quasi-static process characterized by slow contraction due to ambipolar diffusion and leakage of flux, loses thermal support and undergoes collapse. This compression is almost isothermal as the compressional heating can be radiated away. However, the central part of the core grows denser and becomes opaque to its own cooling radiation thus increasing its temperature and breaking the isothermal assumption. The rise of thermal pressure decelerates the contraction and eventually makes the first hydrostatic core, known as the "first core", at the center.

At this point the first core has a mass of $\sim 10^{-2}\ M_\odot$, a size of ~ 5 AU, and it is essentially formed of molecular hydrogen. During its lifetime, more material falls onto the outer surface of the first core that can still radiate energy away, thus causing compression. This mass addition and further compression rise the temperature up to 2000 K where collisional dissociation of H_2 begins. The increase of thermal energy is absorbed by molecular dissociation and temperature starts to level off. The object can support only a low density contrast, because it is nearly isothermal, so the configuration becomes unstable and the second collapse begins. The central density increases rapidly and within a short period of time the dissociation degree approaches unity at the center. Then, the second collapse ceases and the second hydrostatic core, the protostar, is formed surrounded by the infalling envelope. The timescale from the start of collapse until the formation of the protostar is a few 10^5 yr and the density achieved is $\sim 10^6\ \mathrm{cm}^{-3}$. This new kind of object is known as a Class 0 source.

3.3 Chemical properties

3.3.1 Observations

Dense core chemical features

Studies of different molecular transitions evidence inhomogeneities among them in the gas-phase chemistry in the form of different size and/or spatial distribution of the emission, or different linewidths even having the same line centroids in *e.g.* CS and NH_3. Many works have been devoted to low-mass cores computing the average Line-Of-Sight (LOS) abundances with respect to H_2[5], which helped to understand that ion-molecule reactions dominate the gas-phase chemistry. In parallel, studies of molecular ices frozen on dust grains have been conducted toward deeply embedded sources ($A_V \gtrsim 20$ mag). The species are detected in absorption against the bright IR background (van Dishoeck, 2004). The grain icy mantles contain mostly H_2O with significant CO and CO_2 (Gibb et al., 2004). However, there exists a threshold for the icy features, meaning that at low extinctions the grains are not mantled. This threshold depends on the molecule and the cloud, and it has a value of a few magnitudes for H_2O, CO and CO_2 (Whittet et al., 2007; Bergin et al., 2005). These observations demonstrate that grains play an important role in the ISM chemistry. The coating ices are a major reservoir of carbon and oxygen, and seem to act as a catalyst for chemistry on the surface in an interchange between gas and solid phases. Another consequence is that CO is not a good tracer of the H_2 column since its abundance vary when freezes onto grains.

These peculiar chemical features are now better understood. This improvement is possible because a number of dense cores are now known with relatively well-described physical and temperature structure. The advance is mostly due to millimeter/submillimeter mapping that allows to determine directly the H_2 column, and to the use of radiative transfer codes that take into account density, temperature, and molecular abundance to reproduce the observed line profiles. An important initial result by comparing the estimated CO column densities with observations is that they differ significantly. The interpretation is that CO molecules freeze onto grain surfaces, being this process dominant for densities higher than $\sim 3\times10^4$ cm^{-3} (Bacmann et al., 2002). Subsequent ice mapping revealed that the abundance of CO ice increases when densities exceed 10^5 cm^{-3}, and that near the core center the majority of CO is frozen. H_2O shows a similar behavior (Pontoppidan et al., 2005; Pontoppidan, 2006). Molecular ices are then important reservoirs of the available oxygen. Molecular freeze-out has revealed to be more complicated. Tafalla et al. (2002) showed that molecules exhibit different behavior in terms of the interactions with grain surfaces. Figure 3.14 shows that carbon-bearing molecules (*e.g.* CO and CS) deplete from gas while nitrogen-bearing molecules (*e.g.* N_2H^+ and NH_3) trace the core center. The former group shows a decline in abundance toward the core center of at least 1-2 orders of magnitude with respect to the core edge, while the latter remains roughly constant or decays slowly. This "selective" freeze-out explains the observed emission differences in size and morphology between carbon- and nitrogen-bearing molecules, as well as the different linewidths since the molecules trace different core regions.

---

[5] H_2 does not emit at $\sim$10 K so optically thin isotopologues of CO, mostly $C^{18}O$, were used to derive the H_2 column using calibrated abundances (*e.g.* $n(C^{18}O)/n(H_2) \equiv X[C^{18}O] \sim 1.7\times10^{-7}$: Frerking et al., 1982)

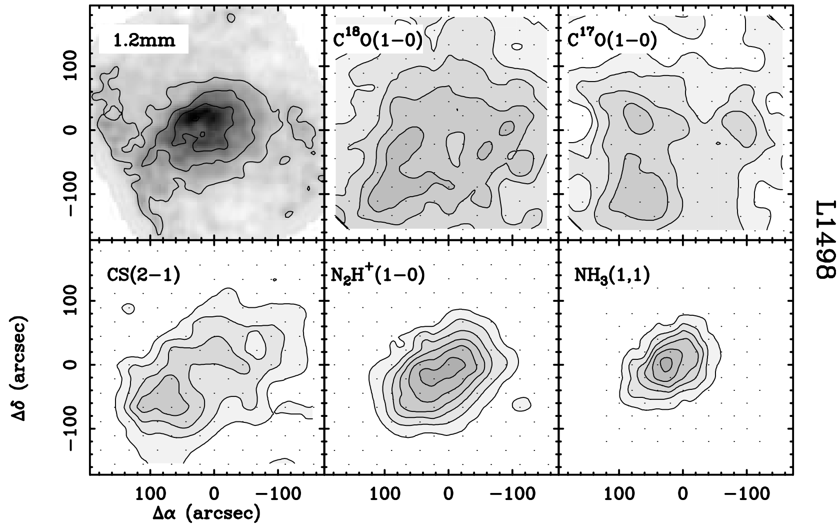

Figure 3.14: Selective molecular freeze-out toward L1498 extracted from Tafalla et al. (2002). Carbon-bearing molecules deplete at high densities and show a ring-like structure. On the other hand, nitrogen-bearing molecules trace the core center in good agreement with the continuum dust emission map.

Ionization fraction

The ionization fraction is a critical factor for magnetized configurations, specially subcritical cores, because ambipolar diffusion has an important dependence on it (Eq. 3.58). Early estimations by McKee (1989) parametrized it as $x_e = 1.3 \times 10^{-5}\, n^{-0.5}$, although freeze-out effects can alter the prefactor and the exponent (Caselli et al., 2002; Walmsley et al., 2004). The ionization fraction is expected to be high at the core edge (A_V<1–2 mag) owing to photodissociation of CO and ionization of carbon. At low densities, the DCO$^+$/HCO$^+$ ratio is predicted to be very sensitive to the electron abundance and LOS ion fractions of $x_e \sim 10^{-7}$ are derived. Detailed modeling implies that heavy metal ions have no significant contribution and that HCO$^+$ is the major charge carrier throughout the core. However, HCO$^+$ does not trace the core center due to depletion of neutrals and the major charge carriers in the densest regions are likely to be H$_3^+$ and its deuterated forms (see Eqs. 3.64–3.66). For the densest cores ($n > 10^6$ cm^{-3}), D$_3^+$ is expected to dominate. Observations and models suggest that the ionization fraction is quite low toward the core center, $x_e \sim 10^{-9}$, thus the gas is decoupled from the field (Caselli et al., 2002).

3.3.2 Models

The freeze-out timescale of atoms and molecules can be estimated as the inverse of the adsorption rate

$$\tau_{\rm fo} = k_{\rm fo}^{-1} = (\sigma\, v\, n_g\, S)^{-1}\,, \tag{3.63}$$

where σ is the grain cross section, v is the typical gas velocity, n_g is the grain volume density, and S is the sticking coefficient (the probability of remaining on the grain after the impact). High densities favor this effect, helped by the fact that dense regions are shielded from the external radiation that can desorb molecules from grains. Therefore, at high densities adsorption of atoms and molecules dominate. Moreover, the free-fall timescale (Eq. 2.1) becomes larger with increasing densities and, because the ambipolar diffusion timescale is longer than the free-fall time, it also becomes larger. This means that as the core evolves and grows denser, the effects of freeze-out increase and may be used to constrain the timescales of core formation. Once on the grain surface, molecules can react with mobile species or, if saturated, remain inert. It is important to note that neutral species freeze onto grains but ions behave differently. Grains are believed to carry negative charge (Weingartner & Draine, 2001) that, when recombined with ions, releases a few eV that exceed the molecule-grain binding energy. Thus, ions can adsorb into grains but do not freeze out.

Recently, several theoretical works combine chemical and dynamical models that follow the chemical evolution of contracting cores (Aikawa et al., 2005, 2008; Keto & Caselli, 2010). Basic gas-grain micro-physics into the models (see Tielens, 2005) can explain and, in some cases, predict the chemical structure described in Section 3.3.1. Figure 3.15 illustrates one of these calculations of a contracting initially marginally unstable BE. As the core contracts, the density toward the center increases and the neutrals start to freeze onto grains ($n(\mathrm{H_2}) \gtrsim 10^5$ cm^{-3}). This behavior is predicted to be more important for carbon- and sulfur-bearing species, while nitrogen-bearing molecules survive longer on the gas phase. This molecular freeze-out does not happen toward the core boundaries, where the density is lower. These predictions explain the selective freeze-out and the ring-like structures observed in *e.g.* CO. Several physical constraints have arisen from chemical modeling. Collapse cannot proceed too fast as the observed non-thermal linewidths ($\sim$0.2 km s^{-1}) would be broader and less depletion would be observed. A best agreement is obtained for timescales shorter than that of ambipolar diffusion ($\sim$0.5–1 Myr), as CO depletion would be produced at densities below where it is observed. Thus, chemical modeling favors a super-critical initial configuration. Open questions still remain, like the process of grain surface catalysis, the strength of the mechanisms that could return molecules to the gas, or how complex molecules can form in the gas phase (*e.g.* $\mathrm{CH_3OH}$). However, current advance already allows to propose relative ages between cores within a sample (Tafalla & Santiago, 2004).

3.3.3 Freeze-out secondary effects

The freeze-out of neutrals (*e.g.* CO, CS, or SO, see Fig. 3.15) has collateral effects. The depletion of chemical species creates a chemical imbalance and the reactions suffer rearrangements. The main effect is the loss of CO, which is the main destroyer of molecular ions. $\mathrm{H_3^+}$, the precursor of $\mathrm{N_2H^+}$ and $\mathrm{HCO^+}$, is particularly affected. $\mathrm{N_2H^+}$ and $\mathrm{HCO^+}$ abundances will decrease as their parent species, $\mathrm{N_2}$ and CO, respectively, deplete. But the depletion of CO has the net effect of an increase of their abundances (Bergin et al., 2002; Jørgensen et al., 2004). $\mathrm{NH_3}$ then forms from $\mathrm{N_2H^+}$. A direct consequence of CO depletion is then that the abundances of nitrogen hydrides are enhanced, thus probing the dense gas.

Another important consequence of CO freeze-out is the increase of deuteration, because it

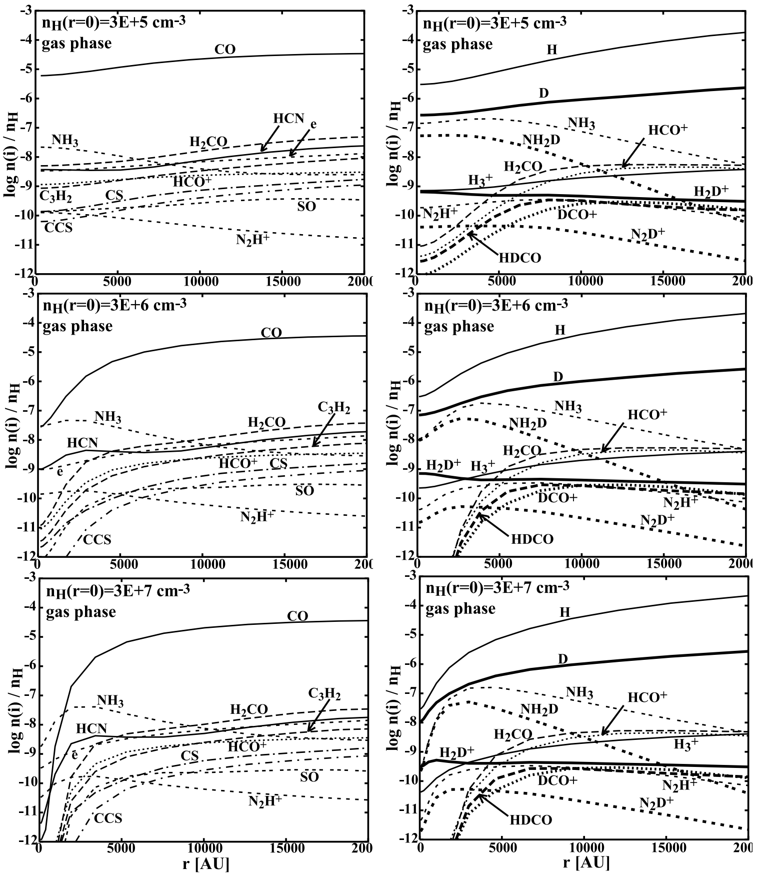

Figure 3.15: Gas-phase chemistry in a contracting BE sphere extracted from Aikawa et al. (2005). Radial distribution of the calculated abundances at $n(H_2) = 3\times10^5$ cm^{-3} (top panels), 3×10^6 cm^{-3} (middle panels), and 3×10^7 cm^{-3} (bottom panels).

is the major destroyer of H_3^+ and H_2D^+. Deuterium chemistry is driven by the following reactions

$$
\begin{aligned}
H_3^+ + HD &\leftrightarrow H_2D^+ + H_2 + 230\ \mathrm{K}, \qquad (3.64)\\
H_2D^+ + HD &\leftrightarrow D_2H^+ + H_2 + 180\ \mathrm{K}, \qquad (3.65)\\
D_2H^+ + HD &\leftrightarrow D_3^+ \quad + H_2 + 230\ \mathrm{K}. \qquad (3.66)
\end{aligned}
$$

The first reaction is exothermical, and thus, the right-hand side is favored, enriching the deuteration of an essential molecule in the ion-molecule chemistry. The depletion of CO increases the rate of the second and third reactions and the deuterium fractionation of the gas phase. The lower energy of deuterium bonds as compared to hydrogen bonds enhances the abundance of deuterium-bearing molecules with respect to their hydrogen counterparts. The deuterated version of H_3^+ passes the deuterium to other species through different reactions (*e.g.* DCO^+ and DCN). The multiply deuterated ions enhance the deuteration levels and allow to achieve values similar to those observed. Additionally, the enhanced atomic (D/H) ratio will accrete onto grains and be available for surface reactions.

IV

Aims, selected sources and work plan

The science case of this thesis is focused on the study of the structure and the physical and chemical evolution of low-mass dense cores, paying special attention to the influence that magnetic fields have on these sort of objects. In this chapter, we introduce the general context and the overall goals of the thesis. Afterwards, we describe the selected sources where the research has been carried out. Finally, we present the methodology and strategy used.

4.1 Context

It is an observational evidence that dense cores are birthplaces of low-mass stars. Dense cores can be starless or pre-stellar and do not contain any YSO yet, or can host deeply embedded YSOs, the so-called Class 0/I sources, and therefore be associated with IR sources, outflows, and other signposts of star-formation. Despite the importance of the dense cores, little is known about the early stages of these objects. These quiescent regions, notoriously distinct from the more turbulent environment that surrounds them, are apparently able to survive several free-fall times and, potentially, collapse and form a star. The question on how these objects form and survive has been the topic of several theoretical approaches with a variety of different ingredients, but the observational challenge that these cores represent, faint but at the same time with significant visual extinctions, is holding the answers back. Ideally, one should study a nearby dark molecular complex with a low star formation efficiency, such as the Pipe nebula, because the star formation feedback does not contaminate the observational data. The energy released by molecular outflows is such that it modifies the environment and the chemistry of the molecular gas affected by them. Thus, the molecular line observations, aimed to study the properties of the dense molecular clouds, can be contaminated by the outflow interaction.

Theoreticians have considered for several decades the effect of magnetic fields in star-formation models. However, predictions could not be confronted with observations because there were no efficient instrumentation or technique to undertake this task. The polarimetric capabilities that many telescopes have developed during the last years have opened a new, promising observational window. The new instrumentation allows to trace the magnetic field direction and, within limits, to estimate its strength. As a consequence, it is now possible to investigate the influence of this potentially key ingredient in dense core birth, survival, and evolution. However, the present instrumentation can only detect the polarized emission of dense cores around Class 0 YSOs. The reasons are that, despite of having a total mass similar to starless dense cores, Class 0 sources have significantly higher temperatures due to the conversion of gravitational energy into heat, and that the increase of density at smaller scales makes the protostellar dense cores more compact, resulting in brighter, more concentrated submillimeter emission. Indeed, the brightest low-mass protostellar dense cores, such as NGC 1333 IRAS 4A, have been observationally studied in great detail including polarization observations. Thus, a possible approach to derive the initial conditions previous to the onset of the gravitational collapse, is to study the physical properties (density, temperature and magnetic field distribution) of collapsing Class 0 sources and trace back their history using models. The statistics and quality of the observational data toward the brightest Class 0 sources is continuously increasing, and thus, it has become possible to reliably compare data and theory.

4.2 Aims

The complex interplay among self-gravity, thermal support, turbulence, rotation, and magnetic fields, and ultimately the observable features that arise from them, are not well characterized observationally and, therefore, not well understood theoretically. The fact that the starless cores are diffuse and cold objects, makes them very difficult of observing because their emission is very faint. Our goal in this work is to deepen into the understanding of the formation, survival and evolution of low-mass dense cores. We doubly face this objective since *we aim: Firstly, to characterize observationally the physical and chemical properties of magnetized starless dense cores in the earliest stages of evolution to derive the initial conditions for star-formation, and to check whether the magnetic field is playing a role in the evolution of the cores and; Secondly, to compare observations of more evolved Class 0 sources with models of collapse of magnetized clouds to find the most likely initial conditions and dominant physical processes.*

In order to achieve the first goal, we have selected a sample of starless cores of the Pipe nebula. This nearby dark molecular cloud complex has a very low star formation efficiency, which makes it an ideal target to study the properties and evolution of pristine starless dense cores. For the second goal, we have selected NGC 1333 IRAS 4A. It is probably the best studied low–mass protostellar dense core, not only through molecular and dust emission, but also through high angular resolution polarimetric observations of the dust emission.

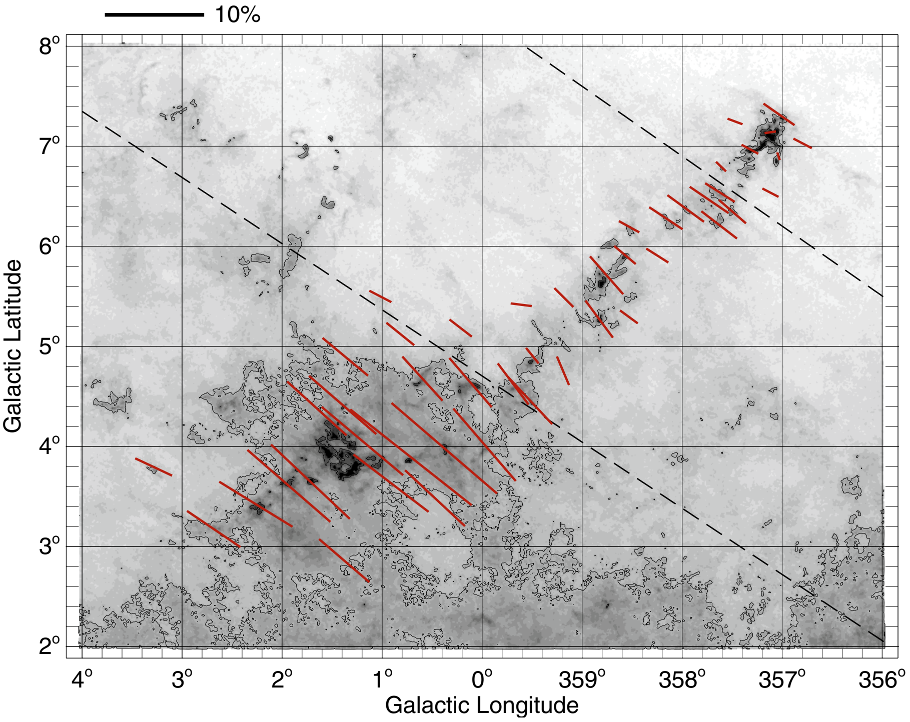

Figure 4.1: Mean polarization vectors of the fields observed with optical polarimetry toward the Pipe nebula extracted from Alves et al. (2008). The lengths of the vectors are proportional to the degree of polarization indicated in the top left-hand corner. The A_V map is that of Lombardi et al. (2006). The overall magnetic field is perpendicular to the filamentary structure.

4.3 Selected sources

4.3.1 Pipe nebula starless cores

The Pipe nebula is a massive (10^4 $M_\odot$: Onishi et al., 1999) filamentary (~15 pc long and ~3 pc wide) dark cloud located in the southern sky ~5° apart from the Galactic Center (see Fig. 4.1). Located only 145 pc away from the sun (Alves & Franco, 2007), this nearby complex serves as a good laboratory for star formation surveys. The main characteristic that distinguishes the Pipe nebula from other star-forming regions is that, despite its large reservoir of mass, it is in an apparently quiescent status, with a very low star-formation efficiency ($\sim$ 0.06% for the entire cloud, Forbrich et al., 2009). Barnard 59 (B59), located at the northwestern end of the cloud, is the only region with active star formation as demonstrated by the fact that it has formed a small cluster of low-mass stars. This observational evidence contrasts with other nearby molecular clouds, such as Ophiuchus or Taurus, with observed star-formation at much higher rates. The Pipe nebula is, hence, an excellent place to study the initial conditions for star formation at scales of a few parsecs.

Onishi et al. (1999) conducted the first extensive survey toward the Pipe nebula through single dish observations of CO isotopologues. These authors detect compact $C^{18}O$ cores in the main body of the cloud suggesting a clumpy distribution. A few years later, Lombardi et al. (2006) constructed a high resolution extinction map of the Pipe nebula using Two Micron All Sky Survey (2MASS) data. A large number (159) of high extinction cores were identified with typical masses between 0.2 and 5 $M_\odot$, and typical densities of 10^4 cm^{-3}. On that basis, Alves et al. (2007) and Rathborne et al. (2009) studied the Pipe nebula Core Mass Function (CMF) and found that it resembles the stellar Initial Mass Function (IMF) downscaled by a factor of 3–4.5. They interpreted this difference in scaling as a measure of the star formation efficiency (∼20–30 %). Recently, Peretto et al. (2012) have presented *Herschel* data toward the half western portion of the Pipe nebula. These authors have found a network of filaments and a bow-shock, most likely formed by the winds of the nearby Sco OB2 association, that could have enhanced the local density and triggered the star formation in the B59 region.

Muench et al. (2007) performed pointed CO molecular line observations that revealed that the Pipe nebula core are truly starless, formed by fairly quiescent gas. These authors distinguish two kinematical structures, a 15 pc long filament very narrow spatially and in radial velocity (typical line widths of 0.4 km s^{-1}), with core-to-core motions close to C_s, and a 2 pc ring-like structure enclosing a tenth of the total mass. Rathborne et al. (2008) performed a molecular line survey toward a subsample of the cores in NH_3 (1,1) and (2,2), CCS (2_1–1_0), and HC_5N (9–8). They found the cores to be associated with dense (10^4 cm^{-3}), relatively cold ($9.5 \leq T_K \leq 17$ K) and quiescent gas (∼0.1–0.2 km s^{-1}). Finally, Lada et al. (2008) presented a study of the physical status of the core population. They found that the non-thermal gas motions inside the cores are sub-sonic and mass independent. Therefore, thermal pressure, whose mean value is 1.6×10^5 K cm^{-3}, would appear to be the dominant source of internal pressure. In addition, most of the cores appear to be gravitationally unbound and confined by an external pressure (these authors estimate that the cloud weight exerts $P_{\rm cloud}/k \approx 10^5$ K cm^{-3}) independent of the core mass and location.

Recently, magnetic fields have revealed to be dynamically important toward the Pipe nebula. Alves et al. (2008) performed an optical polarimetric survey on 46 $12' \times 12'$ fields toward the diffuse gas. These authors find a large scale magnetic field that appears to be mostly perpendicular to the cloud main axis. The field is likely responsible for driving the collapse of the gas and dust cloud along the field lines and generate the filamentary structure. In addition, they found that the mean polarization level and the dispersion of the polarization position angle (tracing $\vec{B}_{\rm turb}$) within each field are clearly anti-correlated. The polarization properties also show a clear gradient along the Pipe nebula. This fact allowed the authors to distinguish three magnetically different regions in the cloud: B59, the *stem*, and the *bowl* (separated by dashed lines in Fig. 4.1). B59 shows low polarization levels but high dispersion of the polarization position angles within the observed fields. Moving through the *stem* toward the *bowl*, the polarization level increases and the dispersion decreases. These authors propose that these three regions might be in different evolutionary stages. B59 is the only magnetically supercritical region and the most evolved of the Pipe nebula, the *stem* would be at an earlier evolutionary stage, with material still collapsing, and finally, the *bowl* would be at the earliest stage, with cloud fragmentation just started. Using the Chandrasekhar-Fermi formula (Chandrasekhar & Fermi, 1953), these authors estimated the magnetic field strength to be 17, 30, and 65 μG in the B59, *stem*, and *bowl* regions. These values of the magnetic field translate into magnetic pressures of $\sim 10^6$ K cm^{-3}, well in excess of the values derived by Lada et al. (2008). Magnetic fields are

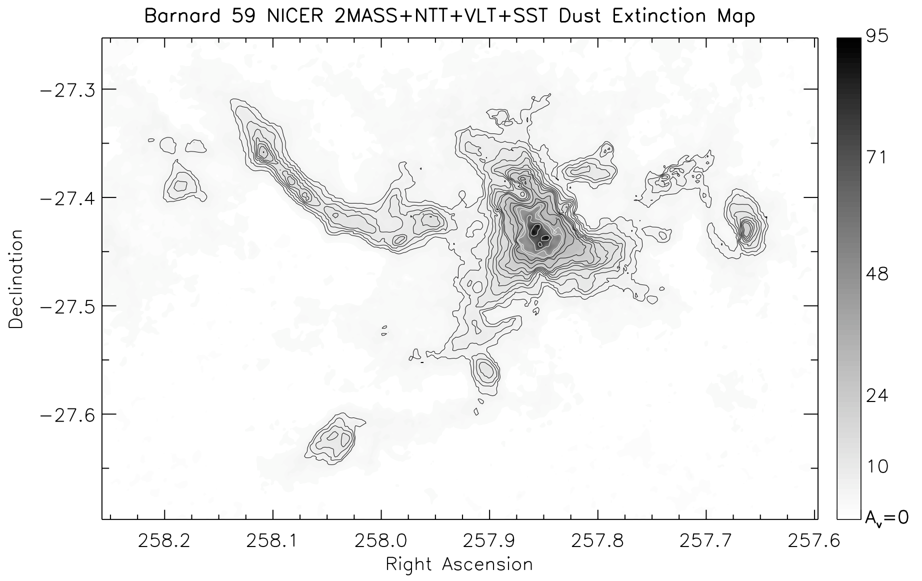

Figure 4.2: Extinction map of Barnard 59 at a resolution of $\sim 20''$ extracted from Román-Zúñiga et al. (2009). The black solid line contours mark levels of extinction from A_V=6.0 to 20.0 mag in 2.0 mag increments, and from A_V= 20.0 to 35.0 mag in 5.0 mag increments; the white contours mark levels of extinction at 40, 45, 60, and 80 mag.

thus an important internal source of cloud support. A more detailed analysis of the data by Franco et al. (2010) showed differences in the magnetic field in a core-to-core basis, and that the dust properties of the Pipe nebula seem to have the same properties as the normal galactic ISM. Their estimates of the second-order structure function suggest that the Pipe nebula is mostly magnetically dominated and that turbulence is sub-Alfvénic.

Barnard 59

The B59 complex is located at the northwestern end of the Pipe nebula (see Fig. 4.1). It hosts one of the less massive and less distant observable young stellar clusters. It is the only active low-mass star-forming cluster in the cloud. Seven Hα stars have been observed in association with B59 (Merrill & Burwell, 1950; The, 1964; Stephenson & Sanduleak, 1977; Kohoutek & Wehmeyer, 2003; Herbig, 2005). Recently, Brooke et al. (2007) identified 16 new candidates through a *Spitzer* survey, four of them with previous detections in the submillimeter regime (Reipurth et al., 1996) or in far-IR InfraRed Astronomical Satellite (IRAS) data. New analysis of *Spitzer* data, as well as ROSAT and XMM observations toward the Pipe nebula, confirm that the B59 complex hosts most of the protostars (Forbrich et al., 2009, 2010), the majority of them in the Class 0/I stage. Finally, Covey et al. (2010) using the NASA Infrared Telescope Facility identified 20 candidates and estimated the median age of the stars in ~2.6 Myr. During this time, the cluster has formed 14 stars, all below 3 $M_{\odot}$, with a total mass of $\sim 10\ M_{\odot}$.

In addition, the analysis of a high-resolution ($24''$) near-IR dust extinction map of the B59 region (Román-Zúñiga et al., 2009) revealed that it is a complex group of dense cores and filamentary structures (see Fig. 4.2). The A_V peak of the region is 89 mag and the

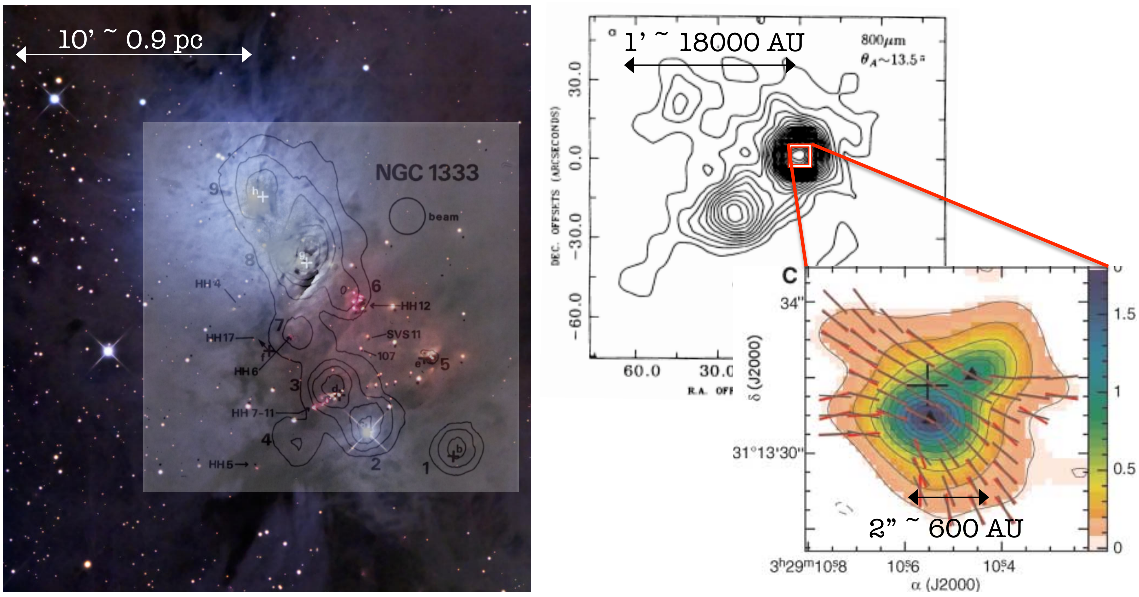

Figure 4.3: *Left*: Optical image of the reflection nebula NGC 1333 (APOD; April 18, 2009) with several contours of the 50μm map overlaid (Jennings et al., 1987). IRAS 4 is located in the bottom middle part. *Top right*: Contours of the submillimeter continuum emission of NGC 1333 IRAS 4 (Sandell et al., 1991), IRAS 4A is the source located at the N-E end of the cloud. *Bottom right*: close up view of IRAS 4A in submillimeter continuum emission (Girart et al., 2006). Red bars show the measures magnetic field vectors. Gray bars show the best-fit parabolic magnetic field model. The pinched magnetic field displays a clear "hourglass" morphology.

estimated mass of the complex is 41 $M_\odot$. Roughly half of the mass (21 $M_\odot$) is contained in the central B59-09 clump that hosts most of the stellar members. The mass of this clump is larger than the BE and Jeans mass, and thus, is prone to gravitational collapse. However, the most massive clump in the Pipe nebulashows a smooth structure compatible with an isothermal quiescent sphere. There are no signs of fragmentation and the little structure seems to be related to stellar feedback (*e.g.* the outflow cavity in the northern region). Moreover, pointed NH_3 observations within the core show that the thermal-to-non-thermal kinetic energy ratio averages well over unity, suggesting that B59-09 remains mostly quiescent despite having formed a star cluster.

The physical properties of the massive B59-09 clump are representative of the core population in the Pipe nebula. It is a quiescent, apparently isothermal structure with thermal linewidths and non-thermal support limited to sub-sonic motions. The magnetic field in the diffuse molecular gas component around the B59 region is $\sim 17\mu$G (Alves et al., 2008), suggesting that it can provide a significant amount of support. It is, then, interesting to study this core in detail.

4.3.2 NGC 1333 IRAS 4A

The Perseus molecular cloud is an active low-mass star forming region located at a distance ranging from 230 pc to 350 pc (Ridge et al., 2006). For this work, we adopted a value of 300 pc (Girart et al., 2006). In the southern part of the reflection nebula NGC 1333, Jennings et al. (1987) were the first to identify the protostar NGC 1333 IRAS 4 through IRAS observations at 50 μm and 100 μm (see Fig. 4.3) reporting an IR luminosity of $L = 21\ L_\odot$. Sandell et al. (1991) resolved the system into two different components, IRAS 4A and IRAS 4B, from submillimetric continuum single-dish observations at 450 μm and 800 μm. The two components are separated by $\sim$31$''$ and the measured total bolometric luminosity is $\sim$ 28 $L_\odot$ at 350 pc (20.5 $L_\odot$ at 300 pc), equally shared between the two components. The estimated temperature for the IRAS 4A component is 37 K, but its emission is optically thick, and therefore, this estimate would correspond to the outer part of the envelope. Subsequent interferometric observations by Looney et al. (2000) with the Berkeley Illinois Maryland Association (BIMA) interferometer, and Girart et al. (2006) with the SubMillimeter Array (SMA), have revealed further multiplicity: IRAS 4A is itself a binary system. The two components, IRAS 4A1 and IRAS 4A2, are separated by 540 AU ($1\overset{''}{.}8$) and are still embedded in a dense molecular and dusty envelope that have a total mass of 1.2 $M_\odot$ (Girart et al., 2006). This low-mass stellar system is in a very early stage of evolution.

Single-dish CO (3–2) observations revealed a NE-SW well-collimated outflow arising from IRAS 4A (Blake et al., 1995). Later on, Di Francesco et al. (2001) detected infall motions from inverse p-Cygni profiles observed in H_2CO (3_{12}–2_{11}) and N_2H^+ (1–0), proving the accretion state of the protostar. These authors also reported hints of rotation toward IRAS 4A from the systematic variations of the N_2H^+ velocities. Choi (2005) reported, through interferometric SiO (1–0) observations, a highly collimated NE-SW outflow with a projected position angle of $\sim$19°, and hints of a N-S outflow. The author proposes that IRAS 4A2 is powering the main outflow while IRAS 4A1 would power the second one.

BIMA spectropolarimetric observations at 1.3 mm have detected and partially resolved the polarization in both dust and CO (2–1) emission (Girart et al., 1999). Recent polarimetric observations with the SMA at 877 μm with a resolution of $1\overset{''}{.}3$ (390 AU) have shown a clearly “pinched” morphology of the magnetic field associated with the infalling envelope (Girart et al. 2006, see Fig. 4.3). This morphology resembles the hourglass shape predicted by the standard theory of low-mass star formation in a magnetized collapsing core (Fiedler & Mouschovias, 1993; Galli & Shu, 1993a,b; Nakamura & Li, 2005). Applying the Chandrasekhar-Fermi equation, the authors derived a magnetic field strength in the Plane Of the Sky (POS) of $B_{\rm POS}\approx5$ mG, corresponding to a mass-to-flux ratio of $\lambda\sim1.7$, thus supercritical and prone to collapse. The low-mass protostar IRAS 4A is then an ideal test site for models of magnetized cloud collapse and star formation.

4.4 Work plan

4.4.1 Strategy

Following the two different approaches described in the *Aims* subsection, the strategy undertaken in the thesis was:

1. **Physical and chemical properties of young dense cores**: To study the properties of these objects at a very early evolutionary phase, the best suited region is

the **Pipe nebula**. As described in Section 4.3.1, it is a dark cloud with a very low star-formation efficiency that hosts more than one hundred starless dense cores at a very early stage of evolution. In addition, the magnetic properties of the cloud vary significantly from one end to another. The strategy was to conduct a wide study of the properties of the magnetic fields in the diffuse molecular component of the Pipe nebula (work led by F. O. Alves and G. A. P. Franco and not presented here: Alves et al., 2008; Franco et al., 2010), as well to study in detail the properties of a sample of starless cores through the observation of dust and molecular line emission for several dense medium tracers (presented in this thesis).

- *Chemical properties of starless cores*: Two different observational approaches were conducted. Firstly, we performed narrow-band high spectral resolution observations of selected molecular transitions of special chemical interests, which allow to trace the chemical evolutionary state, toward a selection of nine dense cores. Chemical features have been used in literature to date cores using chemical models. We studied those properties and looked for correlations with the physical and magnetic parameters. The resulting publications of this study are presented in Chapter 5. Secondly, we performed wide-band low spectral resolution observations aiming for a wide unbiased chemical inventory toward a larger number of cores. We compared the molecular lines detected and their properties to compose an observational chemical classification related to their physical properties. The published results are presented in Chapter 6.
- *Physical properties of the starless cores*: We performed dust continuum emission maps toward the selected core sample of the high spectral resolution molecular line observations. We derived the observational physical properties and used them for a better interpretation of the status of each core. The results are included in the publications presented in Chapter 5. In addition, we performed accurate density profile fits to the studied sources and derived the best fitting BE model parameters. The article (to be submitted) is presented in Chapter 7.
- *B59*: In addition, we studied in detail the dust continuum emission of the central clump of the **B59** complex, the most massive Pipe nebula structure. This complex has formed a small cluster of low-mass stars, but still retains a large reservoir of mass in the form of a central quiescent massive clump. The structure is compatible to an isothermal dense core. We performed high angular resolution dust continuum observations to describe in detail the structure and look for possible fragmentation. We also studied the plausible mechanisms that can hold still the large amount of mass prone to collapse. The published article is presented in Chapter 8. My contribution to this project, of which I am not the Principal Investigator (PI), was to carry out the observations and data reduction of the dust continuum map, analyze it (physical parameter derivation, subtraction of the stellar contribution to the emission, and derive the radial density profile), and write the corresponding section of the paper. Finally, I contributed to the general discussion.

2. **Comparison of observations with collapse models of magnetized clouds**: To start the study of the dynamical evolution in a more evolved collapsing magnetized Class 0 source, the best choice is a prototypical example of the predicted magnetic field pinched topology. **NGC 1333 IRAS 4A** is a low-mass magnetized

Class 0 source with an infalling dusty envelope of $\sim$1 $M_{\odot}$ and a clear magnetic field "hourglass" morphology. The strategy was to properly compare the predictions of several theoretical models, using different assumptions, with the observational interferometric data. We compared the envelope density structure and magnetic field morphology by generating synthetic maps from the models and transforming them to SMA interferometric visibilities in the same conditions of the observations. Then, we sought for the best suited theoretical scenario describing the observations. The resulting publication is shown in Chapter 9.

4.4.2 Selected telescopes

Most of the energy, if not all, radiated away by dense cores has a thermal origin. To calculate the wavelength at which the thermal emission peaks we can use the Wien's law

$$[\lambda_{\rm max}/{\rm mm}] \approx \frac{2.9}{[T/{\rm K}]}, \tag{4.1}$$

where $\lambda_{\rm max}$ is the peak wavelength of the black body emission curve. The typical temperature of dense cores is $\sim$10 K, and therefore, the maximum thermal emission is at far-IR to sub-mm wavelengths. IR light is absorbed and scattered easily, therefore, to study these objects, the best instruments to use are radio telescopes operating at sub-mm/mm wavelengths. Regarding molecular line observations, at this low temperature only the molecular rotational states are excited.

The resolution or Half Power Beam Width (HPBW) of radio telescopes, which operate at the diffraction limit, can be calculated as

$$\left[{\rm HPBW}/''\right] \approx \frac{252\ [\lambda/{\rm mm}]}{[\oslash_{\rm tel}/{\rm m}]} \approx \frac{7.55\times10^{4}}{[\nu/{\rm GHz}]\ [\oslash_{\rm tel}/{\rm m}]}, \tag{4.2}$$

where λ and ν are the observed wavelength and frequency, respectively, and $\oslash_{\rm tel}$ the telescope diameter. Taking into account that the starless dense cores in the Pipe nebula are large and faint objects, high sensitivity observations are required to detect them. In addition, a large collecting area is preferred in order to accumulate as much radiation as possible on the receiver. This last requirement favors the use of single-dish telescopes, which provide resolutions ranging from a few arcseconds to a few tens of arcsecond. In the case of the Class 0 sources, which are usually more compact than starless cores, it is more convenient to use an interferometer that can provide a sub-arcsecond resolution. In this case, Eq. 4.2 applies but using the distance between the furthest pair of antennas instead of the dish diameter. Since the distance between a pair of antennas can vary depending on the mounting place, the resolution of an interferometer can be selected according to the specific needs of the project. A major drawback is that interferometers detect the correlated emission arising only from structures of sizes comparable to the resolution associated to each pair of antennas. As a consequence, the diffuse starless cores cannot be observed because the large scale stuctures are filtered out and no embedded compact dense component exists yet.

Table 4.1: Telescopes used in this thesis

Telescope	Latitude h m s	Longitude ° ′ ″	Height m	$\oslash_{\mathrm{tel}}$ m	$\mathrm{BL}_{\mathrm{max}}{}^{a}$ m	λ^{b} mm	ν^{c} GHz	HPBW^{d} ″
IRAM-30m	37 04 06.3 N	3 23 55.5 W	2850	30	–	0.85 – 3.6	352 – 83	7.0 – 29.6
SMA (SC^{e})	19 45 32.4 N	155 27 22.8 W	4080	6	25	0.43 – 1.7	700 – 176	4.3 – 17.2
SMA (C^{f})					70			1.5 – 6.1
SMA (E^{g})					220			0.49 – 1.95
SMA (VE^{h})					509			0.21 – 0.84

[a] Longest baseline. [b] Shortest and longest observable wavelength. [c] Highest and lowest observable frequency corresponding to the wavelengths in the previous column. [d] Angular resolution range, corresponding to the minimum and maximum observable wavelength, from Eq. 4.2 using $\oslash_{\mathrm{tel}}$ for the single-dish, and $\mathrm{BL}_{\mathrm{max}}$ for the interferometer. [e] SubCompact configuration. [f] Compact configuration. [g] Extended configuration. [h] Very Extended configuration.

We chose to perform the observations of young dense cores with the *Institut de RadioAstronomie Millimétrique* (IRAM)-30m single dish antenna located at Pico Veleta, Granada, Spain. It operates in the 0.8–3.6 (352–83 GHz) range and has a diameter of 30 m. For the observations of the evolved Class 0 source, we chose the **SMA** interferometer located at Pu'u Poli'ahu, Hawai'i, US. It operates in the 0.3–1.7 mm (1000–176 GHz) range with 8 antennas of 6 m in diameter. The baselines range from a minimum of 8 m up to a maximum of 509 m depending on the configuration. More information about the telescopes is listed in Table 4.1.

Both instruments are the best suited of its class to perform these observations, and both can carry out molecular line and dust continuum emission observations. The IRAM-30m telescope has a large collecting area, is located at a site with excellent meteorological conditions, and has the most sensitive receivers equipped in a single-dish antenna. The SMA itnterferometer is also located in a place with excellent weather conditions. It has only eight antennas, and thus, relatively long integrations are needed to obtain a good u, v coverage. It is the best interferometer available to perform polarimetric observations because of the simplicity of its polarizing system and the great sensitivity of the receivers.

Part II

Publications
&
Conclusions

V

Starless cores in the magnetically dominated Pipe nebula I. Narrow band high spectral resolution observations

The Astrophysical Journal, 723:1665–1677, 2010 November 10 doi:10.1088/0004-637X/723/2/1665

© 2010. The American Astronomical Society. All rights reserved. Printed in the U.S.A.

YOUNG STARLESS CORES EMBEDDED IN THE MAGNETICALLY DOMINATED PIPE NEBULA*

P. Frau[1], J. M. Girart[1], M. T. Beltrán[2], O. Morata[3,4], J. M. Masqué[5], G. Busquet[5],
F. O. Alves[1], Á. Sánchez-Monge[5], R. Estalella[5], and G. A. P. Franco[6]
[1] Institut de Ciències de l'Espai (CSIC-IEEC), Campus UAB, Facultat de Ciències, Torre C-5p, 08193 Bellaterra, Catalunya, Spain
[2] INAF-Osservatorio Astrofisico di Arcetri, Largo Enrico Fermi 5, 50125 Firenze, Italy
[3] Institute of Astronomy and Astrophysics, Academia Sinica, P.O. Box 23-141, Taipei 106, Taiwan
[4] Department of Earth Sciences, National Taiwan Normal University, 88, Section 4, Ting-Chou Road, Taipei 11677, Taiwan
[5] Departament d'Astronomia i Meteorologia and Institut de Ciències del Cosmos (IEEC-UB), Universitat de Barcelona,
Martí i Franquès 1, 08028 Barcelona, Catalunya, Spain
[6] Departamento de Física-ICEx-UFMG, Caixa Postal 702, 30.123-970, Belo Horizonte, Brazil

Received 2010 March 10; accepted 2010 September 9; published 2010 October 26

ABSTRACT

The Pipe Nebula is a massive, nearby dark molecular cloud with a low star formation efficiency which makes it a good laboratory in which to study the very early stages of the star formation process. The Pipe Nebula is largely filamentary and appears to be threaded by a uniform magnetic field at scales of a few parsecs, perpendicular to its main axis. The field is only locally perturbed in a few regions, such as the only active cluster-forming core B59. The aim of this study is to investigate primordial conditions in low-mass pre-stellar cores and how they relate to the local magnetic field in the cloud. We used the IRAM 30 m telescope to carry out a continuum and molecular survey at 3 and 1 mm of early- and late-time molecules toward four selected starless cores inside the Pipe Nebula. We found that the dust continuum emission maps trace the densest regions better than previous Two Micron All Sky Survey (2MASS) extinction maps, while 2MASS extinction maps trace the diffuse gas better. The properties of the cores derived from dust emission show average radii of ∼0.09 pc, densities of $\sim 1.3 \times 10^5$ cm^{-3}, and core masses of ∼2.5 $M_\odot$. Our results confirm that the Pipe Nebula starless cores studied are in a very early evolutionary stage and present a very young chemistry with different properties that allow us to propose an evolutionary sequence. All of the cores present early-time molecular emission with CS detections in the whole sample. Two of them, cores 40 and 109, present strong late-time molecular emission. There seems to be a correlation between the chemical evolutionary stage of the cores and the local magnetic properties that suggests that the evolution of the cores is ruled by a local competition between the magnetic energy and other mechanisms, such as turbulence.

Key words: ISM: individual objects (Pipe Nebula) – ISM: lines and bands – stars: formation

Online-only material: color figures

1. INTRODUCTION

The Pipe Nebula is a massive (10^4 $M_\odot$; Onishi et al. 1999) filamentary (∼15 pc long and ∼3 pc wide) dark cloud located in the southern sky ∼5° apart from the Galactic center. Its short distance to the Sun (145 pc; Alves & Franco 2007) places this complex in the group of nearby molecular clouds which serve as good laboratories for star formation surveys. Despite the large reservoir of mass, the Pipe Nebula molecular cloud is characterized by being apparently quiescent, with a very low star formation efficiency (∼0.06% for the entire cloud; Forbrich et al. 2009). Barnard 59 (B59), located at the northwestern end of the cloud, has formed a small cluster of low-mass stars (Brooke et al. 2007). The low global star-forming efficiency of the cloud contrasts with that of other nearby molecular clouds such as Ophiuchus or Taurus, where important star formation activity is observed. The Pipe Nebula is, hence, an excellent place to study the initial conditions of star formation at scales of a few parsecs.

The first extensive survey of the Pipe Nebula was done by Onishi et al. (1999) through single dish observations of CO isotopologues. These authors were the first to suggest a clumpy distribution for the dense gas by detecting compact C^{18}O cores in the main body of the cloud. It was not until the last few years that several surveys (Lombardi et al. 2006; Muench et al. 2007; Brooke et al. 2007; Rathborne et al. 2008; Lada et al. 2008) were carried out to explore the physical properties of the cloud. Lombardi et al. (2006) use Two Micron All Sky Survey (2MASS) data to construct a high-resolution extinction map of the Pipe Nebula through which they identify a large number of high extinction cores with typical masses between 0.2 and 5 $M_\odot$. Molecular line observations reveal that they are starless cores in a very early evolutionary stage, associated with dense (10^4 cm^{-3}), relatively cold ($9.5 \leqslant T_K \leqslant 17$ K), and fairly quiescent gas (typical line widths of 0.4 km s^{-1}, Muench et al. 2007; Rathborne et al. 2008). Non-thermal gas motions inside the cores are sub-sonic and mass-independent. Therefore, thermal pressure appears to be the dominant source of internal pressure. In addition, these cores appear to be pressure-confined, but gravitationally unbound (Lada et al. 2008).

Recently, Alves et al. (2008) performed an optical polarimetric survey of the diffuse gas in the Pipe Nebula. They found a large-scale magnetic field that appears to be mostly perpendicular to the cloud's main axis. The magnetic field exerts a pressure (∼10^6 K cm^{-3}) that is likely responsible for driving the collapse of the gas and dust cloud along the field lines. The polarization properties significantly change along the Pipe Nebula. This fact allowed the authors to distinguish three regions in the cloud: B59, the *stem*, and the *bowl* (see Figure 1). B59 shows low polarization levels but high dispersion of the polarization position angles. Moving through the *stem* toward the *bowl*, the polarization level increases and the dispersion decreases. These

---

[*] Based on observations carried out with the IRAM 30 m telescope. IRAM is supported by INSU/CNRS (France), MPG (Germany), and IGN (Spain).

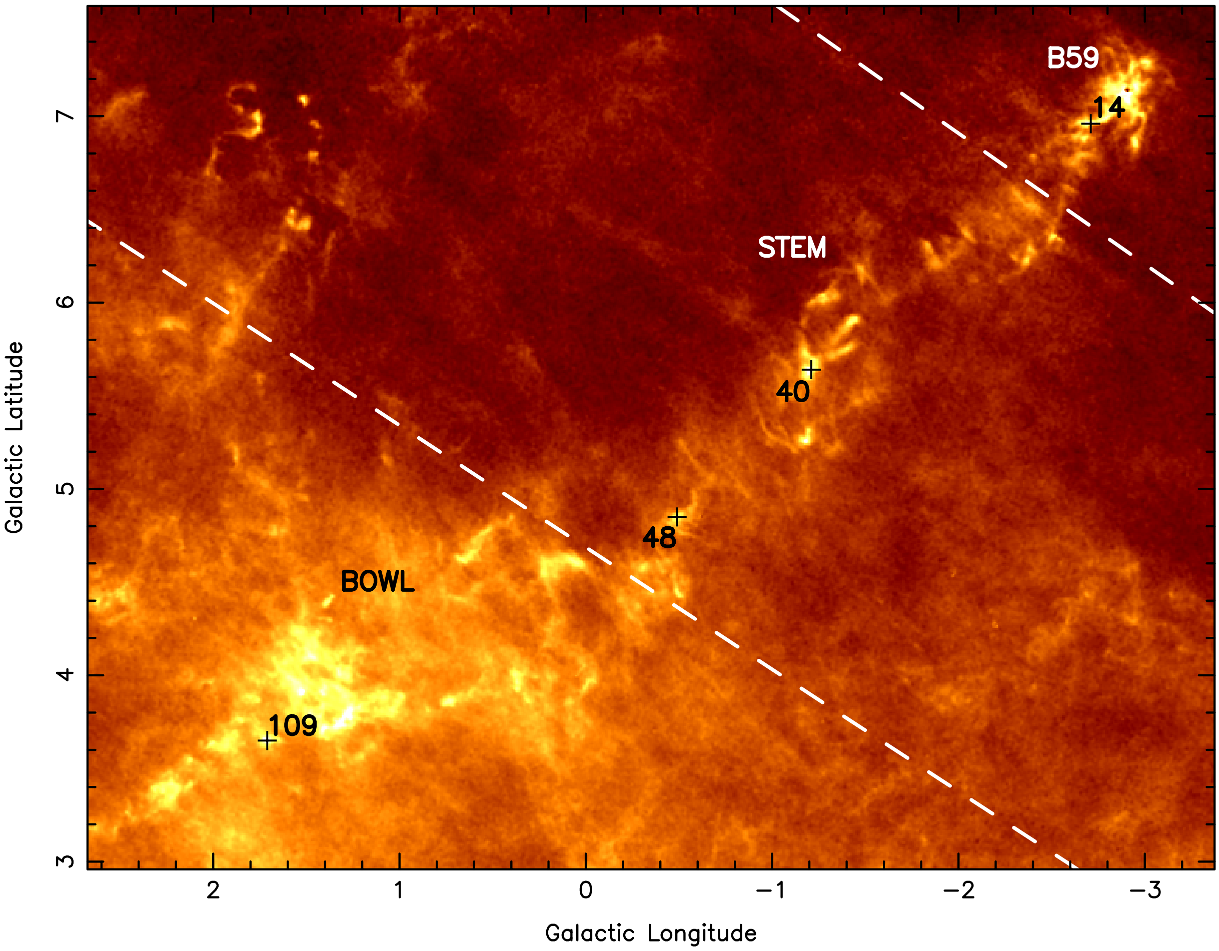

Figure 1. Position of the observed cores plotted over the 2MASS extinction map of the Pipe Nebula (Lombardi et al. 2006). The dashed lines separate the three different magnetically defined regions (Alves et al. 2008). The lowest visual extinction (A_V) corresponds to 0.5 mag. The highest A_V is observed toward the *bowl* of the Pipe and the B59 region, where it reaches approximately 20 mag (Lombardi et al. 2006). We selected cores located in all three regions of the Pipe *bowl*, *stem*, and B59).

(A color version of this figure is available in the online journal.)

authors propose that these three regions might be in different evolutionary stages. B59 is the only magnetically supercritical region and the most evolved of the Pipe Nebula, the *stem* would be at an earlier evolutionary stage with material still collapsing, and finally, the *bowl* would be at the earliest stage, with cloud fragmentation having just started.

Based on Alves et al.'s (2008) results, we selected a sample of cores distributed in the different regions of the Pipe Nebula. We started an extensive molecular survey of these cores using the IRAM 30 m telescope. The aim of this study is to probe their chemical evolutionary stage, which could be related to the dynamical age according to chemical modeling of starless cores (Taylor et al. 1998; Morata et al. 2003; Tafalla et al. 2006). These models predict that some molecules, such as carbon-containing molecules, are formed very early in the chemical evolution, and are known as early-time molecules. These species are expected to be abundant in chemically young or low-density cores, and most of them seem to experience earlier depletion effects (see, e.g., Taylor et al. 1998; Ohashi et al. 1999; Bergin et al. 2001; Tafalla et al. 2006). Other species, such as nitrogen-bearing molecules and deuterated species, require a longer time to form. Thus, they are formed later in the chemical evolution and are known as late-time molecules. They are not expected to be depleted until densities of 10^6 cm^{-3} are reached (see, e.g., Caselli et al. 2002; Flower et al. 2006; Bergin & Tafalla 2007; Aikawa et al. 2008). The qualitative comparison of the relative abundances of different types of molecules in each core can provide us with some clues about their possible evolutionary stage. From the observational point of view, there have been several authors who have studied the evolutionary stage of pre- and protostellar cores through molecular surveys. For instance, Kontinen et al. (2000) have used a large sample of molecules in a prestellar and a protostellar core. They found very different chemical compositions, specially in N_2H^+ and long carbon-chain molecule abundances. The former is typical of a pure gas-phase chemistry, while the latter requires an evolved chemistry to form. According to time-dependent chemistry models they interpret the differences as different stages of the chemical evolution. Later, Tafalla et al. (2004) made a chemical analysis of L1521E, which helped to determine the extreme youth of this prestellar core. From the theoretical point of view, Aikawa et al. (2003) have simulated the evolution of a prestellar core

Table 1
Source List

Source[a]	α(J2000) (h m s)	δ(J2000) (° ′ ″)	$v_{\rm LSR}$ (km s^{-1})	Region[b]
Core 14	17 12 34.0	−27 21 16.2	+3.6	B59
Core 40	17 21 16.4	−26 52 56.7	+3.3	*stem*
Core 48	17 25 59.0	−26 44 11.8	+3.6	*stem*
Core 109	17 35 48.5	−25 33 05.8	+5.8	*bowl*

Notes.
[a] According to Lombardi et al. (2006) numbering.
[b] According to Alves et al. (2008) diffuse gas polarimetric properties.

and identified the different molecular abundances at different evolutionary stages to finally compare the results with the sample of Tafalla et al. (2002). Morata et al. (2003, 2005) have used the modeling results of Taylor et al. (1998) to compare with observations toward the L673 molecular cloud.

Based on this, we observed four selected cores (see Table 1) in a set of early- and late-time molecules (see Table 2) for a subsequent comparison. In addition, we mapped the 1.2 mm dust continuum emission of the cores to obtain a complete description of the structure, chemistry, and evolutionary stage of the four selected Pipe Nebula cores.

2. OBSERVATIONS AND DATA REDUCTION

2.1. MAMBO-II Observations

We mapped cores 14, 40, 48, and 109 (according to the Lombardi et al. 2006 numbering) at 1.2 mm with the 117-receiver MAMBO-II bolometer (array diameter of 240″) of the 30 m IRAM telescope in Granada (Spain). The positions and velocity of the local standard of rest ($v_{\rm LSR}$) for each core are listed in Table 1. The observations were carried out in 2009 April and May and in 2010 January and March in the framework of a flexible observing pool. A total of 13 usable maps were selected for analysis: three for cores 14, 40, and 109, and four for core 48. The weather conditions were good, with zenith optical depths between 0.1 and 0.3 for most of the time. The maps were taken at an elevation of $\lesssim 25°$ due to the declination of the sources.

The beam size of the telescope is ∼11″ at the effective frequency of 250 GHz. The sources were observed with the on-the-fly technique, with the secondary chopping between 46″ and 72″ parallel to the scanning direction of the telescope. The telescope was constantly scanning at a speed of 8″ s^{-1} for up to 65 s. This resulted in typical integration times for each map of ∼1 hr. When possible, each source was mapped with different scanning directions (in equatorial coordinates) or rotating the secondary mirror of the telescope to avoid scanning artifacts in the final maps. We measured the zenith optical depth with a skydip and checked pointing and focus before and after each map. The average corrections for pointing and focus stayed below 3″ and 0.2 mm, respectively. Flux density calibrators were observed every few hours.

The data were reduced using MOPSIC with the iterative reduction strategy developed by Kauffmann et al. (2008). The main advantages of the new scheme are that (1) sources much larger than in the classical approach can be recovered, (2) the signal-to-noise ratio (S/N) of the final map increases, and (3) they suffer from less artifacts. The figures were created using the GREG package, from the GILDAS[7] software.

Table 2
Molecular Transitions Observed in the
Pipe Nebula Cores with the IRAM 30 m Antenna

Molecule	Transition	Frequency (GHz)	Beam (″)	Beam Efficiency[a]	Δv[b] (km s^{-1})	Type[c]
C_3H_2	$(2_{1,2}–1_{1,0})$	85.3389	29.0	0.78/0.81	0.07	E
HCN	(1–0)	88.6318	28.0	0.78/ ···	0.07	E
N_2H^+	(1–0)	93.1762	26.5	0.77/0.81	0.06	L
$C^{34}S$	(2–1)	96.4130	26.0	··· /0.81	0.06	E
CS	(2–1)	97.9809	25.5	0.76/0.81	0.06	E
CN	(1–0)	113.4909	21.5	0.75/0.81	0.05	E
N_2D^+	(2–1)	154.2170	15.0	0.77/0.74	0.04	L
DCO^+	(3–2)	216.1126	10.5	0.57/0.63	0.03	L
CN	(2–1)	226.8747	10.0	0.53/0.63	0.03	E
N_2D^+	(3–2)	231.3216	10.0	0.67/0.63	0.03	L
$H^{13}CO^+$	(3–2)	260.2554	9.0	0.53/0.63	0.02	L

Notes.
[a] ABCD and EMIR receiver, respectively.
[b] Spectral resolution.
[c] E: early-time; L: late-time. See Sections 1 and 4.3 for details.

All the maps have been convolved with a 21.″5 Gaussian, larger than the telescope beam, in order to improve the S/N and to smooth the appearance of the maps. The size of the Gaussian was chosen to be the one of the CN (1–0) molecular transitions (see Table 2), which provides good spatial resolution and large S/N for the four maps.

2.2. Line Observations

We made several pointed observations within the regions of the cores 14, 40, 48, and 109 with the heterodyne receivers of the 30 m IRAM telescope (ABCD and EMIR receivers). The observations were carried out in three epochs. The first epoch was 2008 August and September. We used the capability of the telescope to perform simultaneous observations at different frequencies to observe the emission of the C_3H_2 $(2_{1,2}–1_{1,0})$, HCN (1–0), N_2H+ (1–0), CS (2–1), CN (1–0), N_2D+ (2–1), DCO^+ (3–2), CN (2–1), N_2D+ (3–2), and $H^{13}CO^+$ (3–2) molecular transitions arranged in three different frequency setups covering the 3, 2, 1.3, and 1.1 mm bands. To do this, we combined the A100/B100/A230/B230 and A100/D150/A230/D270 SIS heterodyne receivers. The observational strategy was first to observe several positions with a 20″ spacing centered on the $C^{18}O$ pointing center reported by Muench et al. (2007) (depicted by star symbols in Figure 2), which is very close to the visual extinction peak position of each core (Lombardi et al. 2006). The visual extinction peak is assumed to be the densest region of the core, and it was defined as the core center by Muench et al. (2007). The second and third epochs were 2009 August and 2010 June, respectively, both using the new EMIR E0/E1/E2 receivers. We observed deeper toward the position of the grid of the first epoch closer to the dust continuum peak (see the circle symbols in Figure 2). We also observed the $C^{34}S$ (2–1) molecular transition. Table 2 shows the transitions and frequencies observed. We used the VESPA autocorrelator as the spectral back end, selecting a channel resolution of 20 kHz, which provided a total bandwidth of 40 MHz. The corresponding velocity resolutions, main-beam efficiencies, and half-power beam widths at all the observed frequencies are also listed in Table 2. We used the frequency-switching mode with a frequency throw between 3.83 and 22.98 MHz, depending on the transition. System temperatures in nights considered "good" were between 200 and 275 K at 3 mm and between 440 and

---

[7] MOPSIC and GILDAS data reduction packages are available at http://www.iram.fr/IRAMFR/GILDAS.

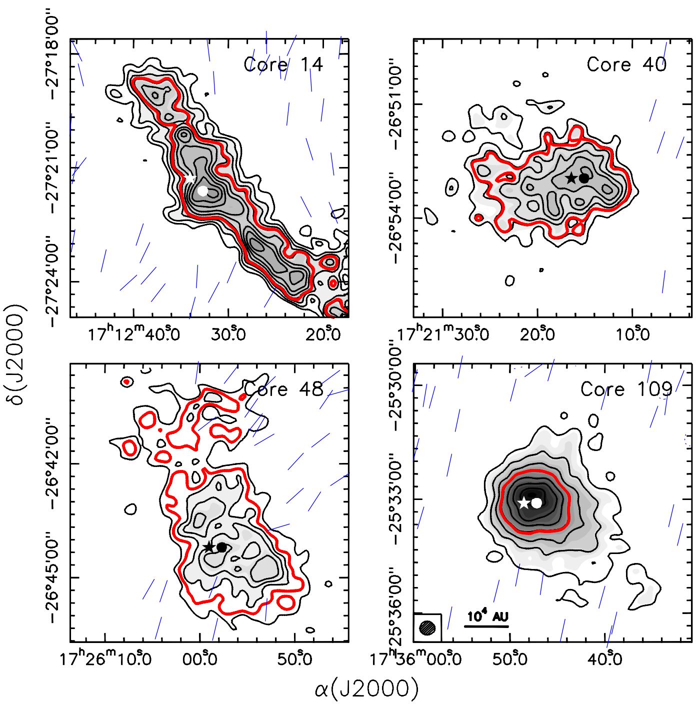

Figure 2. IRAM 30 m MAMBO-II maps of the dust continuum emission at 1.2 mm toward four cores of the Pipe Nebula. The gray-scale levels for all the maps are 3–18 times 5.75 mJy beam^{-1}. The contour levels are 3–11 times σ in steps of 1σ, for cores 14, 40, and 48, and 3–21σ in steps of 3σ for core 109. 1σ is 4.5, 5.0, 3.5, and 4.5 mJy beam^{-1} for cores 14, 40, 48, and 109, respectively. The red thick contour marks the half-maximum emission level of the source (see Table 3). Black or white stars indicate the C^{18}O pointing center reported by Muench et al. (2007), which is very close to the visual extinction peak position of each core (Lombardi et al. 2006). Black or white filled circles indicate the position where line observations have been performed, close to the dust continuum emission maximum which falls into the beam area. The blue vectors depict the magnetic field vector found by Franco et al. (2010). Note that for core 40 there are no optical polarimetry measurements on the eastern side due to the high visual extinction. In the bottom left corner of the bottom right panel the convolved beam and the spatial scale for the maps is shown.

(A color version of this figure is available in the online journal.)

Table 3
1.2 mm Continuum Emission Parameters

Source	α(J2000)[a] (h m s)	δ(J2000)[a] (° ′ ″)	$T_{\rm dust}$ (K)	rms (mJy beam^{-1})	S_ν (Jy)	$I_\nu^{\rm Peak}$ (mJy beam^{-1})	Diameter (pc)	$N_{\rm H_2}$[b] (10^{21} cm^{-2})	$n_{\rm H_2}$[b] (10^4 cm^{-3})	Mass[b] ($M_\odot$)
Core 14 (filament)	17 12 31.5	−27 21 41.0	12.0[c]	4.5	2.56	51.6	0.106	12.21	5.59	2.87
Core 14 (core)					1.24		0.071	13.27	9.09	1.40
Core 40	17 21 14.7	−26 52 47.8	10.3[c]	5.0	1.73	42.0	0.104	11.05	5.16	2.51
Core 48	17 25 57.3	−26 44 22.3	10.0[d]	3.5	1.44	27.9	0.127	6.14[d]	2.35[d]	2.09[d]
Core 109	17 35 47.7	−25 32 52.9	9.5[c]	4.5	2.76	105.3	0.063	47.60	36.57	4.00

Notes.

[a] Pointing position of the chemical observations which lies inside the same beam area of the dust continuum emission peak.

[b] Assuming $\kappa_{250\,\rm GHz}$= 0.0066 cm^2 g^{-1} as a medium value between dust grains with thin and thick ice mantles (Ossenkopf & Henning 1994). See Appendix A for details on the calculation.

[c] Adopted to be equal to the kinetic temperature derived for NH$_3$ (Rathborne et al. 2008).

[d] No kinetic temperature estimate, therefore, we assumed 10 K based on the temperatures of the other cores (Rathborne et al. 2008).

960 K at 1 mm ($T_{\rm sys}$ reached 450 K and 3200 K in bad nights, respectively). Pointing was checked every two hours.

We reduced the data using the CLASS package of the GILDAS[1] software. We obtained the line parameters either from a Gaussian fit or from calculating their statistical moments when the profile was not Gaussian.

3. RESULTS AND ANALYSIS

3.1. Dust Continuum Emission

In Figure 2, we present the MAMBO-II maps of the dust continuum emission at 1.2 mm toward the four selected cores of the Pipe Nebula, convolved to a 21.″5 beam. Table 3 gives the peak position of the 1.2 mm emission after convolution with a Gaussian, the dust temperature (Rathborne et al. 2008), the rms noise of the emission, the flux density, and the value of the emission peak. Additionally, we also give the derived FWHM equivalent diameter, which is the diameter of the circular area equal to the area within the FWHM level, depicted by a red contour in Figure 2. Table 3 also lists the H$_2$ column and volume density, as well as the mass for each core. These parameters are derived from the emission within the 3σ level and discussed in Section 4.

The flux density of the cores ranges between ∼1.24 and ∼2.76 Jy. Note, however, that the extinction maps show that the studied cores are surrounded by a diffuse medium (see Figure 1

Table 4

H_2 Column Densities[a], N_{H_2}, of the Pipe Nebula Cores in cm^{-2}

Source	10″.5	15″.0	21″.5	27″.0
Core 14	1.75×10^{22}	1.38×10^{22}	1.21×10^{22}	1.11×10^{22}
Core 40	1.32×10^{22}	1.28×10^{22}	1.12×10^{22}	1.07×10^{22}
Core 48	1.09×10^{22}	8.88×10^{21}	7.38×10^{21}	6.99×10^{21}
Core 109	4.19×10^{22}	3.73×10^{22}	3.23×10^{22}	3.08×10^{22}

Notes. [a] Average column densities are calculated within one beam area toward the dust continuum emission peak. The values of $\kappa_{250\,\mathrm{GHz}}$ and T_{dust} are the same as for Table 3. These values are combined with the molecular column densities to find the molecular abundances in the same beam area. The correspondence is: 10″.5 with DCO^+, 15″.0 with N_2D^+(2–1), 21″.5 with CN (1–0) and, finally, 27″.0 with C_3H_2, HCN, N_2H^+, CS, and $C^{34}S$.

Table 5

Summary of Detections and Upper Levels in K Toward the Pipe Nebula Cores[a]

Molecular	Core			
Transitions	14	40	48	109
C_3H_2 ($2_{1,2}$–$1_{1,0}$)	✓	✓	<0.07	✓
HCN (1–0)	<0.21	✓	✓	✓
N_2H^+ (1–0)	✓	✓	<0.07	✓
$C^{34}S$ (2–1)	✓	✓	✓	✓
CS (2–1)	✓	✓	✓	✓
CN (1–0)	✓	✓	<0.17	✓
N_2D^+ (2–1)	<0.12	✓	<0.08	✓
DCO^+ (3–2)	<1.71	<0.61	<0.76	✓
CN (2–1)	<0.97	<1.70	<0.76	<0.90
N_2D^+ (3–2)	<1.01	<0.93	<1.94	<0.91
$H^{13}CO^+$ (3–2)	<1.52	<1.40	<2.38	<1.34

Note. [a] The transitions marked with ✓ have been detected toward the corresponding core. Otherwise, the 3σ upper limit is shown.

and Lombardi et al. 2006). The on-the-fly reduction algorithms assume that the map limits have a zero emission level. Due to the presence of the diffuse material, this could not be true for the observed cores, and, therefore, the measured flux density of the maps might be lower than the actual value. We derived average H_2 column densities (N_{H_2}; see Appendix A) toward the dust continuum emission peak for the different resolutions (listed in Table 4) of the detected molecular transitions (see Table 5). We derived their abundances with respect to H_2. The results are discussed in Section 4.

The maps of Figure 2 show the different morphology of the cores. Following the results of Alves et al. (2008), it is interesting to compare the shape of the cores with their location along the Pipe Nebula. Core 14, located in B59, belongs to a clumpy and filamentary structure of ~500″ (~0.35 pc) elongated along the NE–SW direction. This is in perfect agreement with previous extinction maps (Lombardi et al. 2006; Román-Zúñiga et al. 2009). On the other hand, core 109, located in the *bowl*, shows a compact and circular morphology with an FWHM of ~90″ (~0.063 pc). Cores 40 and 48, both located in the *stem*, have elliptical morphologies with extended diffuse emission.

3.2. Molecular Survey of High-density Tracers

Muench et al. (2007) reported $C^{18}O$ pointed observations toward the Pipe Nebula cores measured with a resolution of 56″. As seen in their Figure 1, the position of the $C^{18}O$ is very close to the visual extinction peak position of each core (Lombardi et al. 2006). Our higher resolution maps show a peak position offset for all the cores. As listed in Tables 1 and 3, and as shown in Figure 2, the dust continuum peak does not coincide exactly with the A_v peak (stars in Figure 2). However, the difference is compatible with the angular resolution of the extinction maps. We decided to present only molecular line data of the observed positions closer to the dust continuum emission peak (circles in Figure 2), defined as the core center and supposed to exhibit brighter emission from molecular transitions. The typical core size is ~90″ or larger (see Table 3). The beam size of the detected lines, except for N_2D^+ (2–1) and DCO^+ (3–2), ranges from 21″.5 to 29″.0, while the initial grid of the pointed position had a separation of 20″.0, thus the emission peak stays within the beam area for these molecular transitions. Therefore, the molecular line properties that we obtain are representatives of the chemistry of the core center.

Table 5 summarizes the detections or the 3σ upper limits of the non-detections toward each core. Table 6 gives the parameters of the detected lines. In Figures 3 and 4, we show the spectra of the different molecular transitions observed toward the dust continuum emission peak of each core. Core 109 shows the stronger emission in all the detected transitions in our sample. This is the core with the most compact and circular morphology (see Figure 2). Core 40 also shows emission in the six molecular transitions at 3 mm (C_3H_2 ($2_{1,2}$–$1_{1,0}$), HCN (1–0), N_2H^+ (1–0), $C^{34}S$ (2–1), CS (2–1), and CN (1–0)), although their intensities are lower than for core 109. Core 14 shows emission in all the 3 mm transitions except in HCN (1–0). Finally, core 48 only shows emission in CS (2–1), $C^{34}S$ (2–1), and HCN (1–0).

In addition to the line parameters, we derived the molecular column densities for all of the detected species (see Appendix B for details) which are listed in Table 7. For the transitions with detected hyperfine components (HCN, N_2H^+, and CN), we derived the opacity using the hyperfine components fitting method of the CLASS package. For the CS and $C^{34}S$ molecular transitions, we numerically derived the opacity using

$$\frac{T_{\mathrm{MB}}(C^{34}S)}{T_{\mathrm{MB}}(CS)} = \frac{1 - \exp(-\tau)}{1 - \exp(-\tau\ r)} \tag{1}$$

where r is the CS to $C^{34}S$ abundance ratio, assumed to be equal to the terrestrial value (22.5, Kim & Koo 2003). We found a high opacity toward cores 14 and 48 for CS (2–1), 10.8 and 6.0, respectively, whose spectra show self-absorption (see Figure 3). For cores 40 and 109, we found lower opacities, $\tau = 3.1$ and 4.2 for CS (2–1), respectively. We assumed optically thin emission in C_3H_2, DCO^+, and N_2D^+ (2–1), the latter with only the main hyperfine component detected. This conservative assumption could not be true, so the column densities should be taken as lower limits. We also derived the molecular abundances with respect to H_2 (see Table 8), taking into account the resolution for each molecular transition (see Table 4).

4. DISCUSSION

We observed four selected cores located in the different regions of the Pipe Nebula (*bowl*, *stem*, and B59), in different molecular tracers and dust continuum emission, to study and compare their physical and chemical properties. The cores were selected based on the results of the optical polarimetric survey carried out by Alves et al. (2008). In the following subsections, we discuss and compare the properties of each individual core, as well as an overall analysis of such properties, and try to relate our results with previous works. In particular, in the next subsection, we compare the dust continuum emission with the

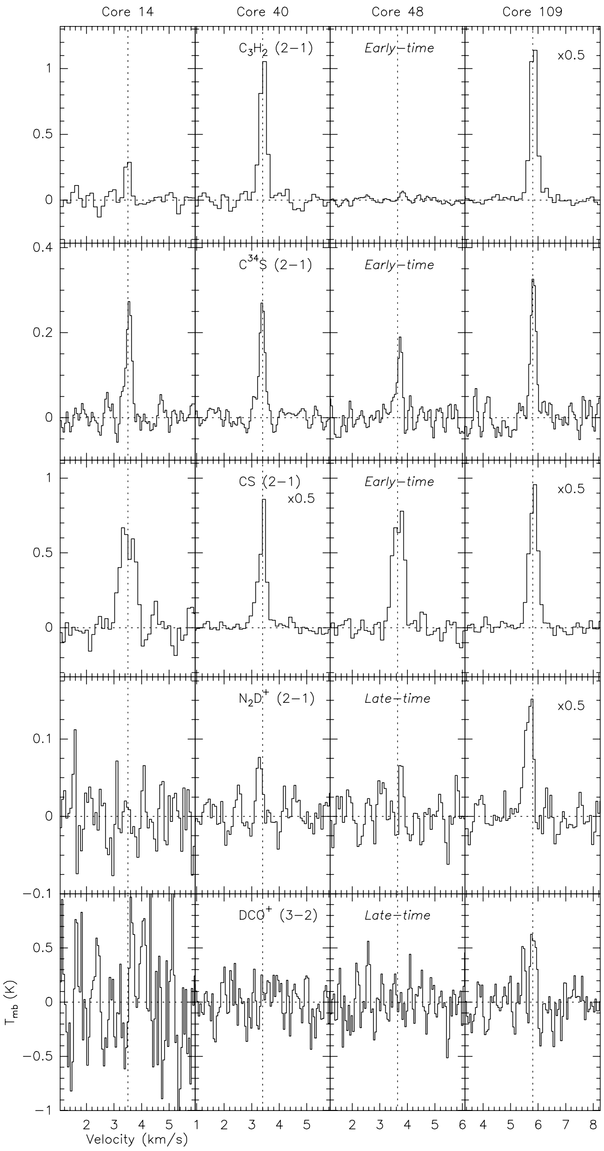

Figure 3. IRAM 30 m line spectra of the molecular transitions with no hyperfine components toward the four selected cores of the Pipe Nebula (see Table 1). The name of the core is indicated above the top panel of each column. Rows correspond to a single molecular transition specified on the second column. The velocity range is 5 km s^{-1} and is centered on the $v_{\rm LSR}$ of each core marked with a vertical dotted line. The vertical axis shows the $T_{\rm MB}$ of the emission, and the zero level is marked by a horizontal dotted line. Some of the spectra, with the highest measured $T_{\rm MB}$, have been divided by 2 to fit to the common scale.

visual extinction maps of Rathborne et al. (2008) and the trend found for the diffuse gas by Alves et al. (2008).

4.1. Comparison of Visual Extinction and 1.2 mm Continuum Emission Maps

The beam size of our observations is 11″, convolved to a Gaussian of 21.″5 in the maps shown (see Section 3.1), while that of Rathborne et al. (2008) is ∼60″. Hence, our maps suffer from less beam dilution and we can resolve smaller structures. The sensitivity limit of the $A_{\rm v}$ observations is fixed at 1.2 mag (Lada et al. 2008), which corresponds to a column density of $\sim 1\times10^{21}$ cm^{-2} (Wagenblast & Hartquist 1989). A conservative estimation of the sensitivity limit of our maps, in the same conditions, can be derived using the 3σ emission level of the noisiest continuum map convolved to a 60″ Gaussian. The resulting beam averaged column density, for a $T_{\rm K}$ of 10 K, is $\sim 4\times10^{20}$ cm^{-2}. Therefore, as seen from the minimum column densities in the same conditions, our data set has slightly better sensitivity. Lada et al. (2008) define the equivalent radius of the core using the region with emission brighter than 3σ, while we use the region with emission brighter than half of the peak value. This difference prevents a direct comparison of the radii and densities. The core masses, however, depend only on the integrated flux density and can be compared. Our masses are on average ∼3.4 times smaller, ranging from ∼0.9 for core 109 to ∼7 for core 14.

We estimated the difference between the 2MASS extinction maps (Lombardi et al. 2006) and the 1.2 mm dust maps. To do this, we first transformed the original near-IR extinction maps to visual extinction maps using $A_{\rm v} = A_{\rm k}/0.118$ (Dutra et al. 2002). Then, we convolved the 1.2 mm dust maps with a Gaussian of 60″ to have the same resolution. We transformed the 1.2 mm dust maps to column density maps (see Appendix A for details). We assumed a uniform typical temperature of 10 K for all of the cores. To estimate the uncertainty caused by this assumption, we also made the calculations for temperatures of 8 and 12 K, which resulted in an average maximum variation over the whole map of ∼2.4 extinction magnitudes. We also assumed for all of the cores $\kappa_{250\,{\rm GHz}} = 0.0066$ cm^2 g^{-1} as the average value between dust grains with thin and thick ice mantles for a volume density of $\sim 10^5$ cm^{-3} (Ossenkopf & Henning 1994) with an uncertainty of about a factor of two. As a final step, we used the relationship $A_{\rm v} = 1.258\times10^{-21} N_{\rm H_2}$ (Wagenblast & Hartquist 1989) to transform the column density to visual extinction. The resulting maps of the difference between the extinction maps derived from near-IR and mm data are shown on the right-hand side panels of Figure 5. For core 40, we found an excess of extinction that could be due to the filtered diffuse emission (see Section 3.1). However, in such a case, one would expect this excess to be present over the whole map. For cores 14 and 48, we found a good agreement between both tracers. On the other hand, at denser regions such as the center of core 109 ($n_{\rm H_2} > 4\times10^5$ cm^{-3}), the $A_{\rm v}$ derived from the 1.2 mm dust is significantly larger, $\gtrsim$10 mag, than that derived from the near-IR. This is the core with the highest column density ($\sim 4.8\times10^{22}$ cm^{-2}); therefore, this suggests that near-IR extinction maps constructed from 2MASS catalogs do not have enough sensitivity or sampling scale to resolve the centers of very dense cores. In such dense regions, the number of 2MASS catalog background stars is not high enough to provide neither a large number of sources per pixel, nor a large number of high extinction measurements; thus, the high-extinction regions might be poorly resolved and underestimated. These biases may explain, combined with the larger radius, the lower densities reported by Rathborne et al. (2008). Extensive observations toward the Perseus cloud in visual extinction and in radio continuum provide similar results (Kirk et al. 2006). Extinction maps with higher resolution, made with deeper observations, are able to resolve better the high-extinction levels. For example, Kandori et al. (2005) observed core 109 (named FeSt 1-457) in $A_{\rm v}$ deeper with a resolution of ∼30″, and found a morphology in perfect agreement with our continuum observations. Their $A_{\rm v}$ intensity peak at the core center of $A_{\rm v}$∼41.0 (the largest in their sample) is very close to our derivation, $A_{\rm v}\sim 39.2$, for a 30″ beam.

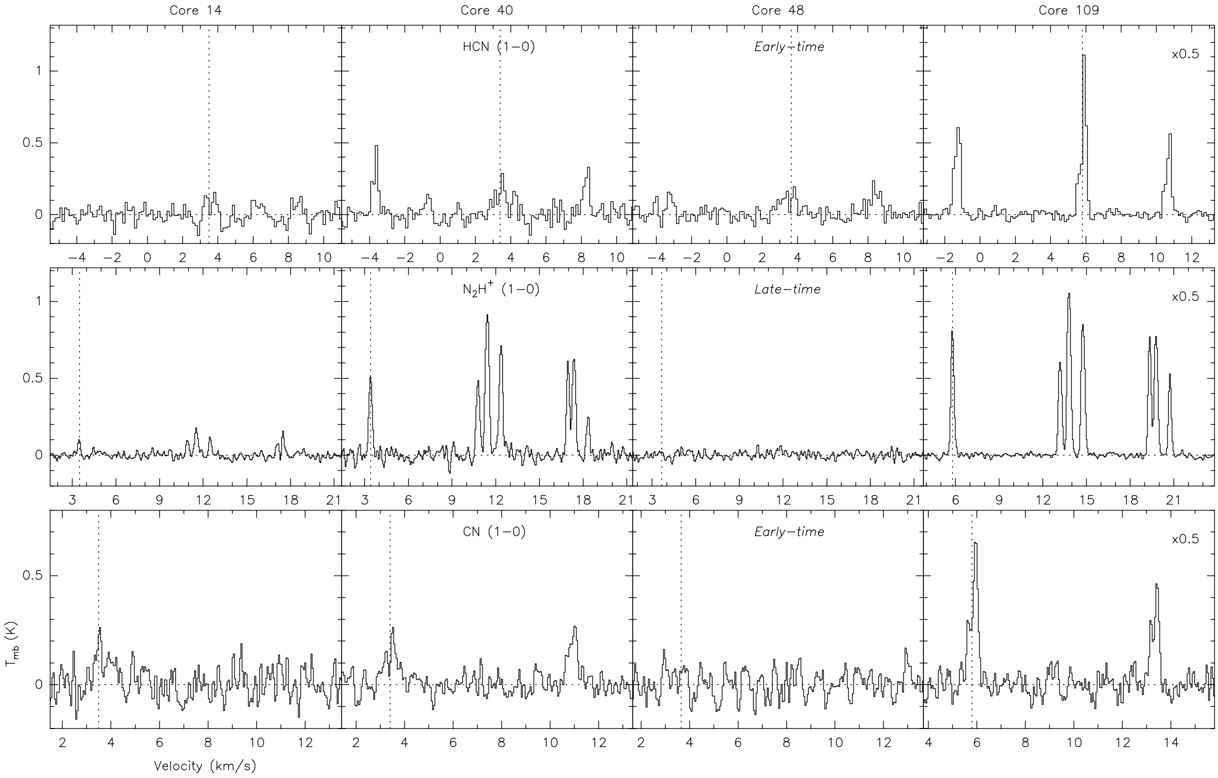

Figure 4. IRAM 30 m line spectra of the molecular transitions with hyperfine components toward the four selected cores of the Pipe Nebula (see Table 1). The name of the core is indicated above the top panel of each column. Rows correspond to a single molecular transition specified on the second column. The velocity range is 16.5, 20, and 12 km s^{-1} for HCN (1–0), N$_2$H$^+$ (1–0), and CN (1–0), respectively. The v_{LSR} of each core is marked with a vertical dotted line. The vertical axis shows the T_{MB} of the emission and the zero level is marked by a horizontal dotted line. Core 109 spectra, with the highest measured T_{MB}, have been divided by 2 to fit to the common scale.

Summarizing, our dust continuum maps seem to be better at tracing the highextinction regions of the prestellar cores, at least at this spacial resolution. These results suggest that the dust continuum emission would trace the dense and cold cores better than the 2MASS derived visual extinction. On the other hand, the visual extinction would be more sensitive to the cloud diffuse extended emission.

4.2. Discussion on the Individual Cores

4.2.1. Core 14

Core 14, located in B59, is a compact and dense core but the less massive in our sample. It is the only core that belongs to a clumpy and filamentary structure, which is elongated along the NE–SW direction with an extent of ∼500″ (∼0.35 pc, see Figure 2), with a morphology quite similar to that shown in A_v maps (Rathborne et al. 2008; Román-Zúñiga et al. 2009). The location of core 14 inside an elongated and clumpy filament suggests that probably it is still undergoing fragmentation, which could lead to the formation of smaller cores. In fact, it is resolved in several small clumps which have sizes comparable to the sizes of the other cores in the Pipe, with radii of about ∼0.04 pc.

Core 14 shows emission in all the early-time molecules at 3 mm. CS (2–1) and C^{34}S (2–1) are clearly detected (see Figure 3), and the abundances are the largest of the sample (see Table 8). On the other hand, C$_3$H$_2$ ($2_{1,2}$–$1_{1,0}$) and N$_2$H$^+$ (1–0) show weak emission and, consequently, low abundances. Rathborne et al. (2008) detected weak NH$_3$ emission in good agreement with our N$_2$H$^+$ measurements. Only the main component of the CN (1–0) transitions is clearly detected. These are signatures of an object very young chemically.

4.2.2. Core 40

Core 40, located in the *stem*, is another core with irregular morphology. This core shows emission in all the transitions at 3 mm, of both early- and late-time molecules, and in the late-time N$_2$H$^+$ transition at 3 mm. The molecular emission of core 40 is strong, and only the emission of core 109 is more intense, except for CS, which shows the same T_{MB} for both cores. These cores are the only ones that show strong late-time molecule emission. Core 40 presents the highest CN and N$_2$H$^+$ abundances (see Table 8). Regarding N$_2$H$^+$, the intense emission with all the hyperfine components detected is in perfect agreement with previous results of NH$_3$ (Rathborne et al. 2008). The HCN emission for core 40 is quite anomalous, because the main hyperfine component is weaker than the satellite components (see Figure 4). This suggests that the emission is not in LTE. González-Alfonso & Cernicharo (1993) investigated with Monte Carlo techniques the variation in HCN (1–0) profiles. According to their work, an infalling cloud with a dense central core (see Figure 2) surrounded by a large diffuse envelope (Lombardi et al. 2006) may produce an HCN (1–0) spectrum as the observed toward Core 40.

Table 6
Line Parameters[a]

Molecular Transition	Source	T_{MB}[b] (K)	$A \times \tau$[c] (K)	$\int T_{MB} dv$[b] (K km s^{-1})	v_{LSR} (km s^{-1})	Δv_{LSR} (km s^{-1})	τ[d]	Profile[e]
C_3H_2 ($2_{1,2}$–$1_{1,0}$)	Core 14	0.37(6)	...	0.086(11)	3.502(14)	0.22(3)	...	G
	Core 40	1.19(5)	...	0.347(9)	3.420(4)	0.273(9)	...	G
	Core 109	2.74(6)	...	0.799(13)	5.8340(20)	0.274(5)	...	G
CS (2–1)	Core 14	0.69(10)	...	0.41(3)	3.439(21)	0.45(4)	10.8(1.1)	SA
	Core 40	1.94(7)	...	0.560(17)	3.369(4)	0.415(14)	3.1(3)	NS
	Core 48	0.79(7)	...	0.402(18)	3.684(11)	0.477(22)	6.0(6)	SA
	Core 109	1.93(8)	...	0.743(17)	5.836(4)	0.361(9)	4.2(4)	G
$C^{34}S$ (2–1)	Core 14	0.267(25)	...	0.068(5)	3.545(8)	0.241(20)	0.5(1)	G
	Core 40	0.268(16)	...	0.069(3)	3.381(5)	0.241(13)	0.14(1)	G
	Core 48	0.187(23)	...	0.041(4)	3.729(11)	0.20(3)	0.26(3)	G
	Core 109	0.34(3)	...	0.083(5)	5.825(7)	0.233(17)	0.19(2)	G
N_2D^+ (2–1)[f]	Core 40	0.084(20)	...	0.019(3)	3.280(15)	0.21(3)	...	G
	Core 109	0.31(4)	...	0.109(7)	5.673(11)	0.331(22)	...	G
DCO^+ (3–2)	Core 109	0.70(11)	...	0.151(18)	5.828(13)	0.202(21)	...	G
HCN (1–0)	Core 40	...	1.55(11)	...	3.410(16)	0.334(22)	6.0(5)	NS
	Core 48	...	0.33(10)	...	3.54(5)	0.90(11)	2.4(1.2)	G
	Core 109 (1)	...	2.53(3)	...	5.93(7)	0.16(22)	0.25(10)	NS
	Core 109 (2)	...	6.10(3)	...	5.72(7)	0.25(22)	10.20(10)	NS
N_2H^+ (1–0)	Core 14	...	0.0341(16)	...	11.500(5)	0.206(10)	0.10(9)	G
	Core 40	...	0.219(12)	...	11.4000(19)	0.249(5)	0.171(25)	G
	Core 109	...	0.904(14)	...	13.8000(5)	0.2150(11)	0.467(11)	G
CN (1–0)	Core 14	...	0.051(9)	...	3.64(8)	0.81(15)	0.1(7)	G
	Core 40	...	0.65(22)	...	3.430(21)	0.36(5)	3.9(1.3)	G
	Core 109 (1)	...	1.41(22)	...	5.930(5)	0.162(11)	1.13(23)	G
	Core 109 (2)	...	2.3(1.3)	...	5.670(7)	0.101(16)	4.(3)	G

Notes.
[a] Line parameters of the detected lines. The former five molecular transitions have no hyperfine components (see note f). The parameters for the transitions labeled as G (see the last column) have been derived from a Gaussian fit, while line parameters of NS and SA profiles have been derived from the intensity peak (T_{MB}), and zero (integrated intensity), first (line velocity), and second (line width) order moments of the emission. The latter three molecular transitions have hyperfine components. The parameters have been derived using the hyperfine component fitting method of the CLASS package. The value in parenthesis shows the uncertainty of the last digit/s. If the two first significative digits of the error are smaller than 25, two digits are given to better constrain it.
[b] Only for molecular transitions with no hyperfine components.
[c] Only for molecular transitions with hyperfine components.
[d] Derived from a CLASS hyperfine fit for molecular transitions with hyperfine components. Numerically derived for CS and $C^{34}S$ using Equation (1). A value of 0.3 is assumed when no measurement is available.
[e] G: Gaussian profile; NS: non-symmetric profile; SA: self-absorption profile.
[f] Only the main component is detected.

Table 7
Molecular Column Densities of the Chemical Species Observed Toward the Pipe Nebula Cores in cm^{-2}

Source	C_3H_2[a]	CS	$C^{34}S$	CN	HCN	N_2H^+	N_2D^+[a]	DCO^+[a]
Core 14	3.84×10^{11}	3.07×10^{13}	6.19×10^{11}	1.16×10^{12}	$< 5.42 \times 10^{10}$	9.70×10^{10}	$< 8.09 \times 10^{09}$	$< 5.13 \times 10^{11}$
Core 40	1.65×10^{12}	7.11×10^{12}	2.94×10^{11}	4.70×10^{12}	2.57×10^{12}	4.89×10^{11}	2.17×10^{09}	$< 4.93 \times 10^{10}$
Core 48	$< 7.93 \times 10^{10}$	1.53×10^{13}	2.94×10^{11}	$< 1.64 \times 10^{11}$	2.59×10^{12}	$< 3.79 \times 10^{10}$	$< 6.88 \times 10^{09}$	$< 7.82 \times 10^{10}$
Core 109	6.36×10^{12}	1.25×10^{13}	3.68×10^{11}	2.76×10^{12}	9.80×10^{12}	6.79×10^{11}	2.72×10^{10}	1.41×10^{11}

Note. [a] Transition with no opacity measurements available, thus optically thin emission is assumed to obtain lower limits of the column densities.

Table 8
Abundances of the Chemical Species with Respect to H_2 Observed Toward the Pipe Nebula Cores[a]

Source	C_3H_2[b]	CS	$C^{34}S$	CN	HCN	N_2H^+	N_2D^+[b]	DCO^+[b]
Core 14	3.45×10^{-11}	2.77×10^{-09}	5.58×10^{-11}	9.58×10^{-11}	$< 4.88 \times 10^{-12}$	8.73×10^{-12}	$< 5.84 \times 10^{-13}$	$< 2.93 \times 10^{-11}$
Core 40	1.55×10^{-10}	6.64×10^{-10}	2.75×10^{-11}	4.19×10^{-10}	2.41×10^{-10}	4.58×10^{-11}	1.69×10^{-13}	$< 3.73 \times 10^{-12}$
Core 48	$< 1.13 \times 10^{-11}$	2.19×10^{-09}	4.21×10^{-11}	$< 2.22 \times 10^{-11}$	3.71×10^{-10}	$< 5.43 \times 10^{-12}$	$< 7.75 \times 10^{-13}$	$< 7.17 \times 10^{-12}$
Core 109	2.06×10^{-10}	4.06×10^{-10}	1.19×10^{-11}	8.54×10^{-11}	3.18×10^{-10}	2.20×10^{-11}	7.30×10^{-13}	3.37×10^{-12}

Notes.
[a] See Tables 4 and 7 for dust and line column densities.
[b] Transition with no opacity measurements available, thus optically thin emission is assumed to estimate a lower limit of the column densities and, consequently, of the abundances.

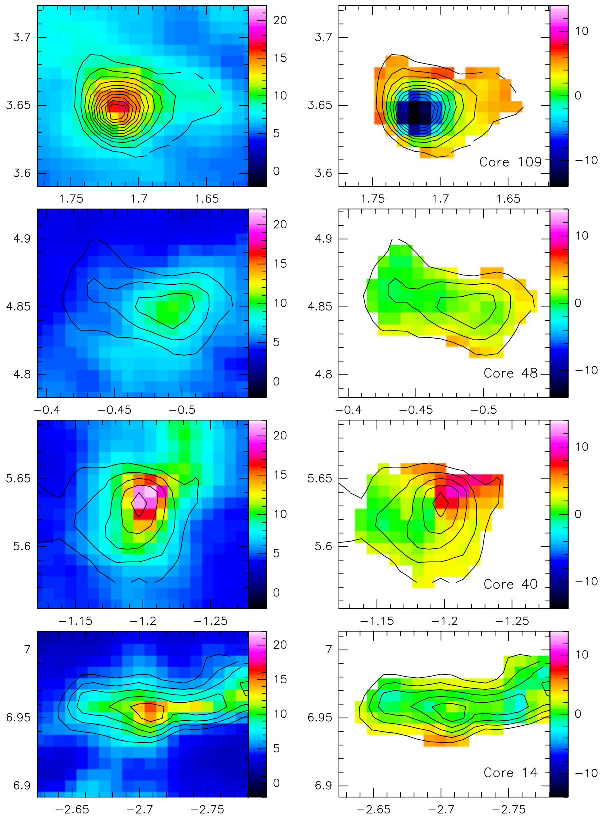

Figure 5. Left panels: color image of the visual extinction map derived from the near-IR observations (Lombardi et al. 2006) superposed with the contour map of the extinction map derived from our 1.2 mm dust continuum maps in galactic coordinates (see Section 4.1). Contours are from 2.5 to 30 visual magnitudes by steps of 2.5. Right panels: color image of the difference between the visual extinction map derived from the near-IR and the 1.2 mm observations within the region of the A_v converted dust continuum maps with $A_v > 2.5$ mag. Contours are the same as in the left panels. The core number is indicated in the lower right corner of the panels. The color scale (in visual magnitudes) is shown on the right-hand side of the panels.

(A color version of this figure is available in the online journal.)

4.2.3. *Core 48*

Core 48, located in the *stem*, has a quite elongated morphology. It is embedded in an environment with high polarization angle dispersion (Alves et al. 2008), which is the exception of this polarimetrically defined region. It is very diffuse, this is the largest and the less dense core in the sample. It shows emission only in three early-time molecules: CS (2–1), $C^{34}S$ (2–1), and, marginally HCN (1–0). The abundances of CS and $C^{34}S$ are among the largest in the sample, slightly lower than those for core 14. The N_2H^+ molecule was undetected, in agreement with previous measurements of NH_3 (Rathborne et al. 2008).

4.2.4. *Core 109*

Core 109, located in the *bowl*, is the most circular and compact core in the sample. The dust continuum emission of this core is similar to that of the other cores. However, it is the densest one in our sample and the most massive ($\sim 4\ M_\odot$). Kandori et al. (2005) find, through a Bonnor–Ebert profile fit, that Core 109 is gravitationally unstable. Aguti et al. (2007) find, through observations of molecular transitions, that this core (designated also as FeSt 1-457) is gravitationally bound. Kandori et al. (2005) suggest other models, apart from a Bonnor–Ebert sphere, including extra supporting mechanisms that might fit the density profile. Aguti et al. (2007) propose that core 109 is pulsating, based on expansion motions of the outer layers. However, their Jeans mass measurement is compatible with the mass of the core and they propose a quasi-stable state near hydrodynamic equilibrium. This core is embedded in a magnetized medium (see Section 4.4); thus, magnetic support could be a plausible source of external support.

This core shows emission of all the detected early- (C_3H_2, HCN, CS, $C^{34}S$, and CN) and late-time molecules (N_2H^+, N_2D^+, and DCO^+). The molecular emission of this core is always the strongest. Core 109 shows a very strong N_2H^+ emission, in agreement with the NH_3 measurements by Rathborne et al. (2008). As seen in Table 8, core 109 has similar abundances for early-time molecules to those of the other cores. Interestingly, the CS and $C^{34}S$ abundances are the lowest in our sample, which suggests CS depletion toward the center (detected on $C^{18}O$; Aguti et al. 2007).

4.3. *Qualitative Chemistry Analysis*

Table 4 shows a variation of about a factor of ∼4 around 10^{22} cm^{-2} of the average H_2 column densities derived for each of the cores with a 27″ beam, the one used to calculate the abundances for the molecular transitions at 3 mm. This represents, using the relationship $A_V = 6.289 \times 10^{-22} N_H$ (Wagenblast & Hartquist 1989), average values of $A_V \sim 4.4$ to ∼19.4. The first case would represent a shallow core, more affected by the external radiation field, which tends to have a younger chemistry. The other extreme probably indicates a denser and more shielded core, where one would expect to find more complex and evolved molecules. However, note that this also depends on the timescale needed to form the core (Tafalla et al. 2004; Crapsi et al. 2005).

We find that CS (see Table 8), an early-time molecule, is detected in all the cores with abundances with respect to H_2 of a few times 10^{-10}, similar to the ones found in other dense cores (Irvine et al. 1987) or the ones obtained in gas–phase chemical models (Taylor et al. 1998; Garrod et al. 2004). It is worth mentioning that cores 14 and 48 show high CS abundance, one order of magnitude higher than cores 109 and 40. A similar result is found for the $C^{34}S$ abundances. The derived abundances for the early-time molecule HCN toward the cores in our sample are very uniform, and seem to be independent of their physical properties. The early-time molecule CN, a molecule that is also commonly detected in dense cores, also has a significantly lower abundance (a factor $\gtrsim 4$) in core 48 than toward the rest of the sample. Where detected, the CN abundance varies only within a factor of five. On the other hand, another early-time molecule such as C_3H_2 shows differences in abundances of at least a factor of five among cores 14 and 48 with respect to cores 40 and 109. Late-time molecules, such as N_2H^+ or deuterated molecules, are not broadly detected in our sample: N_2H^+ is detected except in core 48. In contrast, N_2D^+ is only detected on cores 40 and 109, and DCO^+ only in core 109. We found a higher abundance of N_2H^+ toward core 40 than toward core 109 by a factor of ∼2, while Rathborne et al. (2008) found an abundance of NH_3 toward core 109 higher than that of core 40 by a factor of ∼3.4. However, both cores 40 and 109 show higher abundances in N_2H^+ than cores 14 and 48. Despite cores 14 and 40 having a similar average column density, the former shows five times less abundance of N_2H^+ than the latter. Moreover, core 14 does

Table 9
Pipe Nebula Core General Properties with Respect to Core 109

Source	Diameter (pc)	Mass ($M_\odot$)	$N_{\mathrm{H_2}}$ (10^{21} cm^{-2})	$n_{\mathrm{H_2}}$ (10^4 cm^{-3})	$p_\%$[a] (%)	δP.A.[a] (^{o})	X(N$_2$H$^+$) (10^{-11})	X(CN) (10^{-11})	X(C$_3$H$_2$) (10^{-11})	X(CS) (10^{-11})
Core 109	0.063	4.00	47.60	36.57	11.0	3.9	2.20	8.54	20.6	40.6
Relative Values										
Core 109	10.0	10.0	10.0	10.0	10.0	10.0	10.0	10.0	10.0	10.0
Core 40	16.5	6.3	2.3	1.4	4.2	22.2	20.8	49.1	7.5	16.4
Core 14	11.3	3.5	2.8	2.5	1.8	40.4	4.0	11.2	1.7	68.2
Core 48	20.2	5.2	1.3	0.6	1.8	83.8	<2.5	<2.6	<0.6	53.9

Note. [a] Franco et al. (2010).

not show emission in any other late-time molecule, while core 40 is detected in N$_2$D$^+$ showing an abundance only a factor of four lower than that of core 109. Briefly, the higher abundances in cores 109 and 40 with respect to core 14 and in particular to core 48 (except for CS) are an indication that cores 109 and 40 are more chemically evolved than cores 14 and 48. However, the molecular abundances of these two late-time species are roughly an order of magnitude lower than the prototypical starless cores L1517B and L1498 (Tafalla et al. 2006), which suggests that cores 109 and 40 may be in an earlier evolutionary stage than cores in Taurus.

Rathborne et al. (2008) observed the emission of the NH$_3$ (1, 1), NH$_3$ (2, 2), CCS (2$_1$–1$_0$), and HC$_5$N (9–8) transitions toward 46 cores of the Pipe Nebula. Cores 14, 40, 48, and 109 were included in their observations. None of the lines were detected in core 48, which is shown to be again the more chemically poor core of our sample. HC$_5$N was not detected in core 14, which also has the weakest CCS and NH$_3$ lines. The four transitions were detected in cores 40 and 109, but with some differences. The NH$_3$ lines are much more intense in core 109, a factor of $\sim$4 for the (1,1) transition and $\sim$9 for the (2,2) line, while the CCS line is more intense in core 40, less than a factor of $\sim$2, and the HC$_5$N lines are very similar in both cores, inside the rms. All these results are consistent with our observations: core 48, which did not show emission of late-time molecules, is very poor chemically and shows a very young chemistry. Core 14 has some very weak emission of late-time molecules (NH$_3$) but only weak emission of CCS, an early-time molecule. Core 40 is more evolved chemically and shows stronger emission of early-time molecules than of late-time molecules. Finally, core 109 is the one showing more diversity of molecules and the more intense emission, in particular, of late-time molecules. Interestingly, the CCS abundance in core 109 is probably lower than in core 40, which is consistent with the view that the CCS molecule is destroyed soon after the formation of a dense core, probably as a result of the contraction of the core (de Gregorio-Monsalvo et al. 2006; Millar & Herbst 1990; Suzuki et al. 1992). This would reinforce the view that this core is in a very advanced evolutionary state.

In summary, core 109 seems to be the more chemically evolved core, probably because it is more dense and because it shows higher abundances of late-time molecules. Core 40, with three times lower column density, also shows large N$_2$H$^+$ abundances. It might be in an intermediate chemical evolutionary stage. These two cores probably are in an evolutionary stage slightly younger than that of the prototypical starless cores (Tafalla et al. 2004; Crapsi et al. 2005). Cores 48 and 14 show similar physical properties in terms of size, mass, and H$_2$ column density, to cores 109 and 40. However, they appear to be very chemically poor and, therefore, they could be in an even younger stage of chemical evolution.

4.4. Evolutionary Trend and Correlation with the Diffuse Gas

Table 9 shows the summary of the main properties of the cores relative to core 109, which is the one that shows the strongest line emission. In this table, we show the physical and chemical properties. Additionally, we added the averaged polarimetric properties of the diffuse envelope around the cores (Alves et al. 2008; Franco et al. 2010): polarization fraction ($p_\%$) and dispersion of the polarization position angle (δP.A.).

As shown in Figure 2, the polarization vectors calculated from optical extinction cannot be derived at the more dense regions, where the visual extinction is higher. In Figure 2, except for the map of core 48 with the lowest rms, the polarization vectors lie in regions below the 3σ noise level. However, the trend of the polarization vectors is in general rather uniform over the whole map. Indeed, there are vectors up to very close to the dense parts of the cores. Consequently, the derived magnetic field properties of the diffuse surrounding medium are also representatives of those of the dense part of the cores.

A relationship between the magnetic and the chemical properties of each core seems to exist. The two more chemically evolved cores, 109 and 40, appear to be embedded in a strongly magnetized environment, as δP.A. values clearly reflect (see Table 9). The other two cores, 14 and 48, do not show very different morphological properties with respect to the previous two (size and mass). However, their chemical properties are completely opposed, and they are likely younger cores in chemical timescale. Interestingly, the magnetic properties of cores 14 and 48 are also opposed to those of cores 40 and 109. Cores 14 and 48 are surrounded by a molecular diffuse medium that is much more turbulent than that surrounding the two previous ones. Core 14 is possibly affected by the star formation undergoing in the nearby region B59. Core 48 appears to be dominated by turbulence and constitutes an exception in the *stem*, whose cores have uniform magnetic properties among them, showing low $p_\%$ and high δP.A. (Franco et al. 2010).

In summary, these four cores of the Pipe Nebula have similar masses and sizes, but they are in different stages of chemical evolution: cores 109 and 40 are much more evolved chemically than cores 48 and 14. The different magnetic properties of the diffuse molecular environment suggest that cores 109 and 40 have grown in a more quiescent and slow way (probably through ambipolar diffusion), whereas the growth of cores 14 and 48 has occurred much faster, an indication that possibly a compression wave that generates turbulence or the turbulence itself (Falle & Hartquist 2002; Ballesteros-Paredes et al. 2007). The longer timescale of the ambipolar diffusion process could explain the more evolved chemistry found toward the cores surrounded by a magnetized medium. These features suggest two different formation scenarios depending on the balance between turbulent and magnetic energy in the surrounding environment. The importance of these results is worth of a more detailed study of the Pipe Nebula cores in order to fully confirm these trends.

5. SUMMARY AND CONCLUSIONS

We carried out observations of continuum and line emission toward four starless cores of the Pipe Nebula spread out along the whole cloud selected in base of their magnetic properties (Alves et al. 2008; Franco et al. 2010). We studied their physical and chemical properties, and the correlation with the magnetic field properties of the surrounding diffuse gas.

1. The dust continuum emission of the observed Pipe Nebula cores shows quite different morphologies. In the sample, there are diffuse cores, such as cores 40 and 48, and compact and dense cores, such as core 109. We have also mapped a clumpy filament, which contains the embedded core 14. This filament is possibly undergoing fragmentation into smaller cores of sizes comparable to that of the others. We derived average radii of ∼0.09 pc (∼18,600 AU), densities of $\sim 1.3 \times 10^5$ cm^{-3}, and core masses of $\sim 2.5\ M_\odot$.
2. The dust continuum peak coincides within the errors with A_v peak derived from the 2MASS catalog. The continuum emission is more sensitive toward the dense regions, up to $\gtrsim 10$ magnitudes for the densest cores. On the other hand, the diffuse emission is better traced by the extinction maps. The masses are in average ∼3.4 times smaller.
3. We have observed several early- and late-time lines of molecular emission toward the cores and derived their column densities and abundances. The starless cores of the Pipe Nebula are all very young, but they present different chemical properties possibly related to a different evolutionary stage. However, there does not seem to be a clear correlation between the chemical evolutionary stage of the cores and their position in the cloud. Cores 109 and 40 show late-time molecular emission and seem to be more chemically evolved. Core 109 shows high abundances of late-time molecules and it seems to be the more chemically evolved. Core 40 has three times lower H_2 column density than that of core 109. It presents a large N_2H^+ abundance and the largest CN abundance, thus, it might be in an intermediate chemical evolutionary stage. Cores 48 and 14 show only early-time molecular emission, and core 14 presents weak N_2H^+ emission, and seem to be chemically younger than the other two cores. Core 14 has a similar mass and size as core 40, but the N_2H^+, C_3H_2, and CS abundances are about one order of magnitude lower than the core 40 abundances. Our results and interpretation of the evolutionary stage of each core are consistent with the previous observations of Rathborne et al. (2008) in these same cores.
4. There seems to be a relationship between the properties of the magnetic field in the cloud medium of the cores and the chemical evolutionary stage of the cores themselves. The two more chemically evolved cores, 109 and 40, appear to be embedded in a strongly magnetized environment, with a turbulent to magnetic energy ratio of 0.05 and 0.27, respectively. The two chemically younger cores, 14 and 48, appear to be embedded in a more turbulent medium. This suggests that the magnetized cores probably grow in a more quiescent way, probably through ambipolar diffusion, in a timescale large enough to develop the richer chemistry found. On the other hand, the less magnetized cores likely grow much faster, probably in a turbulence dominated process, in a timescale too short to develop late-time chemistry.
5. The Pipe Nebula has revealed to be an excellent laboratory for the study of the very early stages of the star formation. The studied cores show different morphologies, chemical evolutionary stages, and magnetic properties. The physical and chemical properties are not directly linked as the competition between the magnetic field, and turbulence at small scales seems to have an important influence in the core evolution. The importance of these results requires a more detailed study of the chemistry and magnetic field properties of the cores to fully confirm these results.

P.F. is supported by MICINN fellowship FPU (Spain). P.F., J.M.G., M.T.B., J.M.M., F.O.A., G.B., A.S.M., and R.E. are supported by MICINN grant AYA2008-06189-C03 (Spain). P.F., J.M.G., M.T.B., O.M., F.O.A., and R.E. are also supported by AGAUR grant 2009SGR1172 (Catalonia). G.A.P.F. is partially supported by CNPQ (Brazil). The authors acknowledge the entire IRAM 30 m staff for their hospitality during the observing runs, the operators and AoDs for their active support, Guillermo Quintana-Lacaci for his help during the observing and reduction process of the bolometer data, and Jens Kauffmann for helping on the implementation of his MAMBO-II new reduction scheme.

APPENDIX A

CALCULATION OF COLUMN DENSITY AND MASS OF DUST EMISSION

A.1. Radiative Transfer Equation and Planck Function

The intensity emitted by an assumed homogeneous medium of temperature $T_{\rm ex}$ and optical depth τ_ν at frequency ν is given by

$$I_\nu = B_\nu(T_{\rm ex})(1 - e^{-\tau_\nu}), \tag{A1}$$

where B_ν is the Planck function,

$$B_\nu = \frac{2h\nu^3}{c^2} \frac{1}{e^{h\nu/kT} - 1}. \tag{A2}$$

Here c is the speed of light, k is the Boltzmann's constant, and h is the Planck's constant. The Rayleigh–Jeans limit, $h\nu \ll kT$ (in practical units $[\nu/\mathrm{GHz}] \ll 20.8\,[T/\mathrm{K}]$), does not hold for MAMBO-II observations (250 GHz) of prestellar cores ($T \simeq 10$ K), preventing the use of this limit simplification.

A.2. Telescope Measurements

The beam solid angle is $\Omega_A = \int_{\rm beam} P d\Omega$, where P is the normalized power pattern of the telescope. Assuming that the telescope has a Gaussian beam profile, P reads $P(\theta) = \exp(-4 \ln 2\theta^2/\theta^2_{\rm HPBW})$, where θ is the angular distance from the beam center. The beam solid angle is

$$\Omega_A = \frac{\pi}{4 \ln(2)} \theta^2_{\rm HPBW}. \tag{A3}$$

For discrete sources, we measure flux densities, S_ν, instead of intensities, I_ν. These two quantities are related by

$$S_\nu = \int_{\rm source} I_\nu\, P\, d\Omega. \tag{A4}$$

This integration for a beam area, S_ν^{beam}, allows us to calculate the beam-averaged intensity as

$$\langle I_\nu \rangle = \frac{S_\nu^{\text{beam}}}{\Omega_A}. \tag{A5}$$

A.3. *From Flux to Column Density and Mass*

One can calculate the opacity of the emission measured inside a beam, τ_ν^{beam}, from Equations (A1) and (A5), relating it to the measured flux by

$$\tau_\nu^{\text{beam}} = -\ln\left(1 - \frac{S_\nu^{\text{beam}}}{\Omega_A\, B_\nu(T)}\right). \tag{A6}$$

On the other hand, the optical depth is defined as

$$\tau_\nu \equiv \int_{\text{line of sight}} \kappa_\nu\, \rho\, ds, \tag{A7}$$

where κ_ν is the absorption coefficient per unit density.

One can relate the column density to the optical depth and, thus, to the measured flux using

$$N_{\mathrm{H}_2} = \int n_{\mathrm{H}_2}\, ds = \int \frac{\rho}{\mu\, m_{\mathrm{H}}} ds = \frac{\tau_\nu}{\mu\, m_{\mathrm{H}}\, \kappa_\nu}, \tag{A8}$$

which particularized to a beam is $N_{\mathrm{H}_2}^{\text{beam}} = \frac{\tau_\nu^{\text{beam}}}{\mu\, m_{\mathrm{H}}\, \kappa_\nu}$, where m_{H} is the hydrogen mass and μ is the mean molecular mass per hydrogen atom. In the case of optically thin emission, the intensity is proportional to the column density as Equation (A1) can be simplified to $I_\nu \approx B_\nu(T)\tau_\nu$.

Then, the mass can be calculated as

$$M = \mu\, m_{\mathrm{H}}\, D^2 \int N_{\mathrm{H}_2}\, d\Omega, \tag{A9}$$

which for a beam is $M^{\text{beam}} = \mu\, m_{\mathrm{H}}\, D^2\, N_{\mathrm{H}_2}^{\text{beam}}\, \Omega_A$, where D is the distance to the source. All these calculations can be applied to any solid angle bigger than a beam.

APPENDIX B

CALCULATION OF COLUMN DENSITY OF LINE EMISSION

The column density for a $J \rightarrow J-1$ transition of a molecule (“Mol”) is

$$\begin{aligned} N_{\text{Mol}} = & \frac{3\,k}{8\pi^3} \frac{Q_{\text{rot}}}{g_K\, g_I} \frac{e^{Eu/T_{\text{ex}}}}{\nu} \frac{1}{S_{JkI}\, \mu^2} \\ & \times \frac{J_\nu\,(T_{\text{ex}})}{J_\nu(T_{\text{ex}}) - J_\nu(T_{\text{bg}})} \frac{\tau}{1 - e^{-\tau}} \int_{\text{line}} T_{\text{MB}}\, d\text{v}, \end{aligned} \tag{B1}$$

which translates into useful units as

$$\begin{aligned} \left[\frac{N_{\text{Mol}}}{\text{cm}^{-2}}\right] = & \; 1.67 \times 10^{14}\, \frac{Q_{\text{rot}}}{g_K\, g_I} \left[\frac{S_{JkI}}{\text{erg}\,\text{cm}^3\,\text{statC}^{-2}\,\text{cm}^{-2}}\right]^{-1} \\ & \times \left[\frac{\mu}{\text{D}}\right]^{-2} e^{Eu/T_{\text{ex}}} \left[\frac{\nu}{\text{GHz}}\right]^{-1} \frac{J_\nu(T_{\text{ex}})}{J_\nu(T_{\text{ex}}) - J_\nu(T_{\text{bg}})} \\ & \times \frac{\tau}{1 - e^{-\tau}} \left[\frac{\int_{\text{line}} T_{\text{MB}}\, d\text{v}}{\text{K}\,\text{km}\,\text{s}^{-1}}\right]. \end{aligned} \tag{B2}$$

Here, J_ν is the energy in units of temperature, and it reads $J_\nu\,(T) = \frac{h\nu/k}{e^{h\nu/kT} - 1}$. See the next subsections for a detailed description of all of the terms involved.

B.1. *Observational Terms*

B.1.1. *Single Transitions*

In the case of single transitions, we have performed a Gaussian fit to the spectrum or a statistical moment calculation, both using tasks from the CLASS package. We obtain from either analysis the main beam temperature, T_{MB}, the line velocity, v, and the integrated emission, $\int T_{\text{MB}}\, dv$.

The opacity, τ, is calculated numerically in those molecules with more than one transition observed. In the other cases, we have assumed $\tau \sim 0.3$. The excitation temperature, T_{ex}, can be calculated from the radiative transfer equation as

$$T_{\text{ex}} = \frac{h\nu}{k}\left[\ln\left(\frac{h\nu/k}{\frac{T_{\text{MB}}}{1-e^{-\tau}} + J_\nu(T_{\text{bg}})} + 1\right)\right]^{-1}, \tag{B3}$$

where T_{bg} is the background temperature.

B.1.2. *Hyperfine Transitions*

In the case of hyperfine transitions, we take into account all of the hyperfine components of the selected transition. We have performed a hyperfine fit using CLASS, which provides $A \times \tau_m$, $v_{\text{LSR}}^{\text{reference line}}$, Δv , τ_m , where A is

$$A = f(J_\nu(T_{\text{ex}}) - J_\nu(T_{\text{bg}})), \tag{B4}$$

and f is the filling factor assumed to be $\sim$1.

To be able to use Equation (B2) as in the single transition case, we need T_{ex}, τ, and $\int T_{\text{MB}}\, dv$. We can calculate T_{ex} as in Equation (B3) calculating T_{MB} as $A \times \tau_m/\tau_m$, and τ_m is given by CLASS. For the integrated emission, we can use

$$\tau_0 \Delta v = \int_{\text{line}} \tau\, dv \simeq \frac{1}{J_\nu(T_{\text{ex}}) - J_\nu(T_{\text{bg}})} \frac{\tau_0}{1 - e^{-\tau_0}} \int_{\text{line}} T_{\text{MB}}(v) dv, \tag{B5}$$

leading to

$$\int_{\text{line}} T_{\text{MB}}(v)\, dv \simeq \tau_0\, \Delta v (J_\nu(T_{\text{ex}}) - J_\nu(T_{\text{bg}})) \frac{1 - e^{-\tau_0}}{\tau_0}. \tag{B6}$$

Making these transformations, Equation (B2) can be used for hyperfine transitions.

B.2. *Non-observational Terms*

B.2.1. *Partition Function (Q_{rot})*

The rotational partition function, $Q_{\text{rot}}(T)$, is defined as

$$Q_{\text{rot}}(T) \equiv \sum g_J\, g_k\, g_I\, e^{-hBJ(J+1)/kT}, \tag{B7}$$

where the g_X factors are the degeneration of the respective quantic number, in particular $g_J = 2J + 1$.

Equation (B7) can be approximated, in the limit of high temperatures, by an integral because generally the energy levels are close together. We are only interested in the high temperature limit because when the transition is activated, this limit is accurate enough.

1. *Linear molecules.* The solution for the diatomic case is general for any lineal molecule, so long as the molecular moment of inertia is computed properly for more than two atoms.

For lineal molecules $g_k = 1$, $g_I = 1$ and $g_J = (2J+1)/\sigma$. σ (the symmetry number) is 1 for heteronuclear diatomic (C–O) or asymmetric linear polyatomic (O–N–N) molecules, and 2 for homonuclear diatomic (H–H) or symmetric linear polyatomic (O–C–O) molecules.

The partition function at high temperatures can be calculated as

$$\begin{aligned} Q_{\rm rot} &\simeq \frac{1}{\sigma}\int_0^\infty (2J+1)e^{-hBJ(J+1)/kT}dJ \\ &\simeq \frac{1}{\sigma}\int_0^\infty e^{-(J^2+J)hB/kT}d(J^2+J)) \\ &\simeq \frac{1}{\sigma}\frac{kT}{hB}, \end{aligned} \tag{B8}$$

where B is the rotational constant available at the catalogs. A more accurate expression (Pickett et al. 1992) used in this work is

$$Q_{\rm rot} \approx \frac{1}{\sigma}\left(\frac{kT}{hB} + \frac{1}{3} + \frac{1}{15}\frac{\sigma hB}{kT} + \cdots\right). \tag{B9}$$

2. *Nonlinear molecules.* Nonlinear molecules have up to three moments of inertia and, thus, three rotational constants (A, B, C). In a similar way as before, but more complicated, the calculation of the rotational partition function at high temperatures is

$$Q_{\rm rot} \approx \frac{\sqrt{\pi}}{\sigma}\left(\frac{KT}{h}\right)^{3/2}\frac{1}{\sqrt{ABC}}. \tag{B10}$$

B.2.2. Upper Level Energy (E_u)

We can calculate the energy of the upper level (E_u) as a function of the lower level (E_l) plus the energy of the photon emitted (both available at catalogues). This is, in units of temperature and using the units given in the catalogs,

$$\left[\frac{E_u}{\rm K}\right] = 1.4388\left[\frac{E_l}{\rm cm^{-1}}\right] + 4.799 \times 10^{-5}\left[\frac{\nu}{\rm MHz}\right]. \tag{B11}$$

B.2.3. Intrinsic Line Strength Times Squared Dipolar Momentum ($S\mu^2$)

We can calculate the product of the *intrinsic* line strength, S_{JkI}, and the squared dipolar momentum, μ^2, from the $Q_{\rm rot}$ at 300 K ($Q_{\rm rot}^{300}$), the line strength (LogINT) at 300 K and the lower state energy (E_l). All of these parameters are available in the catalogs.

In a usable form,

$$\begin{aligned} \left[\frac{S\mu^2}{\rm erg\,cm^3\,statC^{-2}\,cm^{-2}\,D^{-2}}\right] &= 24,025 \times \left[\frac{10^{\rm logINT}}{\rm MHz\,nm^2}\right] \\ &\times Q_{\rm rot}^{300}\left[\frac{\nu}{\rm MHz}\right]^{-1}\left(\exp\left\{4.796\times10^{-3}\left[\frac{E_l}{\rm cm^{-1}}\right]\right\}\right) \\ &\times \left(1-\exp\left\{-1.6\times10^{-7}\left[\frac{\nu}{\rm MHz}\right]\right\}\right)^{-1}. \end{aligned} \tag{B12}$$

REFERENCES

Aguti, E. D., Lada, C. J., Bergin, E. A., Alves, J. F., & Birkinshaw, M. 2007, ApJ, 665, 457

Aikawa, Y., Ohashi, N., & Herbst, E. 2003, ApJ, 593, 906

Aikawa, Y., Wakelam, V., Garrod, R. T., & Herbst, E. 2008, ApJ, 674, 984

Alves, F. O., & Franco, G. A. P. 2007, A&A, 470, 597

Alves, F. O., Franco, G. A. P., & Girart, J. M. 2008, A&A, 486, L13

Ballesteros-Paredes, J., Klessen, R. S., Mac Low, M.-M., & Vazquez-Semadeni, E. 2007, in Protostars and Planets V, ed. B. Reipurth, D. Jewitt, & K. Keil (Tucson, AZ: Univ. of Arizona Press), 63

Bergin, E. A., Ciardi, D. R., Lada, C. J., Alves, J., & Lada, E. A. 2001, ApJ, 557, 209

Bergin, E. A., & Tafalla, M. 2007, ARA&A, 45, 339

Brooke, T., et al. 2007, ApJ, 655, 364

Caselli, P., Benson, P. J., Myers, P. C., & Tafalla, M. 2002, ApJ, 572, 238

Crapsi, A., Caselli, P., Walmsley, C. M., Myers, P. C., Tafalla, M., Lee, C. W., & Bourke, T. L. 2005, ApJ, 619, 379

de Gregorio-Monsalvo, I., Gómes, J. F., Suárez, O., Kuiper, T. B. H., Rodríguez, L. F., & Jiménez-Bailón, E. 2006, ApJ, 642, 319

Dutra, C. M., Santiago, B. X., & Bica, E. 2002, A&A, 381, 219

Falle, S. A. E. G., & Hartquist, T. W. 2002, MNRAS, 329, 195

Flower, D. R., Pineau Des Forêts, G., & Walmsley, C. M. 2006, A&A, 456, 215

Forbrich, J., Lada, C. J., Muench, A. A., Alves, J., & Lombardi, M. 2009, ApJ, 704, 292

Franco, G. A. P., Alves, F. O., & Girart, J. M. 2010, ApJ, 723, 146

Garrod, R. T., Williams, D. A., Hartquist, T. W., Rawlings, J. M. C., & Viti, S. 2004, MNRAS, 356, 654

González-Alfonso, E., & Cernicharo, J. 1993, A&A, 279, 506

Irvine, W. M., Goldsmith, P. F., & Hjalmarson, A. 1987, in Interstellar Processes, ed. D. J. Hollenbach & H. A. Thronson (Dordrecht: Reidel), 561

Kandori, R., et al. 2005, AJ, 130, 2166

Kauffmann, J., Bertoldi, F., Bourke, T. L., Evans, N. J., II., & Lee, C. W. 2008, A&A, 487, 993

Kim, K.-T., & Koo, B.-C. 2003, ApJ, 596, 362

Kirk, H., Johnstone, D., & Di Francesco, J. 2006, ApJ, 646, 1009

Kontinen, S., Harju, J., Heikkilä, A., & Haikala, L. K. 2000, A&A, 361, 704

Lada, C. J., Muench, A. A., Rathborne, J. M., Alves, J. F., & Lombardi, M. 2008, ApJ, 672, 410

Lombardi, M., Alves, J., & Lada, C. J. 2006, A&A, 454, 781

Millar, T., & Herbst, E. 1990, A&A, 231, 466

Morata, O., Girart, J. M., & Estalella, R. 2003, A&A, 397, 181

Morata, O., Girart, J. M., & Estalella, R. 2005, A&A, 435, 113

Muench, A. A., Lada, C. J., Rathborne, J. M., Alves, J. F., & Lombardi, M. 2007, ApJ, 671, 1820

Ohashi, N., Lee, S. W., Wilner, D. J., & Hayashi, M. 1999, ApJ, 518, L41

Onishi, T., et al. 1999, PASJ, 51, 871

Ossenkopf, V., & Henning, T. 1994, A&A, 291, 943

Pickett, H. M., Poynter, R. L., & Cohen, E. A. 1992, Submillimeter, millimeter, and microwave spectral line catalog, Tech. rep., Jet Propulsion Laboratory, 80–23 (Rev.3; Pasadena, CA: California Institute of Technology)

Rathborne, J. M., Lada, C. J., Muench, A. A., Alves, J. F., & Lombardi, M. 2008, ApJS, 174, 396

Román-Zúñiga, C., Lada, C. J., & Alves, J. F. 2009, ApJ, 704, 183

Suzuki, H., Yamamoto, S., Ohishi, M., Kaifu, N., Ishikawa, S., Hirahara, Y., & Takano, S. 1992, ApJ, 392, 551

Tafalla, M., Myers, P. C., Caselli, P., & Walmsley, C. M. 2004, A&A, 416, 191

Tafalla, M., Myers, P. C., Caselli, P., Walmsley, C. M., & Comito, C. 2002, ApJ, 569, 815

Tafalla, M., Santiago-García, J., Myers, P. C., Caselli, P., Walmsley, C. M., & Crapsi, A. 2006, A&A, 455, 577

Taylor, S. D., Morata, O., & Williams, D. A. 1998, A&A, 336, 309

Wagenblast, R., & Hartquist, T. W. 1989, MNRAS, 237, 1019

Preprint typeset using LaTeX style emulateapj v. 08/22/09

YOUNG STARLESS CORES EMBEDDED IN THE MAGNETICALLY DOMINATED PIPE NEBULA. II. EXTENDED DATASET *

P. F[1], J. M. G[1], M. T. B´[2], M. P[1], G. B[3], O. M[4],
J. M. M´[5], F. O. A[6], Á. S´-M[2], G. A. P. F[7], R. E[5]
[1] Institut de Ciències de l'Espai (CSIC-IEEC), Campus UAB, Facultat de Ciències, Torre C-5p, 08193 Bellaterra, Catalunya, Spain
[2] INAF-Osservatorio Astrofisico di Arcetri, Largo Enrico Fermi 5, 50125 Firenze, Italy
[3] INAF-Istituto di Astrofisica e Planetologia Spaziali, via Fosso del Cavaliere 100, 00133 Roma, Italy
[4] Institute of Astronomy and Astrophysics, Academia Sinica, P.O. Box 23-141, Taipei 10617, Taiwan
[5] Departament d'Astronomia i Meteorologia and Institut de Ciències del Cosmos (IEEC-UB),
Universitat de Barcelona, Martí i Franquès 1, 08028 Barcelona, Catalunya, Spain
[6] Argelander-Institut für Astronomie der Universität Bonn, Auf dem Hügel 71, 53121 Bonn, Germany and
[7] Departamento de Física - ICEx - UFMG, Caixa Postal 702, 30.123-970, Belo Horizonte, Brazil

(Dated: *Received 2012 May 9; accepted ; published)*

ABSTRACT

The Pipe nebula is a massive, nearby, filamentary dark molecular cloud with a low star-formation efficiency threaded by a uniform magnetic field perpendicular to its main axis. It harbors more than a hundred, mostly quiescent, very chemically young starless cores. The cloud is, therefore, a good laboratory to study the earliest stages of the star-formation process. We aim to investigate the primordial conditions and the relation among physical, chemical, and magnetic properties in the evolution of low-mass starless cores. We used the IRAM 30-m telescope to map the 1.2 mm dust continuum emission of five new starless cores, which are in good agreement with previous visual extinction maps. For the sample of nine cores, which includes the four cores studied in a previous work, we derived a A_V to N_{H_2} factor of $(1.27\pm0.12)\times10^{-21}$ mag cm^2 and a background visual extinction of ~6.7 mag possibly arising from the cloud material. We derived an average core diameter of ~0.08 pc, density of ~10^5 cm^{-3}, and mass of ~1.7 $M_\odot$. Several trends seem to exist related to increasing core density: (*i*) diameter seems to shrink, (*ii*) mass seems to increase, and (*iii*) chemistry tends to be richer. No correlation is found between the direction of the surrounding diffuse medium magnetic field and the projected orientation of the cores, suggesting that magnetic fields seem to play a secondary role in shaping the cores. We also used the IRAM 30-m telescope to extend the previous molecular survey at 1 and 3 mm of early- and late-time molecules toward the same five new Pipe nebula starless cores, and analyzed the normalized intensities of the detected molecular transitions. We confirmed the chemical differentiation toward the sample and increased the number of molecular transitions of the "diffuse" (e.g. the "ubiquitous" CO, C_2H, and CS), "oxo-sulfurated" (e.g. SO and CH_3OH), and "deuterated" (e.g. N_2H^+, CN, and HCN) starless core groups. The chemically defined core groups seem to be related to different evolutionary stages: "diffuse" cores present the cloud chemistry and are the less dense, while "deuterated" cores are the densest and present a chemistry typical of evolved dense cores. "Oxo-sulfurated" cores might be in a transitional stage exhibiting intermediate properties and a very characteristic chemistry.

Subject headings: ISM: individual objects: Pipe Nebula – ISM: lines and bands – ISM – stars: formation

1. INTRODUCTION

The Pipe nebula is a massive (10^4 $M_\odot$: Onishi et al. 1999) nearby (145 pc: Alves & Franco 2007) filamentary dark cloud located in the southern sky (Fig. 1). What differentiates the Pipe nebula from other low-mass star-forming regions such as Taurus and ρ-Ophiuchus is that it is very quiescent and has a very low star-formation efficiency, only the Barnard 59 (B59) region shows star formation (Forbrich et al. 2009; Brooke et al. 2007; Román-Zúñiga et al. 2009, 2012). The cloud harbors more than one hundred low-mass starless dense cores in a very early evolutionary stage (Muench et al. 2007; Rathborne et al. 2008). Thermal pressure appears to be the dominant source of internal pressure of these cores: most of them appear to be pressure confined, but gravitationally unbound (Lada et al. 2008). Through simulations of an unmagnetized cloud compatible to the Pipe nebula, Heitsch et al. (2009) predicted pressures lower than those required by Lada et al. (2008). This result suggests that an extra source of pressure, such as magnetic fields, is acting. In fact, Franco et al. (2010) found that most of the Pipe nebula is magnetically dominated and that turbulence appears to be sub-Alfvénic. Alves et al. (2008) have distinguished three regions in the cloud with differentiated polarization properties, proposed to be at different evolutionary stages (Fig. 1). B59, with low polarization degree ($p_{\%}$) and high polarization vector dispersion (δP.A.), is the only magnetically supercritical region and might be the most evolved, the *stem* would be at an earlier evolutionary stage, and finally, the *bowl*, with high $p_{\%}$ and low δP.A., would be at the earliest stage. The Pipe nebula is, hence, an excellent place to study the initial conditions of core formation which may eventually undergo star formation.

Frau et al. (2010, hereafter Paper I) presented the first results of a molecular line study at high spectral resolution for a sample of four cores distributed in the different regions of the Pipe nebula. The aim of the project was to chemically date the cores through an extensive molecular survey based in two main categories of molecules: early- and late-time (e.g., Taylor et al. 1998). In addition, we mapped the 1.2 mm dust continuum emission of the cores. We found no clear correla-

---

[*] Based on observations carried out with the IRAM 30-m telescope. IRAM is supported by INSU/CNRS (France), MPG (Germany), and IGN (Spain).

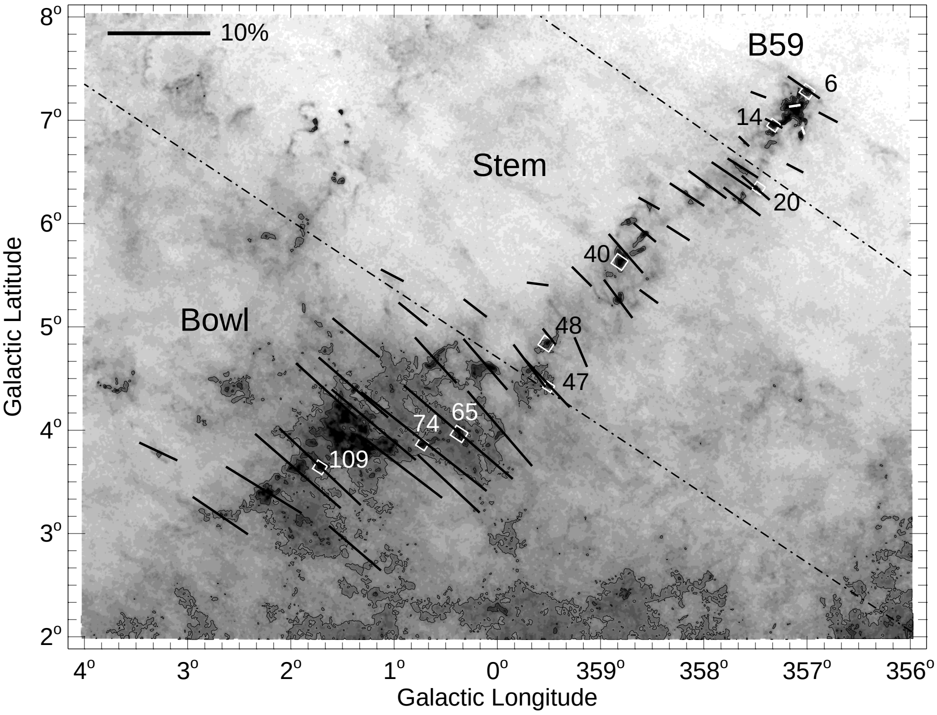

Figure 1. Position of the observed cores plotted over the 2MASS extinction map of the Pipe nebula (Lombardi et al. 2006). Black segments represent the mean polarization vector of the region (Alves et al. 2008) with the scale shown on the top left corner of the figure. White boxes depict the size of the 1.2 mm continuum maps (Section 2.1 and Fig. 2 of both Paper I and the present work). The dashed lines separate the three different magnetically defined regions (Alves et al. 2008). The lowest visual extinction (A_V) corresponds to 0.5 magnitudes. The highest A_V is observed toward the *bowl* and B59 regions, where it reaches approximately 20 magnitudes.

Table 1
Source List Observed in Paper I and in this Work.

Source[a]	α(J2000) h m s	δ(J2000) ° ′ ″	v_{LSR}[b] (km s^{-1})	Region[c]
Core 06	17 10 31.6	-27 25 51.6	+3.4	B59
Core 14	17 12 34.0	-27 21 16.2	+3.5	B59
Core 20	17 15 11.2	-27 35 06.0	+3.5	*Stem*
Core 40	17 21 16.4	-26 52 56.7	+3.3	*Stem*
Core 47	17 27 29.6	-26 59 06.0	+2.8	*Stem*
Core 48	17 25 59.0	-26 44 11.8	+3.6	*Stem*
Core 65	17 31 20.5	-26 30 36.1	+5.0	*Bowl*
Core 74	17 32 35.3	-26 15 54.0	+4.2	*Bowl*
Core 109	17 35 48.5	-25 33 05.8	+5.8	*Bowl*

[a] According to Lombardi et al. (2006) numbering.
[b] Rathborne et al. (2008).
[c] According to Alves et al. (2008) diffuse gas polarimetric properties.

tion between the chemical evolutionary stage of the cores and their location in the Pipe nebula and, therefore, with the large scale magnetic field. However, at core scales, there are hints of a correlation between the chemical evolutionary stage of the cores and the local magnetic properties. Recently, Frau et al. (2012, hereafter Paper II) have presented a 3 mm ~15 GHz wide chemical survey toward fourteen starless cores in the Pipe nebula. In order to avoid a density bias, we defined the molecular line normalized intensity by dividing the spectra by the visual extinction (A_V) peak, similar to the definition of the abundance. We found a clear chemical differentiation, and normalized intensity trends among the cores related to their A_V peak value. We defined three groups of cores: “diffuse” cores ($A_V \lesssim 15$ mag) with emission only of “ubiquitous” molecular transitions present in all the cores (C_2H, $c\text{-}C_3H_2$, HCO^+, CS, SO, and HCN), “oxo-sulfurated” cores ($A_V \simeq 15\text{-}22$ mag) with emission of molecules like ^{34}SO, SO_2, and OCS, only present in this group, and finally, “deuterated” cores ($A_V \gtrsim 22$ mag), which present emission in nitrogen- and deuterium-bearing molecules, as well as in carbon chain molecules.

In this paper, we further explored observationally the relationship among structure, chemistry, and magnetic field by extending the sample in five new Pipe nebula cores, for a total of nine, and several new molecular transitions. We repeated and extended the analysis conducted in Paper I for molecular (temperature, opacity, and column density estimates) and continuum (dust parameters estimates and comparison with previous maps) data. We also derived and analyzed the molecular line normalized intensities as in Paper II. For the sake of simplicity, we omit here technical details, which are widely explained in Papers I and II.

2. OBSERVATIONS AND DATA REDUCTION

2.1. *MAMBO-II observations*

We mapped cores 06, 20, 47, 65, and 74 (according to Lombardi et al. 2006 numbering) at 1.2 mm with the 117-receiver MAMBO-II bolometer (array diameter of 240″) of the IRAM 30-m telescope in Granada (Spain). Core positions are listed in Table 1. The beam size is ~11″ at 250 GHz. The observations were carried out in March and April 2009 and in January and March 2010, in the framework of a flexible observing pool, using the same technique and strategy as in Paper I. A total of 16 usable maps were selected for analysis: 4

Table 2
Molecular transitions observed toward the Pipe nebula cores with the IRAM 30-m antenna.

Molecule	Transition	Frequency (GHz)	Beam[a] ($''$)	Beam efficiency[b]	Δv[c] ($\mathrm{km\,s^{-1}}$)	Type[d]
C_3H_2	$(2_{1,2}–1_{1,0})$	85.3389	28.8	0.78/0.81	0.07	E
C_2H	(1–0)	87.3169	28.1	– /0.81	0.07	E
HCN	(1–0)	88.6318	27.7	0.78/0.81	0.07	E
N_2H^+	(1–0)	93.1762	26.4	0.77/0.80	0.06	L
$C^{34}S$	(2–1)	96.4130	25.5	– /0.80	0.06	E
CH_3OH	$(2_{-1,2}–1_{-1,1})$	96.7394	25.4	– /0.80	0.06	L?
CH_3OH	$(2_{0,2}–1_{0,1})$	96.7414	25.4	– /0.80	0.06	L?
CS	(2–1)	97.9809	25.1	0.76/0.80	0.06	E
$C^{18}O$	(1–0)	109.7822	22.4	– /0.78	0.05	E
^{13}CO	(1–0)	110.2014	22.3	– /0.78	0.05	E
CN	(1–0)	113.4909	21.7	0.75/0.78	0.05	E
$C^{34}S$	(3–2)	146.6171	16.8	– /0.74	0.04	E
CS	(3–2)	146.6960	16.8	– /0.73	0.04	E
N_2D^+	(2–1)	154.2170	16.0	0.77/0.72	0.04	L
DCO^+	(3–2)	216.1126	11.4	0.57/0.62	0.03	L
$C^{18}O$	(2–1)	219.5603	11.2	– /0.61	0.03	E
^{13}CO	(2–1)	220.3986	11.2	– /0.61	0.05	E
CN	(2–1)	226.8747	10.9	0.53/0.60	0.03	E
N_2D^+	(3–2)	231.3216	10.6	0.67/0.59	0.03	L
$H^{13}CO^+$	(3–2)	260.2554	9.5	0.53/0.53	0.02	L

[a] $[\mathrm{HPBW}/''] = 2460 \times [\mathrm{freq/GHz}]^{-1}$
(http://www.iram.es/IRAMES/telescope/telescopeSummary/telescope_summary.html)
[b] ABCD and EMIR receiver, respectively
[c] Spectral resolution.
[d] E = Early-time. L = Late-time. See Paper I for details.

for cores 06 and 74, 3 for cores 20 and 47, and 2 for core 65. The weather conditions were good, with zenith optical depths between 0.1 and 0.3 for most of the time. The average corrections for pointing and focus stayed below $3''$ and 0.2 mm, respectively. The maps were taken at an elevation of $\lesssim 25^\circ$ because of the declination of the sources.

The data were reduced using MOPSIC and figures were created using the GREG package (both from the GILDAS[1] software).

2.2. *Line observations*

We performed pointed observations within the regions of the cores 06, 20, 47, 65, and 74 with the ABCD and EMIR heterodyne receivers of the IRAM 30-m telescope covering the 3, 2, 1.3 and 1.1 mm bands. The observed positions were either the $C^{18}O$ pointing center reported by Muench et al. (2007, depicted by star symbols in Fig. 2), or the pointing position closer to the dust continuum peak (circle symbols in Fig. 2). The epochs, system configuration, technique, and methodology used are the same as in Paper I. We present also new molecular transitions observed toward the whole sample of nine cores in the same epochs as Paper I: CH_3OH, ^{13}CO and $C^{18}O$ in the (1–0) and (2–1) transitions, and CS and $C^{34}S$ in the (3–2) transition. System temperatures, in $T_{\rm MB}$ scale, ranged from 200 to 275 K (3 mm) and from 440 to 960 K (1 mm) for good weather conditions, and reached 450 K (3 mm) and 3200 K (1 mm) for bad weather conditions.

Additional pointed observations were performed in August 2011 toward the dust emission peak of cores 06, 14, 20, 40, 47, 48, 65, and 109 (Table 3 of both Paper I and the present work). The EMIR E0 receiver, together with the VESPA autocorrelator at a spectral resolution of 20 kHz, was tuned to the C_2H (1–0) transition. Six spectral windows were set to the six hyperfine components of the transition (spanning from 87.284 to 87.446 GHz; Table 4 of Padovani et al. 2009). Frequency switching mode was used with a frequency throw of 7.5 MHz. System temperatures ranged from ~100 to ~125 K.

Table 2 shows the transitions and frequencies observed, as well as the beam sizes and efficiencies. Column 6 lists the velocity resolution corresponding to the channel resolution of the VESPA autocorrelator (20 kHz). Column 7 specifies the evolutive category of each molecule (i.e. early- or late-time molecule). We reduced the data using the CLASS package of the GILDAS software. We obtained the line parameters either from a Gaussian fit or from calculating their statistical moments when the profile was not Gaussian.

3. RESULTS AND ANALYSIS

In this Section, we present the dust continuum emission maps for five new Pipe nebula cores to be analyzed together with the four cores already presented in Paper I. We also present molecular line observations for the new five cores in the same transitions presented in Paper I, as well as several new transitions for the nine cores. Finally, following Paper II analysis, we derive the normalized intensities of the detected molecular transitions. A detailed explanation of the methodology can be found in Papers I and II.

3.1. *Dust continuum emission*

In Fig. 2 we present the MAMBO-II maps of the dust continuum emission at 1.2 mm toward the five new cores of the Pipe nebula, convolved to a $21.''5$ Gaussian beam in order to improve the signal-to-noise ratio (SNR), and to smooth the appearance of the maps. Table 3 lists the peak position of the 1.2 mm emission after convolution, the dust temperature (Rathborne et al. 2008), the rms noise of the maps, the flux density and the value of the emission peak. Additionally, we also give the derived full width half maximum (FWHM) equivalent diameter, H_2 column density ($N_{\rm H_2}$), H_2 volume density ($n_{\rm H_2}$) density, and mass for each core (see Appendix A in Paper I for details). These parameters are derived from the emission within the 3-σ level and discussed in Section 4.

The flux density of the cores ranges between ~0.40 and ~1.52 Jy, while the peak value ranges between ~21 and ~43 mJy beam^{-1}. The maps of Fig. 2 show the different morphology of the five cores. Core 06, located in the most evolved B59 region, shows one of the weakest emission levels (~0.6 Jy) of the present sample. It is the most compact (~0.05 pc) and densest (~1.5×10^5 cm^{-3}) core of the five. It shows similar physical properties to core 14 (Paper I), also in the B59 region. The two cores located in the *stem*, 20 and 47, show a very diffuse nature with elliptical morphologies similar to the previously presented *stem* core 48. The three of them have similar physical properties in terms of size (~0.09 pc) and density (~3×10^4 cm^{-3}). The *bowl* cores, 65 and 74, do not show a defined morphology. Their sizes, densities and masses are very different. Core 65 is more compact and denser, while core 74 shows properties comparable to those of the *stem* cores. The morphology of the dust continuum emission for all the cores is in good agreement with that of previous extinction maps (Lombardi et al. 2006; Román-Zúñiga et al. 2009).

3.2. *Molecular survey of high density tracers*

We present molecular line data observed toward the dust continuum emission peak or toward the $C^{18}O$ peak position

---

[1] MOPSIC and GILDAS data reduction packages are available at http://www.iram.fr/IRAMFR/GILDAS

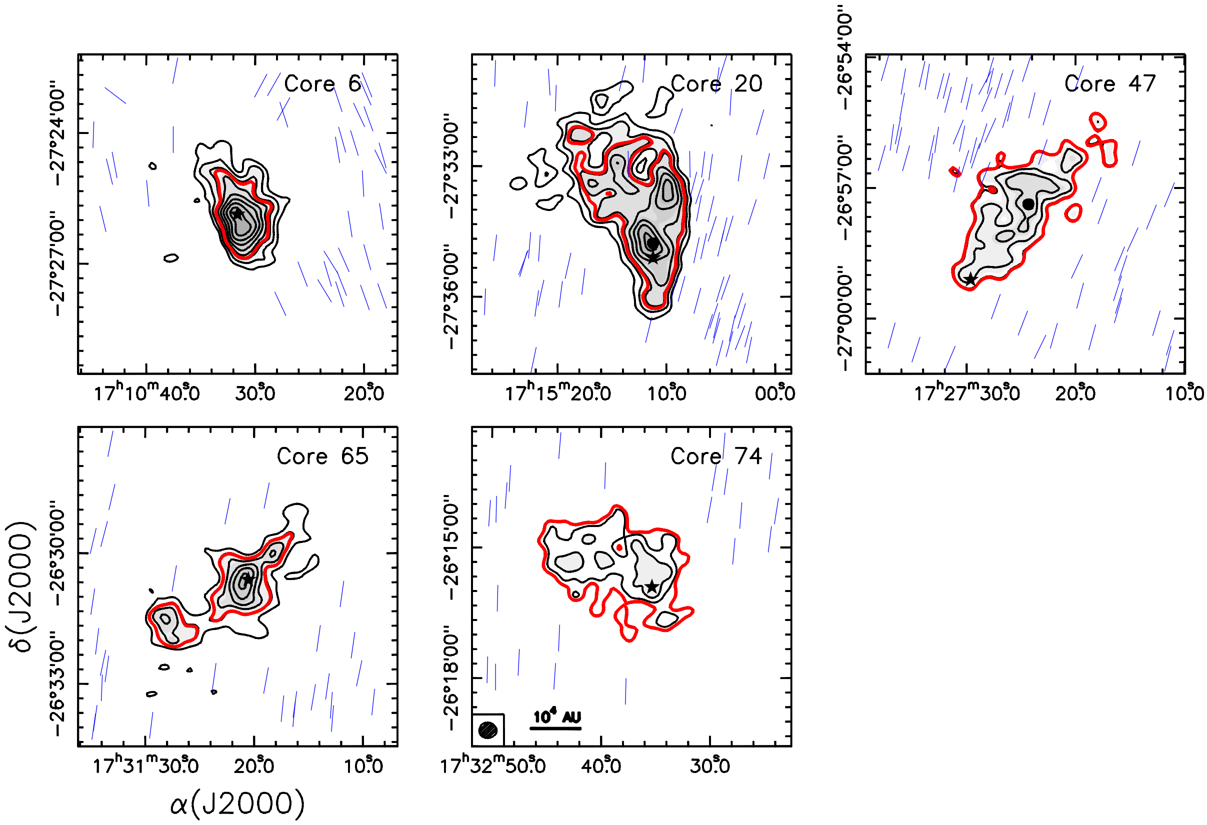

Figure 2. IRAM 30-m MAMBO-II maps of the dust continuum emission at 1.2 mm toward five cores of the Pipe nebula. The grayscale levels for all the maps are 3 to 18 times 5.75 mJy beam^{-1}. The contour levels are 3 to 10 times σ in steps of 1-σ, where 1-σ is 4.0, 4.5, 4.9, 4.4, and 4.3 mJy beam^{-1} for core 06, 20, 47, 65, and 74, respectively. The red thick contour marks the half maximum emission level of the source (Table 3). Black stars indicate the C^{18}O pointing center reported by Muench et al. (2007). Black filled circles indicate the position where line observations have been performed, if different from the Muench et al. (2007) position, closer to the dust continuum emission maximum which falls into the beam area. The blue vectors depict the polarization vectors found by Franco et al. (2010). In the bottom left corner of the bottom middle panel the convolved beam and the spatial scale for the maps are shown.

Table 3
1.2 mm continuum emission parameters.

Source	α(J2000) ^{a} h m s	δ(J2000) ^{a} ° ′ ″	$T_{\rm dust}$ (K)	rms (mJy beam^{-1})	S_ν (Jy)	$I_\nu^{\rm Peak}$ (mJy beam^{-1})	Diameter ^{b} (pc)	$N_{\rm H_2}$ ^{c} (10^{21}cm^{-2})	$n_{\rm H_2}$ ^{c} (10^4cm^{-3})	Mass ^{c} ($M_\odot$)
Core 06	17 10 31.8	−27 25 51.3	10.0^{d}	4.0	0.58	42.6	0.051	16.18 ^{d}	15.44 ^{d}	0.88 ^{d}
Core 20	17 15 11.5	−27 34 47.9	15.2^{e}	4.5	1.52	42.6	0.088	7.33	4.04	1.20
Core 47	17 27 24.3	−26 57 22.2	12.6^{e}	4.9	0.73	28.5	0.093	4.17	2.18	0.76
Core 65	17 31 21.1	−26 30 42.8	10.0^{d}	4.4	0.48	36.1	0.053	12.39 ^{d}	11.38 ^{d}	0.73 ^{d}
Core 74	17 32 35.3	−26 15 54.0	10.0^{d}	4.3	0.40	21.4	0.097	3.11 ^{d}	1.56 ^{d}	0.61 ^{d}

[a] Dust continuum emission peak.

[b] Diameter of the circle with area equal to the source area satisfying $I_\nu > I_\nu^{\rm Peak}/2$

[c] Assuming $\kappa_{250\ \rm GHz}$=0.0066 cm^2 g^{-1} as a medium value between dust grains with thin and thick ice mantles (Ossenkopf & Henning 1994). See Appendix 1 in Paper I for details on the calculation.

[d] No kinetic temperature estimate, therefore we assumed 10 K based on the average temperatures of the other cores in the Pipe nebula (Rathborne et al. 2008).

[e] Adopted to be equal to the kinetic temperature estimated from NH$_3$ (Rathborne et al. 2008).

reported by Muench et al. (2007, for more details see Fig. 2), defined as the core center and supposed to exhibit brighter emission from molecular transitions. As discussed in Paper I, the chemical properties derived toward the dust emission peak are representative of the chemistry at the core center. Our higher resolution dust emission maps show a peak offset with respect to the C^{18}O for cores 20 and 47. For the former one, the offset is only ∼20″ while for the latter, more diffuse one, the offset is of ∼130″(see Section 4.4).

In Figs. 8–12, we show the spectra of the different molecular transitions observed toward the dust continuum emission peak of each core. Figures 8–9 show the molecular transitions with and without hyperfine components, respectively, for the five new cores. The new molecular transitions for the whole sample of nine cores are shown in Figs. 10–11, for those with hyperfine components, and Fig. 12, for those without hyperfine components. Table 4 summarizes the detections or the 3σ upper limits of the non detections toward

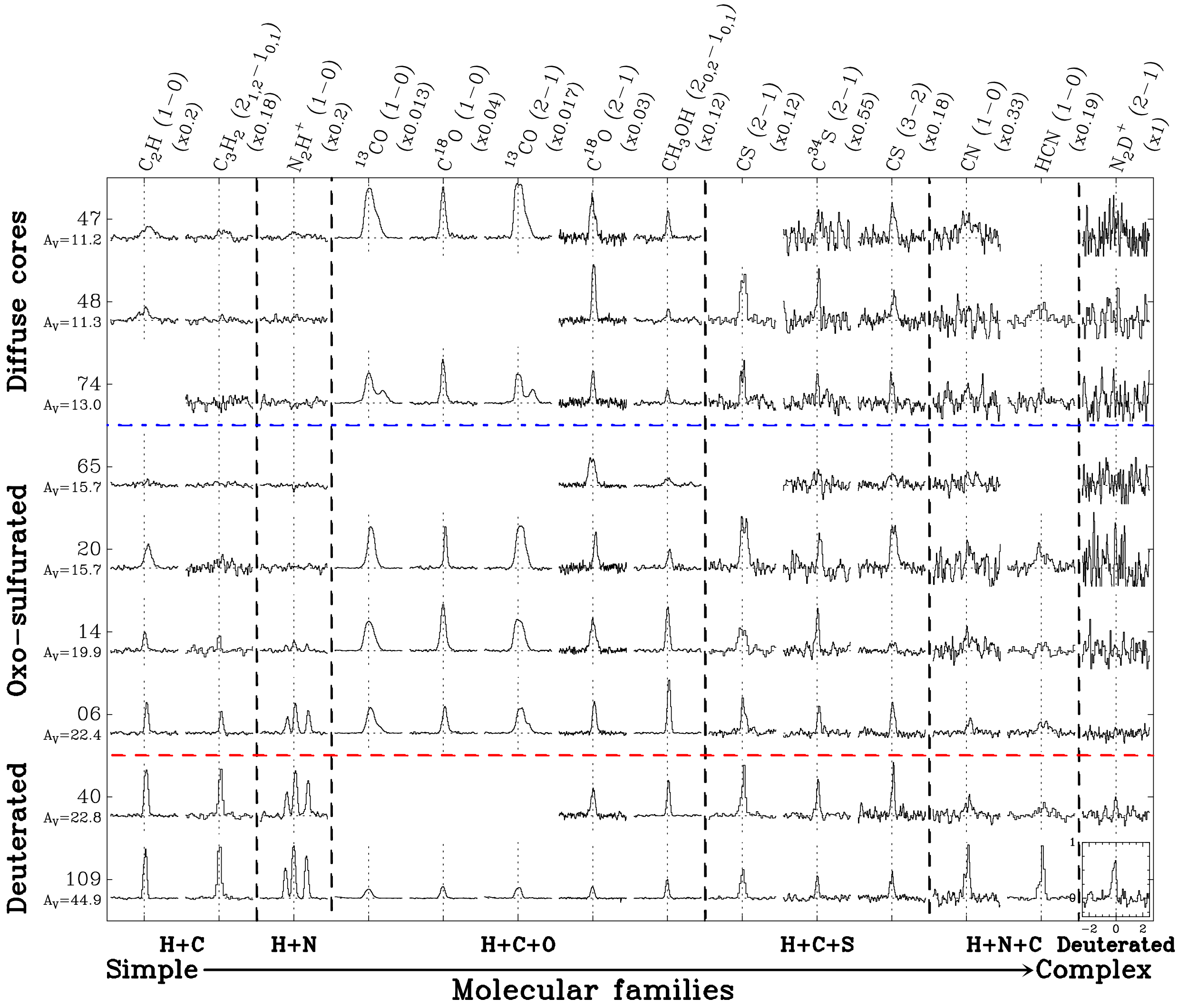

Figure 3. Selected normalized molecular transitions toward the observed cores. The brightest transition is shown for the C_2H, CH_3OH, and HCN lines. The scale is shown in the bottom right spectrum. The normalized intensity axis ranges from -0.33 to 1, while the velocity axis spans 5 km s^{-1} centered at the systemic velocity of the core. *Rows*: individual cores, labeled on the left-hand side of the figure, ordered by its A_V peak. *Columns*: molecular transition, ordered by molecular families, labeled on the top of the figure. The spectra have been divided by $[A_V/100\,\mathrm{mag}]$ to mimic the abundance, where the A_V value is that at the respective core center (Román-Zúñiga et al. 2010) given below the core name. Each molecular transition has been multiplied by a factor, given below its name, to fit in a common scale.

the whole sample of nine cores. We found that early-time molecules are broadly detected over the whole sample. Several of them were detected toward all the cores: CH_3OH (2–1), CS in the (2–1) and (3–2) transitions, and ^{13}CO and $C^{18}O$ in the (1–0) and (2–1) transitions. On the other hand, only a few cores present emission of late-time molecules. The cores with $n_{H_2} \gtrsim 10^5$ cm^{-3} (06, 14, 40, and 109 but not 65) presented more detections than shallower cores and, indeed, were the only cores presenting N_2H^+ emission. Tables 6–7 give the parameters of the detected lines. Regarding the line properties, the v_{LSR} measured for different species are generally consistent within 0.2 km s^{-1}. Intensities vary significantly over the sample: cores 06, 40 and 109 are generally bright while the rest of the sample shows fainter emission. "Bright" lines (T_{MB}>0.2 K) are mostly very narrow ($0.2 \lesssim \Delta v \lesssim 0.3$ km s^{-1}), although transitions of CO and CS isotopologues can show broader profiles ($\Delta v \lesssim 0.5$ km s^{-1} if "bright"). In some cases, this broadening can be explained in terms of a second velocity component generally merged with the main one (cores 06 and 20 in CS, and cores 06, 14, 47, 74, and 109 in ^{13}CO).

In addition to the line parameters, we derived the molecular column densities for all the detected species (see Appendix B in Paper I for details) which are listed in Tables 8–9. For the transitions with detected hyperfine components (C_2H, HCN, N_2H^+, CH_3OH, and CN), we derived the opacity using the hyperfine components fitting method (HFS) of the CLASS package. For the molecular transitions observed in more than one isotopologue, this is CS and $C^{34}S$ in the (2–1) and (3–2) transitions, and ^{13}CO and $C^{18}O$ in the (1–0) and (2–1) transitions, we derived numerically the opacity. Table 10 shows the H_2 column density of the cores for different angular resolutions. Tables 11–12 give the molecular abundances with respect to

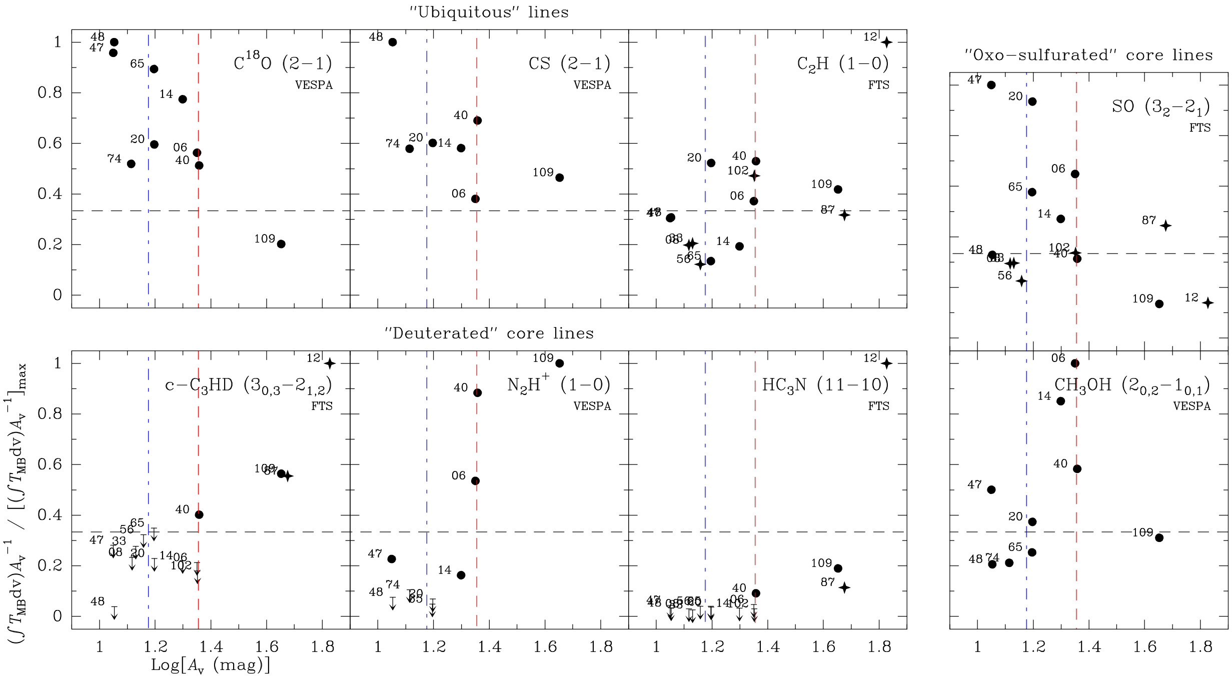

Figure 4. Normalized integrated intensity ($A_V^{-1}\int T_{\rm MB}dv$) of selected molecular transitions divided by its maximum value as a function of the logarithm of the core A_V peak. Each panel shows the molecular transition in the top right corner. The backend is labeled below the molecular transition: VESPA panels present the nine cores of Paper I and present work, while FTS panels present the fourteen cores of Paper II. Filled circles represent the nine cores of Paper I and present work, stars represent the other six cores from Paper II (08, 12, 33, 56, 87, and 102), and arrows represent upper limits. Molecules have been split into the three categories defined in Paper II, labeled on the top of each group. The blue dot-dashed and red dashed vertical lines mark the transition from "diffuse" to "oxo-sulfurated", and from "oxo-sulfurated" to "deuterated" cores, respectively. The horizontal dashed line marks a third of the peak value which helps to show the behavior change of the "oxo-sulfurated" and "deuterated" lines in our sample. The maximum values for each molecular transition are, in K km s^{-1} mag^{-1}, 0.114, 0.036, and 0.030 for the ubiquitous C^{18}O, CS, and C$_2$H, 0.059 and 0.025 for the "oxo-sulfurated" SO and CH$_3$OH, and 0.003, 0.010, and 0.019 for the "deuterated" c-C$_3$HD, N$_2$H$^+$, and HC$_3$N, respectively.

Table 4
Summary of detections and upper levels in K toward the Pipe nebula cores[a].

Molecular transitions	Core								
	06	14	20	40	47	48	65	74	109
C_3H_2 ($2_{1,2}$–$1_{1,0}$)	√	√	0.22	√	√	0.07	0.06	0.17	√
C_2H (1–0)	√	√	√	√	√	√	0.06	–	√
HCN (1–0)	√	0.21	√	√	√[b]	√	–	0.18	√
N_2H^+ (1–0)	√	√	0.08	√	√	0.07	0.06	0.11	√
$C^{34}S$ (2–1)	√	√	√	√	√	√	0.07	√	√
CH_3OH (2–1)	√	√	√	√	√	√	√	√	√
CS (2–1)	√	√	√	√	√[b]	√	–	√	√
$C^{18}O$ (1–0)	√	√[b]	√[b]	–	√[b]	–	–	√	√[b]
^{13}CO (1–0)	√	√[b]	√[b]	–	√[b]	–	–	√	√[b]
CN (1–0)	√	√	0.25	√	√	0.17	0.11	0.19	√
$C^{34}S$ (3–2)	0.10	√	√	–	0.06	0.16	0.08	0.24	√
CS (3–2)	√	√	√	√	√	√	√	√	√
N_2D^+ (2–1)	0.04	0.12	0.17	√	0.09	0.08	0.08	0.09	√
DCO^+ (3–2)	√	1.71	2.33	0.61	–	0.76	–	0.50	√
$C^{18}O$ (2–1)	√	√[b]	√[b]	√[b]	√[b]	√	√	√	√[b]
^{13}CO (2–1)	√	√[b]	√[b]	–	√[b]	–	–	√	√[b]
CN (2–1)	0.80	0.97	–	1.70	–	0.76	–	0.84	0.90
N_2D^+ (3–2)	1.00	1.01	1.27[b]	0.93	–	1.94	–	1.32	0.91
$H^{13}CO^+$ (3–2)	1.29	1.52	1.94[b]	1.40	–	2.38	–	1.84	1.34

[a] Paper I results are included. The transitions marked with – have not been observed. Those marked with √ have been detected toward the corresponding core. Otherwise, the 3σ upper limit is shown. In the seventh column of Table 2, early- and late-time labels are listed for each molecule.
[b] Observed toward the extinction peak.

H$_2$.

Figure 3 shows the normalized intensities with respect to the core A_V peak of a selection of detected molecular transitions toward the sample of Paper I and the present work. Some of the lines were already presented in Paper II (except for core 74), although here are shown with a higher spectral resolution (e.g., the 3 mm C$_2$H, c-C$_3$H$_2$, and HCN line). The ^{13}CO and C^{18}O isotopologues can be considered as "ubiquitous" because they are present in all the observed cores (for cores 40, 48, and 65, the CO lines present intense emission but were observed toward a position that is offset from the core peak position). Their general trend is to decrease as density increases. The C^{34}S (2–1) line, which is optically thin, shows a similar trend as the main isotopologue (see Paper II), considered also as "ubiquitous". The decrease in the normalized intensity in the CS lines is only apparent for the densest core 109. The CN normalized intensities are larger toward the densest cores, which suggests that CN is typically associated with the "deuterated" group. Late time species, such as N$_2$H$^+$ and N$_2$D$^+$, are only present in the densest cores and their emission tends to be brighter with increasing density, confirming that both species are typical of the "deuterated" group. These general results are in agreement with the observational classification of cores presented in Paper II, which is based on a wider molecular survey at 3 mm.

Finally, we defined the observational normalized integrated intensity (NII) as $\left(\int T_{\rm MB}dv\right)/A_V$, to illustrate the different behavior of the molecular transitions that motivated the observational core classification proposed in Paper II. Figure 4 shows NII divided by its maximum value in the sample for selected molecular transitions typical of the three core groups: “diffuse”, “oxo-sulfurated”, and “deuterated”. “Ubiquitous” species are present in all the cores and their NII tends to decrease as the central density increases indicating possible depletion. “Oxo-sulfurated” species show low NII values except for a narrow range of densities (A_V≃15-22 mag). CH_3OH ($2_{0,2}$–$1_{0,1}$) shows a similar behavior to the “oxo-sulfurated” species previously identified (e.g. SO, SO_2, and OCS; Paper II) but seems to peak at slightly larger densities (A_V∼20–23 mag). “Deuterated” species are only present toward the densest cores and their NII values increase with increasing density.

3.3. *LTE status through hyperfine structure*

We followed the procedure developed in Padovani et al. (2009) to study the departures from Local Thermodynamic Equilibrium (LTE) of two of the molecular transitions with hyperfine components, C_2H (1–0) and HCN (1–0), toward the Pipe nebula starless cores. By comparing ratios of integrated intensities between couples of the i-th and j-th component, R_{ij}, it is possible to check for opacity degree and LTE departures (Fig. 5). Under LTE and optically thin conditions, the relative weightings of C_2H (1–0) hyperfine components have the form 1:10:5:5:2:1, whereas for HCN (1–0) the relative intensities are 3:5:1. Figure 5 suggests that cores 40 and 109 are the most optically thick, in agreement with the determination of τ from the HFS fit in CLASS (Table 6), while the other cores are optically thin. Core 20 is a particular case because it shows R_{54} and R_{13} values in C_2H that cannot be reproduced with any value of τ. This can be explained as the result of enhanced trapping due to an overpopulation of the $(N, J, F) = (0, 1/2, 1)$ level, where most $N = 1 - 0$ transitions end (except for components 3 and 6; Padovani et al. 2009). This means that these results have to be thought in a qualitative way, since lines of very different intrinsic intensities experience different balance between trapping and collisions leading to excitation anomalies. The hyperfine components of HCN (1–0) do not obey the LTE weightings. For instance, as shown in Fig. 8, core 6 is affected by strong auto-absorption of the F=1–1 and F=2–1 components. Similarly, F=1–1 is stronger than F=2–1 in core 20. A more reliable determination of the HCN abundance would be given by the ^{13}C (or ^{15}N) isotopologue of HCN (Padovani et al. 2011). In general, cores seem to be close to LTE with those next to the optically thin limit showing the smallest LTE departures.

4. DISCUSSION

4.1. *Observational maps and physical structure of the cores*

The extinction maps show that the cores in the Pipe nebula are surrounded by a diffuse medium (see Fig. 1 and Lombardi et al. 2006). Román-Zúñiga et al. (2012) show that the 1.2 mm continuum MAMBO-II maps underestimate the emission from the diffuse molecular component due to the reduction algorithms (see also Paper I). To study this effect, we compared, at the center of the nine cores, the N_{H_2} derived from the MAMBO-II maps (Table 10) with the A_V value from the extinction maps of Román-Zúñiga et al. (2009, 2010). We found a statistically significant correlation that can be expressed as

$$A_V = (6.7 \pm 1.5) + (1.27 \pm 0.12) \times 10^{-21} N_{H_2}. \qquad (1)$$

The proportionality factor is compatible with the standard value (1.258×10^{-21} mag cm^2; Wagenblast & Hartquist 1989).

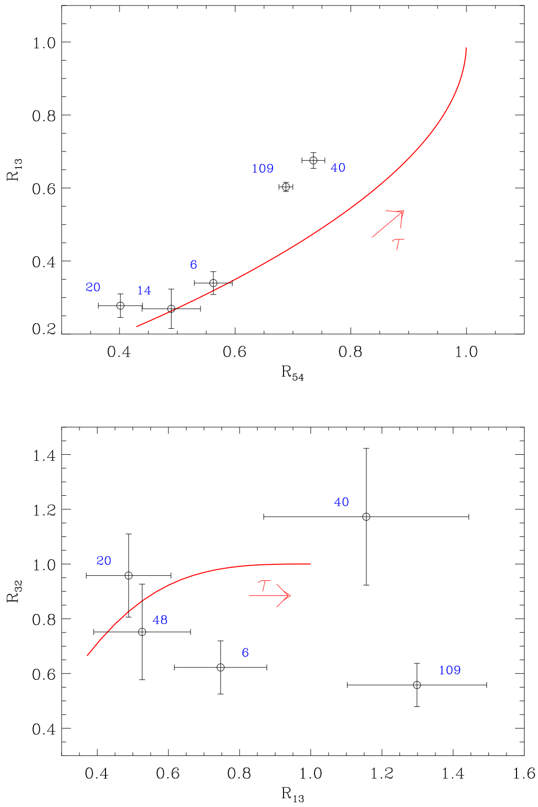

Figure 5. Ratio of the integrated intensities of couples of components of C_2H (1–0) (*upper panel*, see Table 5 in Padovani et al. 2009 for labels) and HCN (1–0) (*lower panel*, see Table B.1 in Padovani et al. 2011 for labels). *Empty circles*: observational data labeled with the respective core number. *Red solid line*: one-slab LTE model, optical depth increases in the arrow direction (see Padovani et al. 2009 for details).

However, the comparison evidences that the 1.2 mm maps underestimate the column density in average by an A_V of 6.7 mag, which is likely the contribution from the diffuse cloud material. As a consequence, the A_V peak values of the cores (from Román-Zúñiga et al. 2009, 2010) should be taken as upper limits of their column densities.

The statistics of this study have increased with the whole nine core sample. In Table 5 we show the main physical, chemical and polarimetric properties of the starless cores with respect to core 109 ordered by its decreasing A_V peak. Column and volume density, and total mass tend to decrease accordingly. On the contrary, the core diameter tends to increase. This suggests that as density increases the core shrinks and it becomes more compact. This is expected for structures in hydrostatic equilibrium such as Bonnor-Ebert spheres (Frau et al., in prep.). Under such assumption, the cores would become denser with time while developing a richer chemistry. This likely trend is supported by the clear correlation of the core chemistry with the visual extinction peak of the core and, therefore, its central density and structure.

4.2. *Relationship between the large scale magnetic field and the elongation of the cores*

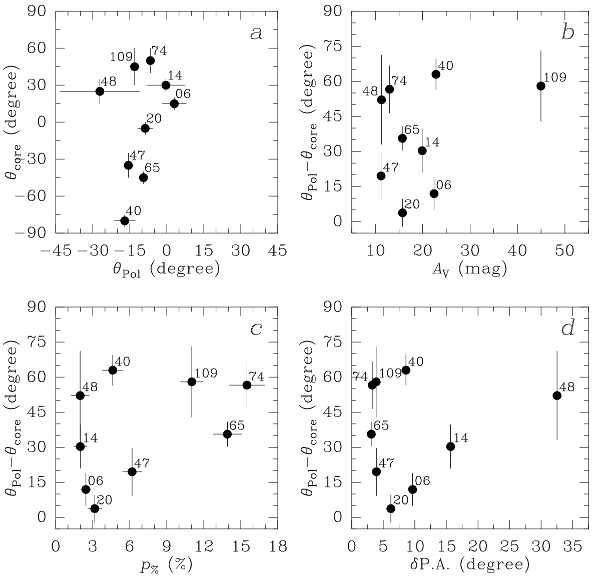

Figure 6. Relation of the core major axis orientation ($\theta_{\rm core}$) to different physical parameters. *a*: $\theta_{\rm core}$ against mean polarization angle ($\theta_{\rm Pol}$) of the corresponding observed field (Franco et al. 2010). *b*-*d*: $\theta_{\rm Pol}$-$\theta_{\rm core}$ as a function of core $A_{\rm V}$ peak (Román-Zúñiga et al. 2009, 2010), polarization fraction ($p_{\%}$) and polarization angle dispersion (δP.A.), respectively.

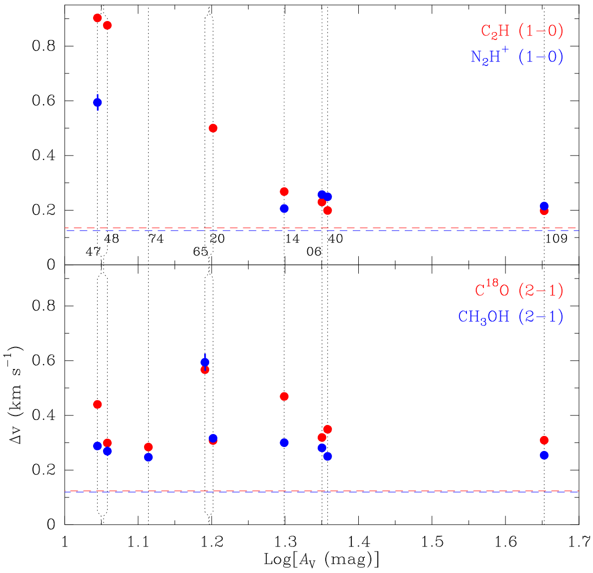

Figure 7. *Top panel*: line width of the C_2H (1–0) and N_2H^+ (1–0) lines, colored in red and blue, respectively, as a function of the logarithm of the core $A_{\rm V}$ peak. *Bottom panel*: Same as top panel but for the $C^{18}O$ (2–1) and CH_3OH (2–1) lines, colored in red and blue, respectively. Colored dashed horizontal lines show the corresponding thermal line width for each molecule for a temperature of 10 K. Vertical dotted lines mark the $A_{\rm V}$ peak of each core, which in the case of similar values (cores 47 and 48, and 20 and 65) have been slightly displaced.

The Pipe nebula cores are embedded in a sub-Alvénic molecular cloud that is threaded with a strikingly uniform magnetic field (Alves et al. 2008; Franco et al. 2010). Thus, it is possible that the core formation is related to the magnetic field and its direction is related to the core elongations. Figure 2 of both Paper I and the present work show that the polarization vectors calculated from optical data cannot trace the densest part of the cores although the vectors lie very close to the core boundaries. To derive the orientation of the core major axis, we computed the integrated flux within the FWHM contour for a series of parallel strips (11″ wide), with position angles in the -90° to 90° range. The major axis is oriented in the direction with the largest integrated flux on the fewest strips. We found no correlation between the orientation of the major axis of the core, $\theta_{\rm core}$, and the mean magnetic field direction around the cores ($\theta_{\rm Pol}$, see Fig. 6*a*). To investigate more subtle effects, we compared for each core the difference between polarization position angle and the major axis orientation ($\theta_{\rm Pol}$-$\theta_{\rm core}$) with respect to the $A_{\rm V}$ peak, the polarization fraction ($p_{\%}$) and polarization angle dispersion (δP.A.) estimated in a region of few arc-minutes around the cores (Franco et al. 2010). The results of these comparisons are shown in panels *b*, *c* and *d* of Fig. 6, respectively. Again, it seems that there are no clear correlations between these quantities.

These results suggest that the well-ordered, large scale magnetic field that may have driven the gas to form the ~15 pc long filamentary cloud has little effect in shaping the morphology of the ~0.1 pc cores. At intermediate scales, Peretto et al. (2012) suggest that a large scale compressive flow has contributed to the formation of a rich, organized network of filamentary structures within the cloud, ~0.1 pc wide and up to a few pc long, which tend to align either parallel or perpendicular to the magnetic field. If this is the case, then, rather than ambipolar diffusion, other mechanisms such as a compressive flow should play a major role in the formation of the Pipe nebula cores. However, as pointed out by Lada et al. (2008), the cores in the Pipe nebula evolve on acoustic, and thus, slow timescales (~10^6 yr), allowing ambipolar diffusion to have significant effects. Furthermore, the lack of spherical symmetry demands an anisotropic active force. Projection effects, together with the small statistical sample, require a deeper study of the magnetic field properties in order to extract firm conclusions.

4.3. *Velocity dispersion analysis*

Figure 7 shows the FWHM line width of four selected molecular transitions at 3 mm as a function of the core $A_{\rm V}$ peak. Whereas the $C^{18}O$ and CH_3OH lines show an almost constant line width of 0.3–0.4 km s^{-1} for most cores (except core 65), the C_2H and N_2H^+ lines have a lower line width, 0.20–0.25 km s^{-1}, except for the cores with lower visual extinction (47, 48 and 20). The values of the $C^{18}O$ line are in agreement with those found by Muench et al. (2007) with lower angular resolution. In most cases, the line widths are only 2–3 times the thermal broadening at 10 K. These line widths imply a subsonic non-thermal velocity dispersion, $\sigma_{\rm NT}$, of 0.06–0.09 km s^{-1} for the N_2H^+ and C_2H lines, respectively, and of 0.12–0.16 km s^{-1} for the $C^{18}O$ and CH_3OH lines, respectively. Therefore, the thermal pressure dominates the internal pressure of the cores, which is a general characteristic of the Pipe nebula (Lada et al. 2008). For the higher density cores ($A_{\rm V}>$ 17 mag), smaller $\sigma_{\rm NT}$ for the N_2H^+ and C_2H lines with respect to $C^{18}O$ and CH_3OH lines suggests that the former transitions are tracing the inner regions of the core. However, cores 47 and 48 present a peculiar reverse case in the line width properties, i.e., the C_2H and N_2H^+ lines are significantly wider and clearly supersonic. This is compatible with the plausible scenario of core 47 (and probably core 48) being a failed core in re-expansion (Frau et al. 2012), on which the centrally synthesized and initially narrow N_2H^+

Table 5
Pipe nebula Core General Properties with Respect to Core 109[a]

Source	Diameter (pc)	Mass ($M_\odot$)	N_{H_2} (10^{21}cm^{-2})	n_{H_2} (10^4cm^{-3})	$p^b_{\%}$ (%)	δP.A.[b] (^{o})	X(C^{18}O) (10^{-11})	X(CS) (10^{-11})	X(C_2H) (10^{-11})	X(C_3H_2) (10^{-11})	X(CH_3OH) (10^{-11})	X(CN) (10^{-11})	X(N_2H^+) (10^{-11})
Core 109	0.063	4.00	47.60	36.57	11.0	3.9	1324.6	40.2	34.1	52.8	44.3	8.7	2.2
						Relative Values (%)							
Core 109	100	100	100	100	100	100	100	100	100	100	100	100	100
Core 40	165	63	23	14	42	222	517	168	335	52	272	480	208
Core 06	86	23	32	38	22	249	323	315	125	12	609	105	243
Core 14	113	35	28	25	18	404	1051	752	89	7	368	121	44
Core 20	141	28	14	10	29	160	752	576	295	< 7	186	< 36	< 37
Core 65	105	26	23	22	126	80	608	–	< 3	< 2	99	< 13	< 20
Core 74	154	16	7	4	140	84	303	435	< 3	< 5	96	< 27	< 36
Core 48	202	52	13	6	18	838	553	539	162	< 2	72	< 20	< 25
Core 47	146	19	9	6	56	101	521	–	298	13	204	511	117

[a] Molecules are ordered from earlier to later synthesization. Cores are ordered in three groups following Paper II.

[b] Franco et al. (2010)

and C_2H (1–0) lines are now part of the disrupted gas. But it is puzzling that the $C^{18}O$ and CH_3OH lines are still narrow and subsonic, unless they trace a part of core that still remains unperturbed. A complete mapping of these cores is needed to reveal their striking nature.

4.4. *Discussion on the individual cores*

Core 06, located in the western part of B59, is a compact and dense core. The dust continuum emission is similar to the extinction maps (Román-Zúñiga et al. 2009). The core shows a rich chemistry with bright detections of all the early-time and some late-time molecules. The core has the brightest emission and highest abundance of CH_3OH of the sample, as well as the highest N_2H^+ abundance. Unlike core 109, it has a high CS abundance suggesting that it has not been depleted yet. All these features suggest that core 06 is in the "oxo-sulfurated" group close to the "deuterated" cores.

Core 20, located in the *stem*, shows in the 1.2 mm map two components: a compact and bright one surrounded by a second one, extended and diffuse. Most of the early-time molecules were detected, and thus, this core seems to be very young chemically showing abundances in CS and CH_3OH among the highest. Normalized intensities are in general quite large for its density (Fig. 3), and it has a very large SO normalized integrated intensity as core 47 (Fig. 4). These signposts suggest that core 20 belongs to the "oxo-sulfurated" group.

Core 47, located between the *stem* and the *bowl*, has extended and diffuse dust emission. It shows a fairly uniform and weak emission all over the A_V and MAMBO-II maps. This can explain the peak position difference of ~130″ between the dust emission map and the position taken by Muench et al. (2007) for the line observations. It shows weak line emission, only in early-time molecules. It is the second least dense core of the sample (~2×10^4 cm^{-3}), yet the molecular abundances tend to be among the highest. Rathborne et al. (2008) report a clear detection of NH_3 (1,1) and hints of emission in the (2,2) transition. Figure 8 shows a marginal detection at 3σ level of the N_2H^+ (1–0) brightest hyperfine component. The high molecular abundances and the emission of certain molecular line tracers of the "oxo-sulfurated" group, together with its diffuse morphology and low density typical of the "diffuse" cores, suggest that core 47 may be an evolved failed core now in re-expansion as already suggested in Paper II. The relatively broad lines in some of the species (see Section 4.3) support this scenario.

Core 65, located in the *bowl*, is the central core of a group of three (see Fig. 2). Its density is in the limit between those of the "diffuse" and "oxo-sulfurated" cores. It has a very poor chemistry with only "ubiquitous" early-time molecules detected (CO, CS, and CH_3OH) with abundances among the lowest of the sample. The line widths, ~0.6 km s^{-1}, appear to be larger than those of the other cores.

Finally, core 74, located in the *bowl*, is extended and diffuse similarly to core 47. It also shows a very poor chemistry with only "ubiquitous" early-time molecules detected (CO, CS, and CH_3OH).

It is useful to review the data from Rathborne et al. (2008). The late-time molecule NH_3 in the (1,1) transition is detected in cores 06, 20, 47, and marginally in 65. These cores belong to the "oxo-sulfurated" group, which suggests that NH_3 is formed in this phase. CCS is considered an early-time molecule with a lifetime of $\lesssim 3\times10^4$ yr (de Gregorio-Monsalvo et al. 2006). It is only marginally detected toward core 06, therefore suggesting that it might be very young. Core 74 does not show any emission, in agreement with the poor chemistry detected in our 3 mm surveys. These results also suggest that the five cores are in a very early stage of evolution.

4.5. *Qualitative chemistry discussion*

The molecular transitions from Paper I and this work increase the number of typical lines of the core categories established in Paper II. Four of the five cores have lower densities than the initial subsample (except for core 48, Table 10), and thus, we are now including in the analysis shallower cores that might be more affected by the external radiation field and that show a younger chemistry (although the timescale to form the core may influence this evolution: Tafalla et al. 2004; Crapsi et al. 2005).

We found a complex chemical scenario toward the Pipe nebula cores. However, as pointed out in Paper II, it seems that there is an evolutionary trend with density in the form of three differentiated core chemical groups. We remind that the A_V values should be interpreted as upper limits for the column density of the cores (Section 4.1), and that the column densities derived from the dust emission maps show larger differences than the A_V values. These facts translate to larger abundance differences among the cores as compared to the normalized intensity differences. The molecular trends, however, are compatible. We will base our analysis in the combination of the results obtained via the normalized intensities and normalized integrated intensities (Figs. 3 and 4), and of the molecular abundances with respect to the H_2 (Table 5), to which we will refer generically as *abundances*. $C^{18}O$ and CS lines appear to be "ubiquitous", as they are detected in all the cores. Their *abundances* decrease with column density due to, probably, an increasingly efficient depletion for both species (and isotopologues) as density grows. The variation of the CN *abundance* among the cores has increased with respect to Paper I (up to a factor of ∼33 in abundance: Table 12), due to the addition of more diffuse cores. The lower limits are indeed very low, and thus, we are now exploring even younger chemical stages of these starless cores. All these features suggest that CN (1–0) is a transition typical of the "deuterated" group. A nitrogen- (N_2H^+) and a deuterium-bearing (c-C_3HD) species, and a carbon chain molecule (HC_3N) are shown in Fig. 4. These late-time molecules, present toward the densest objects, are not detected in low density cores. They are only present after achieving a density threshold, and exhibit increasing *abundances* as density grows. These transitions seem to be typical of the "deuterated" cores, which is consistent with the detection of NH_2D ($1_{1,1}$–$1_{0,1}$) toward this core group in Paper II.

CH_3OH deserves a special mention. This molecule is clearly detected in the gas phase toward all the observed cores in the ($2_{0,2}$–$1_{0,1}$) (shown normalized in Fig. 3) and ($2_{1,2}$–$1_{1,1}$) transitions (Fig. 10). It shows a behavior similar to that of the "oxo-sulfurated" species but peaking at slightly larger densities. Thus, this species is likely to peak in the transition from the "oxo-sulfurated" core chemistry to the typical dense core chemistry found toward the "deuterated" cores, suggesting that CH_3OH could be actually an early-time molecule. It is expected to be formed efficiently in grain surfaces, with abundances for the gas phase of $\sim10^{-9}$ at most (Cuppen et al. 2009; Garrod & Pauly 2011), very close to the observational abundances derived ($\sim3\times10^{-10}$–$\sim3\times10^{-9}$: Table 11). Abundances for the gas phase of 6×10^{-10}, comparable to the lowest values for the Pipe nebula cores, have been derived in the literature through modeling of more evolved low-mass cores (Tafalla et al. 2006). However, the higher densities and comparable temperatures product of this modeling with respect to the Pipe nebula core values suggest that other mechanisms are needed to explain the high gas phase CH_3OH abundances found here. In addition, the abundances in the Pipe nebula cores seem to correlate with their location in the cloud, being larger in the B59 region and decreasing as going toward the *bowl*. This fact could be explained by the slightly higher temperatures reported toward the B59 region (Rathborne et al. 2008), which could enhance evaporation from grains.

In summary, our high spectral resolution dataset shows the existence of a clear chemical differentiation toward the Pipe nebula cores. The chemical signatures agree with the results of previous Papers I and II. Chemistry seems to become more rich and complex as cores grow denser therefore suggesting an evolutionary gradient among the sample. The tentative correlation found in Paper I between magnetic field and chemical evolutionary stage of the cores is less clear with the whole nine core sample.

5. SUMMARY AND CONCLUSIONS

We carried out observations of continuum and line emission toward five starless cores, located on the three different regions of the Pipe nebula, and combined them with the observations of the four additional cores of Paper I to extend the dataset to nine cores. We studied the physical and chemical properties of the cores, and their correlation following Paper II. We also studied the correlation with the magnetic field properties of the surrounding diffuse gas following Paper I.

1. The Pipe nebula starless cores show very different morphologies. The complete sample of nine cores contains dense and compact cores (6, 65, and 109; $n_{H_2}\gtrsim10^5$ cm^{-3}), diffuse and elliptical/irregular ones (20, 40, 47, 48, and 74; $n_{H_2}\lesssim5\times10^4$ cm^{-3}), and a filament containing the relatively dense core 14 ($n_{H_2}\sim9\times10^4$ cm^{-3}). The average properties of the nine cores of the sample are diameter of ∼0.08 pc (∼16,800 AU), density of $\sim10^5$ cm^{-3}, and mass of $\sim1.7\ M_\odot$. These values are very close to the initial values used in simulations of evolving prestellar cores (Aikawa et al. 2008; Keto & Caselli 2008) and, therefore, typical of very early stages of evolution.
2. MAMBO-II maps are in a general good morphological agreement with previous extinction maps (Lombardi et al. 2006). By comparing the A_V peak values of the nine cores from deeper NICER maps (Román-Zúñiga et al. 2009, 2010), we derived a proportionality factor $A_V/N_{H_2}=(1.27\pm0.12)\times10^{-21}$ mag cm^2, compatible with the standard value (1.258×10^{-21} mag cm^2; Wagenblast & Hartquist 1989). In addition, we found that dust continuum maps underestimate the column density by an A_V of ∼6.7 mag that may be arising from the diffuse material of the cloud.
3. The orientation of the cores is not correlated with the surrounding magnetic field direction, which suggests that magnetic fields are not important in shaping the cores. On the other hand, the lack of spherical symmetry demands an important anisotropic force. Projection effects might be important, thus, demanding a deeper study of the magnetic field morphology.
4. The analysis of the line widths reports two behaviors depending on the molecular transition: (*i*) a roughly constant value of subsonic turbulent broadening for all the cores (e.g. $C^{18}O$ (1–0) and CH_3OH (2–1), see also Lada et al. 2008) and (*ii*) a roughly constant slightly narrower broadening for cores with $A_V\gtrsim20$ mag and supersonic turbulent broadenings otherwise (e.g. C_2H (1–0) and N_2H^+ (1–0)).
5. We observed a set of early- and late-time molecular transitions toward the cores and derived their column densities and abundances. The high spectral resolution molecular normalized line data is in agreement with the lower spectral resolution data presented in Paper II. The nine starless cores are all very chemically young but show different chemical properties. "Diffuse" cores ($A_V\lesssim15$ mag: 48 and 74) show emission only in "ubiquitous" lines typical of the parental cloud chemistry (e.g. CO, CS, CH_3OH). The denser "deuterated" cores ($A_V\gtrsim22$ mag: 40 and 109) show weaker *abundances* for "ubiquitous" lines and present emission in nitrogen- (N_2H^+) and deuterium-bearing (c-C_3HD) molecules, and in some carbon chain molecules

(HC_3N), signposts of a prototypical dense core chemistry. “Oxo-sulfurated” cores ($A_V \simeq 15$–22 mag: 6, 14, 20, and 65) are in a chemical transitional stage between cloud and dense core chemistry. They are characterized by presenting large *abundances* of CH_3OH and oxo-sulfurated molecules (e.g. SO and SO_2) that disappear at higher densities, and they still present significant emission in the “ubiquitous” lines. CH_3OH was detected toward the nine cores of the complete sample with abundances of $\sim 10^{-9}$, close to the maximum value expected for gas-phase chemistry.

6. Core 47 presents high abundance of CH_3OH and N_2H^+, in spite of being the core with the lowest H_2 column density, and broad line width in some species (C_2H and N_2H^+). All this is in agreement with the hypothesis given in Paper II, which suggests that Core 47 could be a failed core.

7. The chemical evolutionary stage is not correlated with the core location in the Pipe nebula, but it is correlated with the physical properties of the cores (density and size). Thus, the chemically richer cores are the denser ones. The tentative correlation between magnetic field and chemical properties found for the initial subsample of four cores is less clear with the current sample.

The Pipe nebula is confirmed as an excellent laboratory for studying the very early stages of star formation. The nine cores studied show different morphologies and different chemical and magnetic properties. Physical and chemical properties seem to be related, although important differences arise, which evidence the complex interplay among thermal, magnetic, and turbulent energies at core scales. Therefore, a larger statistics is needed to better understand and characterize the Pipe nebula starless core evolution. In addition, other young clouds with low-mass dense cores, such as the more evolved star-forming Taurus cloud, should be studied in a similar way to prove the presented results as a general trend or, on the contrary, a particular case for a filamentary magnetized cloud.

The authors want to acknowledge all the IRAM 30-m staff for their hospitality during the observing runs, the operators and AoDs for their active and invaluable support, G. Quintana-Lacaci for his help during the observing and reduction process of MAMBO-II data, J. Kauffmann for kindly helping on the implementation of his MAMBO-II new reduction scheme, and C. Román-Zúñiga for gently allowing us to make use of the NICER maps. P.F. was partially supported by MINECO predoctoral fellowship FPU (Spain). P.F., J.M.G., M.P., F.O.A., and R.E. are partially supported by MINECO grants AYA2008-06189-C03-02 and AYA2011-30228-C03-02 (Spain), as well as by AGAUR grant 2009SGR1172 (Catalonia). F.O.A. is also supported by Deutsche Forschungsgemeinschaft (DFG) through the Emmy Noether Research grant VL 61/3-1 and through SFB 956. G.B. is funded by an Italian Space Agency (ASI) fellowship under contract number I/005/07/01. G.A.P.F. is partially supported by CNPq and FAPEMIG (Brazil). O.M. is supported by the NSC (Taiwan) ALMA-T grant to the Institute of Astronomy & Astrophysics, Academia Sinica. We made extensive use of NASA’s Astrophysics Data System (NASA/ADS).

REFERENCES

Aikawa, Y., Wakelam, V., Garrod, R. T., Herbst, E. 2008, ApJ, 674, 984
Alves, F. O. & Franco, G. A. P. 2007, A&A, 470, 597
Alves, F. O., Franco, G. A. P., & Girart, J. M. 2008, A&A, 486, L13
Brooke, T., Huard, T. L., Bourke, T. L., Boogert, A. C. A. et al. 2007, ApJ, 655, 364
Crapsi, A., Caselli, P., Walmsley, C. M., Myers, P. C., Tafalla, M., Lee, C. W., & Bourke, T. L. 2005, ApJ, 619, 379
Cuppen, H. M., van Dishoeck, E. F., Herbst, E., & Tielens, A. G. G. M. 2009, A&A, 508, 275
Forbrich, J., Lada, C. J., Muench, A. A., Alves, J., Lombardi, M. 2009, ApJ, 704, 292
Franco, G. A. P., Alves, F. O., & Girart, J. M. 2010, ApJ, 723, 146
Frau, P., Girart, J. M., Beltrán, M. T., Morata, O., Masqué, J. M., Busquet, G., Alves, F. O., Sánchez-Monge, A., & Estalella, R., & Franco, G.A.P. 2010, ApJ, 723, 1665 (Paper I)
Frau, P., Girart, J. M., & Beltrán, M. T. 2012, A&A, 537, L9 (Paper II)
Garrod, R. T., & Pauly, T. 2011, ApJ, 735, 15
de Gregorio-Monsalvo, I., Gómes, J. F., Suárez, O., Kuiper, T. B. H., Rodríguez, L. F., Jiménez-Bailón, E. 2006, ApJ, 642, 319
Heitsch, F., Ballesteros-Paredes, J., & Hartmann, L. 2009, ApJ, 704, 1735
Kandori, R., Nakajima, Y., Tamura, M., Tatematsu, K., Aikawa, Y., Naoi, T., Sugitani, K., Nakaya, H., Nagayama, T., Nagata, T., Kurita, M., Kato, D., Nagashima, C., Sato, S. 2005, AJ, 130, 2166
Kauffmann, J., Bertoldi, F., Bourke, T. L., Evans, N. J., II, & Lee, C. W. 2008, A&A, 487, 993
Keto, E., & Caselli, P. 2008, ApJ, 683, 238
Keto, E., & Caselli, P. 2010, MNRAS, 402, 1625
Kirk, H., Johnstone, D., & Di Francesco, J. 2006, ApJ, 646, 1009
Lada, C. J., Muench, A. A., Rathborne, J. M., Alves, J. F., & Lombardi, M. 2008, ApJ, 672, 410
Lombardi, M., Alves, J., & Lada, C. J. 2006, A&A, 454, 781
Masunaga, H., & Inutsuka, S. 2000, ApJ, 531, 350
Muench, A. A., Lada, C. J., Rathborne, J. M., Alves, J. F., & Lombardi, M. 2007, ApJ, 671, 1820
Onishi, T., Kawamura, A., Abe, R., Yamaguchi, N. et al. 1999, PASJ, 51, 871
Ossenkopf, V. & Henning, T. 1994, A&A, 291, 943
Padovani, M., Walmsley, C. M., Tafalla, M., Galli, D., Müller, H. S. P. 2009, A&A, 505, 1199
Padovani, M., Walmsley, C. M., Tafalla, M., Hily-Blant, P., & Pineau Des Forêts, G. 2011, A&A, 534, A77
Peretto, N., André, P., Könyves, V., et al. 2012, A&A, 541, A63
Rathborne, J. M., Lada, C. J., Muench, A. A., Alves, J. F., & Lombardi, M. 2008, ApJS, 174, 396
Román-Zúñiga, C., Lada, C. J., & Alves, J. F. 2009, ApJ, 704, 183
Román-Zúñiga, C., Alves, J. F., Lada, C. J., & Lombardi, M. 2010, ApJ, 725, 2232
Román-Zúñiga, C., Frau, P., Girart, J. M., & Alves, J. F. 2012, ApJ, 747, 149
Tafalla, M., Myers, P. C., Caselli, P., Walmsley, C. 2004, A&A, 416, 191
Tafalla, M., Santiago-García, J., Myers, P. C., Caselli, P., Walmsley, C. M., Crapsi, A. 2006, A&A, 455, 577
Taylor, S. D., Morata, O., Williams, D. A. 1998, A&A, 336, 309
Wagenblast, R., Hartquist, T. W., 1989, MNRAS, 237, 1019

APPENDIX

A. ON LINE MATERIAL: TABLES AND FIGURES

Table 6
Line parameters[a].

Molecular transition	Source	$T_{\rm MB}$ [b] (K)	$A \times \tau$ [c] (K)	$\int T_{\rm MB}{\rm d}v$ [b] (K km s^{-1})	v$_{\rm LSR}$ (km s^{-1})	Δv$_{\rm LSR}$ (km s^{-1})	τ [d]	Profile[e]
C_3H_2 ($2_{1,2}$–$1_{1,0}$)	Core 06	0.502(24)	–	0.140(5)	3.574(4)	0.262(11)	–	G
	Core 14	0.37(6)	–	0.086(11)	3.502(14)	0.22(3)	–	G
	Core 40	1.19(5)	–	0.347(9)	3.420(4)	0.273(9)	–	G
	Core 47	0.079(22)	–	0.071(8)	3.11(5)	0.85(8)	–	G
	Core 109	2.74(6)	–	0.799(13)	5.8340(20)	0.274(5)	–	G
C_2H (1–0)	Core 06	–	0.389(7)	–	3.6200(8)	0.2300(19)	0.655(21)	G
	Core 14	–	0.1650(24)	–	3.5800(13)	0.268(3)	0.450(9)	G
	Core 20	–	0.1140(25)	–	3.7900(19)	0.500(6)	0.193(16)	G
	Core 40	–	2.03(3)	–	3.4700(4)	0.1990(8)	2.58(4)	G
	Core 47	–	0.0345(5)	–	3.140(7)	0.903(15)	0.1000(4)	G
	Core 48	–	0.0255(5)	–	3.630(9)	0.876(21)	0.1000(16)	G
	Core 109	–	2.280(9)	–	5.89000(13)	0.1980(3)	1.530(8)	G
HCN (1–0)	Core 06	–	0.025(6)	–	3.56(3)	0.76(8)	0.11(5)	G
	Core 20	–	0.059(16)	–	3.58(3)	0.68(7)	0.24(8)	G
	Core 40	–	1.55(11)	–	3.410(16)	0.334(22)	6.0(5)	NS
	Core 47	–	0.051(13)	–	2.93(3)	0.72(7)	0.27(8)	G
	Core 48	–	0.33(10)	–	3.54(5)	0.90(11)	2.4(1.2)	G
	Core 109	–	2.53(3)	–	5.93(7)	0.16(22)	0.25(10)	NS
		–	6.10(3)	–	5.72(7)	0.25(22)	10.20(10)	
N_2H^+ (1–0)	Core 06	–	0.119(5)	–	3.5000(16)	0.257(4)	0.10(10)	G
	Core 14	–	0.0341(16)	–	3.500(5)	0.206(10)	0.10(9)	G
	Core 40	–	0.219(12)	–	3.4000(19)	0.249(5)	0.171(25)	G
	Core 47	–	0.0100(9)	–	3.00(4)	0.59(6)	0.10(3)	G
	Core 109	–	0.904(14)	–	5.8000(5)	0.2150(11)	0.467(11)	G
$C^{34}S$ (2–1)	Core 06	0.207(16)	–	0.055(3)	3.551(7)	0.247(15)	0.182(18)	G
	Core 14	0.267(25)	–	0.068(5)	3.545(8)	0.241(20)	0.48(5)	G
	Core 20	0.18(4)	–	0.057(7)	3.718(19)	0.30(4)	0.154(15)	G
	Core 40	0.268(16)	–	0.069(3)	3.381(5)	0.241(13)	0.140(14)	G
	Core 47	0.07(4)	–	0.042(10)	3.00(7)	0.53(13)	0.036(4)	G
	Core 48	0.187(23)	–	0.041(4)	3.729(11)	0.20(3)	0.26(3)	G
	Core 74	0.137(21)	–	0.027(3)	4.236(12)	0.186(23)	0.228(23)	G
	Core 109	0.34(3)	–	0.083(5)	5.825(7)	0.233(17)	0.185(18)	G
CH_3OH ($2_{0,2}$–$1_{0,1}$)	Core 06	1.841(15)	–	0.55(3)	3.512(7)	0.281(15)	–	G
	Core 14	1.30(3)	–	0.416(21)	3.519(7)	0.300(17)	–	G
	Core 20	0.43(3)	–	0.145(10)	3.653(10)	0.316(24)	–	G
	Core 40	1.230(15)	–	0.327(16)	3.375(6)	0.250(14)	–	G
	Core 47	0.45(3)	–	0.138(10)	2.845(10)	0.288(24)	–	G
	Core 48	0.199(25)	–	0.057(6)	3.652(13)	0.27(3)	–	G
	Core 65	0.15(3)	–	0.098(9)	5.04(3)	0.59(6)	–	G
	Core 74	0.257(21)	–	0.068(5)	4.201(9)	0.247(22)	–	G
	Core 109	1.27(3)	–	0.343(18)	5.778(6)	0.254(15)	–	G
CH_3OH ($2_{-1,2}$–$1_{-1,1}$)	Core 06	1.432(15)	–	0.417(4)	3.5055(10)	0.273(3)	–	G
	Core 14	1.04(3)	–	0.306(6)	3.508(3)	0.276(7)	–	G
	Core 20	0.35(3)	–	0.094(6)	3.672(8)	0.250(20)	–	G
	Core 40	0.998(15)	–	0.252(3)	3.3705(10)	0.237(3)	–	G
	Core 47	0.33(3)	–	0.119(7)	2.847(10)	0.344(22)	–	G
	Core 48	0.134(25)	–	0.047(5)	3.641(19)	0.33(5)	–	G
	Core 65	0.12(3)	–	0.063(7)	4.98(3)	0.48(6)	–	G
	Core 74	0.212(21)	–	0.059(4)	4.201(9)	0.261(20)	–	G
	Core 109	1.03(3)	–	0.263(5)	5.7705(20)	0.240(6)	–	G
CS (2–1)	Core 06	1.20(6)	–	0.30(3)	3.429(11)	0.237(21)	4.1(4)	G
		0.56(6)	–	0.14(3)	3.698(22)	0.23(5)	–	
	Core 14	0.69(10)	–	0.41(3)	3.439(21)	0.45(4)	10.7(1.1)	SA
	Core 20	1.18(9)	–	0.34(4)	3.469(12)	0.27(3)	3.5(3)	G
		1.10(9)	–	0.35(4)	3.820(14)	0.30(3)	–	
	Core 40	1.94(7)	–	0.560(17)	3.369(4)	0.415(14)	3.1(3)	NS
	Core 47	1.16(9)	–	0.609(24)	2.817(10)	0.495(23)	0.81(8)	G
	Core 48	0.79(7)	–	0.402(18)	3.684(11)	0.477(22)	6.0(6)	SA
	Core 74	0.66(8)	–	0.268(17)	4.245(13)	0.38(3)	5.1(5)	G
	Core 109	1.93(8)	–	0.743(17)	5.836(4)	0.361(9)	4.2(4)	G

[a] Line parameters of the detected lines. Multiple velocity components are shown if present. For the molecular transitions with no hyperfine components, the parameters for the transitions labeled as G (last column) have been derived from a Gaussian fit while line parameters of NS and SA profiles have been derived from the intensity peak ($T_{\rm MB}$), and zero (integrated intensity), first (line velocity) and second (line width) order moments of the emission. For the molecular transitions with hyperfine components, the parameters have been derived using the hyperfine component fitting method of the CLASS package. The value in parenthesis shows the uncertainty of the last digit/s. If the two first significative digits of the error are smaller than 25, two digits are given to better constrain it.

[b] Only for molecular transitions with no hyperfine components.

[c] Only for molecular transitions with hyperfine components.

[d] Derived from a CLASS hyperfine fit for molecular transitions with hyperfine components. Derived numerically for CS, $C^{34}S$, ^{13}CO, and $C^{18}O$ using Eq. 1 from Paper I. A value of 0.1 is assumed when no measurement is available.

[e] G: Gaussian profile. NS: Non-symmetric profile. SA: Self-absorption profile.

Table 7
Line parameters[a] (Continuation).

Molecular transition	Source	$T_{\rm MB}$ [b] (K)	$A\times\tau$ [c] (K)	$\int T_{\rm MB}{\rm d}v$ [b] (K km s^{-1})	v$_{\rm LSR}$ (km s^{-1})	Δv$_{\rm LSR}$ (km s^{-1})	τ [d]	Profile[e]
$C^{18}O$ (1–0)	Core 06	2.61(6)	–	1.137(13)	3.5180(20)	0.409(6)	0.33(3)	G
	Core 14	4.10(6)	–	1.875(13)	3.4890(10)	0.430(4)	0.84(8)	G
	Core 20	2.97(6)	–	0.798(10)	3.6600(20)	0.253(4)	0.31(3)	G
	Core 47	2.51(6)	–	1.116(14)	2.791(3)	0.417(6)	0.50(5)	G
	Core 74	2.51(5)	–	0.961(10)	4.1920(20)	0.360(5)	0.59(6)	G
	Core 109	2.42(5)	–	0.991(11)	5.7640(20)	0.384(5)	0.51(5)	G
^{13}CO (1–0)	Core 06	7.78(6)	–	4.98(11)	3.536(5)	0.601(6)	1.83(18)	G
		1.96(6)	–	1.44(11)	4.133(24)	0.69(3)	–	
	Core 14	7.13(6)	–	4.407(18)	3.4280(10)	0.581(4)	4.7(5)	G
		4.13(6)	–	2.639(4)	3.8680(20)	0.600(6)	–	
	Core 20	9.12(6)	–	5.903(16)	3.7060(10)	0.6080(20)	1.71(17)	G
	Core 47	5.99(5)	–	3.647(12)	2.7550(10)	0.5720(20)	2.8(3)	G
		4.27(5)	–	3.912(14)	3.2300(20)	0.862(4)	–	
	Core 74	5.41(5)	–	3.598(21)	4.2320(20)	0.625(4)	3.3(3)	G
		2.15(5)	–	1.829(22)	5.221(5)	0.800(11)	–	
	Core 109	5.68(6)	–	3.577(18)	5.7990(10)	0.591(3)	2.8(3)	G
		0.83(6)	–	1.11(3)	3.275(14)	1.26(4)	–	
CN (1–0)	Core 06	–	0.17(5)	–	3.640(15)	0.30(3)	1.2(4)	G
	Core 14	–	0.051(9)	–	3.64(8)	0.81(15)	0.1(7)	G
	Core 40	–	0.65(22)	–	3.430(21)	0.36(5)	3.9(1.3)	G
	Core 47	–	0.10(4)	–	2.98(5)	0.80(13)	0.9(5)	G
	Core 109	–	1.41(22)	–	5.930(5)	0.162(11)	1.13(23)	G
		–	2.3(1.3)	–	5.670(7)	0.101(16)	4.(3)	
$C^{34}S$ (3–2)	Core 14	0.12(3)	–	0.034(4)	3.488(17)	0.27(4)	1.70(17)	G
	Core 20	0.15(5)	–	0.064(11)	3.59(3)	0.40(8)	0.25(3)	G
	Core 109	0.18(6)	–	0.064(8)	5.82(3)	0.340(00)	0.189(19)	G
CS (3–2)	Core 06	0.68(6)	–	0.220(10)	3.480(7)	0.303(15)	–	G
	Core 14	0.14(4)	–	0.072(7)	3.59(3)	0.48(4)	38.(4)	G
	Core 20	0.67(6)	–	0.179(8)	3.502(8)	0.2500(00)	5.7(6)	G
		0.65(6)	–	0.173(8)	3.797(9)	0.2500(00)	–	
	Core 40	1.09(9)	–	0.270(13)	3.414(6)	0.234(15)	–	G
	Core 47	0.35(6)	–	0.148(11)	2.896(15)	0.39(3)	–	G
	Core 48	0.28(5)	–	0.122(10)	3.772(17)	0.41(4)	–	G
	Core 65	0.16(4)	–	0.124(11)	5.07(4)	0.73(9)	–	G
	Core 74	0.34(5)	–	0.100(8)	4.200(11)	0.277(20)	–	G
	Core 109	1.01(8)	–	0.366(14)	5.810(7)	0.339(15)	4.2(4)	G
N_2D^+ (2–1)[f]	Core 40	0.084(20)	–	0.019(3)	3.280(15)	0.21(3)	–	G
	Core 109	0.31(4)	–	0.109(7)	5.673(11)	0.331(22)	–	G
DCO^+ (3–2)	Core 06	0.44(13)	–	0.22(3)	3.58(3)	0.48(11)	–	G
	Core 109	0.70(11)	–	0.151(18)	5.828(13)	0.202(21)	–	G
$C^{18}O$ (2–1)	Core 06	4.23(13)	–	1.437(18)	3.5240(20)	0.319(5)	1.11(11)	G
	Core 14	3.52(23)	–	1.76(4)	3.522(5)	0.469(13)	0.94(9)	G
	Core 20	3.26(25)	–	1.07(4)	3.712(5)	0.308(12)	0.52(5)	G
	Core 40	3.6(3)	–	1.33(4)	3.323(5)	0.349(12)	–	G
	Core 47	2.61(22)	–	1.22(4)	2.779(6)	0.440(15)	0.52(5)	G
	Core 48	4.05(15)	–	1.287(19)	3.6750(20)	0.299(5)	–	G
	Core 65	2.65(14)	–	1.599(24)	4.936(4)	0.567(10)	–	G
	Core 74	2.54(21)	–	0.77(3)	4.216(5)	0.284(12)	0.89(9)	G
	Core 109	3.15(11)	–	1.035(16)	5.7820(20)	0.309(5)	0.86(9)	G
^{13}CO (2–1)	Core 06	6.23(12)	–	4.51(5)	3.604(4)	0.681(9)	6.2(6)	G
		1.50(12)	–	0.56(4)	4.260(10)	0.35(3)	–	
	Core 14	5.66(12)	–	2.88(5)	3.378(4)	0.477(4)	5.2(5)	G
		5.05(12)	–	2.88(7)	3.819(5)	0.536(11)	–	
	Core 20	7.50(13)	–	6.00(4)	3.7100(20)	0.751(5)	2.9(3)	G
	Core 47	6.01(12)	–	5.05(8)	3.005(6)	0.790(9)	2.9(3)	G
		3.08(12)	–	0.95(7)	2.631(5)	0.291(12)	–	
	Core 74	4.24(6)	–	2.417(17)	4.2550(20)	0.536(4)	4.9(5)	G
		1.79(6)	–	1.168(19)	5.259(5)	0.614(12)	–	
	Core 109	5.36(11)	–	2.80(3)	5.8310(20)	0.491(5)	4.8(5)	G
		0.61(11)	–	0.70(4)	3.38(3)	1.09(8)	–	

Footnotes [a] to [e] as in Table 6.
[f] Only the main component is detected.

Table 8

Molecular column densities of the chemical species observed toward the Pipe nebula cores in cm^{-2}.

Source	C_3H_2 ($2_{1,2}$–$1_{1,0}$)[a]	C_2H (1–0)	HCN (1–0)	N_2H^+ (1–0)	$C^{34}S$ (2–1)[b]	CH_3OH ($2_{0,2}$–$1_{0,1}$)[a]	CS (2–1)[b]	$C^{18}O$ (1–0)
Core 06	6.40×10^{11}	4.15×10^{12}	2.22×10^{11}	5.20×10^{11}	2.95×10^{11}	2.62×10^{13}	1.23×10^{13}	1.42×10^{15}
Core 14	3.50×10^{11}	3.05×10^{12}	$< 5.42 \times 10^{10}$	9.70×10^{10}	6.01×10^{11}	1.64×10^{13}	3.05×10^{13}	2.78×10^{15}
Core 20	$< 1.78 \times 10^{11}$	5.12×10^{12}	3.08×10^{11}	$< 4.09 \times 10^{10}$	3.05×10^{11}	4.18×10^{12}	1.18×10^{13}	1.05×10^{15}
Core 40	2.91×10^{12}	1.22×10^{13}	2.57×10^{12}	4.89×10^{11}	2.94×10^{11}	1.28×10^{13}	7.19×10^{12}	–
Core 47	3.52×10^{11}	5.12×10^{12}	–	1.30×10^{11}	2.86×10^{11}	4.54×10^{12}	–	1.40×10^{15}
Core 48	$< 7.68 \times 10^{10}$	3.85×10^{12}	2.59×10^{12}	$< 3.79 \times 10^{10}$	2.95×10^{11}	2.23×10^{12}	1.51×10^{13}	–
Core 65	$< 7.25 \times 10^{10}$	$< 1.33 \times 10^{11}$	–	$< 3.68 \times 10^{10}$	$< 1.07 \times 10^{11}$	3.64×10^{12}	–	–
Core 74	$< 1.37 \times 10^{11}$	–	$< 4.76 \times 10^{10}$	$< 4.46 \times 10^{10}$	2.20×10^{11}	2.39×10^{12}	9.88×10^{12}	1.24×10^{15}
Core 109	1.63×10^{13}	1.05×10^{13}	9.67×10^{12}	6.79×10^{11}	3.67×10^{11}	1.36×10^{13}	1.24×10^{13}	1.24×10^{15}

[a] Transition with no opacity measurements available, thus optically thin emission is assumed to obtain lower limits of the column densities.

[b] We assume optically thin emission for some cores with no data or no detection in CS/$C^{34}S$ to obtain a lower limit of the column density.

Table 9

Molecular column densities of the chemical species observed toward the Pipe nebula cores in cm^{-2} (continuation).

Source	^{13}CO (1–0)	CN (1–0)	$C^{34}S$ (3–2)[a]	CS (3–2)[a]	N_2D^+ (2–1)[b]	DCO^+ (3–2)[b]	$C^{18}O$ (2–1)	^{13}CO (2–1)
Core 06	2.30×10^{16}	1.20×10^{12}	$< 7.39 \times 10^{10}$	4.49×10^{11}	$< 8.58 \times 10^{8}$	7.39×10^{11}	9.05×10^{14}	2.12×10^{16}
Core 14	4.14×10^{16}	1.16×10^{12}	1.12×10^{12}	4.26×10^{13}	$< 7.91 \times 10^{9}$	$< 1.43 \times 10^{13}$	1.04×10^{15}	1.16×10^{16}
Core 20	1.39×10^{16}	$< 1.58 \times 10^{11}$	3.19×10^{11}	8.71×10^{12}	$< 1.73 \times 10^{10}$	$< 3.54 \times 10^{13}$	5.21×10^{14}	6.96×10^{15}
Core 40	–	4.69×10^{12}	–	6.18×10^{11}	3.63×10^{9}	$< 7.60 \times 10^{11}$	9.33×10^{14}	–
Core 47	2.11×10^{16}	2.49×10^{12}	$< 6.22 \times 10^{10}$	3.02×10^{11}	$< 4.38 \times 10^{9}$	–	5.96×10^{14}	1.17×10^{16}
Core 48	–	$< 1.23 \times 10^{11}$	$< 9.17 \times 10^{10}$	2.62×10^{11}	$< 3.02 \times 10^{9}$	$< 1.37 \times 10^{12}$	9.77×10^{14}	–
Core 65	–	$< 9.79 \times 10^{10}$	$< 6.79 \times 10^{10}$	3.24×10^{11}	$< 3.09 \times 10^{9}$	–	9.35×10^{14}	–
Core 74	2.36×10^{16}	$< 1.31 \times 10^{11}$	$< 1.18 \times 10^{11}$	2.06×10^{11}	$< 3.76 \times 10^{9}$	$< 4.30 \times 10^{11}$	4.66×10^{14}	9.66×10^{15}
Core 109	2.10×10^{16}	2.82×10^{12}	2.34×10^{11}	5.09×10^{12}	1.39×10^{11}	1.13×10^{12}	5.94×10^{14}	1.04×10^{16}

[a] We assume optically thin emission for some cores with no data or no detection in $C^{34}S$ to obtain a lower limit of the column density.

[b] Transition with no opacity measurements available, thus optically thin emission is assumed to obtain lower limits of the column densities.

Table 10

H_2 column densities, N_{H_2}, of the Pipe nebula cores in cm^{-2} [a].

	Molecular survey[b]				CO survey[c]	
Source	10.5″	15.0″	21.5″	27.0″	11.0″	22.5″
Core 06	2.12×10^{22}	1.43×10^{22}	1.31×10^{22}	9.73×10^{21}	2.12×10^{22}	1.18×10^{22}
Core 14	1.59×10^{22}	1.26×10^{22}	1.10×10^{22}	1.01×10^{22}	7.48×10^{21}	7.79×10^{21}
Core 20	7.66×10^{21}	6.26×10^{21}	5.39×10^{21}	5.08×10^{21}	5.22×10^{21}	4.41×10^{21}
Core 40	1.32×10^{22}	1.28×10^{22}	1.12×10^{22}	1.07×10^{22}	1.36×10^{22}	1.06×10^{22}
Core 47	1.03×10^{22}	6.93×10^{21}	5.59×10^{21}	5.03×10^{21}	8.64×10^{21}	3.96×10^{21}
Core 48	1.09×10^{22}	8.88×10^{21}	7.38×10^{21}	6.99×10^{21}	1.34×10^{22}	6.71×10^{21}
Core 65	1.16×10^{22}	1.15×10^{22}	1.12×10^{22}	8.34×10^{21}	1.16×10^{22}	1.01×10^{22}
Core 74	6.98×10^{21}	6.75×10^{21}	5.96×10^{21}	5.65×10^{21}	1.16×10^{22}	5.74×10^{21}
Core 109	4.19×10^{22}	3.73×10^{22}	3.23×10^{22}	3.08×10^{22}	4.49×10^{22}	3.10×10^{22}

[a] Average column densities are calculated within one beam area. The values of $\kappa_{250\ \mathrm{GHz}}$ and T_{dust} are the same as for Table 3. These values are combined with the molecular column densities to find the molecular abundances in the same beam area.

[b] Observations toward the dust continuum emission peak (Table 3). The correspondence is: 10.″5 with DCO^+, CN (2–1), N_2D^+ (3–2) and $H^{13}CO^+$ (3–2); 15.″0 with $C^{34}S$ (3–2), CS (3–2), and N_2D^+ (2–1); 21.″5 with CN (1–0); and, finally, 27.″0 with C_3H_2 (2–1), HCN (1–0), N_2H^+ (1–0), $C^{34}S$ (2–1), CH_3OH (2–1) and CS (2–1).

[c] Observations toward the extinction peak (Table 1). The correspondence is: 11.″0 with $C^{18}O$ (2–1), and ^{13}CO (2–1); 22.″5 with $C^{18}O$ (1–0), and ^{13}CO (1–0).

Table 11
Abundances[a] of the chemical species with respect to H_2 observed toward the Pipe nebula cores.

Source	C_3H_2[b]	C_2H	HCN	N_2H^+	$C^{34}S$[c]	CH_3OH[b]	CS[c]	$C^{18}O$
Core 06	6.58×10^{-11}	4.27×10^{-10}	2.28×10^{-11}	5.35×10^{-11}	3.03×10^{-11}	2.69×10^{-9}	1.27×10^{-9}	1.21×10^{-7}
Core 14	3.47×10^{-11}	3.02×10^{-10}	$< 5.37 \times 10^{-12}$	9.61×10^{-12}	5.95×10^{-11}	1.63×10^{-9}	3.02×10^{-9}	3.57×10^{-7}
Core 20	$< 3.50 \times 10^{-11}$	1.01×10^{-9}	6.06×10^{-11}	$< 8.05 \times 10^{-12}$	6.01×10^{-11}	8.23×10^{-10}	2.32×10^{-9}	2.38×10^{-7}
Core 40	2.73×10^{-10}	1.14×10^{-9}	2.41×10^{-10}	4.58×10^{-11}	2.76×10^{-11}	1.20×10^{-9}	6.74×10^{-10}	–
Core 47	6.99×10^{-11}	1.02×10^{-9}	–	2.58×10^{-11}	5.68×10^{-11}	9.02×10^{-10}	–	3.52×10^{-7}
Core 48	$< 1.10 \times 10^{-11}$	5.51×10^{-10}	3.71×10^{-10}	$< 5.43 \times 10^{-12}$	4.21×10^{-11}	3.19×10^{-10}	2.17×10^{-9}	–
Core 65	$< 8.70 \times 10^{-12}$	$< 1.15 \times 10^{-11}$	–	$< 4.41 \times 10^{-12}$	$< 9.29 \times 10^{-12}$	4.36×10^{-10}	–	–
Core 74	$< 2.42 \times 10^{-11}$	–	$< 8.43 \times 10^{-12}$	$< 7.90 \times 10^{-12}$	3.89×10^{-11}	4.23×10^{-10}	1.75×10^{-9}	2.15×10^{-7}
Core 109	5.28×10^{-10}	3.41×10^{-10}	3.14×10^{-10}	2.20×10^{-11}	1.19×10^{-11}	4.43×10^{-10}	4.02×10^{-10}	3.99×10^{-8}

[a] See Tables 8, 9, and 10 for line and dust column densities.

[b] Transition with no opacity measurements available, thus optically thin emission is assumed to estimate a lower limit of the column densities and, consequently, of the abundances.

[c] We assume optically thin emission for some cores with no data or no detection in CS/$C^{34}S$ to obtain a lower limit of the column density and, as a result, also for the abundance.

Table 12
Abundances[a] of the chemical species with respect to H_2 observed toward the Pipe nebula cores.

Source	^{13}CO	CN	N_2D^+[b]	DCO^+[b]
Core 06	1.95×10^{-6}	9.16×10^{-11}	$< 8.82 \times 10^{-14}$	3.49×10^{-11}
Core 14	5.31×10^{-6}	1.06×10^{-10}	$< 7.84 \times 10^{-13}$	$< 1.83 \times 10^{-9}$
Core 20	3.15×10^{-6}	$< 3.10 \times 10^{-11}$	$< 3.41 \times 10^{-12}$	$< 8.02 \times 10^{-9}$
Core 40	–	4.19×10^{-10}	2.83×10^{-13}	$< 7.19 \times 10^{-11}$
Core 47	5.32×10^{-6}	4.45×10^{-10}	$< 8.70 \times 10^{-13}$	–
Core 48	–	$< 1.76 \times 10^{-11}$	$< 4.33 \times 10^{-13}$	$< 2.04 \times 10^{-10}$
Core 65	–	$< 1.17 \times 10^{-11}$	$< 3.71 \times 10^{-13}$	–
Core 74	4.11×10^{-6}	$< 2.33 \times 10^{-11}$	$< 6.65 \times 10^{-13}$	$< 7.50 \times 10^{-11}$
Core 109	6.76×10^{-7}	8.72×10^{-11}	3.73×10^{-12}	2.69×10^{-11}

[a] See Tables 8, 9, and 10 for line and dust column densities.

[b] Transition with no opacity measurements available, thus optically thin emission is assumed to estimate a lower limit of the column densities and, consequently, of the abundances.

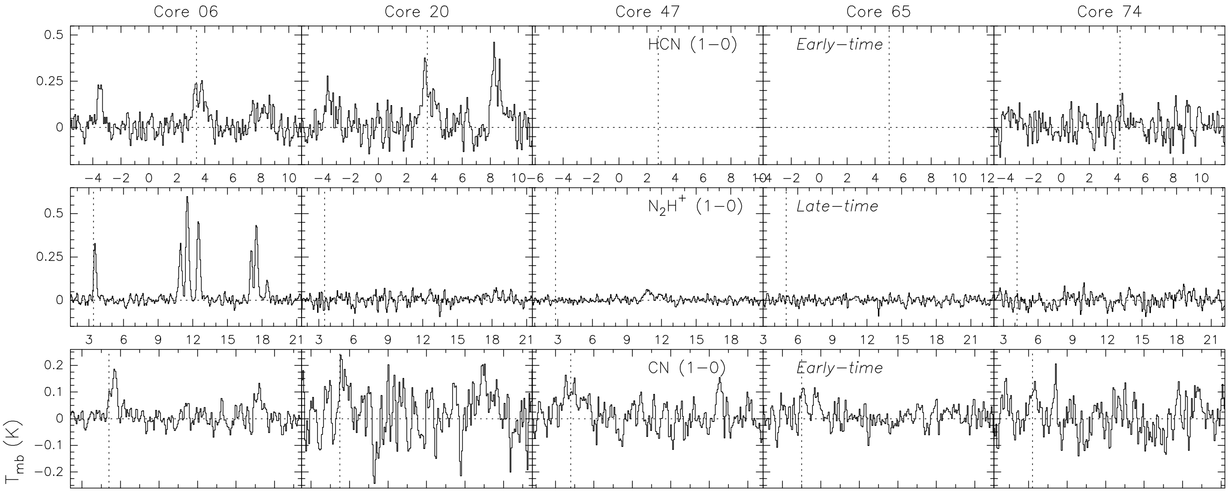

Figure 8. IRAM 30-m line spectra of the molecular transitions with hyperfine components presented in Paper I toward the five new selected cores of the Pipe nebula presented in this work (Table 1). *Columns*: single cores named above the top panel of each column. *Rows*: single molecular transition specified on the third column. Empty panels represent non-observed molecular lines. The velocity range is 16.5, 20 and 12 km s^{-1} for HCN (1–0), N_2H^+ (1–0), and CN (1–0), respectively. Horizontal axis shows the velocity, and the v_{LSR} of each core is marked with a vertical dotted line. Vertical axis shows the T_{MB} of the emission, and the zero level is marked by a horizontal dotted line.

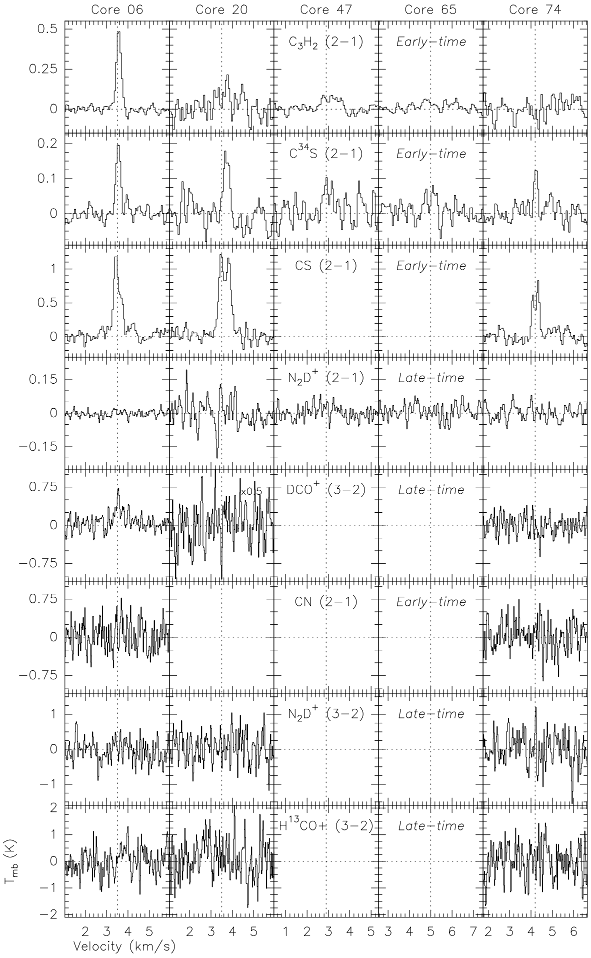

Figure 9. IRAM 30-m line spectra of the molecular transitions without hyperfine components presented in Paper I toward the five new selected cores of the Pipe nebula presented in this work (Table 1). *Columns*: single cores named above the top panel of each column. *Rows*: single molecular transition specified on the third column. Empty panels represent non-observed molecular lines. Axes and dotted lines are as in Fig. 8. The velocity range is 5 km s^{-1} centered on the v$_{\rm LSR}$ of each core.

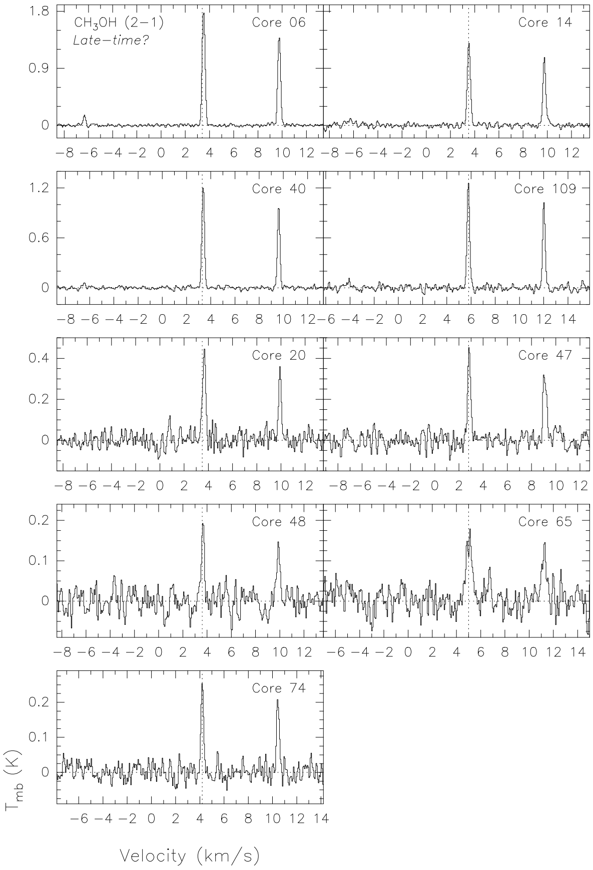

Figure 10. IRAM 30-m line spectra of CH$_3$OH (2–1) toward the nine selected cores of the Pipe nebula (Table 1). This molecular transition is not presented in Paper I. The name of the core is indicated in the top right corner of each panel. Axes and dotted lines are as in Fig. 8. The velocity range is 22 km s^{-1}.

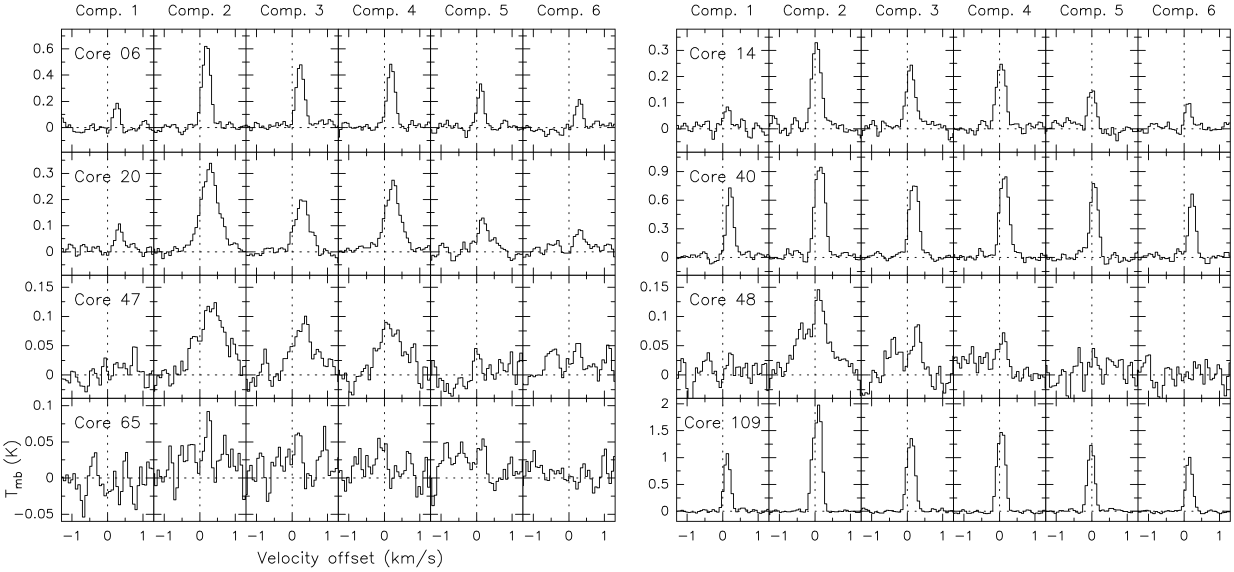

Figure 11. IRAM 30-m line spectra of C_2H (1–0) (*early-time*) toward eight cores of the Pipe nebula (Table 1). This molecular transition is not presented in Paper I. The component number following Padovani et al. (2009) is indicated above each column. The name of the core is indicated in the left panel of each row. Axes and dotted lines are as in Fig. 8. The velocity range is 2.5 km s^{-1}.

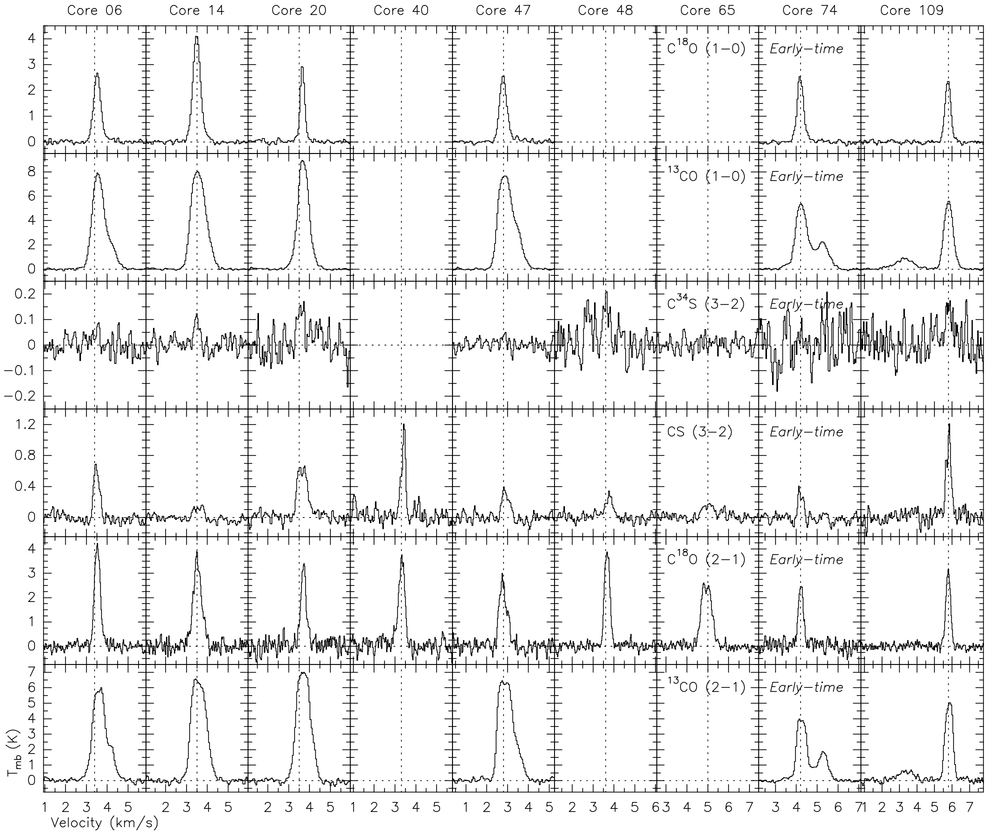

Figure 12. IRAM 30-m line spectra of the molecular transitions without hyperfine components toward the nine selected cores of the Pipe nebula (Table 1). These molecular transitions are not presented in Paper I. *Columns*: single cores named above the top panel of each column. *Rows*: single molecular transition specified on the seventh column. Empty panels represent non-observed molecular lines. Axes and dotted lines are as in Fig. 8. The velocity range is 5 km s^{-1} except for Core 109 (6 km s^{-1}).

VI

Starless cores in the magnetically dominated Pipe nebula II. Wide band low spectral resolution observations

A&A 537, L9 (2012)
DOI: 10.1051/0004-6361/201118612
© ESO 2012

Astronomy & Astrophysics

L E

Chemical differentiation toward the Pipe nebula starless cores

P. Frau[1], J. M. Girart[1], and M. T. Beltrán[2]

[1] Institut de Ciències de l'Espai (CSIC-IEEC), Campus UAB, Facultat de Ciències, Torre C5p, 08193 Bellaterra, Catalunya, Spain
e-mail: `[frau;girart]@ice.cat`
[2] INAF-Osservatorio Astrofisico di Arcetri, Largo Enrico Fermi 5, 50125 Firenze, Italy
e-mail: `mbeltran@arcetri.astro.it`

Received 8 December 2011 / Accepted 22 December 2011

ABSTRACT

We use the new IRAM 30-m FTS backend to perform an unbiased ~15 GHz wide survey at 3 mm toward the Pipe nebula young diffuse starless cores. We discover an unexpectedly rich chemistry. We propose a new observational classification based on the 3 mm molecular line emission normalized by the core visual extinction (A_V). On the basis of this classification, we report a clear differentiation between cores in terms of chemical composition and line emission properties, which enables us to define three molecular core groups. The "diffuse" cores, $A_V \lesssim 15$, have a poor chemistry with mainly simple species (e.g. CS and C_2H). The "oxo-sulfurated" cores, $A_V \simeq 15$–22, appear to be abundant in species such as SO and SO_2, but also in HCO, which seem to disappear at higher densities. Finally, the "deuterated" cores, $A_V \gtrsim 22$, have a typical evolved chemistry prior to the onset of the star formation process, with nitrogenated and deuterated species, as well as carbon chain molecules. On the basis of these categories, one of the "diffuse" cores (core 47) has the spectral line properties of the "oxo-sulfurated" ones, which suggests that it is a failed core.

Key words. stars: formation – ISM: lines and bands – ISM: individual objects: Pipe nebula

1. Introduction

A new generation of sensitive receivers and wideband backends allows the detailed study of the chemistry of faint starless cores. Several surveys have been performed toward them reporting a rich but relatively simple chemistry consisting of essentially carbon with significant sulfur and nitrogen bearing molecules, in addition to later deuteration that can be used as a chemical clock (e.g., Turner 1994; Turner et al. 2000; Hirota & Yamamoto 2006; Tafalla et al. 2006; Bergin & Tafalla 2007). From the theoretical side, several papers have tried to model the starless core chemistry self-consistently (Aikawa et al. 2001; Garrod et al. 2005; Keto & Caselli 2008).

The Pipe nebula is a nearby (145 pc: Alves & Franco 2007) cloud that harbors more than one hundred low-mass (~1 $M_\odot$) starless cores, most of them gravitationally unbound but confined by the thermal/magnetic pressure of the whole cloud (Alves et al. 2008; Lada et al. 2008; Franco et al. 2010). The Pipe nebula differs from the other nearby dark cloud complexes such as Taurus or ρ Ophiuchus because it has a very low star formation efficiency (Onishi et al. 1999; Forbrich et al. 2009; Román-Zúñiga et al. 2010; Román-Zúñiga et al. 2012). Thus, the Pipe nebula is an ideal target for studying the physical and chemical conditions in a pristine environment prior to the onset of the star formation process, as numerous studies have shown (e.g., Brooke et al. 2007; Muench et al. 2007; Rathborne et al. 2008). Frau et al. (2010) presented the first results of an extensive continuum and molecular line study of a subset of a selected sample of cores distributed in the different regions of the Pipe nebula: *bowl*, *stem*, and B59. The cores are in general less dense and less chemically evolved than starless cores in other star forming regions that have been studied (e.g. Crapsi et al. 2005). We find very different morphologies and densities, and no clear correlation of the chemical evolutionary stage of the cores with their location in the cloud. The Pipe nebula starless cores have been shown to be more heterogeneous than expected.

In this work, we present a wide (~15 GHz) unbiased chemical survey at 3 mm toward a larger sample of Pipe nebula starless cores, spanning a factor of six in their visual extinction (A_V) peaks. This is a first step in characterizing their varied chemistry before proceeding to in-depth modeling in the future.

2. FTS observations and data reduction

We performed pointed observations toward the Pipe nebula cores 06, 08, 12, 14, 20, 33, 40, 47, 48, 56, 65, 87, 102, and 109, following the numbering of Rathborne et al. (2008), and toward a position with no cores. We pointed either toward the continuum emission peak (Frau et al. 2010), if available, or toward the $C^{18}O$ pointing center reported by Muench et al. (2007). We assumed that the pointing centers were the densest region of the cores, hence have the richest chemistry. We used the EMIR heterodyne receiver of the IRAM 30-m telescope tuned at the C_2H (1–0) transition (87.3169 GHz). At this frequency, the telescope delivers $\theta_{\mathrm{HPBW}} = 28.''1$, $B_{\mathrm{eff}} = 0.81$, and $F_{\mathrm{eff}} = 0.95$. The observations were carried out in August 2011, when we were the first astrophysicists to use the FTS spectrometer as the spectral backend. We selected a channel resolution of 195 kHz (≃0.6 km s^{-1} at 3 mm), which provided a total bandwidth of 14.86 GHz covering the frequency ranges from 82.01 to 89.44 GHz, and from 97.69 to 105.12 GHz. We used the frequency-switching mode with a frequency throw of 7.5 MHz. System temperatures ranged from ~110 K to ~150 K. The accuracy of the pointing was checked every two hours. We reduced the data using the CLASS package of the GILDAS[1] software. The baseline in the frequency switching mode for such a large bandwidth (~3.7 GHz for each chunk) has

---

[1] Available at `http://www.iram.fr/IRAMFR/GILDAS`

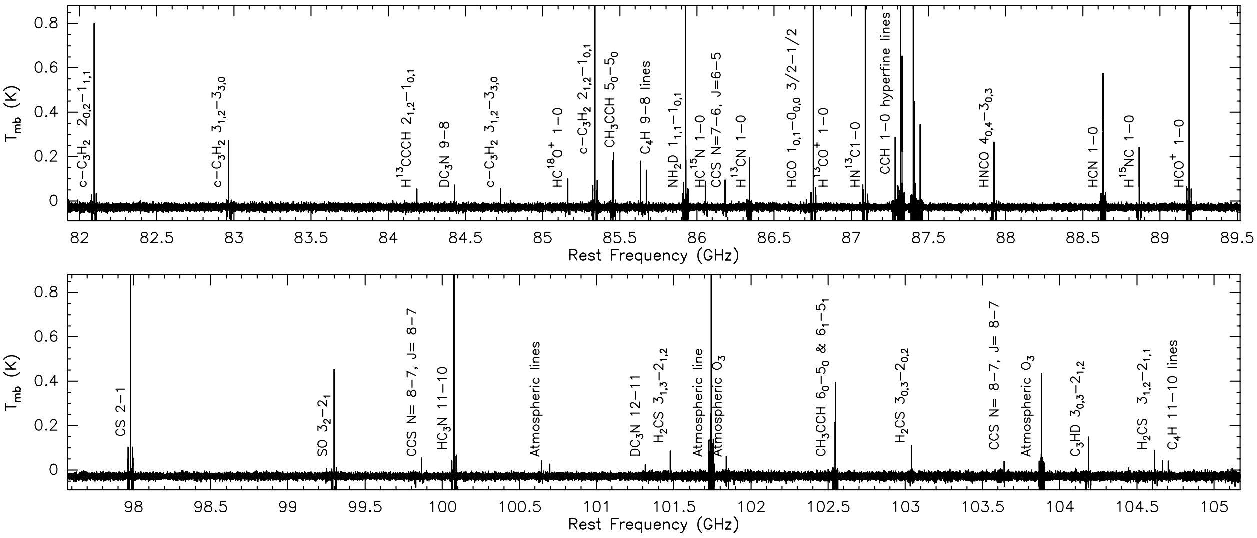

Fig. 1. IRAM 30-m EMIR+FTS full bandwidth spectrum toward core 12. The most important detected molecular transitions are labeled within the plot. *The upper and lower panels* show the ~7.6 GHz lower and upper sidebands, respectively. The noise rarely exceeds 10 mK. The negative emission are the twin negative counterparts of the positive emission due to the frequency-switching observing mode.

a complicated shape with sinusoidal-like ripples. Nevertheless, since the observed lines are very narrow ($\lesssim$0.5 km s^{-1}, similar to the effective spectral resolution), the baselines can be efficiently removed if narrow frequency windows are used ($\lesssim$20 MHz). The resulting typical rms noise was $\simeq$8 mK at the 195 kHz spectral resolution.

3. Results

The large width of the available bandwidth, 14.86 GHz, has allowed us to carry out an unbiased survey, covering about a third of the observable 3 mm window. We used the *Splatalogue*[2] tool to identify possible lines. We considered as tentative detections those lines with intensities in the 3–5σ range, and fiducial detections those higher than 5σ. We detected 53 transitions from a total of 31 molecules (including isotopologues). In Fig. 1, we indicate the observed bandwidth toward core 12 and the main molecular species. Most of the detected lines were identified in this core, the one with the highest A_V and the brightest molecular line emission of the sample. However, there are a few sulfur-bearing molecular lines that were not detected toward core 12 but found to be present in other cores: SO_2 $3_{1,3}$–$2_{0,2}$, ^{34}SO 3_2–2_1, and OCS 7–6. We reported tentative detections (~4σ) of $HOCO^+$ (cores 6 and 102), l-C_3H (cores 12 and 109), and HCCNC (core 12). In all the cores, we also identified several Earth atmospheric lines, mostly from ozone.

The cores with the brightest detected lines are those with the highest A_V (cores 12, 87 and 109) owing to their larger gas column densities. To avoid a column density bias (our core sample spans a factor of six in A_V), we normalized the intensity by dividing the spectra by the A_V peak of the core. We used the values obtained by Román-Zúñiga et al. (2010) from dust extinction maps that have an angular resolution similar to our observations. This definition is similar to that of molecular abundance for optically thin lines. Figure 2 shows a selected sample of the brightest normalized lines toward all of the sample, with the cores ordered by their A_V peak. In this figure, we ordered the molecules into families taking into account their atomic composition.

In general, the 3 mm transitions of the lightest species of most of the molecular families (blue spectra in Fig. 2) were detected in all the cores of our sample: C_2H, HCO^+, CS, SO, and HCN. The molecule c–C_3H_2 was detected in all but two cores. The 3 mm main transitions of these molecules can be assumed to be "ubiquitous lines" in starless cores. The molecular transitions HCO^+ 1–0, CS 2–1, and HCN 1–0 display little variations in normalized intensity. These molecules have large dipole moments and high abundances, hence are likely to have large optical depths. In addition, the HCO^+ 1–0 and HCN 1–0 transitions can be affected by absorption by low density foreground gas (Girart et al. 2000). Indeed, the relative HCN 1-0 hyperfine line intensities of cores 12, 40, and 87 suggest that this transition is out of LTE. The normalized intensities of the other three ubiquitous lines show significant variations within the sample. However, while C_2H 1–0 and c–C_3H_2 $2_{1,2}$–$1_{0,1}$ tend to increase with A_V, the SO 3_2–2_1 line appears to have the largest normalized intensities in the cores with visual extinction in the range of 15 to 22 mag.

Several molecular transitions were only detected toward cores with $A_V \gtrsim 15$. The optically thin $H^{13}CO^+$ 1–0 and $HC^{18}O^+$ 1–0 transitions, and the transition HNCO $4_{0,4}$–$3_{0,3}$, have larger normalized intensities with increasing column densities. The detected transitions from oxo-sulfurated molecules (SO 2_2–1_1, ^{34}SO 3_2–2_1, SO_2 $3_{1,3}$–$2_{0,2}$, and OCS 7–6) are detected mainly toward the cores with the brightest SO 3_2–2_1 emission, that is, mainly in the cores with $A_V \simeq 15$–22 mag. The HCO 1–0 transition exhibits the same behavior. Despite its low density ($A_V = 11.2$ mag), core 47 displays emission in most of the oxo-sulfurated molecular transitions as well as in HCO 1–0. The H_2CS $3_{1,3}$–$2_{1,2}$ transition appears to show a similar trend to the oxo-sulfurated molecules, although it peaks at slightly denser cores (for which $A_V \simeq 20$ mag) and clearly survives at larger A_V values. The emission of the other two lines of this group, HCS^+ 2–1 and $^{13}C^{18}O$ 1–0, is too weak to show a clear trend.

---

[2] `http://www.splatalogue.net/`

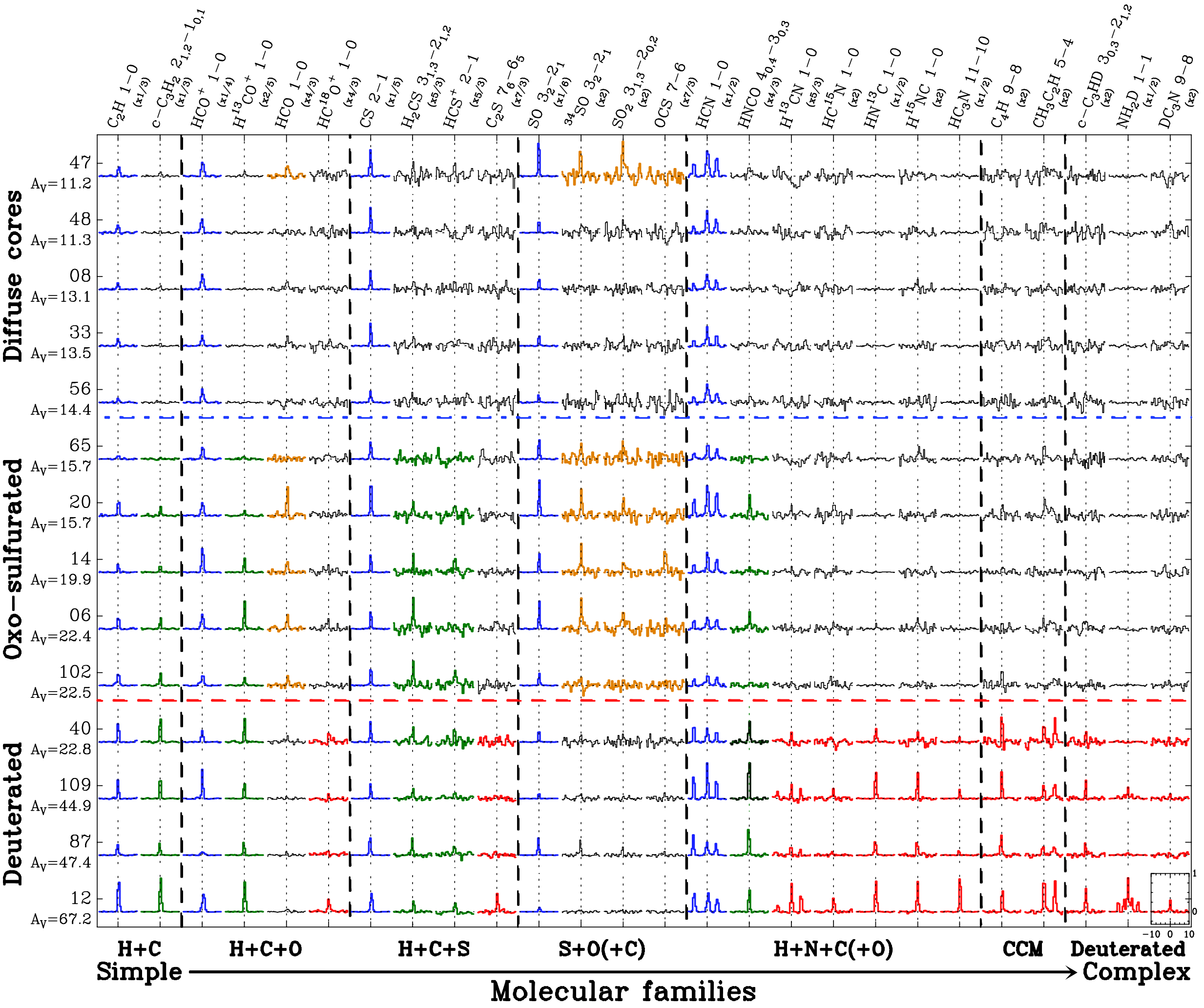

Fig. 2. Selected normalized molecular transitions toward the observed cores. The scale is shown in the bottom right spectrum. The normalized intensity axis ranges from –0.33 to 1, while the velocity axis spans 20 km s^{-1} centered at the $v_{\rm LSR}$. *Rows*: individual cores, labeled on the left-hand side of the figure, ordered by its $A_{\rm V}$ peak. *Columns*: molecular transition, ordered by molecular families, labeled on the top of the figure. The spectra have been divided by [$A_{\rm V}$/100 mag] to mimic the abundance, where the $A_{\rm V}$ value is that at the respective core center (Román-Zúñiga et al. 2010) given below the core name. Each molecular transition has been multiplied by a factor, given below its name, to fit in a common scale. *Colors* are used to highlight the distinctive emission of the different core groups: blue for ubiquitous lines, green dense-medium molecular transitions, orange molecular transitions typical in oxo-sulfurated cores (see Sect. 4), red molecular transitions typical in deuterated cores, and black mostly undetected species.

The number of detected molecular transitions increased significantly for the four cores with the highest column density ($A_{\rm V} \gtrsim 22$ mag) owing to either (i) excitation/column density reasons or (ii) the length of the synthesization timescales. The c–C_3H_2 molecule is a good example of the former molecules. Although ubiquitous in the $2_{1,2}$–$1_{0,1}$ transition, the $3_{1,2}$–$3_{0,3}$ one is only detected at these column densities. The rarer isotopologic counterparts of the HCN and c–C_3H_2 1–0 ubiquitous lines ($H^{13}CN$, $HC^{15}N$, and c–$H^{13}CCCH$) are detected only in these four cores. This is also the case for $HN^{13}C$ and $H^{15}NC$ in the 1–0 transition, which suggests that the HNC 1–0 is also likely to be an ubiquitous line. Most of the transitions detected in these four cores have higher normalized intensities with increasing $A_{\rm V}$ (e.g. HC_3N 11–10). The carbon-chain molecular transitions (C_4H 9–8 and 11–10, and CH_3C_2H 5_n–4_n and 6_n–5_n) are the exception, displaying little variations in normalized intensity. We also detected several transitions of three deuterated forms of abundant species, namely C_3HD $3_{0,3}$–$2_{1,2}$, NH_2D 1–1, and DC_3N in the 9–8 and 12–11 (see Fig. 2). Only the first transition is detected in the four cores.

4. Discussion and conclusions

The chemistry detected toward the sample of fourteen starless cores is unexpectedly rich taking into account their low temperatures (10–15 K: Rathborne et al. 2008) and visual extinctions. The apparent correlation within the sample of the 3 mm molecular transition normalized intensities to visual extinction allow us to propose an observational classification (see Fig. 2). We have defined three groups of starless cores, which are probably related to their dynamical age: *"diffuse"*, *"oxo-sulfurated"*, and *"deuterated"* cores. This classification can be useful in future wide band 3 mm observations of molecular clouds.

The first group consists of so-called *"diffuse" cores*, a set of cores with small column densities ($A_V \lesssim 15$ mag ~ $N_{H_2} \lesssim 1.2 \times 10^{22}$ cm^{-2}) lies above the blue dot-dashed horizontal line in Fig. 2. Their spectra is rather poor, showing only significant normalized intensity in the transitions of the main isotopologues of abundant species such as C_2H, HCN (and likely HNC), HCO^+, and SO. Such a simple observational chemistry suggests that these are very young starless cores, or even transient clumps for which essentially the cloud chemistry is more clearly detected owing to density enhancements. Core 47 is a clear exception as we have discussed later in the main paper text.

Our second are the *"oxo-sulfurated" cores*, which are denser cores ($A_V \simeq 15$–22 mag ~$N_{H_2} \simeq 1.2 \times 10^{22}$–$1.7 \times 10^{22}$ cm^{-2}) that have a richer chemistry for which no significant deuteration has been observed. In Fig. 2, this group lies between the blue dot-dashed and red dashed horizontal lines. All the transitions detected in the *"diffuse"* cores are also present. The SO 3_2–2_1 transition is the main signpost as it is very bright. Many other oxo-sulfurated molecules (^{34}SO, SO_2, and OCS), as well as HCO, exhibit a similar trend but are not detected at higher densities. This suggests that there has been an increase in the abundances of these chemically related species in the gas-phase in this A_V range, followed by a later depletion/destruction as density increases. These cores might be in-the-making cores, which have developed a richer chemistry and piled up more material, probably in a stage close to the onset of collapse (Ruffle et al. 1999). Core 102 is an exception in this group as we have discussed later in the text.

Our third of *"deuterated" cores* are the densest in our sample ($A_V \gtrsim 22$ mag ~ $N_{H_2} \gtrsim 1.7 \times 10^{22}$ cm^{-2}), and shown below the red dashed horizontal line in Fig. 2. Core 12, the densest one, sets the upper limit at $A_V = 67.2$ mag ($N_{H_2} \simeq 5.3 \times 10^{22}$ cm^{-2}). These cores are generally bright in the transitions typical of the other two groups. The oxo-sulfurated molecules are the exception, because they are hardly present and probably depleted/destructed at the densities reached. The main signpost is the emission that is only present in this group, in rare isotopologues of the nitrogenated ubiquitous lines ($H^{13}CN$, $HC^{15}N$, $HN^{13}C$, and $H^{15}NC$), deuterated forms of abundant species (C_3HD, NH_2D, and DC_3N), and carbon-chain molecules (C_4H and CH_3C_2H). These cores might be stable starless cores with a life-time long enough to achieve the densities needed to synthesize efficiently carbon chains and deuterated species (Roberts & Millar 2000; Gwenlan et al. 2000).

As we have previously noted, core 47 does not share the chemical properties of the diffuse cores. It has a similar chemistry to the oxo-sulfurated group, which proved to be very sensitive to density. This suggests that it might be a failed core that has developed a rich chemistry and is now merging back into the cloud. This scenario is consistent with the high abundances of oxo-sulfurated species (Garrod et al. 2005). Core 47 is located close to core 48 in the only Pipe nebula region with superalfvénic turbulence, as shown by optical polarization observations (Franco et al. 2010). Therefore, it is possible that an external source of turbulence is disrupting the medium in this area and dispersing the cores.

In contrast, core 102, in the oxo-sulfurated group, has a similar chemistry to that of the diffuse cores. Similarly, core 87, among the deuterated cores, has similar features to the oxo-sulfurated group. This suggests that these cores might have piled up material so rapidly that a more complex chemistry had no time to be synthesized. Both cores lie in the same N-S oriented high-density structure (Román-Zúñiga et al. 2010) where Franco et al. (2010) reported a N-S magnetic field. This rapid evolution might have been driven by magnetic fields with the surrounding mass collapsing in this direction.

Our FTS chemical survey toward the starless cores of the Pipe nebula has demonstrated that it has a chemistry far richer than expected for a cloud giving birth to low-mass stars at very low efficiency. A fully consistent interpretation of the results would require chemical modeling to investigate the possible evolutionary tracks, and will be the purpose of a forthcoming study.

Acknowledgements. P.F. is partially supported by MICINN fellowship FPU (Spain). P.F., J.M.G. and M.T.B. are supported by MICINN grant AYA2008-06189-C03 (Spain). P.F., J.M.G., and M.T.B. are also supported by AGAUR grant 2009SGR1172 (Catalonia). We thank Carlos Román-Zúñiga for kindly providing their A_V maps. The authors wish to acknowledge all the IRAM 30-m staff for their hospitality during the observing runs, the operators, and the AoDs for their active support. We thank the anonymous referee for useful comments. This research has made use of NASA's Astrophysics Data System.

References

Aikawa, Y., Ohashi, N., Inutsuka, S.-I., et al. 2001, ApJ, 552, 639
Alves, F. O., & Franco, G. A. P. 2007, A&A, 470, 597
Alves, F. O., Franco, G. A. P., & Girart, J. M. 2008, A&A, 486, L13
Bergin, E. A., & Tafalla, M. 2007, ARA&A, 45, 339
Brooke, T., Huard, T. L., Bourke, T. L., et al. 2007, ApJ, 655, 364
Crapsi, A., Caselli, P., Walmsley, C. M., et al. 2005, ApJ, 619, 379
Forbrich, J., Lada, C. J., Muench, A. A., et al. 2009, ApJ, 704, 292
Franco, G. A. P., Alves, F. O., & Girart, J. M. 2010, ApJ, 723, 146
Frau, P., Girart, J. M., Beltrán, M. T., et al. 2010, ApJ, 723, 1665
Garrod, R. T., Williams, D. A., Hartquist, T. W., et al. 2005, MNRAS, 356, 654
Girart, J. M., Estalella, R., Ho, P. T. P., & Rudolph, A. L. 2000, ApJ, 539, 763
Gwenlan, C., Ruffle, D. P., Viti, S., et al. 2000, A&A, 354, 1127
Hirota, T., & Yamamoto, S. 2006, ApJ, 646, 258
Keto, E., & Caselli, P. 2008, ApJ, 683, 238
Lada, C. J., Muench, A. A., Rathborne, J. M., et al. 2008, ApJ, 672, 410
Muench, A. A., Lada, C. J., Rathborne, J. M., et al. 2007, ApJ, 671, 1820
Onishi, T., Kawamura, A., Abe, R., et al. 1999, PASJ, 51, 871
Rathborne, J. M., Lada, C. J., Muench, A. A., et al. 2008, ApJS, 174, 396
Roberts, H., & Millar, T. J. 2000, A&A, 361, 388
Román-Zúñiga, C., Alves, J. F., Lada, C. J., & Lombardi, M. 2010, ApJ, 725, 2232
Román-Zúñiga, C., Frau, P., Girart, J. M., & Alves, J. F. 2012, ApJ, accepted
Ruffle, D. P., Hartquist, T. W., Caselli, P., & Williams, D. A. 1999, MNRAS, 306, 691
Tafalla, M., Santiago-García, J., Myers, P. C., et al. 2006, A&A, 455, 577
Turner, B. E. 1994, ApJ, 420, 661
Turner, B. E., Herbst, E., & Terzieva, R. 2000, ApJS, 126, 427

VII

Starless cores in the magnetically dominated Pipe nebula
III. Physical structure

Astronomy & Astrophysics manuscript no. article˙tesi
May 11, 2012

© ESO 2012

Physical structure of the diffuse starless cores in the Pipe nebula[⋆]

P. Frau[1], J. M. Girart[1], and M. T. Beltrán[2]

[1] Institut de Ciències de l'Espai (CSIC-IEEC), Campus UAB, Facultat de Ciències, Torre C5p, 08193 Bellaterra, Catalunya, Spain
e-mail: `frau@ice.cat`
[2] INAF-Osservatorio Astrofisico di Arcetri, Largo Enrico Fermi 5, 50125 Firenze, Italy

Paper in preparation

ABSTRACT

Context. In previous works, we have conducted a molecular line and dust continuum survey of a selected sample of cores in the Pipe nebula. When compared with most of the starless cores studied in the literature, the selected Pipe nebula cores are quite diffuse and chemically young.
Aims. We want to better constrain the physical properties of the Pipe nebula cores using a combination of our 1.2 mm dust emission continuum maps and the best available extinction maps obtained at a similar angular resolution.
Methods. We have performed simultaneous fits to the radial profiles of the 1.2 mm dust continuum maps and of the extinction maps assuming that the physical structure of the cores is that of a Bonnor–Ebert sphere model.
Results. All the cores in our sample show radial profiles, both in mm emission and in extinction, that are compatible with the expected Bonnor–Ebert profile. We confirm that most of the Pipe nebula cores are quite diffuse and gravitationally unbound, with central volume densities of only few times 10^4 cm^{-3}, and a very small density contrast with respect to the confining ambient gas. Core 109 is the exception, since it is not only much denser, but it is the only one of the sample that it is gravitationally bound. All the cores are surrounded by a significant diffuse molecular component with a visual extinction in the 4–9 mag range, being larger in the *bowl* region, ≃ 9 mag, than in the rest of the Pipe nebula.
Conclusions. The Pipe nebula is an ideal target to study the formation and evolution of the starless dense cores since most of the studied objects are in an extremely early stage of evolution prior to the onset of collapse.

Key words. ISM: individual objects: Pipe Nebula – ISM: lines and bands – ISM – stars: formation

1. Introduction

1.1. The Pipe nebula cores

Frau et al. (2010, hereafter Paper I), and Frau et al. (2012b, hereafter Paper II) present continuum and high spectral resolution molecular line data of nine Pipe nebula young diffuse starless cores. The observations were carried out with the IRAM 30-m telescope using MAMBO-II (continuum maps) and EMIR+VESPA (spectra). The authors report a clear chemical and morphological differentiation. Frau et al. (2012a, hereafter Paper III) analyze the wide band molecular line data toward fourteen of the Pipe nebula starles cores. The observations were carried out using the IRAM 30-m EMIR+FTS combination. The authors propose a plausible evolutionary track based on the chemistry detected as a function of the A_V peak of the cores.

In this work we model our dust continuum emission maps (Paper I, Paper II) simultaneously with the best available visual extinction maps (Román-Zúñiga et al., 2009, 2010) of the Pipe nebula starless cores assuming the density profile of a Bonnor-Ebert sphere.

1.2. The Bonnor-Ebert sphere model

A suitable model to fit the Pipe nebula starless cores is the Bonnor-Ebert sphere (Bonnor, 1956; Ebert, 1955). It describes a self-graviting, pressure-confined, isothermal gas sphere in hydrostatic equilibrium. The density profile can be derived by solving the Lane-Emden equation

$$\frac{1}{\xi}\frac{d}{d\xi}\left(\xi\frac{d\phi}{d\xi}\right) = e^{-\phi}, \tag{1}$$

where ξ is the non-dimensional radius,

$$\xi = r\frac{\sqrt{4\pi G\rho}}{C_s}, \tag{2}$$

and ϕ the logarithm of the density contrast,

$$\phi = \ln\left(\frac{\rho_c}{\rho}\right). \tag{3}$$

r, ρ, and ρ_c are the radius, volume density and central volume density, respectively. C_s is the sound speed defined as $C_s = \sqrt{KT/m}$. G, K, T, and m are the gravitational constant, the Boltzmann constant, the temperature, and the mean molecular mass assumed to be 2.33. Imposing boundary conditions at the core center, forcing the density to be ρ_c and its derivative to be 0 (i.e. $\rho = \rho_c$ and $d\rho/dr = 0$ at $r = 0$), Eq. 1 can be solved numerically. The last ingredient left is the outer confining pressure, $P_{\rm Out}$, exerted at the outer radius, $R_{\rm Out}$, from which one can derive the $\xi_{\rm max}$ parameter ($\xi_{\rm max} = (R_{\rm Out}/C_s)\sqrt{4\pi G\rho}$) that uniquely characterizes the Bonnor-Ebert solution. The critical value is $\xi_{\rm max} = 6.5$ that corresponds to $(\rho_c/\rho)_{\rm max} = 14.1$. For values larger than $\xi_{\rm max}$ the equilibrium is unstable to gravitational collapse.

[⋆] Based on observations carried out with the IRAM 30-m telescope. IRAM is supported by INSU/CNRS (France), MPG (Germany), and IGN (Spain).

2. Observational data

We mapped the dust continuum emission of cores 06, 14, 20, 40, 47, 48, 65, 74, and 109 at 1.2 mm with the 117-receiver MAMBO-II bolometer (array diameter of 240″) of the 30-m IRAM telescope (see Paper I and Paper II for details). In Fig. 1 we present the maps convolved with a Gaussian to have a 21.″5 final angular resolution, larger than the telescope beam, in order to improve the SNR, and to smooth the appearance of the maps. Table 1 gives the peak position of the 1.2 mm emission after convolution, the dust temperature (Rathborne et al., 2008), the RMS noise of the emission, the flux density and the value of the emission peak. Additionally, we also give the derived FWHM equivalent diameter, the H_2 column and volume density, as well as the mass for each core (see Papers I and II for details and further discussion).

The flux density (S_ν) of the cores ranges between 0.40 and 2.77 Jy, while the intensity peak (I_ν) ranges between 21.4 and 105.3 mJy beam^{-1}. Note, however, that the extinction maps show that the studied cores are surrounded by a diffuse medium (Lombardi et al., 2006; Román-Zúñiga et al., 2009, 2010) and Román-Zúñiga et al. (2012) show, by comparing visual extinction maps to MAMBO-II maps toward B59, flux accuracy problems for the diffuse material due to the MAMBO-II reduction algorithms (as discussed in Papers I and II).

The maps of Fig. 1 show the different morphology of the cores and are in perfect agreement with visual extinction maps (Lombardi et al., 2006; Román-Zúñiga et al., 2009, 2010). Following the results of Alves et al. (2008), it is interesting to compare the shape of the cores with their location in the different regions of the Pipe nebula. The most evolved region, B59, harbors cores 06 and 14. Core 06 located in shows one of the weakest emission levels (~0.6 Jy). However, it is one of the most compact (~1.1×10^4 AU) and dense (~1.4×10^5 cm^{-3}) cores. Core 14 belongs to a clumpy and filamentary structure of ~500″(~0.35 pc) elongated along the NE–SW direction. It is also very dense and compact. The *stem*, the region with intermediate magnetic properties, hosts cores 20, 40, 47, and 48. The maps show very diffuse structures and elliptical morphologies. The physical properties derived are very similar in terms of size (1.8–2.4×10^4 AU), density (2.2–5.9×10^4 cm^{-4}), and mass (0.8–2.7 $M_\odot$). The *bowl*, the region in the earliest stage, harbors cores 65, 74, and 109. Cores 65 and 109 show a defined morphology, and are very compact and dense (>10^5 cm^{-3}). On the other hand, Core 74 do not show a defined morphology and is similar to the *stem* cores. The sizes, densities and masses of these cores are very different.

We have also used the high angular resolution extinction maps by Román-Zúñiga et al. (2009, 2010). These maps were constructed from a concerted deep near-infrared imaging survey using several telescopes (ESO-VLT, ESO-NTT and CAHA 3.5 m) as well as the 2MASS data. These maps have a resolution three times higher than the previous extinction map of this cloud by Lombardi et al. (2006), allowing to resolve structures down to 19″ or 2600 AU.

3. Results

In order to fit the observational data, a synthetic 3D source was generated with a density profile obeying the numerical integration of a Bonnor-Ebert sphere (Eqs. 1, 2, and 3) with a given set of parameters. Then, ray tracing was performed as described in Frau et al. (2011). Two maps were simultaneously generated, a visual extinction map and a 1.2 mm dust continuum emission map, convolved to the respective observational beams. Finally, radial profiles of the observational and synthetic maps for both wavelengths were created and compared simultaneously. The quality of the fit was assessed by a χ^2 analysis using the two wavelengths. Figure 2 shows the good agreement between the observational and synthetic Bonnor-Ebert emission radial profiles.

Table 2 lists the input parameters of the best fitting Bonnor-Ebert profiles (ρ_c, R_{Out}, and T), the physical parameters derived ($\xi_{\max}$, ρ_c/ρ_R, P_{Out}, and mass), the background visual extinction arising from the surrounding ambient medium ($A_{\mathrm{V}}^{\mathrm{bg}}$), the gravitational stability status, and an estimate of the age (Aikawa et al., 2005). For the cores with the temperature derived from ammonia observations (Rathborne et al., 2008), we found that the values derived from Bonnor-Ebert are in fair agreement. Most of the core show temperatures around 10 K, except for core 48, which can only be fitted with a temperature of 18 K.

Interestingly, for all the cores the background ambient medium contribution is quite high, in the 4–9 mag range, being highest in the *bowl* (∼ 9 mag). This large amount of surrounding molecular gas is important since it may yield to an overestimation of the volume and column density of the core from mm dust continuum maps and specially from extinction maps. Indeed, the volume densities derived directly from the 1.2 mm continuum maps is, in most of the cases, roughly a factor 2 higher than the values derived using the Bonnor-Ebert fit. This does not happen as clearly in the computed mass, since this also depend sensibly to the derived outer radius of the core. Thus, we found that for some cores the mass obtained from the Bonnor-Ebert fit is similar to the value estimated from the 1.2 mm continuum maps (cores 06, 20, 40 and 47), whereas for some cores the discrepancy can be as large as a factor 4 (cores 14 and 6).

Excluding core 109 (see following paragraph for a specific discussion of the results of this core), the cores in our sample are gravitational unbound and quite diffuse, with densities ranging from only 6×10^3 cm^{-3} up to 7×10^4 cm^{-3}. More interestingly, these diffuse cores show a strikingly small density contrast with respect to the surrounding molecular ambient gas: from $\simeq$ 1.4 for the most diffuse cores up to $\simeq$ 4 for more compact cores such as cores 40 and 06.

The densest core, 109, is also the brightest one, providing an excellent signal-to-noise to well test the Bonnor-Ebert scenario. The observed visual extinction profile can be fitted reasonably well, but the 1.2 mm continuum data show some departure with respect to the Bonnor-Ebert profile.

4. Preliminary discussion

The Bonnor-Ebert radial profile fits at both wavelengths provide remarkable results for all the sample but core 109. This implies that most of the studied cores have structures compatible with a Bonnor-Ebert sphere. Furthermore, the fact that the fit for both wavelengths uses the same physical parameters allow to avoid degeneracies of some of them. Thanks to the combined fit we find an evidence that these objects are isothermal, given that the dust emission depends critically on T while the visual extinction does not.

A different case is core 109, which shows a good fit for the A_{V} map but non-negligible differences in the dust emission profile. This can be interpreted as a departure from the isothermal approximation. Previous studies in starless cores (e.g. Crapsi et al., 2007) show that those with n_{H_2}>10^5 cm^{-3} may have an inner temperature gradient. These cores are colder at the center, reaching temperatures as low as 6 K, than at the outer shells where they may be heated by the interstellar radiation.

Core 48 is also a special case. It is impossible to fit both profiles without a temperature of 18 K, high as compared to the typical values for dense cores. Onishi et al. (1999) find $T_{\rm ex}$ $\sim$15 K from CO data in the surrounding diffuse medium. Such a high temperature, together with the low density contrast of this core, can be explained in an scenario with external radiation permeating the core and heating the internal material up to temperatures comparable to the cloud.

The cores in B59 (06 and 14) show larger confining pressures probably due to the effect of the nearby star-formation. Core 65, at the center of a three core structure, also show a larger value. These three cores might have formed by compression of the local material. The rest of the cores show confining pressures compatible with the estimates of the cloud weight (Lada et al., 2008).

Regarding the general properties of the best fitting Bonnor-Ebert spheres to the Pipe nebula cores, the central densities are of the order of $\sim 10^4$ cm^{-3}, typical values in literature of starless dense cores but lower than the values of those studied in detail so far. The density contrast and $\xi_{\rm max}$ values are very low in general, >2 for five cores in both parameters, what brings up the question of whether these are real cores or just transient density enhancements due to the cloud internal turbulence. Four of these cores (47, 48, 65, and 74) are located in the the transition region from the *stem* and the *bowl*, where the homogeneous filament and the ring-like structure described by Muench et al. (2007) coincide, probably generating turbulence in the local environment.

The age estimate using Kandori et al. (2005) simulations may suffer from high uncertainties. The densities of these cores are very close to the inital conditions adopted by the simulations (10^4 cm^{-3}). A prove of this is that for three of the cores (47, 48, and 74) it was impossible to estimate the age because densities are below the initial value. The densities achived by the rest of the cores are not significantly higher and, at these evolutionary stages, its variation with time is very slow causing a high uncertainty in the age estimate.

Acknowledgements. PF was partially supported by MICINN fellowship FPU (Spain). PF, JMG are supported by MICINN grant AYA2011-30228-C03-02 (Spain) and by AGAUR grant 2009SGR1172 (Catalonia). The authors want to acknowledge again all the IRAM 30-m staff for their hospitality during the observing runs, the operators and AoDs for their active support, Guillermo Quintana-Lacaci for his help during the observing and reduction process of the bolometer data, and Jens Kauffmann for helping on the implementation of his MAMBO-II new reduction scheme.

References

Aguti, E. D., Lada, C. J., Bergin, E. A., Alves, J. F., & Birkinshaw, M. 2007, ApJ, 665, 457

Aikawa, Y., Ohashi, N., & Herbst, E. 2003, ApJ, 593, 906

Aikawa, Y., Herbst, E., Roberts, H., & Caselli, P. 2005, ApJ, 620, 330

Aikawa, Y., Wakelam, V., Garrod, R. T., Herbst, E. 2008, ApJ, 674, 984

Alves, F. O. & Franco, G. A. P. 2007, A&A, 470, 597

Alves, F. O., Franco, G. A. P., & Girart, J. M. 2008, A&A, 486, L13

Ballesteros-Paredes, J., Klessen, R. S., Mac Low, M.-M., & Vazquez-Semadeni, E. 2007, Protostars and Planets V, 63

Bergin, E. A., Ciardi, D. R., Lada, C. J., Alves, J., Lada, E. A. 2001, ApJ, 557, 209-225

Bergin, E. A. & Tafalla, M. 2007, ARA&A, 45, 339

Bonnor, W. B. 1956, MNRAS, 116, 351

Brooke, T., Huard, T. L., Bourke, T. L., Boogert, A. C. A. et al. 2007, ApJ, 655, 364

Caselli, P., Benson, P. J., Myers, P. C., Tafalla, M. 2002, ApJ, 572, 238

Crapsi, A., Caselli, P., Walmsley, C. M., Myers, P. C., Tafalla, M., Lee, C. W., Bourke, T. L. 2005, ApJ, 619, 379

Crapsi, A., Caselli, P., Walmsley, C. M., Tafalla, M. 2007, A&A, 470, 221

Dutra, C. M., Santiago, B. X., Bica., E. 2002, A&A, 381, 219

Ebert, R. 1955, ZAp, 37, 217

Falle, S. A. E. G., & Hartquist, T. W. 2002, MNRAS, 329, 195

Flower, D. R., Pineau Des Forêts, G., Walmsley, C. M. 2006, A&A, 456, 215

Forbrich, J., Lada, C. J., Muench, A. A., Alves, J., Lombardi, M. 2009, ApJ, 704, 292

Franco, G. A. P., Alves, F. O., & Girart, J. M. 2010, ApJ, 723, 146

Frau, P., Girart, J. M., Beltrán, M. T., Morata, O., Masqué, J. M., Busquet, G., Alves, F. O., Sánchez-Monge, A., Estalella, R., & Franco, G.A.P. 2010 ApJ, 723, 1665 (Paper I)

Frau, P., Galli, D., Girart, J. M. 2011, A&A, 535, A44

Frau, P., Girart, J. M., & Beltrán, M. T. 2012, A&A, 537, L9 (Paper III)

Frau, P., Girart, J. M., Beltrán, M. T., Padovani, M., Busquet, G., Morata, O., Masqué, J. M., Alves, F. O., Sánchez-Monge, A., Franco, G.A.P., & Estalella, R. 2012, Submitted to ApJ (Paper II)

Garrod, R. T., Williams, D. A., Hartquist, T. W., Rawlings, J. M. C., Viti, S. 2004, MNRAS, 356, 654-664

González-Alfonso, E. & Cernicharo, J. 1993, A&A, 279, 506

de Gregorio-Monsalvo, I., Gómes, J. F., Suárez, O., Kuiper, T. B. H., Rodríguez, L. F., Jiménez-Bailón, E. 2006, ApJ, 642, 319

Heitsch, F., Ballesteros-Paredes, J., & Hartmann, L. 2009, ApJ, 704, 1735

Irvine, W. M., Goldsmith, P. F., Hjalmarson A. 1987, in Hollenbach D. J., Thronson H. A. (eds), Interstellar Processes. Reidel, Dordrecht, p. 561

Kandori, R., Nakajima, Y., Tamura, M., Tatematsu, K., Aikawa, Y., Naoi, T., Sugitani, K., Nakaya, H., Nagayama, T., Nagata, T., Kurita, M., Kato, D., Nagashima, C., Sato, S. 2005, AJ, 130, 2166

Kauffmann, J., Bertoldi, F., Bourke, T. L., Evans, N. J., II, & Lee, C. W. 2008, A&A, 487, 993

Keto, E., & Caselli, P. 2008, ApJ, 683, 238

Keto, E., & Caselli, P. 2010, MNRAS, 402, 1625

Kim, K.-T., & Koo, B.-C. 2003, ApJ, 596, 362

Kontinen, S., Harju, J., Heikkilä, A., & Haikala, L. K. 2000, A&A, 361, 704

Lada, C. J., Muench, A. A., Rathborne, J. M., Alves, J. F., & Lombardi, M. 2008, ApJ, 672, 410

Lombardi, M., Alves, J., & Lada, C. J. 2006, A&A, 454, 781

Millar, T., Herbst, E. 1990, A&A, 231, 466

Morata, O., Girart, J. M., & Estalella, R. 2003, A&A, 397, 181

Morata, O., Girart, J. M., & Estalella, R. 2005, A&A, 435, 113

Muench, A. A., Lada, C. J., Rathborne, J. M., Alves, J. F., & Lombardi, M. 2007, ApJ, 671, 1820

Ohashi, N., Lee, S. W., Wilner, D. J., Hayashi, M. 1999, ApJ, 518, L41

Onishi, T., Kawamura, A., Abe, R., Yamaguchi, N. et al. 1999, PASJ, 51, 871

Ossenkopf, V. & Henning, T. 1994, A&A, 291, 943

Padovani, M., Walmsley, C. M., Tafalla, M., Galli, D., Müller, H. S. P. 2009, A&A, 505, 1199

Rathborne, J. M., Lada, C. J., Muench, A. A., Alves, J. F., & Lombardi, M. 2008, ApJS, 174, 396

Román-Zúñiga, C., Lada, C. J., & Alves, J. F. 2009, ApJ, 704, 183

Román-Zúñiga, C., Alves, J. F., Lada, C. J., & Lombardi, M. 2010, ApJ, 725, 2232

Román-Zúñiga, C., Frau, P., Girart, J. M., & Alves, J. F. 2012, ApJ, 747, 149

Suzuki, H., Yamamoto, S., Ohishi, M., Kaifu, N., Ishikawa, S., Hirahara, Y., Takano, S. 1992, ApJ, 392, 551

Tafalla, M., Myers, P. C., Caselli, P., Walmsley, C. M., & Comito, C. 2002, ApJ, 569, 815

Tafalla, M., Myers, P. C., Caselli, P., Walmsley, C. 2004, A&A, 416, 191

Tafalla, M., Santiago-García, J., Myers, P. C., Caselli, P., Walmsley, C. M., Crapsi, A. 2006, A&A, 455, 577

Taylor, S. D., Morata, O., Williams, D. A. 1998, A&A, 336, 309

Wagenblast, R., Hartquist, T. W., 1989, MNRAS, 237, 1019

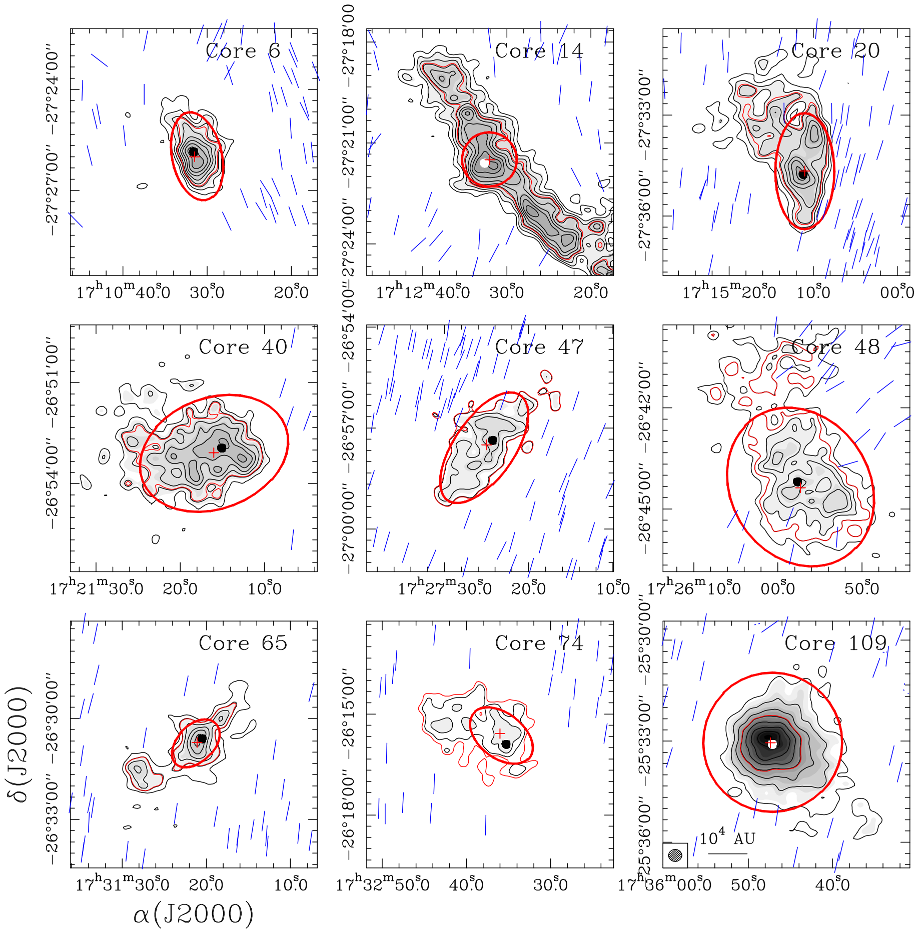
Core 6
Core 14
Core 20
Core 40
Core 47
Core 48
Core 65
Core 74
Core 109
10^4 AU
δ(J2000)
α(J2000)
−27°27'00'' −27°24'00''
17h10m40s.0 30s.0 20s.0
−27°24'00'' −27°21'00'' −27°18'00
17h12m40s.0 30s.0 20s.0
−27°36'00'' −27°33'00''
17h15m20s.0 10s.0 00s.0
−26°54'00'' −26°51'00''
17h21m30s.0 20s.0 10s.0
−27°00'00'' −26°57'00'' −26°54'00''
17h27m30s.0 20s.0 10s.0
−26°45'00'' −26°42'00''
17h26m10s.0 00s.0 50s.0
−26°33'00'' −26°30'00''
17h31m30s.0 20s.0 10s.0
−26°18'00'' −26°15'00''
17h32m50s.0 40s.0 30s.0
−25°36'00'' −25°33'00'' −25°30'00''
17h36m00s.0 50s.0 40s.0

Fig. 1. IRAM 30-m MAMBO-II maps of the dust continuum emission at 1.2 mm toward nine cores of the Pipe nebula presented in Papers I and II. In the bottom left corner of the bottom right panel the convolved beam and the spatial scale for the maps are shown. *Grayscale*: levels are common for all the maps and range from 3 to 18 times 5.75 mJy beam^{-1}. *Contour levels*: 3 to 10 times σ in steps of 1-σ for all the cores but core 109, for which the contour levels are 3 to 21σ in steps of 3σ. 1-σ is 4.0, 4.5, 4.5, 5.0, 4.9, 3.5, 4.4, and 4.3 mJy beam^{-1} for cores 06, 14, 20, 40, 47, 48, 65, 74, and 109, respectively. *Red thin contour*: half maximum emission level of the source (see Table 1). *Black or white filled circles*: line observation pointing positions of Paper I and Paper II, very close to the dust continuum emission maximum. *Blue vectors*: polarization vectors found by Franco et al. (2010). *Red cross*: center of the concentric rings used to calculate the intensity profile. *Red thick ellipse*: external boundary of the best fitting Bonnor-Ebert profile.

Table 1. 1.2 mm Dust Continuum Emission Parameters

Source	α(J2000) [a] h m s	δ(J2000) [a] ° ′ ″	$T_{\rm dust}$ (K)	RMS (mJy beam^{-1})	S_ν (Jy)	$I_\nu^{\rm Peak}$ (mJy beam^{-1})	Diameter (pc)	$N_{\rm H_2}$ [b] (10^{21}cm^{-2})	$n_{\rm H_2}$ [b] (10^4cm^{-3})	Mass [b] ($M_\odot$)
Core 06	17 10 31.8	-27 25 51.3	10.0 [c]	4.0	0.58	42.6	0.051	16.18 [c]	15.44 [c]	0.88 [c]
Core 14	17 12 31.5	-27 21 41.0	12.0 [d]	4.5	1.23	51.6	0.073	12.28	8.14	1.39
Core 20	17 15 11.5	-27 34 47.9	15.2 [d]	4.5	1.52	42.6	0.088	7.33	4.04	1.20
Core 40	17 21 14.7	-26 52 47.8	10.3 [d]	5.0	1.85	42.0	0.101	12.44	5.96	2.69
Core 47	17 27 24.3	-26 57 22.2	12.6 [d]	4.9	0.73	28.5	0.093	4.17	2.18	0.76
Core 48	17 25 57.3	-26 44 22.3	10.0 [c]	3.5	1.41	27.9	0.115	7.66 [c]	3.23 [c]	2.14 [c]
Core 65	17 31 21.1	-26 30 42.8	10.0 [c]	4.4	0.48	36.1	0.053	12.39 [c]	11.38 [c]	0.73 [c]
Core 74	17 32 35.3	-26 15 54.0	10.0 [c]	4.3	0.40	21.4	0.097	3.11 [c]	1.56 [c]	0.61 [c]
Core 109	17 35 47.7	-25 32 52.9	9.5 [d]	4.5	2.77	105.3	0.062	57.93	45.69	4.62

[a] Pointing position of the chemical observations which lies inside the same beam area of the dust continuum emission peak.

[b] Assuming $\kappa_{250\ \rm GHz}$=0.0066 cm^2 g^{-1} as a medium value between dust grains with thin and thick ice mantles (Ossenkopf & Henning, 1994). See Appendix 1 in Paper I for details on the calculation.

[c] No kinetic temperature estimate, therefore we assumed 10 K based on the average temperatures of the other cores in the Pipe nebula (Rathborne et al., 2008).

[d] Adopted to be equal to the kinetic temperature derived for NH_3 (Rathborne et al., 2008).

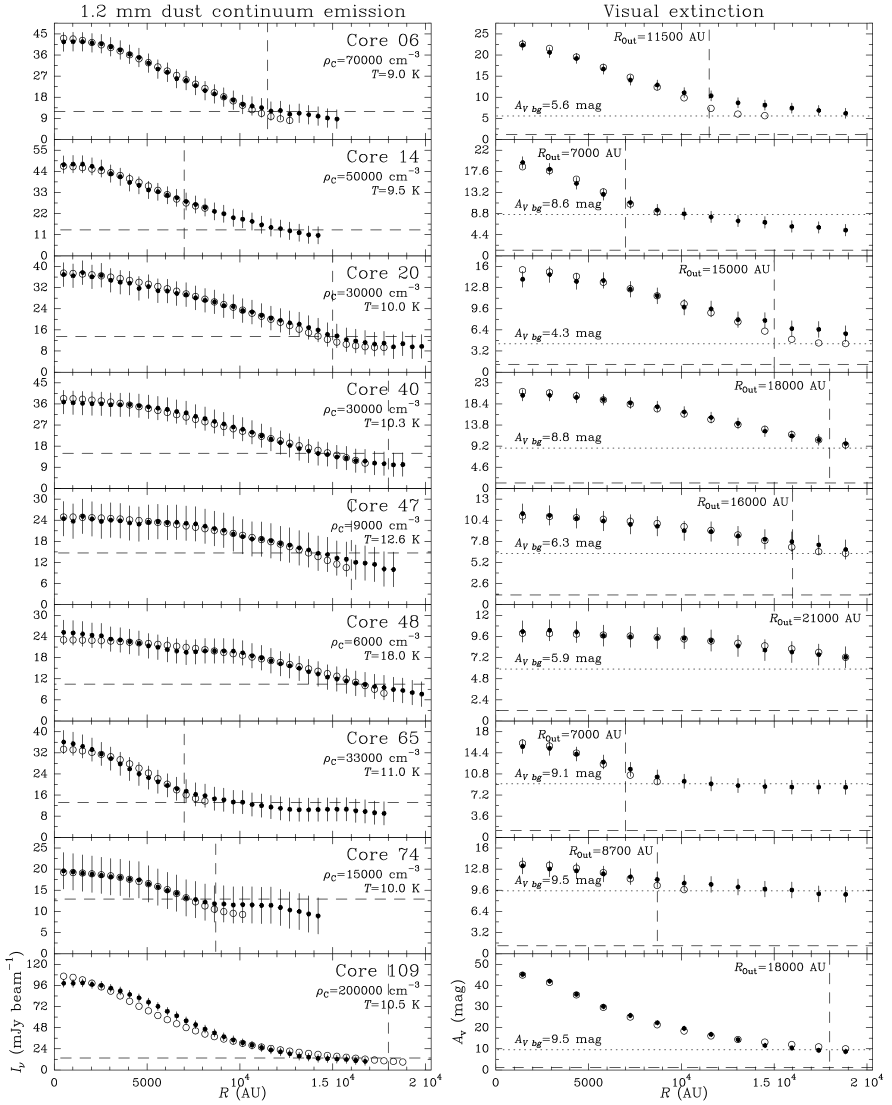

Fig. 2. Radial intensity profiles of the Pipe nebula starless cores presented in Papers I and II. *Left column*: intensity profile from the 1.2 mm dust continuum emission maps (Papers I and II). *Right column*: A_V profile from the dust extinction maps (Román-Zúñiga et al., 2009, 2010). *Rows*: each row corresponds to a single core labeled on left panels. *Black dots*: represent the observed values with vertical bars depicting the ±1-σ range. *Empty circles*: represent the value of the fitted Bonnor-Ebert profile. On each left panel, the best fitting central density, ρ_C, and dust temperature, T, are shown. The core boundary radius, R_{Out}, and A_V value of the surrounding medium, $A_V{}^{bg}$, are labeled on right panels and shown as a vertical dashed line and horizontal dotted line, respectively. Horizontal dashed line represent the 3-σ level (left panels) or the cutoff A_V (right panels).

Table 2. Bonnor-Ebert fit parameters.

Source	a/b	PA °	ρ_c 10^3 cm^{-3}	R_{Out} 10^3 AU	T K	ξ_{max}	ρ_c/ρ_R	P_{Out} 10^5 K cm^{-3}	Mass $M_\odot$	$A_V{}^{bg}$ mag	Stable?	Age[a] yr
Core 47	1.15	−30	9	16	12.6	1.6	1.46	1.1	0.8	6.3	Yes	–
Core 48	1.15	–	6	21	18.0	1.4	1.35	1.1	1.1	5.9	Yes	–
Core 74	1.41	45	15	8.7	10.0	1.2	1.25	1.7	0.2	9.5	Yes	–
Core 20	2	0	30	15	10.0	3.1	3.05	1.4	1.3	4.3	Yes	1.4×10^5
Core 40	1.15	−60	30	18	10.3	3.7	4.15	1.0	1.9	8.8	Yes	1.4×10^5
Core 65	1.41	−37	33	7	11.0	1.4	1.35	3.7	0.2	9.1	Yes	1.8×10^5
Core 14	1	–	50	7	9.5	1.9	1.67	4.0	0.3	8.6	Yes	4.2×10^5
Core 06	2	60	70	11.5	9.0	3.8	4.36	2.0	1.1	5.6	Yes	7.0×10^5
Core 109	1	–	200	18	10.5	9.5	36.88	0.8	2.7	9.5	No	9.6×10^5

[a] Based on Aikawa et al. (2005) results following the evolution of a marginally unstable Bonnor-Ebert sphere (T=10 K, α=1.1).

VIII

Barnard 59

The Astrophysical Journal, 747:149 (5pp), 2012 March 10 doi:10.1088/0004-637X/747/2/149

© 2012. The American Astronomical Society. All rights reserved. Printed in the U.S.A.

BARNARD 59: NO EVIDENCE FOR FURTHER FRAGMENTATION

C. G. Román-Zúñiga[1], P. Frau[2], J. M. Girart[2], and João F. Alves[3]
[1] Instituto de Astronomía, Universidad Nacional Autónoma de México, Km 103 Carr. Tijuana-Ensenada, Ensenada BC 22860, Mexico; croman@astrosen.unam.mx
[2] Institut de Ciències de l'Espai (CSIC-IEEC), Campus UAB, Facultat de Ciències, Torre C-5p, 08193 Bellaterra, Catalunya, Spain
[3] Institute of Astronomy, University of Vienna, Türkenschanzstr. 17, 1180 Vienna, Austria

Received 2011 October 16; accepted 2012 January 12; published 2012 February 24

ABSTRACT

The dense molecular clump at the center of the Barnard 59 (B59) complex is the only region in the Pipe Nebula that has formed a small, stellar cluster. The previous analysis of a high-resolution near-IR dust extinction map revealed that the nuclear region in B59 is a massive, mostly quiescent clump of 18.9 $M_\odot$. The clump shows a monolithic profile, possibly indicating that the clump is on the way to collapse, with no evident fragmentation that could lead to another group of star systems. In this paper, we present new analysis that compares the dust extinction map with a new dust emission radio-continuum map of higher spatial resolution. We confirm that the clump does not show any significant evidence for prestellar fragmentation at scales smaller than those probed previously.

Key words: infrared: ISM – ISM: clouds – radio continuum: ISM – radio lines: ISM – stars: formation

Online-only material: color figure

1. INTRODUCTION

The formation of a stellar cluster proceeds when a molecular cloud clump hosts multiple dense fragments capable of collapsing independently. Cluster-forming clumps populate the high-end bins of the mass and density distributions in a cloud (Williams et al. 1995; Di Francesco et al. 2010), but very few details are known about the process of fragmentation, since cluster-forming clumps in very early stages of evolution are relatively rare.

The recently popular Pipe Nebula (see Alves et al. 2008b and references therein) has become a prototype case for a cloud in a very early stage of evolution. The Pipe Nebula hosts only one star-cluster-forming clump, Barnard 59 (B59), and one core hosting a single young source in a nearby filament (Forbrich et al. 2009). The rest of the cloud contains more than 130 starless cores that resemble stars in the way their masses are distributed (Alves et al. 2007; Rathborne et al. 2009) and how they are distributed spatially (Román-Zúñiga et al. 2010). Dense cores in the Pipe appear to be still mostly quiescent and stable against collapse (Lada et al. 2008), despite some of them being already chemically evolved (Frau et al. 2010; Frau et al. 2011a, 2011b). Currently, the best candidate for a mechanism that supports cores in the Pipe against collapse is the magnetic field that appears to permeate the cloud (Alves et al. 2008a; Franco et al. 2010).

The B59 complex hosts one of the less massive and less distant ($d = 130$ pc) young stellar clusters observable. During the last 2.6 Myr, B59 has formed 14 stars, all below 3 $M_\odot$ (Covey et al. 2010, hereafter CLR10). The analysis of a high-resolution (24″) near-infrared dust extinction map of the B59 region (Román-Zúñiga et al. 2009, hereafter RLA09) revealed that B59 is a complex group of dense cores and filamentary structures, in which the central clump, B59-09, hosts most of the cluster members. The analysis of the dust extinction map suggests that the central clump has a smooth profile that compares well with that of an isothermal sphere, with no evidence of internal fragmentation. Moreover, pointed NH_3 observations inside the core show that the thermal-to-non-thermal kinetic energy ratio averages well over unity, suggesting that B59-09 remains mostly quiescent despite having formed a star cluster. The main goal of this study is to confirm such a scenario by showing that a radio continuum dust emission map with higher spatial resolution also lacks evidence for fragmentation in the central core.

The paper is divided as follows: in Section 2, we describe the observations and data reduction process. Our results are detailed in Section 3 and, to conclude, we elaborate a discussion about their significance in Section 4.

2. OBSERVATIONS

2.1. MAMBO-II

We mapped B59 at 1.2 mm (250 GHz) with the MAMBO-II bolometer at the 30 m IRAM telescope atop Sierra Nevada (Spain). MAMBO-II features a 117-receiver array that covers 240″ in diameter. The observations were carried out in 2009 November in the framework of a flexible observing pool. The weather conditions were good and zenith optical depth remained within 0.1–0.3. A total of five usable on-the-fly maps were completed and combined. The beam size of the telescope is 11″ at the effective frequency of 250 GHz; we used a constant scanning at a speed of 8″ s^{-1} in the azimuthal direction for up to 65 s. This strategy resulted in average integration times per map of ∼1 hr. Each map was performed with a different secondary chopping, which varied between 30″ and 80″, parallel to the scanning direction of the telescope. This procedure assured that we had a different OFF position for each ON position within the map. The scanning direction was also changed for each map, giving a different zero emission level, which helped to avoid spatial filtering effects. The zenith optical depth was measured with a skydip at the start and end of a map. Pointing and focus were checked also at the start and end of a map, with corrections below 3″ and 0.2 mm, respectively. Flux density calibrators were observed every few hours. The data reduction was done with standardized routines from MOPSIC software included in the GILDAS package.[4]

---

[4] GILDAS and MOPSIC are available at http://www.iram.fr/IRAMFR/GILDAS.

2.2. *Near-infrared Dust Extinction Map and Additional Radio Data*

We make use of the dust extinction map of RLA09 constructed with the NICER technique (Lombardi & Alves 2001) and a combined photometric catalog obtained from ground- (ESO) and space-based (*Spitzer*) observations. In addition to the infrared data, we also make use of a series of pointed observations made with the Green Bank 100 m telescope to determine the variation of the emission of the (1,1) and (2,2) rotation–inversion transitions of ammonia (NH_3) across the central clump B59-09. These data were also used and described in RLA09. Finally, we also make use of a $C^{18}O$ (2–1) line emission map obtained with the detector HERA at the IRAM 30 m telescope (C. G. Román-Zúñiga et al., in preparation).

3. DATA ANALYSIS AND RESULTS

In the top panel of Figure 1, we show our MAMBO-II map toward B59. The map detected mostly the emission from the clump 09ab[5] and, less prominently, the core 09c at the northwestern end. Five young stellar objects were detected with very high signal-to-noise ratios (S/Ns). They correspond to sources 6, 7, 9, 10, and 11 in the list of (Brooke et al. 2007, hereafter BHB07). The 250 GHz continuum emission properties of these sources are listed in Table 1. Note that sources BHB07-6 and BHB07-7 lie very close together and they are not resolved as separated sources in the MAMBO-II map. As our main purpose is to study the emission of the core, we subtracted out the contribution of the young stars. For this purpose, a two-dimensional Gaussian profile was fit to each of the sources, using a background emission level corresponding to the average in the vicinity region of the clump. The fit parameters are listed in Table 1. The smoothness of the resulting map (see the central panel in Figure 1) seems to confirm that most of the subtracted emission arises from the YSO warm circumstellar material rather than from the core cold dust.

After subtracting the contribution from the YSOs, we transformed the dust emission maps to column density and then into visual extinction for a direct comparison with the NICER map of RLA09. The conversion was done following the method described in Section 4.1 and Appendix A of Frau et al. (2010). We note that the conversion is very sensitive to the assumed value for gas temperature, T_k (see Appendix 1 of Frau et al. 2010), and also the dust emissivity (κ_ν) and the dust temperature assumed. Following Ossenkopf & Henning (1994), we assumed $\kappa_\nu = 0.007$ cm^2 g^{-1} for grains in a dense medium ($n \sim 10^5$ cm^{-3}). Then, we computed visual extinction maps for gas/dust temperatures in the 10–12 K range in steps of 0.25 K (ammonia observations yield $T_K = 11.3$ K $\pm$ 0.7 K; Rathborne et al. 2009). We selected a temperature of 10.25 K as this value showed the best agreement with respect to the previous extinction map, and we made the assumption that this temperature is constant within the entire clump. The derived radius, mass, and average density of the clump are listed in Table 2. Given the high S/N achieved, we restricted analysis to the region satisfying $I_\nu > 0.2 I_{\nu,\max}$ ($\sim 4.5\sigma$). The total mass of the clump 09ab in B59 estimated from the MAMBO-II map is about half of that estimated from the NICER map (i.e., cores 09ab and 09c sum about 21 $M_\odot$ according to RLA09). This difference is mostly because MAMBO-II maps are not as sensitive as the near-infrared excess method in detecting the diffuse gas at the

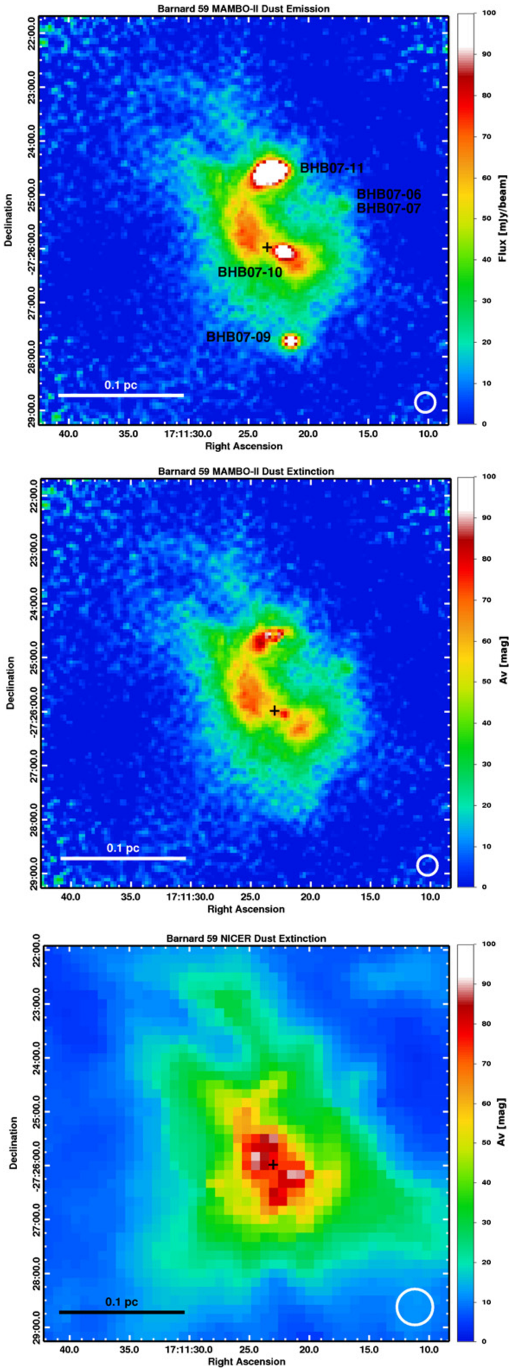

Figure 1. Top: MAMBO-II dust emission map of Barnard 59 from our observations. For purposes of clarity, the flux scale has been clipped from 0 mJy beam^{-1} to 100 mJy beam^{-1}. Numbers refer to YSO sources identified and listed in Table 1. The circle at the bottom right corner indicates the beam size. Middle: MAMBO II dust extinction map after conversion of the flux and subtraction of the YSO's emission. The extinction level has also been clipped from 0 to 100 mag. The circle at the bottom right corner indicates the beam size. Bottom: NICER dust extinction map, as in RLA09, also scaled from 0 to 100 mag. The circle at the bottom right corner shows the size of the Gaussian filter used to construct the map. In all panels, the cross symbol marks the center around which radial profiles were constructed, at J2000 $(\alpha, \delta) = (17{:}11{:}23, 0, -27{:}25{:}59.3)$.

(A color version of this figure is available in the online journal.)

---

[5] We follow the nomenclature of RLA09, see their Table 1.

Table 1
Properties of YSOs Counterparts

ID[a]	Class[a]	Spectral Type[b]	Peak Flux (mJy beam^{-1})	Mass[b] ($M_\odot$)	Gaussian Fit $\Delta\alpha$, $\Delta\delta$[c] ($''$)	Gaussian Fit Deconvolved Size[d] ($''$), (deg)
BHB07-11	I	···	270.0	···	−11.0, 55.5	18.0 × 17.0, −68.0
BHB07-10	0/I	···	65.0	···	65.0, −24.0	16.0 × 16.0, 0.0
BHB07-09	Flat	K5	115.0	0.77–0.79	−29.4, −133.0	13.7 × 12.1, −89.5
BHB07-06	II	M2	15.0	0.24–0.62	15.0, −80.0	14.0 × 12.0, 79.4
BHB07-07	Flat	K5	15.0	0.75–1.16	15.0, −80.0	14.0 × 12.0, 79.4

Notes.
[a] From Brooke et al. (2007).
[b] From Covey et al. (2010).
[c] Offsets from center of map at (α, δ) = (17:11:24.0, −27:25:30.0).
[d] Indicates major and minor axes, and position angle.

Table 2
Barnard 59: Dust Emission Map

Parameter	Value
T_k[a]	10.25 K
rms	4 mJy beam^{-1}
Total flux	8.28 Jy
Peak flux	90.7 mJy beam^{-1}
Diameter[b]	0.11 pc
$N_{\rm H_2}$[c]	2.96×10^{22} cm^{-2}
$n_{\rm H_2}$[c]	1.30×10^{5} cm^{-3}
Mass	9.19 $M_\odot$

Notes.
[a] Corresponds to our best fit to the A_V profile, not to a measured value.
[b] Size of region with emission above $I_\nu > 0.2 I_{\nu,\rm max}$.
[c] Average value over region with emission above $I_\nu > 0.2 I_{\nu,\rm max}$.

external parts of dense cores ($A_V < 25$ mag in this case), rather than a technical effect. The partial detection of cores 09cd and 04a seems to confirm the good quality of the emission maps despite their lack of sensitivity. The NICER technique relies on having enough sources per beam to average reddening, and background sources toward the edges of B59 are abundant. On the other hand, the continuum emission relies on the amount of dust that contributes to the signal, which decreases at lower column densities (see Frau et al. 2010, for additional discussions on this effect). Also, the assumption of a constant temperature for the entire region is less accurate toward the core boundaries that might be heated by external sources.

Morphologically, the MAMBO-II dust extinction map shows features that are equivalent features to those found in the NICER map of RLA09, which is shown in the bottom panel of Figure 1. Both maps show a relatively flat central region toward the clump 09ab with a shallow "dent" near the location of source BHB07-10, discussed in Section 5.1 of RLA09. A radial profile of the MAMBO-II map was constructed by averaging flux in circular, concentric rings centered on J2000 (α, δ) = (17:11:23,0, −27:25:59.3), as in RLA09. Figure 2 shows that observed profiles compare well with each other and trace equivalent structures within $\sim 10^4$ AU ($A_V > 35$ mag). Below $A_V \approx 35$ mag, the MAMBO profile plunges and appears to be truncated below an average radius of 2×10^4 AU, while the NICER profile continues until it reaches the background level near 5×10^4 AU.

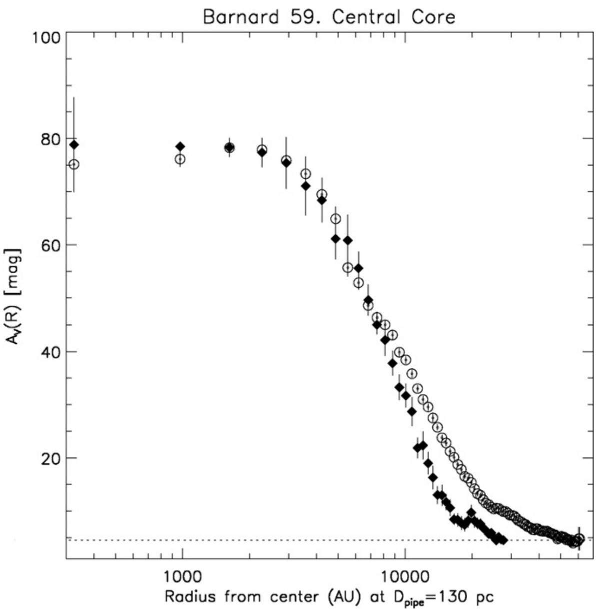

Figure 2. Open circle symbols show the radial profile of the NICER extinction map. The black diamond symbols show the radial profile of the MAMBO-II dust emission map. The profiles were constructed by averaging flux in circular, concentric rings centered on J2000 (α, δ) = (17:11:23, 0, −27:25:59.3). For the MAMBO-II profile, the data were convolved to the resolution of the NICER map (20$''$) and re-gridded to match pixels in both maps.

We used our pointed NH$_3$ observations (RLA09) and the C^{18}O(2–1) map to categorize the variation of the LSR velocity near the center of the clump. Twelve NH$_3$ pointed observations were made within the central 10^4 AU of B59. All of them indicate variations of $v_{\rm LSR}$ smaller than 0.088 km s^{-1} from the central value of 3.485 km s^{-1}. Moreover, these variations are below the average velocity dispersion $\langle\sigma_v\rangle = 0.210 \pm 0.0498$ km s^{-1} and below the sound speed in a 10 K gas ($c_s = 0.12$ km s^{-1}). The C^{18}O (2–1) map reveals variations below 0.05 km s^{-1} from the central velocity value. The linewidths, although being significantly wider than those of the NH$_3$, also show very small variations (less than 0.08 km s^{-1}) from the average value of 0.87 km s^{-1}, indicating very uniform kinematics near the center of B59-09ab. Rathborne et al. (2009) discussed how kinematically independent cores in the Pipe Nebula must show radial velocity differences larger than c_s.

Following this prescription, the differences we observe are too small to suggest the presence of kinematically independent substructure.

4. DISCUSSION

The radio continuum map has twice the resolution of the NICER map (11″ FWHM beam versus 24″ FWHM Gaussian filter), resolving a projected size of 1420 AU (assuming a distance of 130 pc to the Pipe Nebula). We could safely say that the MAMBO-II map should resolve structures with minimum sizes of 2000–5000 AU. Our map, however, does not reveal any significant substructure (other than the sources or the dent) below $\sim 1.5 \times 10^4$ AU. This result is in good agreement with those of Román-Zúñiga et al. (2010), who reported a possible limiting scale of fragmentation in the Pipe Nebula of about 1.4×10^4 AU. As also noted there, this scale agrees with the results of Schnee et al. (2010) who found no evidence of fragmentation in cores of the Perseus Molecular Cloud at scales of 10^3–10^4 AU.

The column density estimations made from near-IR extinction and dust emission are very similar near the center. Both maps fail to show evidence of substructure suggestive of significant fragmentation in R09ab. The dust emission map confirms that the dent is real and thus it suggests that source BHB07-10 is possibly affecting the material surrounding it. The decrement of column density near source BHB07-10, however, is equivalent to a decrement of only 3% in the total mass of the clump (RLA09). Also, CLR10 showed that BHB07-10 is not embedded at the level at which it is projected against the map. In contrast, source BHB07-11 has been suggested to be the origin of a moderate gas outflow (Onishi et al. 1999) that seems to be carving the northern part of the clump, forming core 09c. Thus, the feedback effect near BHB07-10 may not account for a bona fide fragmentation process as in core 09c.

The young stellar cluster in B59 is likely too small to hold itself together dynamically. Following Adams & Myers (2001), for the B59 cluster to remain stable, its relaxation timescale, $t_{\rm rlx}$, should be at least larger than its formation timescale, which in turn should be comparable to the age of the cluster. The age of the B59 cluster is estimated as being 2–3 Myr (CLR10). The relaxation parameter, $Q_{\rm rlx}$, i.e., the number of crossings per relaxation time, can be estimated in terms of the star-forming efficiency, ϵ, and the number of stars, $N_\star$, approximately as $N_\star/(10\epsilon^2 \ln(N_\star/\epsilon))$. Using the present-day value, $\epsilon = 0.3$ (CLR10) and, for 10 sources projected within B59-09ab, we obtain $Q_{\rm rlx} = 3.2$. Therefore, given the crossing time of the clump, $t_{\rm cr} \approx 0.06$ Myr, then $t_{\rm rlx} = Q_{\rm rlx} t_{\rm cr} \approx 0.2$ Myr, which is much shorter than its formation time. It is thus very unlikely that the B59 stellar cluster will remain together longer than a few more crossing times.

Experimental fits of isothermal sphere profiles, particularly Bonnor–Ebert and Dapp & Basu (2009) to the NICER profile, suggest that the core is already out of equilibrium, although it is not possible to estimate its state of evolution toward collapse (see also RLA09). The velocity dispersion from the NH_3 data and the parameters from Table 2 yield a virial parameter value $\alpha_{\rm vir} = 0.25$, which suggests that the B59-09ab clump is gravitationally bound. Thus, we should expect the clump to be presently moving toward collapse. As shown in RLA09, B59-09ab remains mostly quiescent. Moreover, our data show that the clump has been able to amass between 9 $M_\odot$ and 19 $M_\odot$ of gas (the latter if we consider the whole dust extinction structure) in an apparently monolithic structure, and we know from the age of the cluster that the period of mass aggregation could be as long as about six crossing times long (CRL10). What is the mechanism that held the clump together, retarding collapse and fragmentation for a relatively long period?

Feedback in the form of outflows could serve as a turbulent energy injection mechanism that could provide the non-thermal support required to maintain the clump against collapse. Several authors have provided evidence of one and possibly two outflows from embedded sources BHB07-09 and BHB07-11 (Onishi et al. 1999; Brooke et al. 2007; Riaz et al. 2009), and RLA09 discussed how these could be carving structures at the outer regions of the clump. The presence of at least four YSOs located at projected distances larger than the Jeans length of the core (see below) could suggest that B59-09ab is more likely a remnant of dense gas after an episode of multiple source formation within a much larger structure. Even source BHB07-10 could also be affecting the core at a shallow level, as discussed above. The numerical experiments of Krumholz et al. (2007) and Offner et al. (2010) have shown that radiative feedback can be a strong agent against fragmentation. For instance, feedback from protostars can inhibit the formation of binaries in a fragmenting disk scenario. These models, however, require stars with masses above 3 $M_\odot$ and the mechanisms work best at spatial scales about one order of magnitude smaller than the observed size of B59. Since sources in B59 have too low of masses and are not numerous, it is thus very unlikely that they can either provide non-thermal support against collapse or do not provide enough feedback energy to inhibit fragmentation (see, e.g., Longmore et al. 2010).

The other plausible candidate for a mechanism that can prevent further collapse and fragmentation of cores in B59 (as well as other regions of the Pipe Nebula) is the magnetic field. Numerical studies like those of Nakamura & Li (2011) concluded that for an initially magnetically subcritical cloud, a strong magnetic field is able to slow down gravitational collapse and fragmentation, decreasing the star formation rate significantly. Also, Price & Bate (2007) showed that support by magnetic fields may deter density perturbations and the fragmentation of disks in the case of binary formation. The optical polarization studies of Alves et al. (2008a) and Franco et al. (2010) strongly suggest that the Pipe is permeated by a magnetic field. Moreover, Frau et al. (2010) have shown that chemically evolved cores in the Pipe are possibly associated with a strong magnetic field, which is suggestive of significant magnetic support.

Following the formulation of Mouschovias (1991), we find a Jeans length scale of $\lambda_{T,\rm cr} = 0.12$ pc, which is about twice as large as the radius of the clump in the dust emission map, within which have demonstrated the monolithic behavior of the clump (although this length is very close to the radius estimated from the dust extinction map). The data of Franco et al. (2010) indicate that B59 may be sub-Alfvénic, so in the overall region the magnetic field is dynamically more important than the turbulence.

From the Jeans length scale and the critical magnetic length scale, $\lambda_M = 0.91(B/[\mu{\rm G}])(1 \times 10^3\ [{\rm cm}^{-3}]/n)$ (Mouschovias 1991), and considering both the visual extinction and dust emission map derived values of the clump radius, we can infer that a magnetic field strength in the range of 0.1–0.2 mG would be enough to support the clump. These values are larger than those calculated from optical polarization data of the diffuse surrounding gas. However, magnetic field is expected to strengthen toward denser regions as the collapse process evolves (e.g., Fiedler & Mouschovias 1993) and these estimates are not unreasonable compared to other dense cores (see Crutcher 1999; Crutcher et al. 2004).

While the profile of B59 suggests that the core is out of equilibrium (C. G. Román-Zúñiga et al., in preparation), our continuum map shows that it has not finished collapse for a time comparable to the age of the stellar cluster. Magnetic field support (or an equivalent combination of supporting mechanisms) could have been active during such a timescale. The age of the cluster suggests that B59-09ab has survived for a period longer than 10 $t_{\rm ff}$ without completely collapsing or fragmenting, and it is unlikely that it will fail to evolve toward protostellar collapse. Experiments by Galván-Madrid et al. (2007) suggest that pre-stellar core survival can be assured for at most 3–10 $t_{\rm ff}$ for cores with densities above 10^5 cm^{-3}, independently of mass to magnetic flux ratio. Despite the lack of fragmentation in B59-09ab at present, we cannot assure from our data only that the clump will not fragment later. We think, however, that further fragmentation is unlikely because fragmentation tends to proceed quite rapidly. For instance, some numerical studies, like those of Boss (2009), show that oblate cores with magnetic fields can form binaries in timescales of less than 2–4 $t_{\rm ff}$. Also, the models of Price & Bate (2009) show that fragmentation in a core with initial mass of 50 $M_\odot$ and initial radius of 0.375 pc—possibly not that much different from a low-mass star-cluster-forming core like B59—proceeds within 1–2 $t_{\rm ff}$ independently of the amount of magnetic and radiative feedback support added to their models.

Our analysis confirms the hypothesis that B59-09ab does not show significant fragmentation at the present time. We speculate that the clump is likely on its way to collapse, but it will not form multiple sources to increase the population of the small stellar cluster. The efficiency of formation in the cluster B59 after the collapse of the B59-09 clump will increase only modestly. B59 probably will remain as a small, low-mass star cluster with too few stars to survive disintegration by evaporation (Lada & Lada 2003).

We thank an anonymous referee for a critical reading and a list of useful comments that greatly improved the content of our original manuscript. This study is based on observations carried out with the IRAM 30 m telescope. IRAM is supported by INSU/CNRS (France), MPG (Germany), and IGN (Spain). This study makes use of data obtained with instruments from the European Southern Observatory facilities at La Silla and Paranal. The National Radio Astronomy Observatory is a facility of the National Science Foundation operated under cooperative agreement by Associated Universities, Inc. C.R.Z. acknowledges support from Instituto de Astronomía, UNAM and a repatriation grant from CONACYT, México. P.F. and J.M.G. are supported by MICINN grant AYA2008-06189-C03 (Spain) and by AGAUR grant 2009SGR1172 (Catalonia).

Facilities: IRAM:30m (MAMBO), CAO:3.5m (OMEGA 2000), GBT

REFERENCES

Adams, F. C., & Myers, P. C. 2001, ApJ, 553, 744
Alves, F. O., Franco, G. A. P., & Girart, J. M. 2008a, A&A, 486, L13
Alves, J., Lombardi, M., & Lada, C. J. 2007, A&A, 462, L17
Alves, J., Lombardi, M., & Lada, C. J. 2008b, in Handbook of Star Formation, Vol. II, ed. B. Reipurth (San Francisco: ASP), 415
Boss, A. P. 2009, ApJ, 697, 1940
Brooke, T. Y., Huard, T. L., Bourke, T. L., et al. 2007, ApJ, 655, 364
Covey, K. R., Lada, C. J., Román-Zúñiga, C., et al. 2010, ApJ, 722, 971
Crutcher, R. M. 1999, ApJ, 520, 706
Crutcher, R. M., Nutter, D. J., Ward-Thompson, D., & Kirk, J. M. 2004, ApJ, 600, 279
Dapp, W. B., & Basu, S. 2009, MNRAS, 395, 1092
Di Francesco, J., Sadavoy, S., Motte, F., et al. 2010, A&A, 518, L91
Fiedler, R. A., & Mouschovias, T. C. 1993, ApJ, 415, 680
Forbrich, J., Lada, C. J., Muench, A. A., Alves, J., & Lombardi, M. 2009, ApJ, 704, 292
Franco, G. A. P., Alves, F. O., & Girart, J. M. 2010, ApJ, 723, 146
Frau, P., Girart, J. M., & Beltrán, M. T. 2011a, A&A, 537, L9
Frau, P., Girart, J. M., & Beltrán, M. T. 2011b, A&A, submitted
Frau, P., Girart, J. M., Beltrán, M. T., et al. 2010, ApJ, 723, 1665
Galván-Madrid, R., Vázquez-Semadeni, E., Kim, J., & Ballesteros-Paredes, J. 2007, ApJ, 670, 480
Krumholz, M. R., Klein, R. I., & Mckee, C. F. 2007, ApJ, 656, 959
Lada, C. J., & Lada, E. A. 2003, ARA&A, 41, 57
Lada, C. J., Muench, A. A., Rathborne, J., Alves, J. F., & Lombardi, M. 2008, ApJ, 672, 410
Lombardi, M., & Alves, J. 2001, A&A, 377, 1023
Longmore, S. N., Pillai, T., Keto, E., Zhang, Q., & Qiu, K. 2010, ApJ, 726, 97
Mouschovias, T. C. 1991, ApJ, 373, 169
Nakamura, F., & Li, Z.-Y. 2011, in IAU Symp. 270, Computational Star Formation, ed. J. Alves, B. G. Elmegreen, J. M. Girart, & V. Trimble (Cambridge: Cambridge Univ. Press), 115
Offner, S. S. R., Kratter, K. M., Matzner, C. D., Krumholz, M. R., & Klein, R. I. 2010, ApJ, 725, 1485
Onishi, T., Kawamura, A., Abe, R., et al. 1999, PASJ, 51, 871
Ossenkopf, V., & Henning, T. 1994, A&A, 291, 943
Price, D. J., & Bate, M. R. 2007, MNRAS, 377, 77
Price, D. J., & Bate, M. R. 2009, MNRAS, 398, 33
Rathborne, J. M., Lada, C. J., Muench, A. A., et al. 2009, ApJ, 699, 742
Riaz, B., Martín, E. L., Bouy, H., & Tata, R. 2009, ApJ, 700, 1541
Román-Zúñiga, C. G., Alves, J. F., Lada, C. J., & Lombardi, M. 2010, ApJ, 725, 2232
Román-Zúñiga, C. G., Lada, C. J., & Alves, J. F. 2009, ApJ, 704, 183
Schnee, S., Enoch, M., Johnstone, D., et al. 2010, ApJ, 718, 306
Williams, J. P., Blitz, L., & Stark, A. A. 1995, ApJ, 451, 252

IX

The collapsing magnetized cloud in NGC 1333 IRAS 4A

A&A 535, A44 (2011)
DOI: 10.1051/0004-6361/201117813
© ESO 2011

Astronomy & Astrophysics

Comparing star formation models with interferometric observations of the protostar NGC 1333 IRAS 4A

I. Magnetohydrodynamic collapse models*

P. Frau[1], D. Galli[2], and J. M. Girart[1]

[1] Institut de Ciències de l'Espai (CSIC-IEEC), Campus UAB, Facultat de Ciències, Torre C-5p, 08193 Bellaterra, Catalunya, Spain
e-mail: `frau@ice.cat`
[2] INAF-Osservatorio Astrofisico di Arcetri, Largo E. Fermi 5, 50125 Firenze, Italy

Received 2 August 2011 / Accepted 26 September 2011

ABSTRACT

Context. Observations of dust polarized emission toward star forming regions trace the magnetic field component in the plane of the sky and provide constraints to theoretical models of cloud collapse.

Aims. We compare high-angular resolution observations of the submillimeter polarized emission of the low-mass protostellar source NGC 1333 IRAS 4A with the predictions of three different models of collapse of magnetized molecular cloud cores.

Methods. We compute the Stokes parameters for the dust emission for the three models. We then convolve the results with the instrumental response of the Submillimeter Array observation toward NGC 1333 IRAS 4A. Finally, we compare the synthetic maps with the data, varying the model parameters and orientation, and we assess the quality of the fit by a χ^2 analysis.

Results. High-angular resolution observations of polarized dust emission can constraint the physical properties of protostars. In the case of NCC 1333 IRAS 4A, the best agreement with the data is obtained for models of collapse of clouds with mass-to-flux ratio >2 times the critical value, initial uniform magnetic field of strength ~0.5 mG, and age of the order of a few 10^4 yr since the onset of collapse. Magnetic dissipation, if present, is found to occur below the resolution level of the observations. Including a previously measured temperature profile of IRAS 4A leads to a more realistic morphology and intensity distribution. We also show that ALMA has the capability of distinguishing among the three different models adopted in this work.

Conclusions. Our results are consistent with the standard theoretical scenario for the formation of low-mass stars, where clouds initially threaded by large-scale magnetic fields become unstable and collapse, trapping the field in the nascent protostar and the surrounding circumstellar disk. In the collapsing cloud, the dynamics is dominated by gravitational and magnetic forces.

Key words. magnetohydrodynamics (MHD) – polarization – stars: formation – ISM: magnetic fields – ISM: individual objects: NGC 1333 IRAS 4A

1. Introduction

Magnetic fields play an important role in the star formation process. Molecular clouds are expected to form dense cores through a combination of loss of magnetic and turbulent support. Eventually, a molecular cloud core overcomes magnetic support ("supercritical" stage), and collapses gravitationally. The magnetic field is then pinched and strengthened in the central regions of the core, and is expected to assume an hourglass shape (Fiedler et al. 1993; Galli & Shu 1993a,b; Nakamura & Li 2005).

Aspherical spinning dust particles tend to align their small axis parallel to the direction of the magnetic field. Thermal emission from such elongated grains is thus partially linearly polarized, with the polarization vector perpendicular to the magnetic field. Consequently, the polarized emission is a good tracer of the magnetic field. To test the influence of magnetic fields we compare high-angular resolution observations of the polarized emission measured at submillimeter wavelengths toward the low-mass protostar NGC 1333 IRAS 4A with non-turbulent magnetohydrodynamic (MHD) models of molecular cloud cores threaded by an initial uniform magnetic field. This first step will help to (*i*) select the best models to describe the structure and evolution of low-mass cores, and, (*ii*) to better understand the importance of the physical processes involved in their formation and evolution. In a subsequent paper we will consider models of magnetized molecular cores formed in a turbulent environment.

The low-mass protostar IRAS 4A is an ideal test site for models of magnetized cloud collapse and star formation. BIMA spectropolarimetric observations at 1.3 mm have detected and partially resolved the polarization in both the dust and CO (2–1) emission (Girart et al. 1999), showing hints of a hourglass morphology of the magnetic field. Recent polarimetric observations with the SMA at 877 μm with a resolution of 1ʺ.3 (390 AU) have shown that the magnetic field associated with the infalling envelope has a clearly "pinched" morphology on a scale of a few hundreds AU (see Fig. 1 in Girart et al. 2006). This morphology resembles the hourglass shape that is predicted by the standard theory of low-mass star formation in a collapsing core with a regular magnetic field dominating the irregular (turbulent) one (Fiedler & Mouschovias 1993; Galli & Shu 1993a,b; Nakamura & Li 2005). Applying the Chandrasekhar-Fermi equation, Girart et al. (2006) derived a magnetic field strength in the plane of the sky (POS) of $B_{\rm POS} \approx 5$ mG, corresponding to a mass-to-flux ratio of ~1.7 times the critical value.

Gonçalves et al. (2008) compared the position angles in the plane of the sky of the polarization vectors determined by Girart et al. (2006) with the inclination of magnetic field lines of ideal (Galli & Shu 1993a,b) and non-ideal (Shu et al. 2006)

---

* Based on observations carried out with the SMA telescope.

MHD collapse models. They found a good qualitative agreement for a source with $\lesssim 1\ M_\odot$ and a mass-to-flux ratio of ~ 2 times the critical value. The present work is a step forward in the modelization and methodology with respect to that of Gonçalves et al. (2008).

This paper is organized as follows: in Sects. 2 and 3 we describe the target source IRAS 4A and the selected MHD models, respectively. In Sect. 4 we describe the synthetic map generation. General results are detailed in Sect. 5. In Sect. 6 we present the MHD models prediction convolved with the SMA interferometer and compare them with IRAS 4A observations. In Sect. 7 we present the ALMA maps of the MHD model prediction. Finally, in Sect. 8 we summarize the results and list the conclusions.

2. NGC 1333 IRAS 4A

The Perseus molecular cloud is an active low-mass star forming region, located at a distance ranging from 230 pc to 350 pc (Ridge et al. 2006). For this work, we adopt the value of 300 pc (Girart et al. 2006). In the southern part of the reflection nebulae NGC 1333, Jennings et al. (1987) were the first to identify the protostar NGC 1333 IRAS 4. Sandell et al. (1991) resolved the system into two different components, IRAS 4A and IRAS 4B, separated by $\sim 31''$. They measured a luminosity of $\sim 28\ L_\odot$ (at 350 pc, 11 $L_\odot$ at 220 pc) equally shared between the two components. Subsequent interferometric observations have revealed further multiplicity: IRAS 4A is itself a binary system. The two components IRAS 4A1 and IRAS 4A2 are separated by 540 AU ($1\farcs8$, Lay et al. 1995; Looney et al. 2000; Girart et al. 2006).

This low-mass stellar system is in a very early stage of evolution. IRAS 4A and 4B are still embedded in a dense molecular and dusty envelope. Sandell et al. (1991) derived from submillimetric continuum single-dish observations a mass of $\sim 9\ M_\odot$. Subsequent interferometric observations derived a mass of 1.2 $M_\odot$ (Girart et al. 2006) for the compact component. Di Francesco et al. (2001) detected infall motions from inverse p-Cygni profiles observed in H_2CO ($3_{12}{-}2_{11}$) and N_2H^+ (1–0). Single-dish CO (3–2) observations revealed a NE-SW well-collimated outflow arising from IRAS 4A (Blake et al. 1995). Choi (2005) reports, through interferometric SiO (1–0) observations, a highly collimated NE-SW outflow with a projected position angle of $\sim 19°$, and hints of a N-S outflow. The author proposes that IRAS 4A2 is powering the main outflow while IRAS 4A1 would power the secondary one.

2.1. New data

For this work we generated new observational maps of IRAS 4A combining compact (Girart et al. 2006), and sub-compact and extended (Ching & Lai, priv. comm.) configuration SMA data (see left panel of Fig. 1), consisting of 8 h tracks in polarization mode at 880 μm. The data reduction was performed using MIRIAD, while the imaging was done using GREG from the GILDAS package. To obtain the maps we used a weighting robust parameter of 0.5 (Briggs 1995) corresponding to a beam of $1\farcs24 \times 1\farcs12$, slightly smaller than that of Girart et al. (2006). Adding the sub-compact configuration improved the map with respect to that of Girart et al. (2006): the sampling of the larger scales is better and allows a better characterization of the circumbinary envelope. In addition, the extended configuration data help in separating the emission arising from either the embedded compact sources or the circumbinary envelope. The combined continuum (Stokes I) map is in good agreement with that of Girart et al. (2006), although the emission is more extended and has a sharper morphology. Furthermore, the polarized intensity map covers a larger area, has a slightly higher intensity peak and a more defined morphology.

The dust emission of IRAS 4A arises from the cold circumbinary envelope and from the warm circumstellar material around each protostar. Since the focus of this paper is on the morphology of the magnetic field in the circumbinary envelope, we have subtracted the contribution from the circumstellar component to the SMA visibility data. To do so, we first derived a map of the longest baselines (100−260 $k\lambda$) corresponding to a beam of $0\farcs70 \times 0\farcs46$. At these u, v-distances, the emission from the circumbinary envelope is resolved out, and the only contribution from the dust emissions arises from the circumstellar material (see central panel of Fig. 1 and Sect. 5.3). Then, the clean components of this map were subtracted from the original visibilities. Finally, we obtained a new map of the circumbinary envelope using the resulting visibilities (see right-hand side panel of Fig. 1).

Table 1 shows the main parameters of the emission associated only with the circumbinary envelope: peak position, $T_{\rm dust}$, rms, S_ν, $I_\nu^{\rm peak}$, $FWHM$, $N_{\rm H_2}$, $n_{\rm H_2}$ and mass. The integrated flux is 4.1 Jy, corresponding to a mass of 0.8 $M_\odot$, both slightly smaller than those of Girart et al. (2006) as we were able to isolate the envelope. The optical depth of the dust emission at 880 μm imply that the observations trace very deep into the source. Therefore, neglecting scattering (see Sect. 4.1) and assuming an anisotropic radiation field, the polarized dust emission is probably originated in the alignment of dust grains to the magnetic field (see Lazarian 2003, for a comprehensive review on this topic). The envelope hourglass morphology of the magnetic field is more evident than in earlier data. A new feature is the double peak in polarized intensity. The map also shows a significant depolarization toward the source main axis, which was not as clear in the Girart et al. (2006) map. This feature can be explained in terms of projections effects intensified by beam smearing (see, e.g., Gonçalves et al. 2005).

3. Theoretical models

We compare the dust polarization map of IRAS 4A described in the previous section with the predictions of three models of magnetized cloud collapse. The models of Galli & Shu (1993a,b) and Allen et al. (2003a,b) give the density profile and magnetic field distribution of an infalling envelope surrounding a low-mass star, the two models differing mainly in the choice of the initial conditions. The Shu et al. (2006) model is similar to the previous two, but contains a parameter representing the spatial scale where the diffusive effects associated to an electric resistivity (assumed uniform) dominate the evolution of the magnetic field. Therefore, our analysis is not able to test the theory of core formation from iniatially subcritical conditions by ambipolar diffusion. This can only be accomplished by spatially resolved Zeeman observations of molecular cloud cores and their surroundings (see e.g., Crutcher et al. 2009). In a following paper (Frau et al., in prep.) we will analyze synthetic polarization maps of protostellar cores extracted from numerical simulations of turbulent clouds.

3.1. Galli & Shu (1993a,b)

This model follows the collapse of a singular isothermal sphere threaded by an initially uniform magnetic field. The cloud is assumed to be non rotating. This initial condition is a highly idealized representation of a non-equilibrium state. Inside the

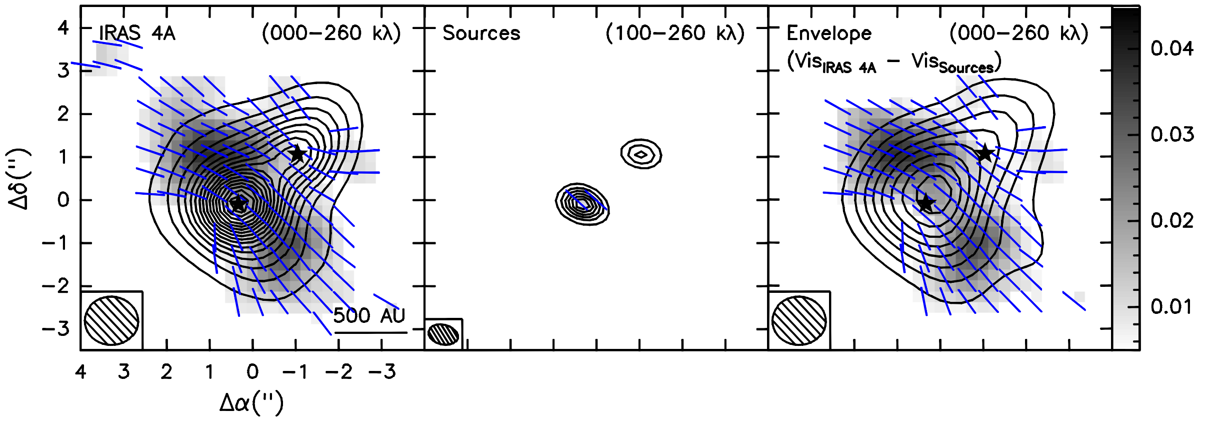

Fig. 1. *Left panel*: IRAS 4A combining SMA sub-compact, compact and extended configurations with robust parameter set to 0.5. The stars mark the two compact sources (see central panel). Top-right corner shows the u, v range used. The synthesized beam is $1\farcs24 \times 1\farcs12$. Contours show the dust emission at 880 μm in steps of 6σ, from 6σ to 96σ, where $\sigma = 0.02$ Jy beam^{-1}. The pixel map shows the polarized intensity (see scale on the right-hand side). Blue bars show the observed magnetic field direction. *Central panel*: IRAS 4A compact components. Legends are the same as in the left panel. The u, v range is restricted to the longest baselines. The synthesized beam is $0\farcs70 \times 0\farcs46$. Contours range from 6σ to 36σ. *Right panel*: IRAS 4A envelope emission (see Sect. 2.1). Legends are the same as in the left panel. Contours range from 6σ to 48σ.

Table 1. IRAS 4A: envelope continuum emission at 880 μm and derived parameters^a.

α(J2000)^b	$3^h29^m10.520^s$
δ(J2000)^b	$31^\circ13'31\farcs12$
$T_{\rm dust}{}^c$	50 K
rms$_{\rm I}$	20 mJy beam^{-1}
rms$_{\rm Q}$	2.5 mJy beam^{-1}
rms$_{\rm U}$	2.5 mJy beam^{-1}
$S_\nu^{\rm I}$	4.1 ± 0.4 Jy
$I^{\rm I}_{\rm peak}$	1.03 ± 0.02 Jy beam^{-1}
FWHM^d	1156 AU ($3\farcs85$)
$S_\nu^{\rm pol}$	160 ± 16 mJy
$I^{\rm pol}_{\rm peak}$	38.2 ± 2.5 mJy beam^{-1}
$\Omega^{{\rm pol}\,e}$	14 arcsec^2
τ	0.07
$N_{\rm H_2}{}^f$	1.2×10^{24} cm^{-2}
$n_{\rm H_2}{}^f$	1.1×10^{8} cm^{-3}
Mass^f	0.8 $M_\odot$

Notes. $^{(a)}$ See Appendix A of Frau et al. (2010) for details. $^{(b)}$ From a 2D Gaussian fit to the source. $^{(c)}$ Girart et al. (2006). $^{(d)}$ Diameter of the circle with the same area as the region of the source with intensity above half of the peak. $^{(e)}$ Solid angle of the region with polarized intensity above 3σ. $^{(f)}$ Assuming $\kappa_{250\,\rm GHz} = 1.5$ cm^2 g^{-1} and a gas-to-dust ratio of 100 (Girart et al. 2006).

collapse region, bounded by an outward propagating slow magnetosonic wave, the magnetic field dragged by the flow (even in the presence of ambipolar diffusion) deflects the infalling gas towards the midplane, forming a large pseudodisk. The initial state depends on two dimensional quantities, $r_0 = 2a^2/\sqrt{G}B_0$ and $t_0 = 2a/\sqrt{G}B_0$, defining the characteristic spatial and temporal scale of the collapse. These depend on the sound speed a, the gravitational constant G and the initial (uniform) magnetic strength B_0. For given r_0 and t_0, the time evolution depends on the non-dimensional parameter $\tau = t/t_0$, where t is the time elapsed since the onset of collapse. Fixing $a = 0.35$ km s^{-1}, the model thus depends only on B_0 and τ.

3.2. *Allen et al. (2003a,b)*

This model is similar to that of Galli & Shu (1993a,b) with some important differences: (*i*) being fully numerical, it overcomes the spatial and temporal limitations of the semi-analytical approach of Galli & Shu (1993a,b); (*ii*) the initial state is a magnetostatic unstable equilibrium configuration (a "singular isothermal toroid" see Li & Shu 1996), already flattened in the direction perpendicular to a magnetic field possessing a hourglass morphology from the start; (*iii*) the cloud can rotate around an axis parallel to the axis of the magnetic field. As in the Galli & Shu (1993a,b), magnetic field lines internal to a "separatrix" are dragged into the accreting protostar.

The initial configuration is specified by the sound speed, a (as in the Galli & Shu 1993a,b model), and the level of magnetic to thermal support, H_0, which represents the fractional overdensity supported by the magnetic field above that supported by the thermal pressure, and the rotational speed, v_0. The parameter H_0 is related to the mass-to-flux ratio of the cloud.

The flattening of the mass distribution (the "pseudodisk") and the magnetic field geometry are little affected by rotation. Conversely, the angular velocity of the infalling gas is strongly influenced by the magnetic braking associated to the strong field created by accretion, assuming ideal MHD. This effect has important implications for the formation of rotationally supported disks around young stars (see Galli et al. 2006).

3.3. *Shu et al. (2006)*

To overcome the difficulties associated to catastrophic magnetic braking and to the huge magnetic flux of the protostar, Shu et al. (2006) consider the consequences of non-ideal MHD effects during the accretion phase of low-mass star formation. In steady state, magnetic dissipation occurs inside a region of radius equal to the so-called "Ohm radius", $r_{\rm Ohm} = \eta^2/(2GM_\star)$, where η is the Ohmic resistivity (assumed uniform), G is the gravitational constant, and $M_\star$ is the mass of the accreting protostar. Outside $r_{\rm Ohm}$, the accreting gas is in free fall along radial field lines, that become straight and uniform inside $r_{\rm Ohm}$. The magnetic flux accreted by the central protostar is zero at all times.

4. Synthetic map generation

4.1. Assumptions

To compare the intensity and the polarized intensity predicted by the models with the observed data, it is important to consider the effects of a temperature gradient, since the sub-mm emission is roughly proportional to the temperature. In this work, we have assumed both a uniform temperature profile (UTP) and a radial temperature profile (RTP) derived for IRAS 4A by Maret et al. (2002) from water emission. Although the theoretical models considered here are computed assuming an isothermal equation of state, the IRAS 4A observed temperature gradient does not significantly affect the dynamics of collapse, because the kinetic energy due to thermal motions is more than one order of magnitude smaller than the kinetic energy of the infalling particles. For example, the temperature expected at 600 AU is 50 K, which leads to a thermal broadening of $\sigma_{\rm therm} \sim 0.4$ km s^{-1}, whereas the infall velocity expected is $v_{\rm ff} \sim 1.7$ km s^{-1}.

We consider optically thin emission with no absorption or scattering effects, in agreement with the sub-mm emission properties (Hildebrand 1983; Novak et al. 1989) and with the opacity derived in IRAS 4A (see Table 1). We have assumed uniform grain properties, represented by the polarizing efficiency parameter α which includes the absorption cross section and the alignment efficiency. Following Fiege & Pudritz (2000), the maximum degree of polarization is

$$p_{\rm max} = \frac{\alpha}{1-\alpha/6}\cdot \tag{1}$$

We assumed $p_{\rm max} = 15\%$, corresponding to $\alpha = 0.15$. Despite the high value of α used, and the fact that the grain properties may change with density (Fiege & Pudritz 2000), we find that the absolute polarized intensities derived in the models match reasonably well the observed values in IRAS 4A. Lower values of α (e.g., $\alpha = 0.1$) did not reproduce the data equally well.

We performed the numerical integration using an equally spaced regular cubic grid and uniform step in the line-of-sight direction.

4.2. Method

We improved the technique developed by Gonçalves et al. (2008) to compare theoretical models with observed data, including in the process the instrumental effects. In practice, we simulated all the steps of a regular observing run with both SMA and ALMA, generating synthetic maps with the same filtering and processing as the observed maps. With this technique we avoid any possible misinterpretation due to the effects of the instrumental response and filtering, as well as the data modification because of the Fourier transform of the observed visibilities and the subsequent application of the dirty map cleaning algorithm. The process consists of a series of 5 consecutive steps for each realization:

1. For any given model we generated three-dimensional (3D) data cubes of density and magnetic field components. The orientation in space of the 3D source models were defined by two viewing angles: the position angle ϕ of the projection of the polar axis in the plane of the sky with respect to the north direction, and the inclination angle ω of the polar axis with respect to the plane of the sky ($\omega = 0°$ for edge-on view). Since the models used have axial symmetry, the optically thin emission assumption allowed us to explore only half of the inclination angle space ($0° \leq \omega \leq 90°$). We restricted ϕ to the range $0° \leq \phi \leq 90°$ (the observations fix the magnetic axis of IRAS 4A at $\phi \approx 50°$, see Girart et al. 2006).
2. In the plane of the sky we simulated a square area with side length of $51\rlap{.}''2$ ($\sim 1.5 \times 10^4$ AU at the distance of IRAS 4A). The map size was chosen to be about twice the SMA primary beam to better process the sidelobes in the final maps. In this plane we used a grid of 512×512 pixels with a pixel size of $0\rlap{.}''1$ ($\sim$30 AU), enough to oversample the smallest beam used in this work ($\sim 0.4'' \sim 120$ AU for ALMA). With this choice we ensured, in the final convolved maps, the independence of points separated more than a beam distance due to beam convolution. In the line-of-sight direction we covered a length of 6×10^3 AU (equivalent to $20''$) sampled with 60 cells. A larger integration length or a larger number of steps did not affect significantly the details of the final maps.
3. Through a ray-tracing scheme, we integrated the emission of the cells along the line-of-sight ℓ generating 2D raw synthetic maps for the Stokes parameter I, Q, and U. We followed a method developed by Lee & Draine (1985), and elaborated by Wardle & Konigl (1990), Fiege & Pudritz (2000), and Padoan et al. (2001). One can calculate the Stokes Q and U intensities as $Q = Cq$ and $U = Cu$, where C is a constant that includes all the terms assumed to be constant (polarization efficiency and polarization and absorption cross sections) that can be interpreted as a polarized intensity scale factor. q and u are the "reduced" Stokes parameters defined as

$$q = \int \rho B_\lambda(T_{\rm d})\ \cos 2\psi \cos^2\gamma\ {\rm d}\ell, \tag{2}$$

$$u = \int \rho B_\lambda(T_{\rm d})\ \sin 2\psi \cos^2\gamma\ {\rm d}\ell, \tag{3}$$

where ρ is the density, $B_\lambda(T_{\rm d})$ is the Planck function at the dust temperature $T_{\rm d}$, ψ is the angle between the north direction in the plane of the sky and the component of $\boldsymbol{B}$ in that plane, and γ is the angle between the local magnetic field and the plane of the sky. Stokes I is given by $I = (C/\alpha)(\Sigma - \alpha\Sigma_2)$ (Fiege & Pudritz 2000) where α is the maximum polarizing efficiency assumed to be 15%, the C/α factor can be interpreted as a total intensity scale factor, while Σ and Σ_2 are defined as

$$\Sigma = \int \rho B_\lambda(T_{\rm d})\ {\rm d}\ell, \tag{4}$$

$$\Sigma_2 = \int \rho B_\lambda(T_{\rm d}) \left(\frac{\cos^2\gamma}{2} - \frac{1}{3}\right) {\rm d}\ell, \tag{5}$$

and represent the emitted Stokes I intensity and the polarization absorption losses respectively. As for Stokes Q and U, one can define the "reduced" Stokes I parameter as

$$i = \frac{\Sigma - \alpha\Sigma_2}{\alpha}\cdot \tag{6}$$

4. Once the synthetic Stokes 2D maps were generated, the flux was rescaled so that the total flux in the region of the map with $I_\nu > 6\sigma$ (see Sect. 2.1) matched that of the synthetic map. A Gaussian noise was added to match the noise of the observations for each Stokes map. These maps were converted to visibilities using the same visibility coverage in the u, v plane as the real observations. In this step we mimicked the effects of the observation noise and the instrumental filtering. This allowed us to be sensitive to the same spatial

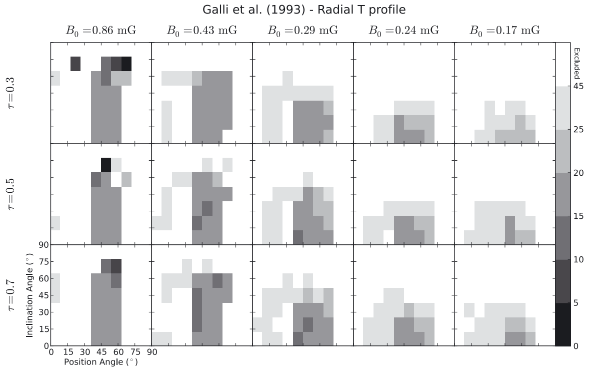

Fig. 2. *Pixel map*: standard deviation of the difference of the synthetic polarization vectors with respect to the observed ones for the Galli & Shu (1993a,b) model with radial temperature profile. White pixels represent excluded models (see text). Grayscale is on the right-hand side of the figure.

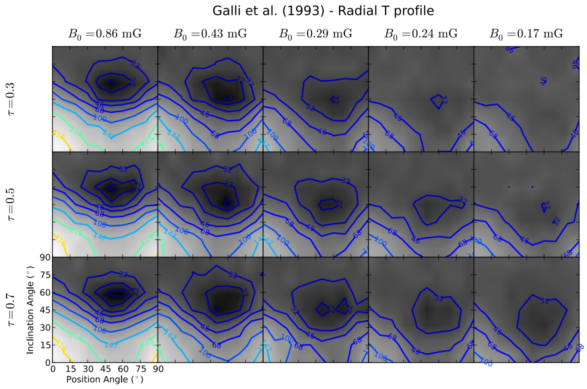

Fig. 3. *Pixel map*: sum of the χ^2 of the Stokes Q and U maps for the Galli & Shu (1993a,b) model with radial temperature profile with respect to the data. *Contours*: 10, $10^{1/6}$, $10^{2/6}$, ..., 10^3 χ^2 levels.

scales and to similar emission levels. Then, the final model maps for the Stokes I, Q and U were obtained from the synthetic visibilities in the same way as the combined SMA maps presented in Fig. 1.

5. The process described in points 1 to 4 is repeated a large number of times for both temperature treatments using different values for (*i*) the position angle ϕ and the inclination angle ω, and (*ii*) the model parameters.

For ALMA, we used the task *simdata* from the CASA package to predict the expected maps for the models with the ALMA capabilities. At the source distance, the cells of the simulations had a typical length of ~30 AU. We chose the full ALMA configuration 09, which provides a synthesized beam of $0.''7 \times 0.''4$ (210 × 120 AU) thus ensuring that the final synthetic maps were not affected by resolution issues. We simulated a 2 h run at 345.8 GHz in polarization mode. As good weather is required for polarization measurements, we assumed 1 mm of precipitable water vapor. The elevation of the source ranged between 30° and 40°.

4.3. Selection

At this point, one has to select the "best" procedure for comparing the synthetic maps with the observational data. This can be accomplished in several ways: (1) using the method of Gonçalves et al. (2008) based on the minimization of the difference between the observed and predicted position angles of the polarization vectors (hereafter simply "angle difference method"); (2) performing a χ^2 analysis of the synthetic Stokes Q and U maps with respect to the observed maps. In the latter case (hereafter simply "χ^2 method"), we positioned the peak of the synthetic map on the peak of the IRAS 4A envelope (see Fig. 1), and we compared the synthetic map with all the region of the observed map with intensity larger than 3σ (see Table 1). As we focus on the polarized emission, we define the best fitting models as those which minimize the sum $\chi^2 = \chi^2_Q + \chi^2_U$. Stokes I was excluded since it shows considerable dependence on the assumed temperature profile.

We illustrate the results for the two selection methods for the Galli & Shu (1993a,b) models with RTP (see Figs. 2 and 3). Figure 2 shows the standard deviation of the distribution of differences in position angles as function of the viewing angles ω and ϕ for the Galli & Shu (1993a,b) models described before. Only runs with average difference value of the position angles with respect to those of IRAS 4A lower than 15° are shown. Best-fitting models are characterized by the smallest values of the standard deviation. The uniform distribution of results makes evident the low discrimination power of the angle difference method. Conversely, the χ^2 method allows to perform a more significant selection of the best-fitting models. Figure 3 shows a difference of more than one order of magnitude between bad- and well-fitting runs thus providing a higher discriminating power among all the runs. Therefore, in the rest of this paper, we adopt the χ^2 selection method.

5. Results

5.1. Orientation angles

Stokes Q and U maps show a significant dependence on the orientation angles of the source, and can be used to constrain the viewing geometry. Figure 4 illustrates the different emission patterns arising from an Allen et al. (2003a,b) source, with $H_0 = 0.125$, $v_0 = 0$, and $t = 2 \times 10^4$ yr, after varying the orientation angles. Stokes Q and U maps are shown for all the combinations of position (ϕ) and inclination (ω) angles of 0°, 30°, 45°, 60°, and 90°. Conversely, Fig. 5 shows Stokes I maps which depend marginally on the position angle, and only for small inclination angles.

As can be seen in Fig. 4, Stokes Q is specially sensitive to the position angle for small inclination angles, while Stokes U appear to vary more with inclination angle at non-extreme position angles. From a practical point of view, one could identify with relatively high precision, by pure comparison with Figs. 4 and 5, both position angles of a source with a magnetic field with hourglass morphology and an inclination angle smaller than ~60°. For inclination angles $\gtrsim$60° the expected magnetic field tend to be mostly radial and the Stokes Q and U maps show very similar morphologies independently of ω. Therefore, polarization observations have shown to be a powerful tool to determine both position angles of a sources with respect to the LOS direction. Figures 4 and 5 could be used as templates for future observations of the dust polarized emission toward star forming cores.

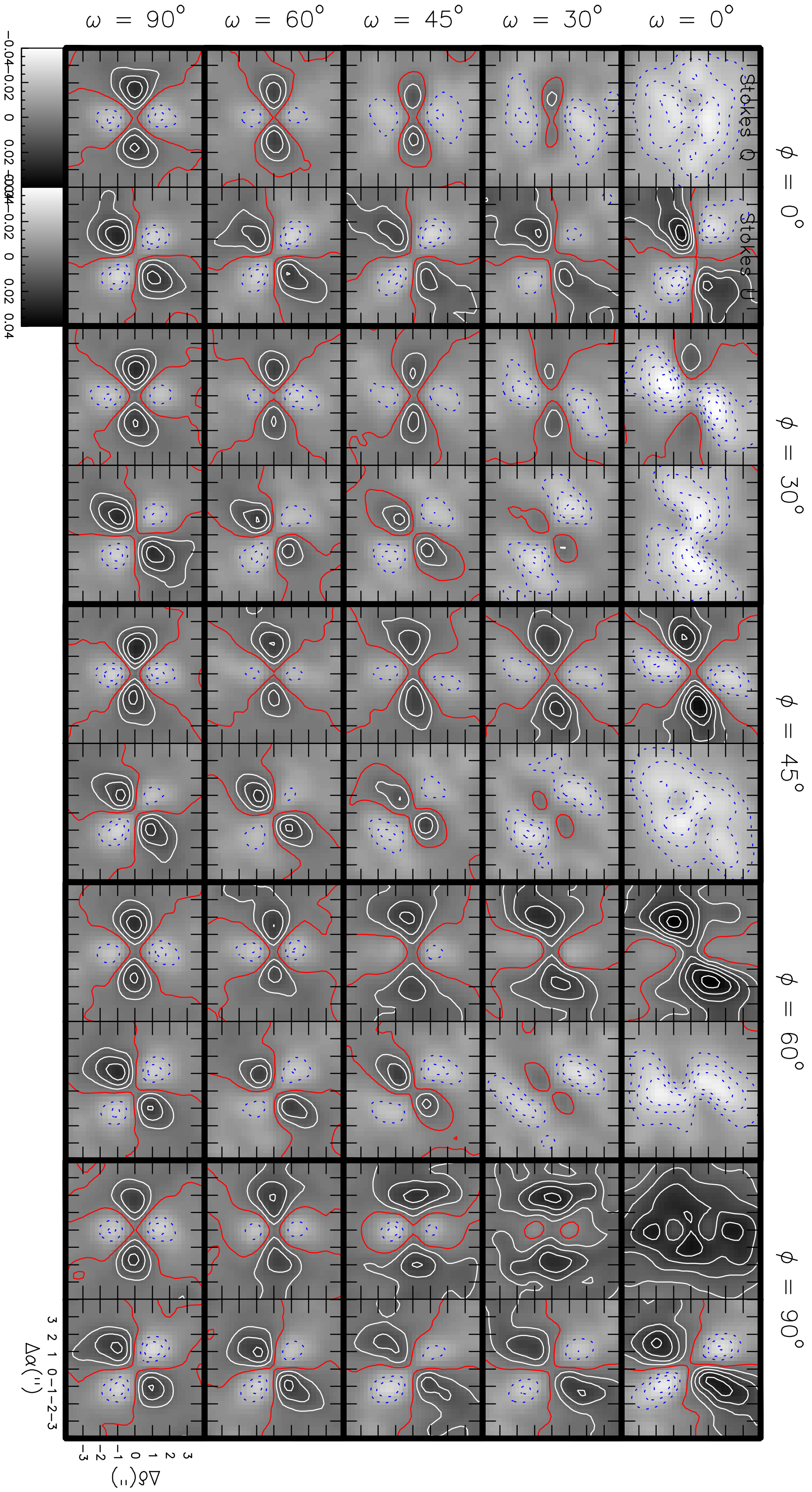

Fig. 4. Dependence of the synthetic Stokes Q and U maps on the orientation angles. The maps shown corresponds to the Allen et al. (2003a,b) model with $H_0 = 0.125$, $v_0 = 0$ and $t = 2 \times 10^4$ yr. Thick contours: correspond to a single combination of position and inclination angle. *Individual panels*: inside thick contours two panels are shown. Stokes Q and U map are shown in the left- and right-hand side panels, respectively. Common color scale for each Stokes map is shown below the first column. The angular scale is shown in the bottom right-hand side panel. Map contours: represent steps of 3-σ starting at 3-σ, where $\sigma = 2.5$ mJy beam^{-1}. Columns: correspond to a position angle, ϕ, shown on the top. Rows: correspond to an inclination angle, ω, shown on the left-hand side of the figure.

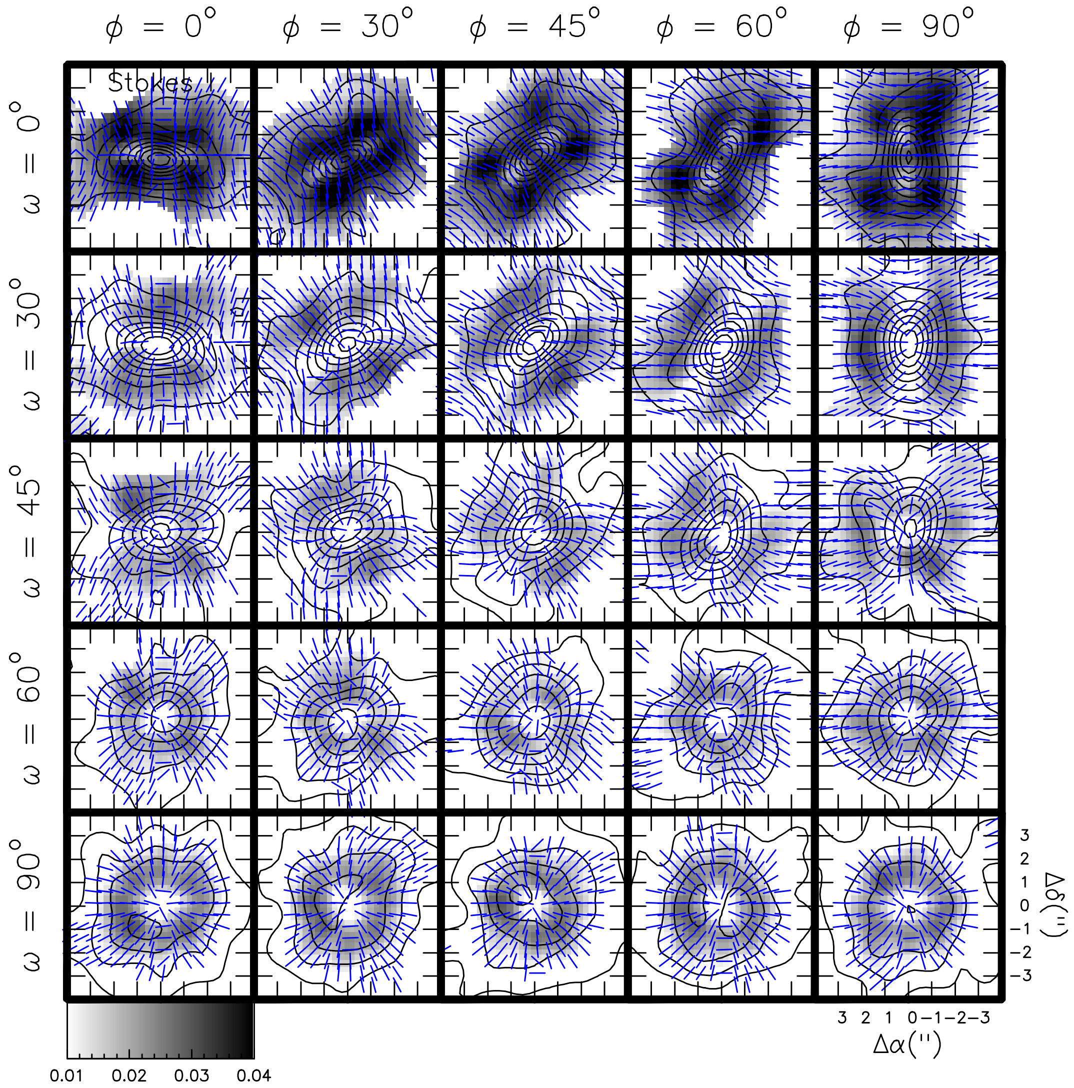

Fig. 5. Same as Fig. 4 but for Stokes I maps. Each panel show the total emission (contours), the polarized emission (pixel map) and the magnetic field direction (segments). *Map contours*: for Stokes I represent steps of 6-σ starting at 6-σ, where σ = 0.02 Jy beam^{-1}.

5.2. Temperature profiles

Figure 6 shows the differences in Stokes I u, v amplitude between both temperature treatments. The models show more realistic amplitudes using the RTP. The models with UTP show lower intensities than IRAS 4A in the $\gtrsim$25 $k\lambda$ range ($\lesssim$4″), while the models with RTP fit the observations up to 15−20 $k\lambda$ ($\lesssim$5.″5). Note that this is remarkable for either temperature treatment as the intensity rescaling was done in the $I_\nu > 6\sigma$ which covered radii $\lesssim$3″ ($\gtrsim$35 $k\lambda$). Figures 7 and 8 show the same information in the image domain for UTP and observed RTP, respectively, for cases with realistic model parameters and orientation angles. UTP maps show more extended emission (larger u, v amplitudes at short baselines) than IRAS 4A and a lower emission peak evident from the residual maps. On the other hand, RTP maps show a slightly more extended morphology than IRAS 4A and realistic intensity peak values. Note that RTP residual maps tend to show zero emission at short radii and slightly negative emission at large ones due to the more extended sources predicted by the models. More realistic fluxes, intensity peaks and masses are derived from the RTP treatment. However, even using the observed temperatures, the radial intensity profile from models is steeper than that of IRAS 4A, which lead to smaller *FWHM* for model synthetic maps and, consequently, higher densities than those observed.

The RTP treatment also predicted more realistic Stokes Q and U maps, shown in the middle left-hand side and middle right-hand side panels of Figs. 7 and 8. Although peak values are similar for both treatments, RTP map show roughly the same polarized flux over the same solid angle with similar morphology to IRAS 4A. On the other hand, UTP map showed roughly twice as much polarized flux over twice the solid angle of IRAS 4A (see Tables 2 and 3). An immediate consequence was the unrealistic UTP vector map whereas the RTP one reasonably match that of IRAS 4A.

Summarizing, RTP maps reproduced with higher fidelity the observed IRAS 4A emission, in the three Stokes parameters, better than UTP maps in the same conditions. Consequently, the physical parameters derived from RTP maps were more realistic.

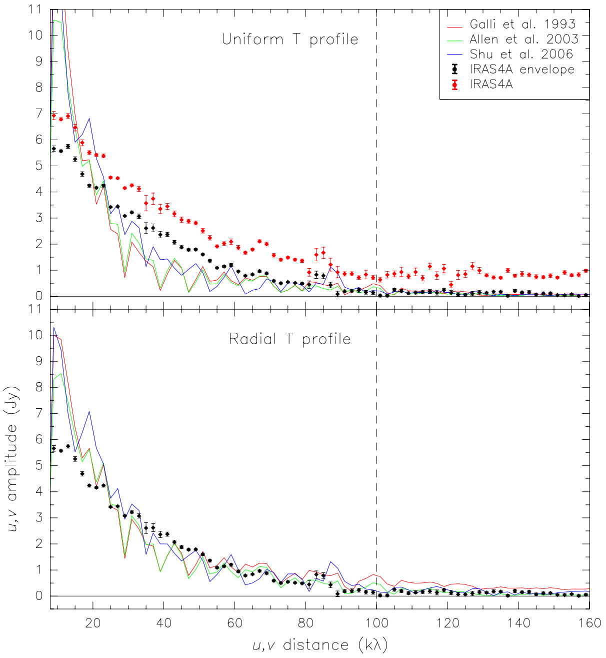

Fig. 6. Stokes I visibility amplitudes vs. u, v distance averaged in bins of $2k\lambda$. *Top panel*: uniform temperature profile. *Bottom panel*: radial temperature profile. Red and black dots: IRAS 4A full data and envelope data, respectively, with their statistical error bars. Vertical dashed line: u, v distance threshold used to derive the compact components map (see Fig. 1). Starting at ~90 $k\lambda$ the emission seems to match with an unresolved source of ~1 Jy. Red, green, and blue solid curves: visibility amplitudes derived after convolving the Galli & Shu (1993a,b), Allen et al. (2003a,b), and Shu et al. (2006) models, respectively, used to generate the maps of left-hand panels of Figs. 7 and 8.

5.3. Visibility amplitudes

Solid curves in Fig. 6 show the total u, v amplitude as a function of the u, v distance for the models using realistic model parameters and orientation angles ($\phi = 50°$ and $\omega = 45°$, see Sects. 5.1 and 6). The oscillations in the synthetic visibilities are due to the added noise. The intensity rescaling of synthetic data was performed in the image domain as it is the output of the simulations. However, a good agreement in the u, v data is important given that it is the output from the telescope. Red and black dots in Fig. 6 show, respectively, the resulting u, v amplitudes before and after subtracting the two circumstellar compact components. We assumed that only emission from the envelope remained after subtraction. To test the goodness of the rescaling method we compared the observed u, v data of IRAS 4A with the synthetic u, v data derived from the models. A remarkable agreement (specially using the observed temperature profile, see Sect. 5.2) is achieved for u, v distances ranging from ~20 $k\lambda$ up to the maximum baseline with significant envelope emission (~90 $k\lambda$). None of the envelope models showed significant emission at u, v distances $\gtrsim$100 $k\lambda$ (equivalent to a radius of 1″ or 300 AU) reinforcing the hypothesis that no envelope emission is detected from the IRAS 4A envelope in this u, v range. At u, v distances shorter than ~20 $k\lambda$ the models show larger emission than the IRAS 4A envelope. At a distance of 300 pc this scale is equivalent to emission with a radius of $\gtrsim$1500 AU ($\gtrsim$5″), which is larger than the radius of IRAS 4A at a 3-σ level (~3″, ~900 AU). This excess has its origin in the fact that the models predict a more extended source than the observed one, with typical radius of ~4″(~1200 AU) at a 3-σ level.

6. SMA synthetic maps

In general, synthetic intensity maps obtained from theoretical models tend to be less concentrated than the observed sources. The flux scaling based on the real data, combined with less compact synthetic sources, cause the synthetic maps to show more extended emission than the observed ones, and also a lower flux intensity peak. In the following subsections (6.1, 6.2, and 6.3) we determine the best fitting parameters for each individual model (see Figs. 3, 9, and 10) and perform a direct comparison of IRAS 4A with all the models (see Figs. 7 and 8, and Tables 2 and 3).

6.1. Galli & Shu (1993a,b)

We selected 5 values of the initial magnetic field (B_0 = 0.86 mG, 0.43 mG, 0.29 mG, 0.24 mG, and 0.17 mG, corresponding to $t_0 = 10^4$ yr, 2×10^4 yr, 3×10^4 yr, 4×10^4 yr, and 5×10^4 yr) and 3 values of the non-dimensional time τ (τ = 0.3, 0.5 and 0.7). The mass-to-flux ratio of the initial configuration is not spatially uniform as in the models of Allen et al. (2003a,b) described in Sect. 5.3. A spherical region centered on the origin and enclosing a mass M has a mass-to-flux ratio $M/\phi = \pi c_s^2/(B_0 G^2 M)$. With the values of B_0 listed above, and for a region enclosing a mass $M = 1\ M_\odot$, this corresponds to a mass-to-flux ratio, in units of the critical value, of 1.0, 2.0, 3.0, 3.6 and 5.1.

For each choice of B_0 and τ we ran 70 cases corresponding to 10 different values of the position angle ϕ and 7 values of the inclination angle ω. We considered both an isothermal source and a radial temperature profile (see Sect. 4.1). For each of the 2100 maps generated, the model Stokes Q and U were compared with the observed values, and the sum of individual χ^2 was evaluated (see the radial temperature profile results in Fig. 3). The results show that the best fit to the data is given by the models with the highest values of the initial magnetic field B_0. In all cases, intermediate values of ϕ and ω are selected. Note also that for smaller values of B_0, the best fit is achieved for lower values of ω. This is due to a zooming effect: a larger B_0 implies a smaller r_0. For large B_0 smaller angular distances mean larger radii, where the magnetic field configuration of the outermost parts of the model are naturally pinched in an edge-on view. On the other hand, for small B_0 (large r_0), the innermost region the magnetic field tend to be radial, and a larger inclination angle combined with the line-of-sight emission integration is needed to produce the pinched morphology.

The fit is not sensitive to the value of the non-dimensional time τ. Thus, the time elapsed since the onset of collapse is not well constrained by these models. For example, for models with B_0 = 0.29 mG (third column in Fig. 3) the time corresponding to the three values of τ is 8.7×10^3 yr, 1.5×10^4 yr, and 2.0×10^4 yr, whereas for models with B_0 = 0.17 mG (fifth column), the time range corresponding to the three values of τ is 1.5–3.5×10^4 yr.

Figures 7 and 8 show the predicted Stokes I, Q, U maps and the Stokes I residuals (second row) compared to the observed maps (first row) for this model, for the case with uniform temperature and temperature gradient, respectively. Both realizations shown have B_0 = 0.43 mG, τ = 0.7 (corresponding to $t = 1.4 \times 10^4$ yr after the onset of collapse), $\phi = 50°$ and $\omega = 45°$. The derived physical parameters are shown in Tables 2 and 3 for the case with uniform temperature and temperature

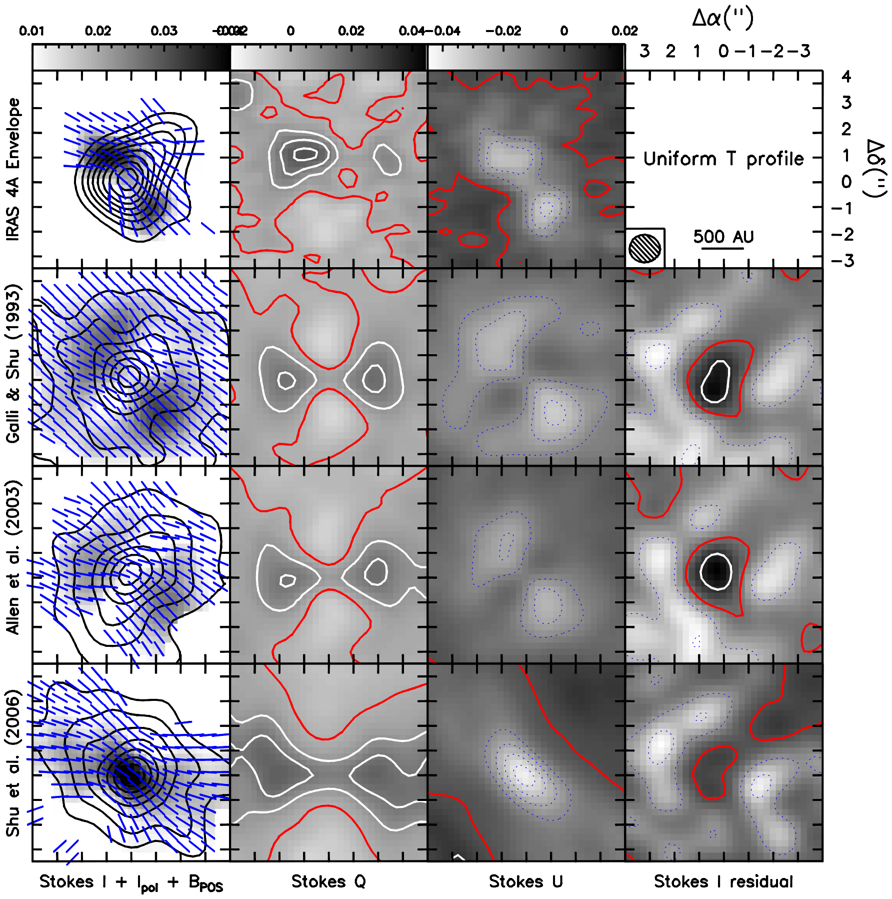

Fig. 7. Comparison of selected models with data assuming a uniform temperature of the gas. The orientation angles are fixed to $\phi = 50°$ and $\omega = 45°$ for a better model comparison. *Rows*: IRAS 4A (first row); model Galli & Shu (1993a,b) with $B_0 = 0.43$ and $\tau = 0.7$ (second row); model Allen et al. (2003a,b) with $H_0 = 0.125$, $v_0 = 0$ and $t = 10^4$ yr (third row); and model Shu et al. (2006) with $r_{\rm Ohm} = 75$ AU (fourth row). Columns: in each row, the panels show: intensity (first panel, contours), polarized intensity (first panel, pixel map) and magnetic field vectors (first panel, segments); map of Stokes Q (second panel, pixel map and contours); map of Stokes U (third panel, pixel and contours); residuals models-data for Stokes I (fourth panel, pixel map and contours). The color scale is shown on the top of each column. Contours: contours for the Stokes I maps (left panels) depict emission levels from 6σ up to the maximum value in steps of 6σ, where $\sigma = 0.02$ Jy beam^{-1}. Coutours for the Stokes Q and U maps depict levels from the minimum up to the maximum in steps of 3σ where $\sigma = 2.5$ mJy beam^{-1}. The solid red contour marks the zero emission level, solid white contours mark positive emission and blue dotted contours mark negative emission. Contours for the residual Stokes I follow the same rule of Stokes Q and U but with steps of 6σ, where $\sigma = 0.02$ Jy beam^{-1}. The top right panel shows the beam and the angular and spatial scale.

Table 2. Models with uniform temperature profile: 880 μm continuum emission and derived parameters^a .

	Unit	Galli & Shu (1993a,b)	Allen et al. (2003a,b)	Shu et al. (2006)
$S_\nu^{\rm I}$	Jy	8.92 ± 0.25	7.73 ± 0.25	8.35 ± 0.25
$I_{\rm Peak}^{\rm I}$	Jy beam^{-1}	0.77 ± 0.03	0.79 ± 0.03	0.98 ± 0.03
$FWHM^b$	AU ('')	919 (3.06)	1015 (3.39)	892 (2.84)
$S_\nu^{\rm pol}$	mJy	390 ± 40	301 ± 30	328 ± 30
$I_{\rm Peak}^{\rm pol}$	mJy beam^{-1}	31 ± 2	34 ± 2	43 ± 2
$\Omega^{{\rm pol}\,c}$	arcsec^2	28	30	23
τ	–	0.27	0.18	0.30
$N_{\rm H_2}{}^d$	10^{24} cm^{-2}	4.61	3.14	5.11
$n_{\rm H_2}{}^d$	10^8 cm^{-3}	5.03	3.10	6.02
Mass^d	$M_\odot$	1.92	1.60	1.82

Notes. $^{(a)}$ See Appendix A of Frau et al. (2010) for details. $^{(b)}$ Diameter of the circle with the same area as the region of the source above the half peak intensity. $^{(c)}$ Solid angle of the region with polarized intensity above 3σ. $^{(d)}$ Assuming $\kappa_{250\ {\rm GHz}} = 1.5$ cm^2 g^{-1} and a gas-to-dust ratio of 100 (Girart et al. 2006).

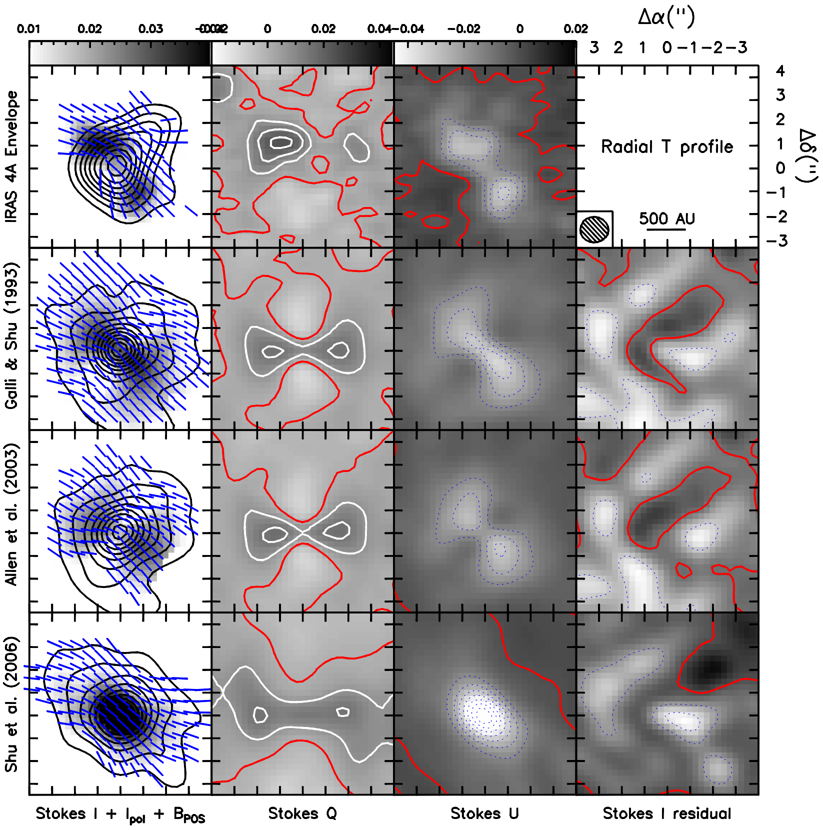

Fig. 8. Same as Fig. 7 for the case with the Maret et al. (2002) observational temperature gradient.

Table 3. Models with radial temperature profile: 880 μm continuum emission and derived parameters[a] .

	Unit	Galli & Shu (1993a,b)	Allen et al. (2003a,b)	Shu et al. (2006)
$S_\nu^{\rm I}$	Jy	6.59 ± 0.25	6.37 ± 0.25	6.90 ± 0.25
$I_{\rm Peak}^{\rm I}$	Jy beam^{-1}	1.08 ± 0.03	1.02 ± 0.03	1.28 ± 0.03
$FWHM^b$	AU ('')	693 (2.31)	744 (2.48)	693 (2.31)
$S_\nu^{\rm pol}$	mJy	239 ± 24	173 ± 17	230 ± 23
$I_{\rm Peak}^{\rm pol}$	mJy beam^{-1}	32 ± 2	30 ± 2	68 ± 2
$\Omega^{{\rm pol}\,c}$	arcsec^2	16	12	12
τ	–	0.37	0.30	0.39
$N_{\rm H_2}{}^d$	10^{24} cm^{-2}	6.28	5.12	6.64
$n_{\rm H_2}{}^d$	10^8 cm^{-3}	9.09	6.91	9.61
Mass^d	$M_\odot$	1.47	1.39	1.57

Notes. [a] See Appendix A of Frau et al. (2010) for details. [b] Diameter of the circle with the same area as the region of the source above the half peak intensity. [c] Solid angle of the region with polarized intensity above 3σ. [d] Assuming $\kappa_{250\ \rm GHz}$ = 1.5 cm^2 g^{-1} and a gas-to-dust ratio of 100 (Girart et al. 2006).

gradient, respectively. The radial temperature profile realizations show a better match to the observational maps for all the Stokes maps, as well as physical parameters closer to the observed toward IRAS 4A. The general morphology of the magnetic field could be reproduced, as well as the depolarization toward the source axis and the double peak in polarized emission.

6.2. Allen et al. (2003a,b)

For the models of Allen et al. (2003a,b) we selected 3 non-rotating models with different values of the parameter H_0 defining the mass-to-flux ratio of the initial state (H_0 = 0.125, 0.25 and 0.5, corresponding to a mass-to-flux ratio in units of the critical value of 8.38, 4.51, and 2.66), and one rotating model, with H_0 = 0.125 and uniform rotation velocity v_0 = 0.125 (in units of the sound speed). For each case, we considered 5 evolutionary times, $t = 10^4$ yr, 2×10^4 yr, 3×10^4 yr, 4×10^4 yr and 5×10^4 yr. As before, the position angles ϕ and ω were varied over a grid of 10×7 values, in both uniform and radial temperature profiles, generating a total of 2660 maps (due to numerical problems it was impossible to simulate the case H_0 = 0.5 with $t = 10^4$ yr). The resulting χ^2 of the comparison with the observed

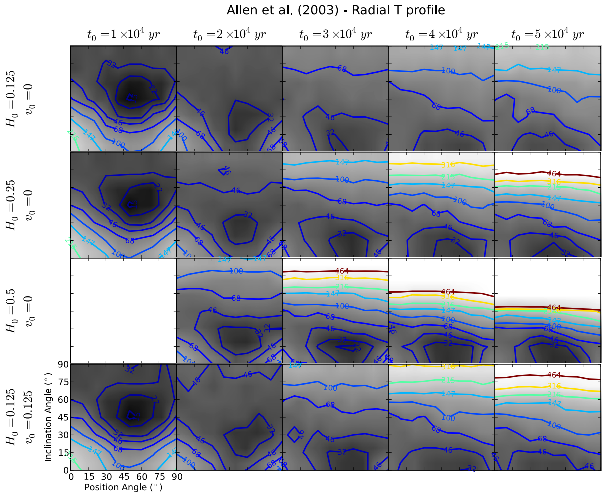

Fig. 9. Same as Fig. 3 for the Allen et al. (2003a,b) model with radial temperature profile.

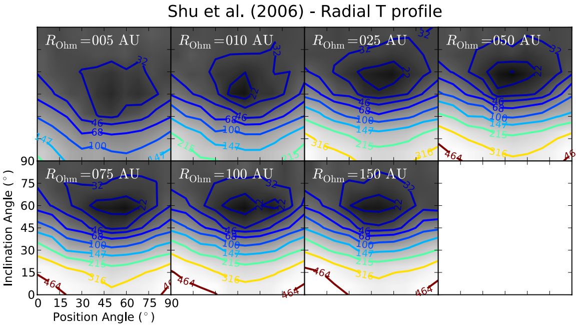

Fig. 10. Same as Fig. 3 for the Shu et al. (2006) model with radial temperature profile.

Stokes Q and U maps for the radial temperature profile cases is shown in Fig. 9.

It is evident from the figure that better fits are obtained with lower values of the time elapsed since the onset of collapse, a few 10^4 yr. The results are not very sensitive to the mass-to-flux ratio nor to the rotation of the initial configuration. There is a clear degeneracy between time and inclination angle with respect to the plane of the sky: a more concentrated field (a more pinched hourglass) can be obtained by letting the model evolve, or by a larger inclination of the magnetic field axis. For this reason, the region of minimum χ^2 moves towards lower values of ω at later times.

Figures 7 and 8 show the predicted Stokes I, Q, U maps and the Stokes I residuals (third row) compared to the observed maps (first row) for this model, for the case with uniform temperature and temperature gradient, respectively. Both realizations shown have $H_0 = 0.125$, $v_0 = 0$, $t = 10^4$ yr, $\phi = 50°$ and $\omega = 45°$. The derived physical parameters are shown in Tables 2 and 3 for the case with uniform temperature and temperature gradient, respectively. As for the Galli & Shu (1993a,b) models, radial temperature profile realizations show a better match. For this model, the magnetic field morphology, source axis depolarization, and double peak in polarized emission could be reproduced like with the Galli & Shu (1993a,b) models, although the polarized intensity derived was smaller in this case.

6.3. *Shu et al. (2006)*

To test this model, we varied the Ohm radius from 5 AU to 150 AU. This parameter controls the size of the region where magnetic dissipation takes place and the magnetic field lines are almost straight. A total of 980 maps were generated, for 7 values of the Ohm radius, 10 × 7 values of the position and inclination angles, and both isothermal and radial temperature profiles. Figure 10 shows the χ^2 of the comparison with the observed Q and U maps for the radial temperature profile case. The best-fit models tend to have $r_{\rm Ohm}$ in the range 10−100 AU, as also found previously (Gonçalves et al. 2008).

Figures 7 and 8 show the predicted Stokes I, Q, U maps and the Stokes I residuals (fourth row) compared to the observed maps (first row) for this model, for the case with uniform temperature and temperature gradient, respectively. Both realizations shown have $r_{\rm Ohm} = 75$ AU, $\phi = 50°$ and $\omega = 45°$. The derived physical parameters are shown in Tables 2 and 3 for the case with uniform temperature and temperature gradient, respectively. As shown by the figure, this model fails to reproduce the double-peaked distribution of polarized intensity. This feature is associated to strongly concentrated, almost radial magnetic field lines in the central region, at variance with the almost uniform field morphology produced by magnetic dissipation. Another characteristic of this model is the relatively high degree of polarization, not supported by the observations.

7. ALMA synthetic maps

The ALMA resolution used ($0\farcs7 \times 0\farcs4 \sim 210 \times 120$ AU^2) was chosen to have several projected cells of the simulations (∼30 AU) inside each beam, allowing the best comparison possible with the models avoiding resolution effects. The ALMA sensitivity and u, v coverage is far much better than that of the SMA and, thus, allows (*i*) to map with a much higher fidelity the polarized emission, and (*ii*) to detect emission from a larger and fainter region.

Figure 11 shows the ALMA maps for the models shown in Fig. 8 using the radial temperature profile. The level of detail of the convolved maps was very close to the original maps thus an almost perfect morphology reconstruction is possible for all the Stokes maps with the ALMA capabilities. Furthermore, the combination of sensitivity and resolution achievable with ALMA makes possible to extract usable information from the maps in a spatial range ∼10 times larger than the resolution. We derived large and accurate polarization maps for all of the models. As Fig. 11 states, it will be possible with ALMA to reach resolution and detail levels which will allow to differentiate among different models, and to select those matching better the observations. In order to make this result more evident we marked in the left-hand side panel of each model a red circle depicting important distances related to the models. In the case of Galli & Shu (1993a,b) and Allen et al. (2003a,b) red circles depict the loci of the isothermal collapse wave ($r = c_{\rm s}t$) which can be compared directly to Figs. 2 and 6 of the original papers, respectively. For the Shu et al. (2006) model, red circle depict the 10 $r_{\rm Ohm}$ distance, comparable with Fig. 4 of their paper. The high power of reproduction of ALMA encourages polarization observation toward all of the sources as a detailed modeling will be possible with the onset of this powerful instrument.

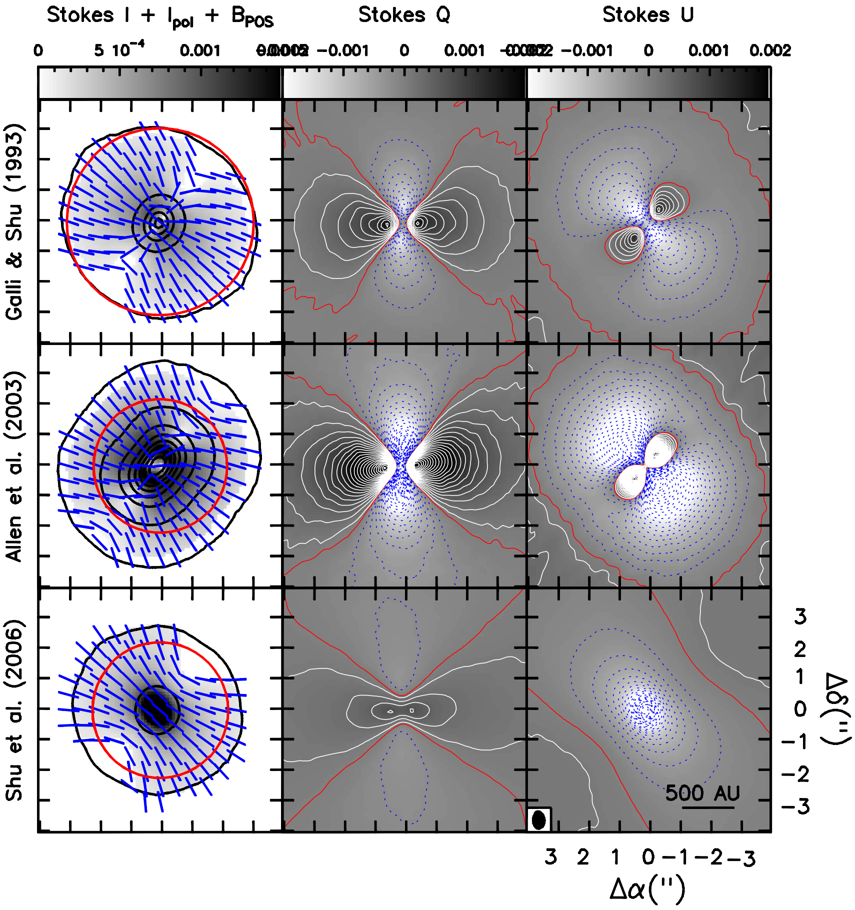

Fig. 11. Same as Fig. 8 for ALMA configuration 09. Contours: contours for the Stokes I maps (*left panels*) depict emission levels from 5σ up to the maximum value in steps of 50σ, where $\sigma = 0.2$ mJy beam^{-1}. Positive contours for the Stokes Q and U maps depict levels from 5σ up to the maximum in steps of 10σ, where $\sigma = 0.02$ mJy beam^{-1}. Negative contours follow the same rule. Red circles: for the Galli & Shu (1993a,b) and Allen et al. (2003a,b) models depict the loci of the front of the isothermal collapse wave ($r = c_s t$, see Fig. 2 of Galli & Shu 1993a and Fig. 6 of Allen et al. 2003a). For the Shu et al. (2006) model it marks the 10 $r_{\rm Ohm}$ distance (see Fig. 4 of Shu et al. 2006).

8. Summary and conclusions

The new data used in this work allowed to obtain a much better u, v coverage for the IRAS 4A region than in previous works, and, therefore, more reliable maps. In addition, the data added from different telescope configurations provided larger baselines, to resolve the compact components, as well as shorter baselines, to better trace the extended envelope emission. This significant improvement allowed to separate the embedded compact sources from the diffuse envelope. A good u, v coverage was essential to perform reliable comparisons with models. To this goal, we developed a selection method, the so-called χ^2 method, with larger discriminating power than in previous studies (e.g., Gonçalves et al. 2008).

The new data confirm that the source emission is optically thin, with no absorption or scattering, as expected for sub-mm emission. The opacity derived from the Stokes I map of the envelope is negligible, implying that the maps trace very deep into the source. As the scattering appear to be negligible, the origin of the alignment of the dust grains is expected to be due to the magnetic field.

Despite the complexity of the NGC 1333 star forming region, MHD models of single star formation assuming quasi-static initial conditions and a uniform (or nearly uniform) magnetic field show remarkable agreement with the observed characteristics of IRAS 4A, like intensity, polarized intensity, and polarization distribution. These facts suggests that the dust polarization pattern resulting from the density and magnetic field distribution of non-turbulent models may apply even in less idealized initial conditions than normally assumed. Once the orientation angles are consistently determined, the comparison of the data with models of magnetized collapse indicate that a strong initial field is required (B_0 larger than a few tenths of mG, see Sect. 3.1), that the source is very young (a few 10^4 yr, see Sects. 3.1 and 3.2), and that the scale where magnetic dissipation occurs is below the resolution of current observations (see Sect. 3.3). However, with the current level of sensitivity and u, v coverage it is not possible to clearly discriminate among different collapse models. The Galli & Shu (1993a,b) and Allen et al. (2003a,b) models fit better than the Shu et al. (2006) model, but no selection can be done between the former two models.

In general, the models predict sources with a more centrally peaked core and a larger less dense envelope with polarized emission less concentrated. A more refined dust grain treatment could help in a more realistic emission treatment. Current SMA observations of IRAS 4A clearly favor models with a temperature gradient. The total emission maps derived from models with a temperature gradient show the right peak value but larger fluxes, steeper profiles and more extended morphologies than IRAS 4A. On the other hand, they predict the right fluxes and morphologies of polarized emission but lower peaks and softer profiles. Conversely, polarization maps obtained with uniform temperature profiles are more extended than IRAS 4A maps (see Sect. 5.2). Therefore, the inclusion of a realistic temperature profile cannot be ignored in modeling the sub-mm emission of low-mass protostars.

An important result from the simulations of protostellar enveloped threaded with an hourglass magnetic field is the possibility of deriving the orientation angles of real sources from polarization measurements. Figures 4 and 5 show that up to inclination angles of ~60° it is possible to estimate both position and inclination angles from the Stokes Q and U maps. For larger inclinations the magnetic field tends to be radial and the Stokes maps do not show significant differences. Therefore, Figs. 4 and 5 can be used as templates for future observations of the dust polarized emission toward star forming cores.

Another remarkable result is the good agreement in the u, v-plane of the observed and synthetic visibility amplitudes obtained assuming a temperature gradient, except for the shortest baselines ($\lesssim 20\ k\lambda$). The observed deficit of emission in IRAS 4A with respect to the models suggest a sharper density decrease at scales of ~1500 AU than predicted by theoretical models.

The ALMA simulations have shown the capability of this new instrument to distinguish fine details even between models of the same family. The methodology used in this work has proved to be a powerful tool to compare observations directly to theoretical models in a consistent way and avoiding instrumental effects. Future polarization measurements with the ALMA will provide real power to select the best models to describe the structure and evolution of low-mass cores and, consequently, to disentangle the medium conditions and the physics ruling the process. Upcoming radiative transfer codes like ARTIST (Padovani et al. 2011) will facilitate this kind of studies. ALMA data, together with powerful radiative transfer codes, may be used together with the technique developed in this work to extract as much information as possible from the data and to constrain the models.

Acknowledgements. P.F. is partially supported by MICINN grant FPU. P.F. and J.M.G. are supported by MICINN grant AYA2008-06189-C03. P.F. and J.M.G. are also supported by AGAUR grant 2009SGR1172. The authors are grateful to Shih-Ping Lai and Tao-Chung Ching for gently sharing their SMA data. The authors also thank José Gonçalves and Jongsoo Kim for useful discussions, and the anonymous referee for useful comments.

References

Allen, A., Shu, F. H., & Li, Z.-Y. 2003a, ApJ, 599, 351
Allen, A., Li, Z.-Y., & Shu, F. H. 2003b, ApJ, 599, 363
Blake, G. A., Sandell, G., van Dishoeck, E. F., et al. 1995, ApJ, 441, 689
Briggs, D. S. 1995, BAAS, 27, #112.02
Chandrasekhar, S., & Fermi, E. 1953, ApJ, 118, 113
Choi, M. 2005, ApJ, 630, 976
Crutcher, R. M., Hakobian, N., & Troland, T. H. 2009, ApJ, 692, 844
Di Francesco, J., Myers, P. C., Willner, D. J., Ohashi, N., & Mardones, D. 2001, ApJ, 562, 770
Frau, P., Girart, J. M., Beltrán, M. T., et al. 2010, ApJ, 723, 1665
Fiedler, R. A., & Mouschovias, T. C. 1993, ApJ, 415, 680
Fiege, J. D., & Pudritz, R. E. 2000, ApJ, 544, 830
Galli, D., & Shu, F. H. 1993a, ApJ, 417, 220
Galli, D., & Shu, F. H. 1993b, ApJ, 417, 243
Galli, D., Lizano, S., Shu, F. H., & Allen, A. 2006, ApJ, 647, 374
Girart, J. M., Crutcher, R. M., & Rao, R. 1999, ApJ, 525, L109
Girart, J. M., Rao, R., & Marrone, D. P. 2006, Science, 313, 812
Gonçalves, J., Galli, D., & Walmsley, M. 2005, A&A, 430, 979
Gonçalves, J., Galli, D., & Girart, J. M. 2008, A&A, 490, L39
Hildebrand, R. H. 1983, QJRAS, 24, 267
Jennings, R. E., Cameron, D. H. M., Cudlip, W., & Hirst, C. J. 1987, MNRAS, 226, 461
Lai, S.-P., Crutcher, R. M., Girart, J. M., & Rao, R. 2002, ApJ, 566, 925
Lay, O. P., Carlstrom, J. E., & Hills, R. E. 1995, ApJ, 452, L73
Lazarian, A. 2003, J. Quant. Spec. Radiat. Transf., 79, 881
Lee, H. M., & Draine, B. T. 1985, ApJ, 290, 211
Lee, J.-E., & Kim, J. 2009, ApJ, 699, L108
Li, Z.-Y., & Shu, F. H. 1996, ApJ, 472, 211
Looney, L. W., Mundy, L. G., & Welch, W. J. 2000, ApJ, 529, 477
Maret, S., Ceccarelli, C., Caux, E., Tielens, A. G. G. M., & Castets, A. 2002, A&A, 395, 573
Mouschovias, T. C., & Spitzer, L., Jr. 1976, ApJ, 210, 326
Myers, P. C., & Goodman, A. A. 1991, ApJ, 373, 509
Nakamura, F., & Li, Z.-Y. 2005, ApJ, 631, 411
Nakano, T., & Nakamura, T. 1978, PASJ, 30, 671
Novak, G., Gonatas, D. P., Hildebrand, R. H., Platt, S. R., & Dragovan, M. 1989, ApJ, 345, 802
Ostriker, E. C., Stone, J. M., & Gammie, C. F. 2001, ApJ, 546, 980
Padoan, P., Goodman, A., Draine, B. T., et al. 2001, ApJ, 559, 1005
Padovani, M., Jorgensen, J. K., Bertoldi, F., et al. 2011, IAU Symp., 270, 451
Rao, R., Girart, J. M., Marrone, D. P., Lai, S.-P., & Schnee, S. 2009, ApJ, 707, 921
Ridge, N. A., Schnee, S. L., Goodman, A. A., & Foster, J. B. 2006, ApJ, 643, 932
Sandell, G., Aspin, C., Duncan, W. D., Russell, A. P. G., & Robson, E. I. 1991, ApJ, 376, L17
Shu, F. H., Galli, D., Lizano, S., & Cai, M. 2006, ApJ, 647, 382
Strittmatter, P. A. 1966, MNRAS, 132, 359
Tang, Y.-W., Ho, P. T. P., Koch, P. M., et al. 2009, ApJ, 700, 251
Tomisaka, K., Ikeuchi, S., & Nakamura, T. 1988, ApJ, 335, 239
Vázquez-Semadeni, E., Kim, J., Shadmehri, M., & Ballesteros-Paredes, J. 2005, ApJ, 618, 344
Wardle, M., & Konigl, A. 1990, ApJ, 362, 120
Zweibel, E. G. 1990, ApJ, 362, 545

X

Summary and conclusions

The ultimate goal of the thesis is to deepen into the knowledge of the first stages of low-mass star-formation through the study of dense cores. In order to achieve our goal, we observed a set of young starless dense cores embedded in the Pipe nebula, which has a very low star-formation rate and has been suggested to be in a very early evolutionary stage. In addition, we observed the central clump of the B59 complex, in the NW end of the Pipe nebula. This object shares most of the physical properties of the dense cores of the cloud, but it is more massive and is forming a small cluster. Finally, and from a different approach, we compared theoretical models of magnetized cloud collapse to the more evolved low-mass Class 0 source NGC 1333 IRAS 4A. We sought for the best suited theoretical scenario to find the initial conditions that allow to achieve the present configuration.

The work presented in this thesis is mostly based on observations. All the data toward the Pipe nebula were obtained during the thesis period submitting original proposals of which I was the PI. I performed most of the observations, data reduction, analysis, and paper writing related to our set of young starless dense cores, which were very useful and allowed me to achieve an important observational background. The B59 project is also an observational work. I was not the PI in this case but I was on charge of the technical part (observation, data reduction, and analysis). Finally, the IRAS 4A project is based on archival interferometric data and theoretical models from the literature. As a PI, my work was to move a step forward with respect to previous efforts to perform reliable comparisons between observational data and models. This last project provided a different approach to the thesis aim and served to enrich the theoretical background.

10.1 Summary of results and conclusions

We proceed to summarize the main results and conclusions for each of the topics tackled and presented in this thesis:

1. **On the young starless dense cores in the Pipe nebula**

   The Pipe nebula is a massive, nearby, filamentary dark molecular cloud with a low star-formation efficiency. The cloud is threaded by a uniform magnetic field perpendicular to its main axis, which is only locally perturbed in a few regions, such as the only active cluster-forming core B59. It harbors more than a hundred, mostly quiescent, very chemically young starless dense cores that appear to be gravitationally unbound and pressure confined. The cloud is, therefore, an ideal laboratory to study the very early stages of the star formation process. The aim of the study was to investigate the primordial conditions in low-mass starless dense cores and the relation among physical, chemical, and magnetic properties within them. We observed nine selected Pipe nebula cores with the IRAM 30-m telescope and carried out a molecular survey at 1 and 3 mm of selected early- and late-time molecules. We also mapped the 1.2 mm dust continuum emission of the cores. In addition, we carried out an unbiased ∼15 GHz wide chemical survey at 3 mm of fourteen dense cores. For the sake of simplicity, we describe the main results separating physical and chemical properties. Finally, we studied the physical properties of the central clump of the B59 complex by mapping the 1.2 mm dust continuum emission.

   (a) **Physical properties.** For the nine cores, we derived an average diameter of 0.08 pc, a density of $\sim 10^5$ cm^{-3}, and a mass of ~ 1.7 $M_\odot$, very close to the prototypical dense core values. We found a good agreement between the 1.2 mm dust continuum emission maps and previous extinction maps (Román-Zúñiga et al., 2009, 2010), although the latter ones seem to trace better the diffuse gas. We derived an A_V/N_{H_2} factor of $(1.27\pm0.12)\times10^{-21}$ mag cm^2, close to the standard value. However, we found the dust emission maps to underestimate the column density by ∼6.7 mag, possibly arising from the cloud diffuse material filtered out in our MAMBO-II maps. We found several trends related to increasing core density: (*i*) diameter seems to shrink, (*ii*) mass seems to increase, and (*iii*) chemistry tends to be richer. Furthermore, we found no correlation between the direction of the surrounding diffuse medium magnetic field and the projected orientation of the cores, suggesting that the large scale magnetic fields have no significant influence shaping the core morphology. These facts motivated simultaneous fits to the radial profiles of the 1.2 mm dust continuum maps and of the extinction maps assuming the physical structure of a BE sphere model. All the cores in our sample show radial profiles compatible with the model. Eight of them are gravitationally unbound, with central volume densities of only few times 10^4 cm^{-3}, and a very small density contrast. Core 109 is the exception, since it is the only one that is gravitationally bound. The combination of the two mapping techniques yields values for the temperature in the 9–12.6 K range except for core 48 (18 K). All the cores are surrounded by a significant diffuse molecular component with a visual extinction in the 4–9 mag range, being larger in the *bowl* region ($\simeq$ 9 mag) than in the rest of the Pipe nebula, compatible with the previous observational estimate.

(b) **Chemical properties.** Our results confirm that the studied Pipe nebula starless cores are in a very early evolutionary stage. We performed an unbiased $\sim$15 GHz wide survey at 3 mm toward fourteen cores and discovered an unexpectedly rich young chemistry. We proposed a new observational classification, in terms of chemical composition and line emission properties, based on the clear chemical differentiation among the cores in the 3 mm molecular line emission normalized by the core A_V. We defined three molecular core groups. The "diffuse" cores ($A_V \lesssim 15$) have a poor chemistry with mainly simple "ubiquitous" species (*e.g.* CO, CS, and C_2H) similar to the parental cloud composition. The denser "deuterated" cores ($A_V \gtrsim 22$ mag) show weaker normalized intensities for "ubiquitous" lines and present emission in nitrogen- (N_2H^+) and deuterium-bearing (C_3HD) molecules, and in some carbon chain molecules (HC_3N), signposts of a prototypical chemistry prior to the onset of the star formation process. Finally, "oxo-sulfurated" cores ($A_V \simeq 15$–22 mag) are in a chemical transitional stage between cloud and evolved dense core chemistry. These cores appear to be abundant in species such as CH_3OH and oxo-sulfurated molecules (*e.g.* SO and SO_2) that disappear at higher densities. On the basis of these categories, one of the "diffuse" cores (core 47) has the spectral line properties of the "oxo-sulfurated" ones, which suggests that it is a failed core. An analysis of the LTE status showed that optically thinner cores present smaller departures from LTE than the optically thicker ones. The analysis of the linewidths reports two behaviors: (*i*) a roughly constant value of subsonic turbulent broadening for all the cores (*e.g.* in $C^{18}O$ (1–0) and CH_3OH (2–1)) that may trace the outer shells, and (*ii*) a roughly constant slightly narrower subsonic turbulent broadening (*e.g.* in C_2H (1–0) and N_2H^+ (1–0)) for cores with $A_V \gtrsim 20$ mag and supersonic values otherwise (*e.g.* toward the failed core 47). These results confirm that the main internal pressure has thermal origin. The chemical evolutionary stage is not correlated with the location of the cores in the Pipe nebula and, therefore, with the magnetic field of the diffuse medium. However, the chemically richer cores are the denser ones, and thus, it seems to exist a correlation with the physical properties of the cores (density and size).

(c) **The quiescent core in the cluster-forming complex Barnard 59.** The dense molecular clump at the center of the B59 complex is the only region in the Pipe nebula with active star formation. It has formed a small, stellar cluster of low-mass stars in a 2–3 Myr period. However, the previous analysis of a high-resolution near-IR dust extinction map and of our dust continuum emission map revealed that the central region is a massive, mostly quiescent clump of 18.9 $M_\odot$. It shows no evidence of fragmentation at scales of a few 10^3 AU. In contrast, it has a smooth profile compatible with a single, isothermal, centrally peaked structure. This profile may resemble a BE sphere like that of the other less massive, smaller dense cores in the Pipe nebula at a much larger scale. However, Kandori et al. (2005) showed that a collapsing sphere resembles an unstable BE for a long time, and therefore, the central clump might be in a collapsing state. In fact, a BE fit suggests that B59 is out of equilibrium and the core itself is sub-virialized ($\alpha_{\rm vir} = 0.25$). Subsonic non-thermal linewidths and the fact that it has survived $\sim$10 $t_{\rm ff}$, seem to point to extra supporting sources. Stellar feedback is likely to be too weak for such a small cluster. An estimated magnetic field strength of 0.1–0.2 mG could support the clump and, although it is larger than the estimates of Alves et al. (2008) for the diffuse environment, it is a reasonable value for this kind of objects and it is expected to increase toward the densest regions. Summarizing, the central clump of B59 shows properties comparable to those of the rest of the cores in the Pipe nebula but with a larger scale and older age. The most plausible scenario is that of a massive core that has been supported against global collapse for several $t_{\rm ff}$ by non-thermal sources, probably magnetic fields, while forming a small cluster of low-mass stars. Numerical simulations show that such object will not hold for more than a few $t_{\rm ff}$. The lack of present fragmentation points to the formation of a single central source or, at most, a binary. This scenario is suggestive of what the evolution of the other low-mass Pipe nebula cores could look like.

2. **On the collapsing magnetized Class 0 NGC 1333 IRAS 4A**

We compared high-angular resolution observations of the submillimeter polarized dust emission, which traces the magnetic field direction in the POS, of a low-mass protostellar source, with the predictions of three different models of collapse of isothermal magnetized molecular cloud cores to constrain their parameters. IRAS 4A is a perfect source to test low-mass magnetized cloud collapse models because it is a young low-mass Class 0 source with an infalling dusty envelope exhibiting a magnetic field with a clear pinched morphology. We computed synthetic Stokes I, Q, and U maps for the dust emission of the three models varying their parameters and orientation. Then, we convolved the results with the instrumental response of the SMA observations toward IRAS 4A, compared the synthetic maps with the data, and assessed the quality of the fit by a χ^2 analysis. We obtained the best agreement with the data for models of collapse of clouds with $\lambda > 2$, initial uniform magnetic field of strength $\sim$0.5 mG, and age of the order of a few 10^4 yr since the onset of collapse. Ideal-MHD models provided better fits and magnetic dissipation, if present, is found to occur below the resolution level of the observations ($\sim$350 AU). This suggests that flux-freezing holds for most of the collapse process. Including an observational temperature profile (Maret et al., 2002) of IRAS 4A led to a more realistic morphology and intensity distribution so, although small departures from isothermality do not affect the collapse process, temperature variations must be considered when estimating the dust emission. An exploration of the possible orientation angles showed that the Stokes maps are very sensitive to different projections and could be used, assuming a given magnetic field topology, to determine the orientation of magnetized sources. We also showed that the Atacama Large Millimeter Array (ALMA) has the capability of distinguishing among the three different models adopted in this work and, therefore, it represents a huge potential to be used to select the best theoretical approaches. Our results show that the standard theoretical scenario for the formation of low-mass stars is consistent with, at least, IRAS 4A. In this scenario, as explained in Chapter 3, clouds initially threaded by large-scale magnetic fields become unstable and collapse. The field is then dragged in and trapped in the nascent protostar and the surrounding circumstellar disk. In the collapsing cloud, the dynamics is dominated by gravitational forces and, even if the cloud is initially supercritical, by magnetic forces.

10.2 General conclusions

The studies undertaken toward the Pipe nebula provide us with more information to understand the low star-formation efficiency within the cloud. Alves et al. (2008) discovered an uniform magnetic field perpendicular to the cloud main axis, and Franco et al. (2010) showed that turbulence in the cloud is sub-Alfénic. These results point to a cloud formation scenario through infall of material along the field lines in a quiescent way. However, the bordering region between the *stem* and the *bowl* appears to be quite turbulent, as the linewidth of some tracers evidence (Frau et al., 2012b). This turbulence could be the cause of the shattering of the failed core 47 (Frau et al., 2012a), which may indicate that star formation is unlikely to happen in this region. In addition, the extinction maps prove the *stem* as the least dense region, and thus, with less matter to achieve the high densities needed. The northeast end of the cloud, the B59 region, is believed to be the oldest region with an estimated age of 2–3 Myr (Covey et al., 2010). It is already forming a small cluster of low-mass stars and distorting the uniform large scale magnetic field, but still showing nearly sub-Alfvénic turbulence. However, at the *bowl*, in the other end of the cloud, the magnetic field still remains well ordered and the chemistry of the most evolved core 109 points to an age of $\sim$1 Myr (Aikawa et al., 2008; Frau et al., 2010, 2012a). The age estimates for B59 and the *bowl* are one order of magnitude shorter than those for other active star-forming clouds such as Orion or Taurus. In fact, Palla & Stahler (1999, 2000) showed for the former clouds that star formation begun $\sim 10^7$ yr in the past, and then accelerated to produce most of the stars during the last few Myr. Therefore, the Pipe nebula is likely to be itself in an extremely young stage of evolution, with no sufficient age to host efficient star formation. The pristine conditions of the Pipe nebula could have been the initial conditions of the other more evolved star-forming clouds, now in a more turbulent stage due to the star-forming activity.

In this thesis, we have faced the study of the earliest stages of star formation. We have mapped dense cores with densities $< 10^5$ cm^{-3} (Frau et al., 2010, 2012b), far below the densities generally reported in literature for these objects. We have also found these cores to be compatible with BE spheres with extremely low density contrasts (Frau et al., 2012c), not reported in the literature either, thus suggesting these sources to be in hydrostatic equilibrium. In addition, we have discovered a rich and varied chemistry toward these very young cores (Frau et al., 2012a), absolutely unexpected taking into account the previous chemical studies focused on denser cores. Even in such young and diffuse objects, it is possible to differentiate characteristic chemical features, and to propose from them a chemical evolutionary sequence related with the central density of the object. Some of these cores present chemical features compatible with ages of $\sim$1 Myr, but the lack of signpost of collapse or gravitational instability points to non-thermal sources of support. The lack of spherical symmetry demands a dynamically important anisotropic force as well. The sub-Alfénic turbulence favors magnetic fields as the most likely non-thermal supporting agent, which may cause the cores to acquire flattened morphologies. The apparent lack of correlation between the magnetic field direction and the core main axis could be an effect of projection and needs further investigation.

Finally, the study of IRAS 4A confirmed that its properties can be explained satisfactorily with the standard theoretical scenario of low-mass star-formation (Frau et al., 2011). Ideal-MHD models provided better results for the collapse of the dusty envelope, and the use of the temperature profile improved the agreement with the data. The initial conditions of these models, with core sizes of ∼0.1 pc and centrally peaked density profiles, are in good agreement with our Pipe nebula dense cores studies. The initial magnetic field strength of the used models, ∼0.5 mG at outer densities of $\simeq 10^5$ cm^{-3}, can be scaled to the values obtained by Alves et al. (2008) for the Pipe nebula diffuse gas, up to ∼65 μG at cloud densities of $\simeq 3\times 10^3$ cm^{-3}, with a $B \propto \rho^{1/2}$ law typical of magnetized clouds. In a more technical point of view, the method used can set up a benchmark in the way the ALMA data will be analyzed in future. The high quality data expected will allow this kind of studies to be performed, and forecast a vast improvement in our understanding of the star-formation process.

10.3 Future prospects

Pipe nebula dense cores: In order to follow up our study of the Pipe nebula dense cores, several options deserve attention. First of all, and focusing on the physical properties of the dense cores, to provide a more robust explanation of their structure is necessary to derive the magnetic field strength within them. The BE fit throws promising results but the lack of spherical symmetry demands a better physical model. It is not possible to study magnetic fields from visual/IR polarimetry due to the high extinction in these cores. It is not possible either to perform dust continuum polarization observations with the current interferometers due to the low density and large scale of the starless cores. The option left is to derive by Zeeman effect the LOS component of the magnetic field using intense lines with hyperfine components, such as C_2H. We successfully submitted a proposal to the IRAM-30m to address this question meant to be observed in April, 2012. A determination of the internal magnetization will provide a better starting point for future modeling and will serve as a direct link with the initial conditions currently used in simulations. In a near future, ALMA will be able to trace angular scales ranging from $2''$ to $18''$ at band 6 (1.3 mm) in its most compact configuration. Its high sensitivity makes it possible to achieve the required rms in short integrations even in polarization mode. As a consequence, it will be a powerful tool to explore the interior of dense cores seeking for compact structures. In addition, it will be possible to trace the direction of the magnetic field in the POS. This is essential to determine its importance and test the hypothesis that the Pipe nebula cores are partially supported by magnetic fields.

Regarding the interesting chemical properties discovered, it is important to assure that they are not an effect of the low statistics. To address this, we submitted a proposal to the IRAM-30m to extend the Fast Fourier Transform Spectrometer (FTS) study toward all the Pipe nebula cores with significant A_V not observed yet, which will provide a source-unbiased chemical study. Moreover, it is also important to check whether this trend is a particularity of the Pipe nebula cores or it is the general trend of starless dense cores. To unveil the answer we submitted an IRAM-30m FTS proposal to study cores located in other low-mass star-forming clouds. Besides that, no ionization fraction estimate exists toward the Pipe nebula cores. We plan to undertake a chemical survey to derive their ionization level using simultaneous observations of "normal" and deuterated species together with chemical models. Finally, and making use of the now extended chemical database in hand, the next natural step is to chemically model the young dense cores. Little has been done up to now on this field for such diffuse objects. The relatively well known physical and chemical properties of the cores, together with the large statistics and the polarimetric studies, allow now for proper modelling.

Comparison of collapsing magnetized clouds with theoretical models: Our first approach to model a prototypical magnetized collapsing Class 0 source threw promising results. The next step is to compare the observations with models on which the magnetic field is not dominant. We already have a paper in preparation comparing the results of magnetized turbulence-dominated simulations of sources comparable to IRAS 4A. This study will serve to check whether a turbulent environment is able to reproduce their physical properties. Up to now, we could not reproduce the "hourglass" morphology, and thus, it seems to be a signature of magnetic field dominance. We also plan to extend the analysis to other magnetized Class 0 sources, such as W51 (Tang et al., 2009) and IRAS 16293 (Rao et al., 2009), to check wether the standard model can explain most of the present observations or a revision is needed.

ALMA will trigger a huge advance on this field according to our findings. As we showed in Chapter 9, ALMA will have enough resolution and sensitivity to distinguish among models. Furthermore, the resolution of our maps ($0.''7\times0.''4$) was limited by the resolution of the original simulations given that ALMA can resolve up to $\sim0.''014$ at 345 GHz. Therefore, we plan to observe IRAS 4A with ALMA in polarimetric mode. By using different configurations, we will be able to resolve in great detail the physical structure and magnetic field topology of the envelope, and to overcome the current resolution limitations. In addition, the high-angular resolution will allow us to probe the innermost regions of the protostar to study the disk. Several magnetized models have been proposed for these deep regions. A major role is given to disks in important processes such as the jet launching mechanism, which remains yet to be proven. Our analysis technique can be used in such regions because it works independently of the kind of model and data used, and thus, a huge increase in our understanding of the protostar phase will be within reach.

References

Adams, F. C., Lada, C. J., & Shu, F. H. 1987, ApJ, 321, 788

Aikawa, Y., Herbst, E., Roberts, H., & Caselli, P. 2005, ApJ, 620, 330

Aikawa, Y., Wakelam, V., Garrod, R. T., & Herbst, E. 2008, ApJ, 674, 984

Allen, A., Shu, F. H., & Li, Z.-Y. 2003, ApJ, 599, 351

Allen, A., Li, Z.-Y., & Shu, F. H. 2003, ApJ, 599, 363

Alves, J. F., Lada, C. J., & Lada, E. A. 2001, Nature, 409, 159

Alves, F. O. & Franco, G. A. P. 2007, A&A, 470, 597

Alves, F. O., Franco, G. A. P., & Girart, J. M. 2008, A&A, 486, L13

Alves, J., Lombardi, M., & Lada, C. J. 2007, A&A, 462, L17

André, P., Ward-Thompson, D., & Barsony, M. 1993, ApJ, 406, 122

André, P., Ward-Thompson, D., & Barsony, M. 2000, in *Protostars and Planets IV*, ed. V. Mannings *et al.* (Tucson: Univ. of Arizona Press) pp 59-96

Bacmann, A., Lefloch, B., Ceccarelli, C., et al. 2002, A&A, 389, L6

Beckwith, S. V., Sargent, A. I., Chini, R. S., & Guesten, R. 1990, AJ, 99, 924

Bergin, E. A., Alves, J., Huard, T., & Lada, C. J. 2002, ApJL, 570, L101

Bergin, E. A., Melnick, G. J., Gerakines, P. A., Neufeld, D. A., & Whittet, D. C. B. 2005, ApJL, 627, L33

Blake, G. A., Sandell, G., van Dishoeck, E. F., Groesbeck, T. D., Mundy, L. G, Aspin, C. 1995, ApJ, 441, 689

Blitz, L. 1993, in *Protostars and Planets III*, eds. E. H. Levy, & J. I. Lunine (Tucson: Univ. of Arizona Press) pp 125-161

Bonnor, W. B. 1956, MNRAS, 116, 351

Brooke, T., Huard, T. L., Bourke, T. L., Boogert, A. C. A. et al. 2007, ApJ, 655, 364

Caselli, P., Walmsley, C. M., Zucconi, A., et al. 2002, ApJ, 565, 344

Chandrasekhar, S., & Fermi, E. 1953, ApJ, 118, 113

Choi, M. 2005, ApJ, 630, 976

Covey, K. R., Lada, C. J., Román-Zúñiga, C., et al. 2010, ApJ, 722, 971

Davis, L. J., & Greenstein, J. L. 1951, ApJ, 114, 206

Di Francesco, J., Myers, P. C., Willner, D. J., Ohashi, N., Mardones, D. 2001, ApJ, 562, 770

Duley, W. W., & Williams, D. A. 1984, *Interstellar Chemistry* (London: Academic Press Inc.)

Ebert, R. 1955, Zeitschrift für Astrophysik, 37, 217

Elmegreen, B. G. 1985, in *Protostars and Planets II*, eds. D. C. Black, & M. S. Matthews (Tucson: Univ. of Arizona Press) pp 33-58

Elmegreen, B. G. 1993, in *Protostars and Planets III*, eds. E. H. Levy, & J. I. Lunine (Tucson: Univ. of Arizona Press) pp 97-124

Estalella, R., & Anglada, G. 1996, "Introduccin a la Fsica del Medio Interestelar", Edicions UB, Textos Docents nm. 50

Fiedler, R. A., & Mouschovias, T. C. 1993, ApJ, 415, 680

Forbrich, J., Lada, C. J., Muench, A. A., Alves, J., Lombardi, M. 2009, ApJ, 704, 292

Forbrich, J., Posselt, B., Covey, K. R., & Lada, C. J. 2010, ApJ, 719, 691

Franco, G. A. P., Alves, F. O., & Girart, J. M. 2010, ApJ, 723, 146

Frau, P., Girart, J. M., Beltrán, M. T., Morata, O., Masqué, J. M., Alves, F. O., Busquet, G., Sánchez-Monge, A., Franco, G.A.P., & Estalella, R. 2010, ApJ, 723, 1665

Frau, P., Galli, D., Girart, J. M. 2011, A&A, 535, A44

Frau, P., Girart, J. M., & Beltrán, M. T. 2012, A&A, 537, L9

Frau, P., Girart, J. M., Beltrán, M. T., Padovani, M., Busquet, G., Morata, O., Sánchez-Monge, A., Franco, G.A.P., Masqué, J. M., Alves, F. O., & Estalella, R. 2012, submitted to ApJ

Frau, P., Girart, J. M., & Beltrán, M. T. 2012, to be submitted to A&A

Freeman, K., & Bland-Hawthorn, J. 2002, ARA&A, 40, 487

Frerking, M. A., Langer, W. D., & Wilson, R. W. 1982, ApJ, 262, 590

Galli, D., & Shu, F. H. 1993, ApJ, 417, 220

Galli, D., & Shu, F. H. 1993, ApJ, 417, 243

Galli, D., Lizano, S., Shu, F. H., & Allen, A. 2006, ApJ, 647, 374

Gibb, E. L., Whittet, D. C. B., Boogert, A. C. A., & Tielens, A. G. G. M. 2004, ApJS, 151, 35

Girart, J. M., Crutcher, R. M., Rao, R. 1999, ApJ, 525, L109

Girart, J. M., Rao, R., & Marrone, D. P. 2006, Science, 313, 812

Goodman, A. A., Benson, P. J., Fuller, G. A., & Myers, P. C. 1993, ApJ, 406, 528

Kolmogorov, A. 1941, Akad. Nauk SSSR Dokl., 30, 301

Hanawa, T., & Matsumoto, T. 2000, PASJ, 52, 241

Hayashi, C. 1966, ARA&A, 4, 171

Hennebelle, P., & Ciardi, A. 2009, A&A, 506, L29

Herbig, G. H. 2005, AJ, 130, 815

Jennings, R. E., Cameron, D. H. M., Cudlip, W., & Hirst, C. J. 1987, MNRAS, 226, 461

Jørgensen, J. K., Schöier, F. L., & van Dishoeck, E. F. 2004, A&A, 416, 603

Kandori, R., Nakajima, Y., Tamura, M., et al. 2005, AJ, 130, 2166

Keto, E., & Caselli, P. 2008, ApJ, 683, 238

Keto, E., & Caselli, P. 2010, MNRAS, 402, 1625

Kohoutek, L., & Wehmeyer, R. 2003, Astronomische Nachrichten, 324, 437

Lai, D. 2000, ApJ, 540, 946

Lada, C. J. 1987, IAUS, 115, 1

Lada, C. J. 1991, in *The Physics of Star Formation and Early Stellar Evolution*, eds. C. J. Lada, & N. D. Kylafis (Dordrecht: Kluwer), 329

Lada, C. J., Muench, A. A., Rathborne, J. M., Alves, J. F., & Lombardi, M. 2008, ApJ, 672, 410

Larson, R. B. 1969, MNRAS, 145, 271

Larson, R. B. 1972a, MNRAS, 156, 437

Larson, R. B. 1972b, MNRAS, 157, 121

Larson, R. B. 1981, MNRAS, 194, 809

Larson, R. B. 1985, MNRAS, 214, 379

Larson, R. B. 2002, MNRAS, 332, 155

Larson, R. B. 2003, Reports on Progress in Physics, 66, 1651

Lay, O. P., Carlstrom, J. E., & Hills, R. E. 1995, ApJL, 452, L73

Lizano, S., & Shu, F. H. 1989, ApJ, 342, 834

Lombardi, M., Alves, J., & Lada, C. J. 2006, A&A, 454, 781

Looney, L. W., Mundy, L. G., & Welch, W. J. 2000, ApJ, 529, 477

Maret, S., Ceccarelli, C., Caux, E., Tielens, A. G. G. M., & Castets, A. 2002, A&A, 395, 573

Masunaga, H. & Inutsuka S. 2000, ApJ, 531, 350

McKee, C. F. 1989, ApJ, 345, 782

McKee, C. F., & Ostriker, E. C. 2007, ARA&A, 45, 565

Merrill, P. W., & Burwell, C. G. 1950, ApJ, 112, 72

Mezger, P. G., Sievers, A., & Zylka, R. 1991, IAUS, 147, 245

Mouschovias, T. C. 1976, ApJ, 206, 753

Mouschovias, T. C. 1976, ApJ, 207, 141

Muench, A. A., Lada, C. J., Rathborne, J. M., Alves, J. F., & Lombardi, M. 2007, ApJ, 671, 1820

Myers, P. C. 1985, in *Protostars and Planets II*, eds. D. C. Black, & M. S. Matthews (Tucson: Univ. of Arizona Press) pp 81-103

Myers, P. C., Fuller, G. A., Mathieu, R. D., Beichman, C. A., Benson, P. J., Schild, R. E., & Emerson, J. P. 1987, ApJ, 319, 340

Nakamura, F., & Li, Z.-Y. 2005, ApJ, 631, 411

Onishi, T., Kawamura, A., Abe, R., Yamaguchi, N. et al. 1999, PASJ, 51, 871

Ossenkopf, V. & Henning, T. 1994, A&A, 291, 943

Palla, F., & Stahler, S. W. 1999, ApJ, 525, 772

Palla, F., & Stahler, S. W. 2000, ApJ, 540, 255

Peretto, N., Andre, P., Konyves, V., et al. 2012, arXiv:1203.3403

Pontoppidan, K. M., van Dishoeck, E. F., Dartois, E., et al. 2005, Astrochemistry: Recent Successes and Current Challenges, 231, 319

Pontoppidan, K. M. 2006, A&A, 453, L47

Price, D. J., & Bate, M. R. 2007, MNRAS, 377, 77

Rathborne, J. M., Lada, C. J., Muench, A. A., Alves, J. F., & Lombardi, M. 2008, ApJS, 174, 396

Rathborne, J. M., Lada, C. J., Muench, A. A., et al. 2009, ApJ, 699, 742

Rao, R., Girart, J. M., Marrone, D. P., Lai, S.-P., & Schnee, S. 2009, ApJ, 707, 921

Reipurth, B., Nyman, L.-A., & Chini, R. 1996, A&A, 314, 258

Ridge, N. A., Schnee, S. L., Goodman, A. A., & Foster, J. B. 2006, ApJ, 643, 932

Román-Zúñiga, C., Lada, C. J., & Alves, J. F. 2009, ApJ, 704, 183

Román-Zúñiga, C., Alves, J. F., Lada, C. J., & Lombardi, M. 2010, ApJ, 725, 2232

Román-Zúñiga, C., Frau, P., Girart, J. M., & Alves, J. F. 2012, ApJ, 747, 149

Sandell, G., Aspin, C., Duncan, W. D., Russell, A. P. G., Robson, E. I. 1991, ApJ, 376, L17

Shu, F. H. 1977, ApJ, 214, 488

Shu, F. H., Adams, F. C., & Lizano, S. 1987, ARA&A, 25, 23

Spitzer, L., Jr. 1962, Physics of Fully Ionized Gases (2d ed., New York: Interscience)

Stahler, S. W., & Palla, F. 2005, The Formation of Stars, by Steven W. Stahler, Francesco Palla, pp. 865. ISBN 3-527-40559-3. Wiley-VCH , January 2005

Stephenson, C. B., & Sanduleak, N. 1977, ApJS, 33, 459

Tafalla, M., Myers, P. C., Caselli, P., Walmsley, C. M., & Comito, C. 2002, ApJ, 569, 815

Tafalla, M., & Santiago, J. 2004, A&A, 414, L53

Tang, Y.-W., Ho, P. T. P., Koch, P. M., et al. 2009, ApJ, 700, 251

Terebey, S., Shu, F. H., & Cassen, P. 1984, ApJ, 286, 529

The, P.-S. 1964, Contrib. Bosscha Obs., 27, 1

Tielens, A. G. G. M. 2005, The Physics and Chemistry of the Interstellar Medium, by A. G. G. M. Tielens, pp. . ISBN 0521826349. Cambridge, UK: Cambridge University Press, 2005

Tomisaka, K., Ikeuchi, S., & Nakamura, T. 1988, ApJ, 326, 208

Tomisaka, K., Ikeuchi, S., & Nakamura, T. 1988, ApJ, 335, 239

van Dishoeck, E. F. 2004, ARA&A, 42, 119

Walker, C. K., Adams, F. C., & Lada, C. J. 1990, ApJ, 349, 515

Walmsley, C. M., Flower, D. R., & Pineau des Forêts, G. 2004, A&A, 418, 1035

Weingartner, J. C., & Draine, B. T. 2001, ApJS, 134, 263

Whittet, D. C. B., Shenoy, S. S., Bergin, E. A., et al. 2007, ApJ, 655, 332

Williams, J. P., Blitz, L., & McKee, C. F. 2000, in *Protostars and Planets IV*, ed. V. Mannings *et al.* (Tucson: Univ. of Arizona Press) pp 97-120